Sigrun Henkenjohann

Dissertation

Highly Sensitive Fluorescent Methods for the Detection of Enzymes and the Determination of their Activity by Means of Specific Hydrolases

Applied Laser Physics and Laser Spectroscopy
Faculty of Physics - Bielefeld University

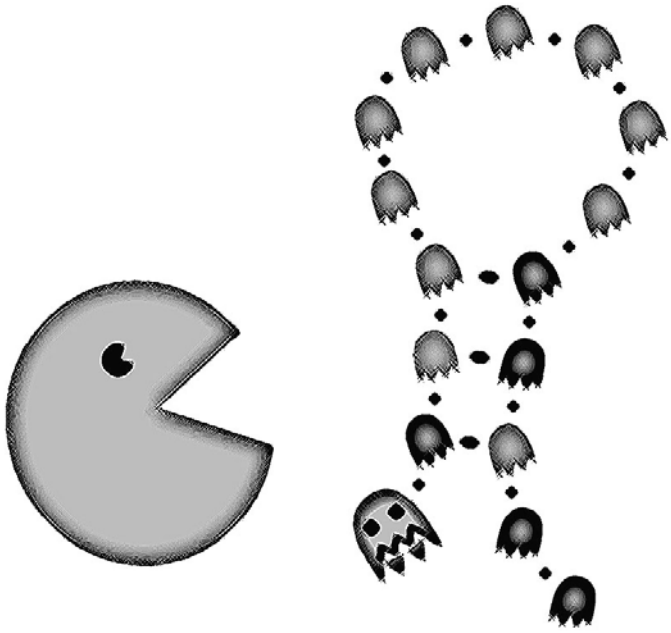

Printed on non-aging, wood- and acid-free paper according to DIN-ISO 9706.
Gedruckt auf alterungsbeständigem, holz- und säurefreiem Papier gemäß DIN-ISO 9706.

Dissertation

Highly Sensitive Fluorescent Methods for the Detection of Enzymes and the Determination of their Activity by Means of Specific Hydrolases

Sigrun Henkenjohann

December 8th 2009

Applied Laser Physics & Laser Spectroscopy
Department of Physics
Bielefeld University

Reviewer:
Markus Sauer
Andreas Hütten

Zusammenfassung

In sehr vielen biologischen und medizinischen Prozessen nehmen Enzyme eine wichtige Schlüsselfunktion ein [1–27], auf die Einfluss genommen werden kann, wenn die betreffenden Enzyme gesteuert werden können. Dies jedoch verlangt nach einem genauen Verständnis der enzymatischen Vorgänge, welches mithilfe der Fluoreszensmikroskopie verbessert werden kann. In dieser Arbeit werden zwei unterschiedliche Ansätze zur fluoreszenten Enzymologie für die Carboxypeptidase A und vier verschiedene Nukleasen vorgestellt und ausgewertet.

Der erste dieser Ansätze nutzt fluoreszierende Enzymsubstrate, die sich die intrinsischen elektronspendenden Eigenschaften der natürlich vorkommenden Aminosäure Tryptophan und der Nukleinsäure Guanosin zu Nutze machen [28–34].

Verschiedene Peptidsubstrate für die Untersuchung der Carboxypeptidase A, und zwei Gruppen von sogenannten '*smart probes*' für die Untersuchung der DNaseI, DNaseII, S1-Nuklease und der DNaseX werden vorgestellt, charakterisiert und im weiteren Verlauf für die Analyse spezifischer Enzymeigenschaften angewandt. Schon kleine Unterschiede in Amino- und Nukleinsäuresequenzen dieser Substrate führen zu großen Veränderungen der relativen Quantenausbeuten, des Hitzeverhaltens der Substrate und des Enzymumsatzes. Die fluoreszenten Substrate werden genutzt, um den Effekt des angebrachten Farbstoffs auf die Akzeptanz und die Umsatzgeschwindigkeit durch das Enzym zu bestimmen. In dieser Arbeit werden außerdem Untersuchungen zu thermischen Eigenschaften der Carboxypeptidase A, der DNaseI und der DNaseX anhand einzelner Messungen bei unterschiedlichen Temperaturen und durch eine innovative Methode, die sich lange stetige Phasen in der Enzymkinetik zu Nutze macht, vorgestellt. Weiterhin wird die Anwendbarkeit fluoreszenter Substrate für die Ermittlung von Michaelis-Menten Parametern und für Messungen auf Einzelmolekülebene sowie in lebenden Zellen belegt.

Der zweite vorgestellte Ansatz macht von der Enzym-Immunofärbung Gebrauch. Hier wird eine optimierte Färbemethode für die Detektion und Lokalisierung eines spezifischen Enzyms in einer Vielzahl nativer Zelllinien ange-

wandt. Außerdem wird eine modifizierte Nieren-Zelllinie in ihrem spezifischen Enzym-Expressionsverhalten mithilfe der konfokalen Fluoreszenzmikroskopie, sowie durch die hochauflösende *d*STORM Methode untersucht [35].

Die vorgestellten fluoreszenten Methoden unterscheiden sich sehr stark in ihrem Wesen, ihrer Anwendbarkeit und in ihren möglichen Ergebnissen. Nichts desto trotz können sie effizient kombiniert werden und somit die Untersuchung einer Vielzahl biologischer und medizinischer Fragestellungen ermöglichen, was in dieser Arbeit erfolgreich präsentiert wird.

Abstract

Enzymes engage key roles in a wide variety of important physical and medical processes [1–27], which thus can be altered by manipulating the behavior of enzymes in charge. The capability for manipulation requires an exact understanding of enzymatic operation modes though, which can be increased by employing fluorescence microscopy. In this work, two approaches for fluorescence based enzyme research are presented and evaluated for Carboxypeptidase A and four different nucleases.

The first presented approach uses fluorescent enzyme substrates, which take advantage of intrinsic electron donating properties of the naturally occurring amino acid tryptophan and the nucleic acid guanosine [28–34].

Several peptide substrates for Carboxypeptidase A and two sets of *smart probes* for DNaseI, DNaseII, S1-Nuclease and DNaseX are introduced, characterized and, furthermore, utilized for the investigation of specific enzyme characteristics. Even small amino and nucleic acid sequence alterations of these substrates are found to result in strong differences concerning relative fluorescence quantum yields, thermal substrate behaviors and enzyme procession velocities. With these fluorescent substrates, the effect of the attached label on enzyme acceptance and velocities is examined. Furthermore, evaluations of the thermal characteristics of Carboxypeptidase A, DNaseI and DNaseX are presented by means of single measurements at various temperatures and by a novel approach, utilizing long steady state kinetics. Additionally, the suitability of fluorescent substrates for the determination of Michaelis-Menten parameters and for enzyme examinations on a single molecule scale and in living cells is proved.

The presented second approach is established on the method of enzyme immunolabeling. Here, an optimized labeling method is utilized for the detection and localization of a specific enzyme in a variety of native cell lines. Furthermore, a modified kidney cell line is examined in its specific enzyme expression characteristics with confocal fluorescence microscopy as well as with the high resolution *d*STORM method [35].

The demonstrated fluorescent approaches vary distinctly in their nature,

suitability and obtainable results. Still, they can be efficiently combined to diminish any disadvantage and allow research on a wide range of biological and medical questions, which will first be described in this work.

Contents

Abbreviations

K_M	Michaelis-Menten constant
v_{max}	maximum reaction velocity
*d*STORM	direct Stochastically Optical Reconstruction Microscopy
E. coli	*Escheria coli*
AFM	Atomic Force Microscopy
Antp	Antennapedia
AOTF	Acousto-Optical Tunable Filter
Ar^+	Argon Ionen
Asp	Aspartic acid
BSA	Bovine Serum Albumin
C-terminus	Carboxyl-terminus
CCD	Charge-Coupled Device
CPA	Carboxypeptidase A
CPP	Cell-Penetrating Peptide
DNA	Deoxyribonucleic Acid
ds	double stranded
EC	Enzyme Commission
ELISA	Enzyme-linked Immunosorbent Assay
EMCCD	Electron-Multiplying Charge-Coupled Device

FRET	Fluorescence Resonance Energy Transfer
GFP	Green Fluorescent Protein
Glu	Glutamic acid
Gly	Glycine
GPI	Glycosylphosphatidylinositol
HBSS	Hanks' Balanced Salt Solution
HEK	Human Embryonic Kidney
HeLa	Henrietta Lacks
HeNe	Helium Neon
His	Histidine
HPLC	High Performance Liquid Chromatograph
HRP	Horse Radish Peroxidase
kDa	kilo Dalton
Kr^+	Krypton Ionen
LSM	Laser Scanning Microscope
MEA	Mercaptoethylamine
NA	Numerical Aperture
NGS	Normal Goat Serum
NMR	Nuclear Magnetic Resonance
PBS	Phosphate Buffered Saline
PET	Photoninduced Electron Transfer
Phe	Phenylalanine
PMT	Photomultiplier Tube

PNG	Portable Network Graphics
PSF	Point Spread Function
SEM	Scanning Electron Microscopy
SP	*Smart Probes*
ss	single stranded
STED	Stimulated Emission Depletion
STORM	Stochastical Optical Reconstruction Microscopy
TEM	Transmission Electron Microscopy
TIRF	Total Internal Reflection Fluorescence
Trp	Tryptophan

List of Figures

List of Tables

1 Introduction

Enzymes are a fundamental principle of life, because they lower required energy barriers that have to be surpassed in a high percentage of biological processes. Therefore, enzymes take over key roles in cell functioning and in genetic engineering. Besides their relevance in these processes, enzymes have become of great importance in diagnostics and medical treatments, since many different enzymes have been related to an immense number of even the severest of diseases - either in respect to their genesis, their causes, their detection or their treatment methods. In 2007, for example, Sarkar *et al.* presented a recombinase[1], which excises integrated HIV pro-viral DNA from the genome of infected cells [1], promising an efficient and precise cure for the Acquired Immune Deficiency Syndrome (AIDS).

One year later, Hanna *et al.* described a possibility of controlling Calpain, an enzyme involved in stroke and heart disease, which could be utilized to minimize the essentially hazardous sanitary aftermath [2]. Also, there have been numerous associations with different enzymes to cancer, e.g. the Wild-type p53-Induced Phosphatase 1 (WIP1) [27], the Anti-Plasmin Cleaving Enzyme (APCE) [26], the triboleum castaneum telomerase catalytic subunit (TERT) [25] and various types of nucleases [3–24].

When a native enzyme is first associated with a certain disease, usually, its precise function and its outcome are completely vague. In some cases even the question arises, whether the enzyme only developed upon the occurrence of the disease and whether the enzyme caused it, or was caused by it. Also, the temporal enzyme concentration can be linked to, or even evoke the process of the disease.

Amongst the nuclease associations to cancer, a lot of them describe variant nuclease levels in miscellaneous compartments of the human organism [4, 5, 8–10, 14–16, 18, 19, 22]. A favorite candidate for these correlations is DNaseI, a 31 kDa globular hydrolase, depicted in figure 1.1.

[1] This artificial recombinase is called 'Tre' recombinase in respect to its natural ancestor 'Cre' recombinase.

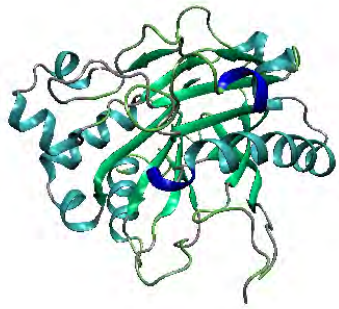

Figure 1.1: Crystal structure of DNaseI, determined by X-ray diffraction with a resolution of 1.6 Å [36].

In 1996, Coy *et al.* detected the enzyme DNaseX, named after its localization on the human X-chromosome. This nuclease was found to have a high homology to DNaseI in respect to their nucleotide and amino acid levels, as well as their exon-intron boundaries. Therefore, it was suggested, that both enzymes are derived from a common ancestor and execute similar functions in the human body [37].

In 2000, Los *et al.* suggested, that DNaseX may be involved in apoptosis [38], which was further examined by Shiokawa *et al.* in 2001 [39], who found DNaseX transcripts in various types of healthy tissue. One year later, J.F. Coy and his colleague A. Poustka finally had enough evidence to claim a connection of DNaseX to early stages of cancer in their European Patent Application [40]. Despite intensive research by Shiokawa and others [41–44], this role has not been fully identified nor understood. Furthermore, early publications connecting DNaseI levels with cancer, might have actually also monitored DNaseX when examining DNaseI levels, regarding the fact that detection methods have advanced immensely only in the past few years.

Summing up, there is a high potential for the utilization of DNaseX in the detection, classification and maybe even the treatment of cancer. To reach that, though, many questions need to be answered: How does DNaseX occurrence correlate with cancer stages? Is DNaseX occurrence cancer-induced? Does DNaseX represent an autogenetic defense mechanism against cancer, or is it actually a cancer inherent instrument in its fight against the immune

system? Which specific function does DNaseX have?

The search for answers to these questions and associations and their utilization, can only be accomplished with confident techniques for sensitive proof of presence and distinct activity determinations of the specific enzymes. Among the high number of investigation techniques, that are commonly applied in enzyme research, fluorescence microscopy is least invasive to enzymes but limited by appropriate fluorescent probes. In the ideal case, the molecular system signals selective recognition or binding events by a change or accumulation of fluorescence intensity, that can be conveniently transmitted into an electronic signal by the appropriate detector, with an efficiency of up to 80%. Another advantage of fluorescence microscopy for enzyme research relies on the fact, that many structural factors of fluorescent dyes and their intra- and intermolecular interactions, which finally control their fluorescence efficiencies are well understood.

Commercially available fluorescent substrates are usually not specific for a certain enzyme. Furthermore, they mostly consist of unpublished structures and are labeled with fluorophores in the green spectral range.

Custom made fluorescent samples, on the other hand, commonly consists of the enzyme's specific substrate, flanked by two fluorophores, showing fluorescence resonance energy transfer (FRET) at short distances between donor and acceptor. These substrates can be adapted to any desired spectral range and, therefore, mostly contain red-absorbing fluorophores [45–47], due to the low autofluorescence intensities at these wavelengths [48, 49].

However, FRET based substrates comprise several disadvantages due to their structure. First, a labeling of the natural substrate with two different fluorophores implies the need for two specific coupling reactions, which is rather complicated and expensive. Additionally, two chemical modifications on a natural substrate can generally hamper the affinity between substrate and enzyme, which can, therefore, diminish the experimental sensitivity. Furthermore, those substrates, that were improperly labeled with only one partner of the FRET pair, can seriously increase the background signal.

These problems can be reduced by the incorporation of only one appropriate fluorophore in combination with naturally occurring compounds of the specific enzyme substrate. At close vicinity, fluorophores like the oxazine derivatives MR 121 and Atto 655 show Photoinduced Electron Transfer (PET) with the naturally occurring amino acid tryptophan and the nucleotide

guanosine. If the quenching interactions between the fluorophore and tryptophan or guanosine diminish by specific target interactions, for example due to the cleavage of the connecting peptide or nucleotide by a hydrolytic enzyme, the fluorescence of the sensor is restored [30–33, 44, 50–56].

This method can elaborately be utilized for the development of a specific DNaseX substrate. A nucleotide sequence can be designed to form a DNA hairpin that comprises the preferred substrate sequence which is recognized by the enzyme in the double stranded or single stranded region of the hairpin. The attachment of an appropriate fluorophore onto the 5'-end and the incorporation of several guanosine residues at the 3'-end of the nucleotide sequence will result in efficient PET quenching, as long as the hairpin structure is intact.

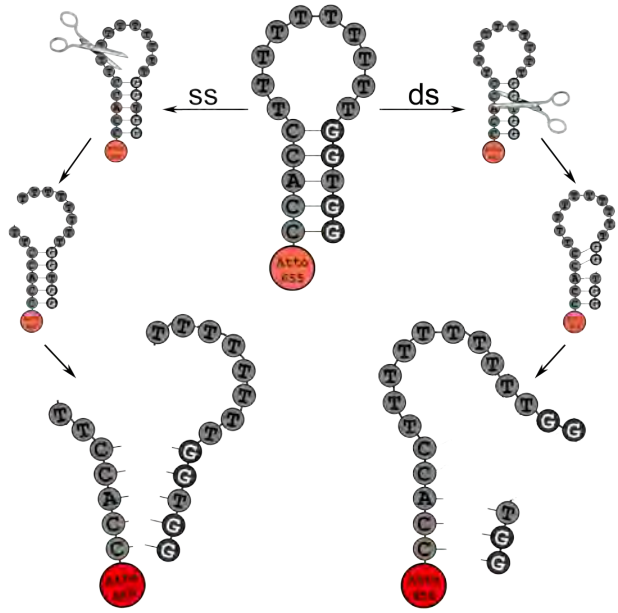

Figure 1.2: Examples of fluorescent hairpin substrates, initially quenched by photoinduced electron transfer to guanosine residues. Upon single stranded and double stranded scission, the hairpin structure is destroyed and fluorescence fully restored.

To date it is not known, whether DNaseX prefers double stranded (ds) or single stranded (ss) regions, nor whether there is a specific nucleotide sequence. Therefore, the hairpins have to be designed carefully, to function at a wide range of cleavage site possibilities. Once the DNaseX processes the hairpin at any position, the spatial contact between fluorophore and quenchers is supposed to get lost, restoring the full fluorescence intensity of the sensor (cf. figure 1.2).

Since tryptophan is an efficient photoinduced electron transfer quencher, the method can also be applied in peptides and therefore for peptidase research.

As a model, the very well studied Carboxypeptidase A (CPA) will be applied. This rather small and globular enzyme is part of the digestive system and secreted by the pancreas [57]. Carboxypeptidase A has not been directly related to any disease, it can be utilized, though, in the detection of other enzymes, connected to specific affections.

In 2004, Marme *et al.* demonstrated the principle by means of the HIV-1 protease[2] [31, 52], which is essential for the HI virus and only occurs upon HIV infection [58,59]. This enzyme is an endoprotease, recognizing substrates with a minimum length of seven amino acids residues [60, 61], with a high preferences for phenylalanine and tyrosine [62], but no specific cleaving position within this heptapeptide [63]. Therefore, the design of a PET quenched peptide probe, that immediately starts fluorescing upon HIV-1 protease scission is not conveniently possible, since either, the substrate would not be sufficiently quenched initially, or there would be a high risk that tryptophan residues stay in close vicinity to the fluorophore.

The elaborate solution to this, presented by Marme *et al.*, is the incorporation of consecutive tryptophans at close distance to the fluorophore and the attachment of three prolines to the C-terminus of the peptide substrate. The substrate cannot be processed solely by Carboxypeptidase A, since this enzyme is only capable of cleaving mono-, di- and tripeptides, beginning from the C-terminus [64–68], but shows no action on proline [65]. If the HIV-1 Protease is present alongside with Carboxypeptidase A, though, first the substrate can be degraded by HIV-1 protease, and is then consecutively processed by Carboxypeptidase A, until all tryptophans have been removed from the fluorophore and the HIV-sensor is fully fluorescent.

[2]HIV-1 protease is also named HIV-1 retropepsin.

Fluorescence based enzyme detection methods show an extraordinary sensitivity with the capability of revealing minute amounts of enzymes, when these PET sensors are carefully designed, as sketched in figure 1.3.

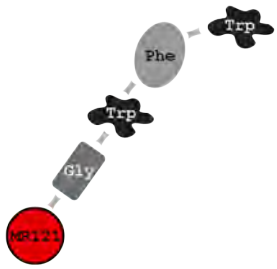

Figure 1.3: Exemplary fluorescently labeled peptide substrates, quenched efficiently by photoinduced electron transfer to tryptophan.

In this work the general validity of enzyme analysis with different PET based substrates will be shown for Carboxypeptidase A as a representative for proteases in general and for DNaseX, to demonstrate the experimental range, that PET sensors provide for a mostly unknown enzyme. Because of the stated DNaseX similarity to DNaseI, this nuclease will also be examined with the very same substrates. Furthermore, DNaseII and S1-Nuclease, both foreign to the DNaseI family, will be utilized to characterize the similarities of DNaseX and DNaseI.

As a prerequisite for their utilization in the presence of enzymes, all substrates will first be characterized, together with a FRET based DNA hairpin and a commercially available substrate of unknown structure. In section 4.1.1, information about the spectral and thermal characteristics, as well as the relative fluorescence quantum yields in the initial states will be given for all tested enzyme substrates. In section 4.1.2, the temporal fluorescence intensity profiles of these substrates in presence of their corresponding enzymes will be presented and discussed, before Michaelis-Menten kinetics will be focused on with one combinational example in section 4.1.3.

When dealing with a chemically modified natural enzyme substrate, of

course the question about modification effects to enzyme acceptance has to be addressed. This will be done for Carboxypeptidase A and its best suited PET substrate MR 121 - Gly - Trp, as well as for DNaseI and its evolutionary most important PET sensor SP2 in section 4.1.4.

In section 4.1.5, different ways for the examination of ideal measurement settings will be presented in respect to Carboxypeptidase A, DNaseI and DNaseX with their appropriate PET substrates. Next to a common way of testing their optimum working temperature, a novel approach, taking advantage of the easy to monitor steady state fluorescence based kinetics, will be introduced. Furthermore, the presented PET sensors will be proven to be generally suitable for single molecule measurements in section 4.1.6 and in heterogeneous samples like living cells in section 4.1.7.

In this last section it will be seen, though, that PET sensors also bare disadvantages. These drawbacks can be solved with another fluorescence based enzymology approach, which will be presented in the second part of this work.

Since there are a lot of enzymes that are able to process one and the same specific substrate, it is not possible, to account a certain enzymatic reaction to the enzyme of interest in a complex environment. Clinical tests for specific enzymes, nonetheless, need to take place in blood, sera, tissue or any other kind of heterogeneous sample. For this, the method of immunostaining has proven to yield fantastic results [69]. Specific antibodies recognize their target antigen even in highly divers samples. Additionally, these antigens are not unspecifically bound by foreign antibodies[3].

The best known fluorescence based immunohistochemical method is the Enzyme-Linked Immunosorbent Assay (ELISA), which has been simultaneously developed by two research groups in 1971 [70–72]. To date, several ELISA versions have emerged. The Sandwich-ELISA, that has first been described in 1976 [73], captures antigens by surface bound specific antibodies. These antigens are then again bound by a specific primary antibody. An enzyme-linked secondary antibody binds the primary antibody, before a substrate is added to the sample, which is converted by the added enzyme to a fluorimetric form. Since the antigen signal is strongly amplified by this enzyme, ELISAs are sensitive enough to detect antigen concentrations of down

[3]Indeed, there are cases, where antibodies bind wrong antigens, which is the case in any auto-immune deficiency.

to 10^{-13} M [74].

Despite, ELISAs also have a high risk of false positive signals[4]. Furthermore, the only task that can be accomplished with this method, is to find out about the existence of antigens in the examined sample. However, for enzyme research, it is not only of interest, whether the antigen is present in in native environments, but also where and how. Therefore, the sandwich ELISA method has to be adapted to native samples. Imagining the enzyme of interest to be solidly bound, may it be by membrane attachment or by the fixation of tissue, allows an attachment of a specific primary antibody, followed by a labeled secondary antibody as depicted in figure 1.4.

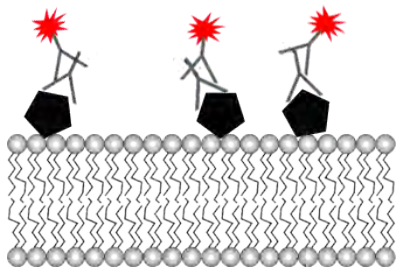

Figure 1.4: Indirect immunolabeling scheme. The enzymes (black pentagons) are solidly bound to a cell membrane. An attached specific primary antibody is indirectly labeled with a fluorophore tagged secondary antibody.

If specific antibody is available, also enzyme research is possible with this immunostaining method, as will be seen in this work. Furthermore, counterstaining procedures can be applied to localize cell membranes and nuclei.

Once a sample is labeled, it can easily be excited at different wavelengths with fluorescence microscopy methods. The most convenient for this research task, though, is the confocal fluorescence microscopy, showing a low background intensity due to detection volume limiting pinholes. Since the focus position can be varied not only axially, but also laterally, a three dimensional image of a sample can be obtained.

[4]One should bear the standard procedure of accomplishing a Western Blot test in any common positive HIV test in mind.

Since confocal microscopes allow an axial resolution determination of a few µm, the localization of labeled enzymes is easily possible, as can be seen in figure 1.5.

Within the last few years, several high resolution fluorescence methods have evolved, among them Stimulated Emission Depletion (STED) Microscopy [75], based on a confocal microscope, and the Stochastic Optical Reconstruction Microscopy (STORM) [76], based on a Total Internal Reflection Fluorescence (TIRF) Microscope. This method was further modified to *direct* STORM (*d*STORM) [35] using standard organic fluorophores, allowing a lateral resolution of down to 20 nm and, therefore, being able to reveal structures that cannot be obtained with a diffraction limited microscope.

In this work, both, the diffraction limited confocal microscope, as wells as the high resolution *d*STORM method was applied for the immunolabeling based detection of DNaseX in native cells in section 4.2.2, after examination of the labeling technique in section 4.2.1.

As a model system, a cell line with a DNaseX over-expression, was examined on a confocal microscope in section 4.2.3 as well as with the high resolution technique in section 4.2.4 for their occurrence and assembly.

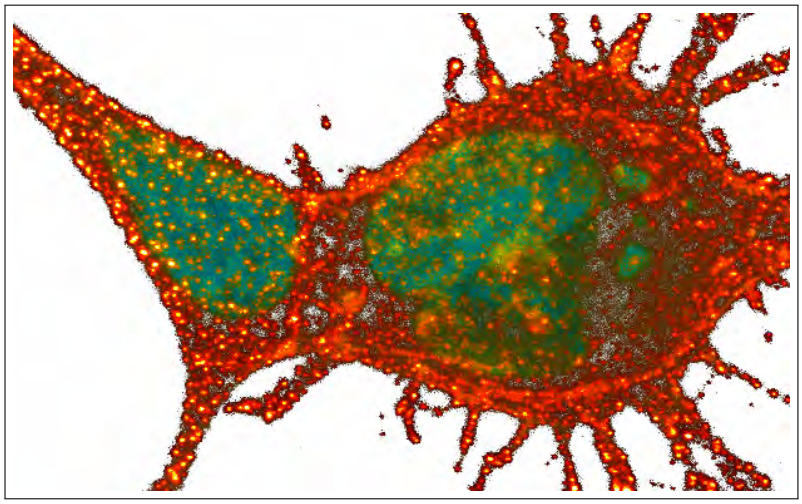

Figure 1.5: Exemplary immunolabeling of HEK 293T cells. The nucleus is labeled with a DNA intercalator and depicted in cyan, the hardly visible cytoskeleton, depicted in grey, is labeled via phalloidin while the red signal results from indirect immunolabeling of membrane bound proteins. The image shows a maximum intensity projection of 50 different cell layers with a distance of 0.3 µm and a dimension of 65 µm x 40 µm.

2 Theoretical Background

This interdisciplinary work naturally utilizes many fundamentals. The following introduction to theoretical backgrounds covers the principles of fluorescence, the corresponding spectroscopy and the microscopic methods, as well as a biological introduction to enzymes. In the end of this chapter, the possibilities and hazards of fluorescence based enzyme research will be presented.

2.1 Principles of Fluorescence

An electron in the energetically lowest possible state of a molecule, the ground state, can be elevated to a higher excited state by the absorption of a photon. The absorption of light can be measured using the Lambert-Beer law:

$$I = I_0 \cdot e^{\varepsilon \cdot C \cdot d}, \tag{2.1}$$

where I_0 is the initial and I the transmitted light intensity, C the sample concentration, d the light path length in the sample and ε the specimens specific absorption coefficient for the applied wavelength.

The complete excitation energy of a molecule does not only consist of the electron excitation but, furthermore, also of rotational and vibrational excitations, which results in the familiar band spectra for molecules instead of the discrete spectra known from single atoms. Rotational energy transitions take place in the far infrared to microwave range and, therefore, usually do not display in electronic energy transition illustrations like the Jablonski diagram in figure 2.1. Vibrational energy transitions, though, take place in the infrared and, therefore, strongly account to the familiar continuous spectra.

When a molecule absorbs a photon of the energy

$$E = h \cdot \nu, \tag{2.2}$$

with the Planck constant h and the frequency ν, an electron is most often not only lifted to the lowest possible energy state, but to a higher excited vibrational state of the 1st (S_1) or nth (S_n) excited electronic state, dependent on the available photon energy and the energy gaps in the concerned molecule. This light absorption process (Abs) happens in the range of femtoseconds.

Due to overlaps of the different vibrational states, the electron relaxes to the lowest excited energy state with the radiation free release of the energy E_- in a timescale of picoseconds. This is known as internal conversion (IC) and is a prerequisite for the *Kasha rule*, which says, that a molecule in condensed phase can only emit out of the lowest excited electronic energy state.

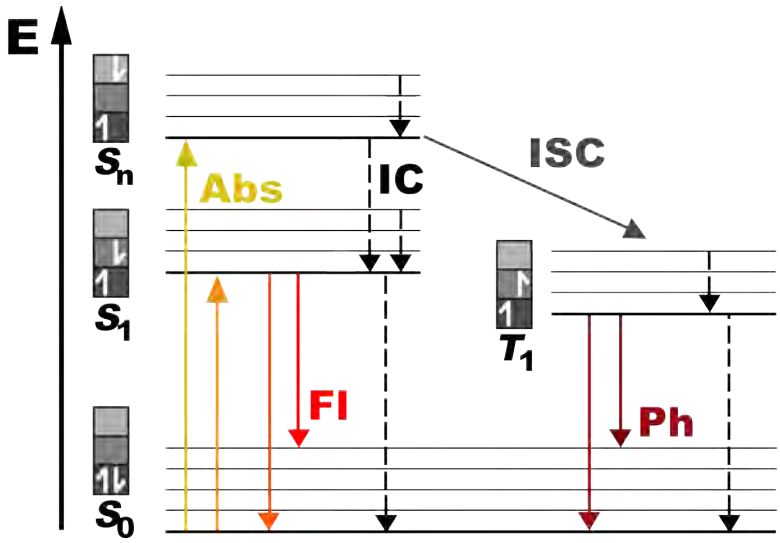

Figure 2.1: Jablonski diagram, describing the possible electronic transitions of a molecule: absorption (Abs), inner conversion (IC), fluorescence emission (Fl), intersystem crossing (ISC) and phosphorescence (Ph).

The emission from this lowest excited singlet state (S_1) to the ground state (S_0) occurs within nanoseconds under emission of radiation, called *Fluorescence* (Fl). The emitted photon carries the energy E^*, with

$$E - E_- = E^*. \tag{2.3}$$

Therefore, the maintained energy is composed of

$$E^* = h \cdot \nu^*, \tag{2.4}$$

with

$$\nu^* \leq \nu. \tag{2.5}$$

Thus, the emitted light most often has a shorter wavelength than the absorbed light, which is called the *Stokes Shift*. For the absorption as well as the emission of photons, the *Franck-Condon Principle* applies, which gives information on probabilities for certain transitions. Since electron transitions are fast in comparison to nucleic movements, the position of nuclear coordinates does not change in an electronic transition (Born - Oppenheimer approximation). Therefore, these transitions are plotted vertically in the Franck-Condon diagram, depicted in figure 2.2 [77].

The graph shows, that transitions are most likely to occur if the two vibrational wave functions overlap significantly. These varying transition probabilities result in an inhomogeneous distribution of photonic energies, that are absorbed and emitted, as can be seen in figure 2.3. Furthermore, the Franck-Condon principle yields a reflection of each resulting absorption peak in the emission spectrum, theoretically resulting in the complete mirroring of absorption and emission spectra.

In the described energetic cycle, each absorbed photon finally results in the emission of fluorescence. Therefore, the quantum yield, defined as ratio of emitted to absorbed quanta, equals 1. Practically, this is a vary rare occasion, though, because there are a number of radiation free competitive processes.

Figure 2.1 shows a transition from an excited electronic singlet state to an energetically lower triplet state, named intersystem crossing (ISC). This transition implies the need of a change in spin orientation, which is quantum mechanically forbidden. Once the electron is in the triplet state, it can relax to the ground state under emission of radiation by another spin transition, called phosphorescence (Ph). Since this, again, is not allowed, the lifetime of this state is comparably long. Furthermore, the electron in the first triplet state can also be excited to higher triplet states and back to the n^{th} singlet

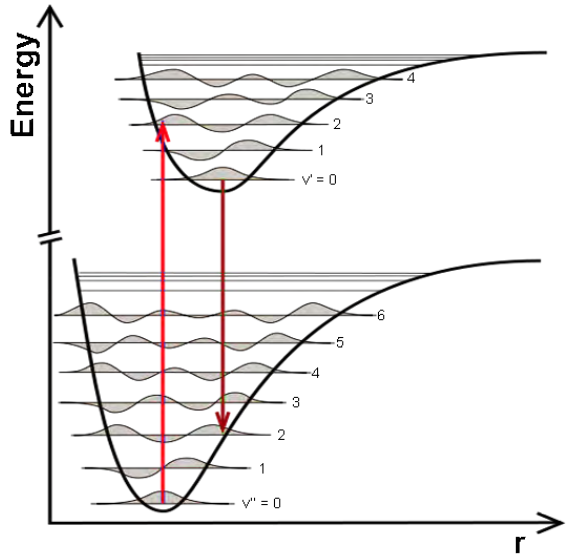

Figure 2.2: Franck-Condon diagram. Possible transitions between electronic states of a molecule most often occur between overlaps of vibrational wave functions. Transitions happen too fast for the nuclear distance r to change.

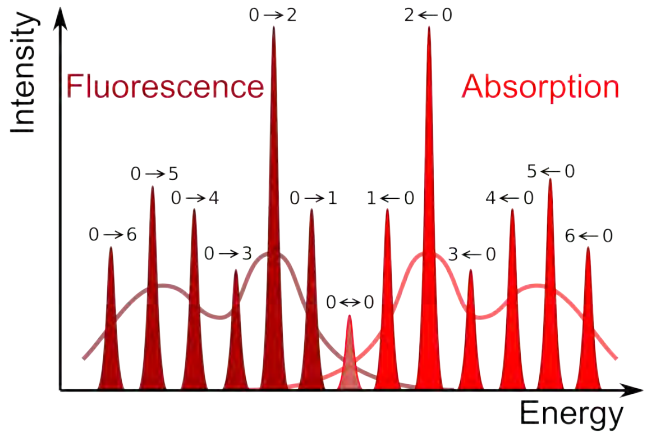

Figure 2.3: Probabilities of electronic transitions in absorption and emission processes (cf. figure 2.2). Excitation and emission probabilities are mirrored, as well as the resulting spectra.

state, undergoing inner conversion again. If the electron then relaxes to the ground state, the process is called delayed fluorescence [49, 78].

Apart from intersystem crossing, the emission of a fluorescence photon can also be prevented by quenching mechanisms, which will be introduced in section 2.2.2.

2.2 Fluorescence Spectroscopy

Every single molecule has its own specific composition of electronic and vibrational states. This results in the fact, that each molecule has its specific absorption and emission spectra, which are not necessarily in the visible range of electromagnetic radiation. Additionally, the probability for competitive processes greatly depends on the molecular electronic states, which effects the specific quantum yields.

2.2.1 Fluorophores

Molecules with an emission spectrum in the visible range and a high quantum yield are generally called fluorophores. There are natural fluorophores like the Green Fluorescent Protein (GFP) [79, 80], which is shown in figure 2.4.

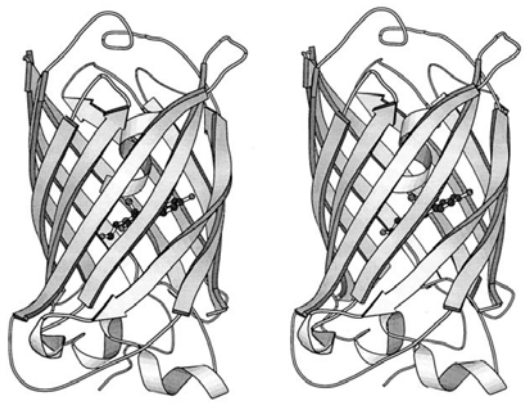

Figure 2.4: Stereo view of the green fluorescent protein 'GFP' [79].

This very popular fluorophore has a quantum yield of 0.72 [81] and was found

in the jellyfish *Aequorea victoria*, where it is excited by another chromophore (aequorin) via FRET (see section 2.2.2) [82].

Fluorescent proteins generally have the great advantage to be applicable for the fusion with other proteins, allowing a specific intrinsic labeling of a protein of interest by the examined organism itself. Still, these natural fluorophores generally have disadvantages in their size, quantum yields and photostability.

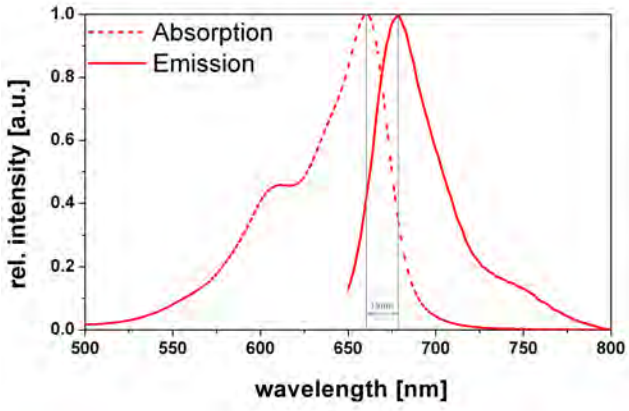

a) absorption and emission spectra

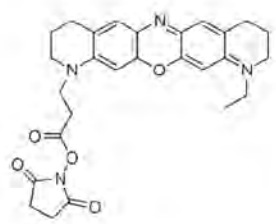

b) chemical structure

Figure 2.5: Spectra and chemical structure of the artificial fluorophore MR 121.

Therefore, a high number of artificial fluorophores have been designed. Figure 2.5 shows the chemical structure and the spectra of one of these fluorophores, named MR 121. As can be clearly seen, there is a stokes shift (see section 2.1) of 19 nm between absorption and emission maxima.

2.2.2 Fluorescence Quenching

There is a variety of processes that diminish fluorescence intensities, which is called *quenching*. Fluorescence decrease upon *collisional quenching*, that occurs, when an excited fluorophore is hit by another molecule in the solution, is mathematically described with the *Stern-Volmer equation*:

$$\frac{F_0}{F} = 1 + K \cdot [Q] = 1 + k_q \cdot \tau_0 \cdot [Q], \tag{2.6}$$

with F_0 and F are the initial and the remaining fluorescence intensity, K the Stern-Volmer quenching constant, $[Q]$ the quencher concentration, k_q the bimolecular quenching constant and τ_0 the unquenched lifetime of the fluorophore.

The most famous collisional quencher is molecular oxygen [83], which is the reason for its removal from surrounding buffer in certain measurements (cf. section 2.3.2).

Aside from this *dynamic* collisional quenching, fluorophores and quenchers can build non fluorescent complexes, which is then entitled *static quenching*. The fluorescence yield upon static quenching can be described by

$$\frac{F_0}{F} = 1 + K_S \cdot [Q], \tag{2.7}$$

with the association constant K_S. This constant can be expressed by the given concentrations of the uncomplexed fluorophore F, the quencher Q and the total fluorophore concentration F_0.

$$K_S = \frac{[F_0]}{[F] \cdot [Q]} - \frac{1}{[Q]}. \tag{2.8}$$

A way to distinguish between dynamic and static quenching is to examine the absorption spectra of the quenched samples in contrast to unquenched fluorophore: While dynamic quenching only affects fluorophores in the excited state, static quenching interferes with the excitation, resulting in a change of absorption intensities. Fluorophores can be quenched dynamically and statically by the same quencher, though. This can be determined by nonlinear behavior in a *Stern-Volmer plot*, where the fraction of quenched fluorophore is plotted against the quencher concentration.

In general, quenching processes are strongly distance dependent, as can be expressed by the formula

$$k_E(r) = A \cdot e^{-\beta \cdot (r - r_c)}, \tag{2.9}$$

with $k_E(r)$ the quenching rate at a distance r between fluorophore and quencher, r_c the closest distance at molecular contact and A and β constants of $10^{13}s^{-1}$ and 1Å^{-1}.
The mechanisms, that explain quenching processes are various. There are intersystem crossing (or heavy atom effect), electron exchange (or dexter interactions) and *photoinduced electron transfer* (PET), of which only the latter is relevant in this work.

In PET, fluorophore and quencher form a complex, that shows two electron exchange processes in two different trails.

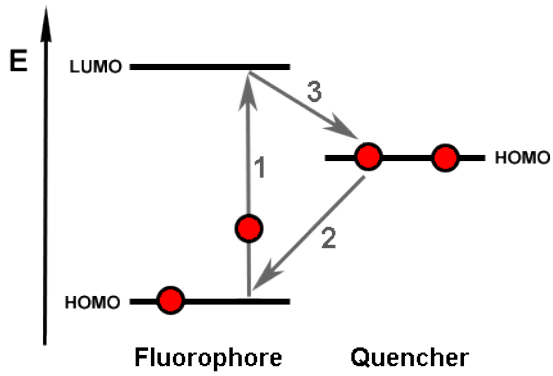

Figure 2.6: Photoinduced electron transfer between fluorophore and quencher. Here, the fluorophore acts as electron acceptor while the quencher donates an electron.

Either, the fluorophore is the electron donor and the quencher accepts the electron, or the fluorophore acts as electron acceptor, while the quencher is the electron donor, as depicted in figure 2.6. Here, the fluorophore is excited by a photon, which results in the elevation of an electron from the highest occupied molecular orbital (HOMO) to the lowest unoccupied molecular orbital (LUMO). Then, an electron from the quenchers highest occupied molecular orbital migrates to the single occupied molecular orbital. The electron in the fluorophores excited state, therefore, cannot relax to its parental state anymore, since this is already occupied. Because the quenchers single occupied molecular orbital is energetically favorable, the electron passes over to the quencher. All of these processes happen without the emission of radiation.

Photoinduced electron quenching does only occur at close contact between appropriate pairs, as the *Rehm-Weller equation* clarifies:

$$\Delta G_{CS} = E_{ox} - E_{red} - E_{0,0} - \frac{e^2}{\varepsilon \cdot d} \tag{2.10}$$

where ΔG_{CS} is the energy released, E_{ox} the oxidation potential, E_{red} the reduction potential and $E_{0,0}$ the fluorophore transition energy from ground to first excited state. The last term $\frac{e^2}{\varepsilon \cdot d}$ is the solvent effect with ε the dielectric constant and d the charge separation distance. This term is rather small though and is, therefore, often neglected.

The potentials of several chromophores and some natural compounds are given in table 2.1.

Table 2.1: Published redox properties of fluorophores, tryptophan (Trp), all nucleic acids and 7-Deaza-2'-deoxyguanosine [32, 50, 84–90]. For further information, see [56].

	E_{ox} $[V/SCE]$	E_{red} $[V/SCE]$	$E_{0,0}$ $[eV]$
R6G	1.39	- 0.95	2.27
MR 121	1.40	- 0.50	1.90
Atto 655[1]	1.40	- 0.50	1.90
Cy 5	0.82	- 0.88	1.88
Trp	0.81		
dG	1.25	<- 3.00	
dG[7]	0.95		
dC	1.90	- 2.59	
dA	1.72	- 2.76	
dT	1.87	- 2.42	

Obviously, MR 121 (as well as Atto 655) has a very high reduction potential at a comparably low transition energy. Among the naturally occurring nucleic

[1] Atto 655 is expected to have an identical structure and, therefore, very similar redox characteristics.

acids, guanosine has the lowest oxidation potential, which is even exceeded by its modification 7-Deaza-2'-deoxyguanosine. This is still overtopped by tryptophan, though.

Many of these combinations have been used for PET sensors, since photoinduced electron transfer is very limited in its distance and, therefore, gives an immediate response about contact loss [91–95]. In this work, the combination of MR 121 with Trp and of Atto 655 with dG and dG^7 have been employed. The energies for these reactions at neglected solvent effect are $\Delta G_{CS} = -0.15eV$ for Atto 655 with dG, $\Delta G_{CS} = -0.35eV$ with dG^7 and $\Delta G_{CS} = -0.59eV$ for MR 121 with Trp.

Whenever a fluorophore in an excited state is in close contact to a molecule, that has an absorption spectrum overlapping with the fluorophore emission spectrum, also *Fluorescence Resonance Energy Transfer* (FRET) by dipole-dipole interaction can occur. The FRET efficiency is determined by the spectral overlap and the distance r between the partners, as equation (2.11) shows.

$$E = \frac{R_0^6}{R_0^6 + r^6}, \tag{2.11}$$

where R_0 equals the *Förster radius*, which is the distance, at which energy transfer is 50% efficient. The Förster radius is related to the energy transfer rate $k_\tau(r)$ via

$$k_\tau(r) = \frac{1}{\tau_D} \cdot (\frac{R_0}{r})^6, \tag{2.12}$$

with the fluorescence donor lifetime τ_D in absence of the fluorescence acceptor and can furthermore be described with the dipole orientation factor κ^2:

$$R_0 = \frac{9 \cdot Q_0 \cdot ln10 \cdot \kappa^2 \cdot J}{128 \cdot \pi^5 \cdot n^4 \cdot N_A}, \tag{2.13}$$

where Q_0 is the donor fluorescence quantum yield in absence of the acceptor, J is the spectral overlap, n is the refractive index of the surrounding medium and N_A the Avogadro number.

Since the Förster distance is in the range from 3 to 6 nm, FRET can be efficiently used as a spectroscopic ruler [96] and for the determination of enzyme activity in a molecular beacon [51], as described in section 2.5 [49,78].

2.3 Fluorescence Microscopy

For as long as human beings roam the Earth, there has been research.
As most of the apparent facts had been discovered, mankind felt the urge for going deeper into detail. This bore many difficulties, though, regardless of the specific direction that was headed. In a lot of these cases, optical instruments could be utilized and aided various important discoveries. One of these directions was the query for small components of familiar structures, that could not be dissolved with the unaided human eye.

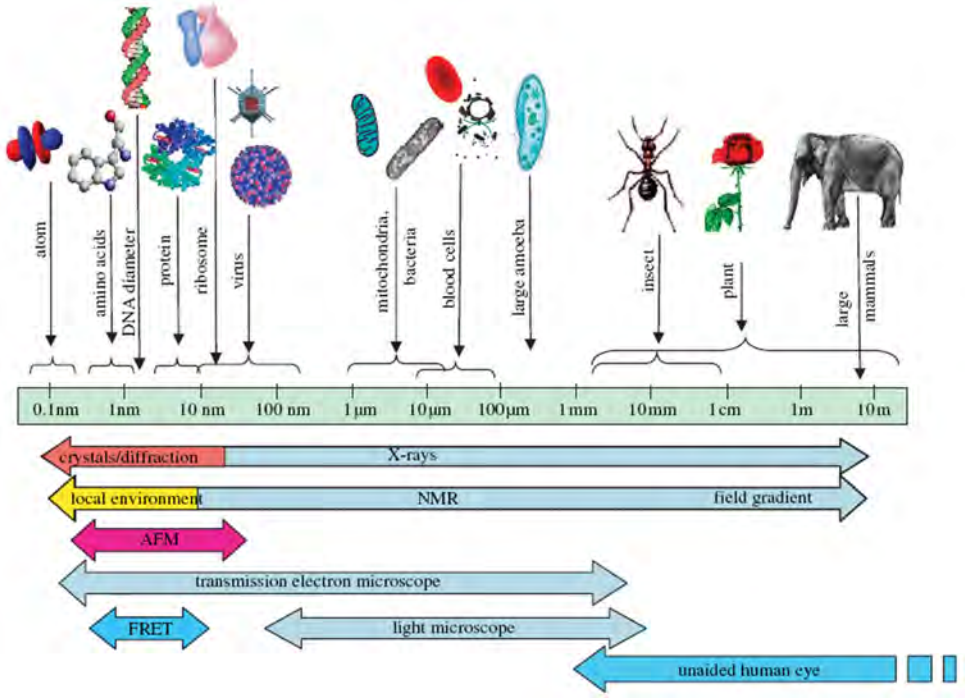

Figure 2.7: Size scale of different components of life with the appropriate detection methods [97].

As figure 2.7 shows, the human eye can dissolve structures down to one millimeter. Below that, auxiliary means have to be applied. Popular methods like X-ray Crystallography, Nuclear Magnetic Resonance (NMR) and Transmission Electron Microscopy (TEM) cover a wide range of sample dimensions, even down to less than a nanometer. As the Atomic Force Microscopy (AFM), that is only applicable for rather small samples, these methods are quite complex and invasive. The light microscope on the other hand, which has greatly evolved over the last 350 years, has become an indispensable method for applications down to several nanometers due to its harmlessness and easy handling. Among the different light microscopic methods, one of the most unlimited and sensitive is fluorescence microscopy. This approach only gained serious attention in the 1950s, although fluorescence had long been an issue by that time.

The drawback of this method lies in its nature, the nature of light. Since visible light has a wavelength of 300 nm to 700 nm, it is self-evident, that structures distinctly below this wavelength can generally not be dissolved. One solution to this is the utilization of FRET as spectroscopic rulers, as described in section 2.2.2. By now, though, there are even much wider applicable fluorescence microscopy means to enhance the natural resolution - or correctly speaking: to circumvent it.

2.3.1 Diffraction limited Techniques

A fluorescing molecule is distinctly smaller, than the wavelength of the photons, it emits. Since it can be regarded as a point light source, the light it emits is not aligned, which results in a fuzzy disk when imaged on a plane. This disk, called *Airy disk*, shows an inhomogeneous intensity distribution. This distribution is mathematically described by the *Point Spread Function* (PSF), a two dimensional Bessel function. An example of the Airy disc and its according PSF is given in figure 2.8.

The Airy disk radius from the center to the first minimum is the aspect that limits the resolution according to the *Rayleigh criterion*: Only if two point light sources are a minimum of the airy disk radius away from each other, it is possible to distinguish between these both. The radius r_{Airy} depends on the wavelength of fluorescence light λ, and the numerical aperture of the applied objective NA with

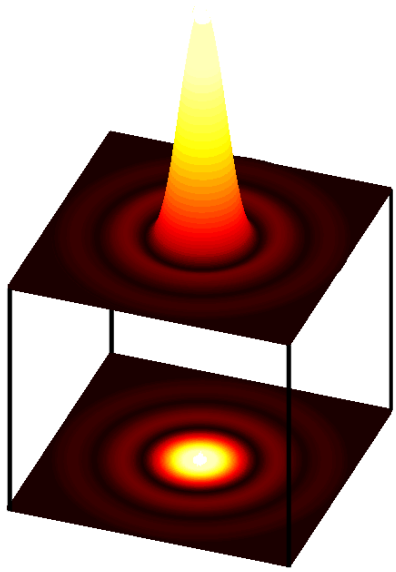

Figure 2.8: 2-dimensional Airy disc and according 3-dimensional point spread function.

$$r_{Airy} = 0.61 \cdot \frac{\lambda}{NA}. \tag{2.14}$$

The lateral resolution that can therefore be obtained for an object emitting fluorescence light of 680 nm with an objective of a numerical aperture of 1.4[2] is 296 nm and with an NA of 1.45[3] the lateral resolution is 286 nm.

The axial resolution, however, is distinctly worse, since it is determined with the formula

$$z_{min} = \frac{2 \cdot \lambda \cdot n}{(NA)^2}, \tag{2.15}$$

resulting in 957 nm for an objective with $NA = 1.45$ and 1027 nm for $NA = 1.40$.

[2] as is applied in this work in confocal microscopy
[3] as is applied in this work in TIRF microscopy

With a limitation of the detection volume, these scales can be lowered. One approach to this incorporates the utilization of total internal reflection and is, therefore, called Total Internal Reflection Fluorescence (TIRF) Microscopy.

Total Internal Reflection Fluorescence Microscopy

At the interface of two different media, a light beam changes its direction due to various refractive indices, following the Snell's law:

$$n_1 \cdot sin\theta_1 = n_2 \cdot sin\theta_2, \tag{2.16}$$

with n_i the refractive indices of the media and θ_i the beam angles in the different media, as depicted in figure 2.9.

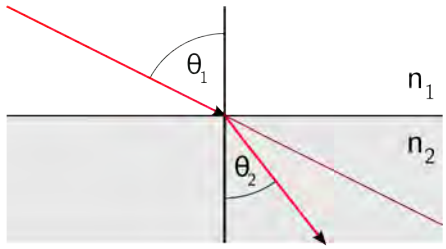

Figure 2.9: Light path variation upon change of refractive indices.

At an intersection from optically denser medium to a medium with lower refractive index, there is a critical angle, at which the beam does not enter the second medium. If the angle is increased further, the beam is totally reflected at the interface. This results in an evanescent wave in the medium with low refractive index, which has a penetration depth d of

$$d = \frac{\lambda_0}{4 \cdot \pi} \cdot (n_2^2 \cdot sin\theta_2 - n_1^2)^{-\frac{1}{2}}, \tag{2.17}$$

where λ_0 is the incident wavelength in a vacuum. For λ_0= 647 nm and an incident angle θ_2 of 72°, the penetration depth at a glass water interface accounts to 90 nm only, which is only a tenth of the axial resolution. The intensity I of the evanescent wave at a certain distance z from the surface naturally relates to the penetration depth with

$$I(z) = I_0 \cdot e^{\frac{-z}{d}}, \tag{2.18}$$

with the initial intensity I_0 at the interface.

This approach to limit the excitation volume has been successfully utilized in the total internal reflection fluorescence microscope, as is schematically depicted in figure 2.10.

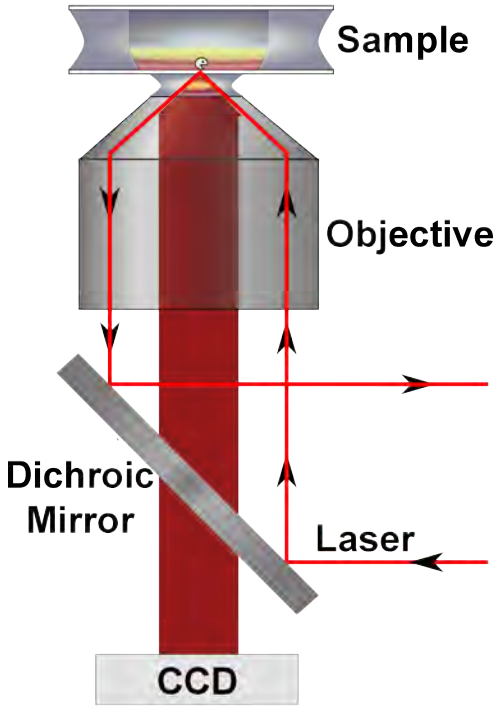

Figure 2.10: TIRF Microscope scheme.

A laser beam is focused onto the back focal plane of an objective with a high numerical aperture, after it has been reflected on a dichroic mirror. If the beam is coupled into the objective, close to its boundary, it experiences a collimating deflection, so that it hits the surface at an angle bigger than

the critical angle, yielding an evanescent field in the sample. The reflected laser beam is again reflected on the dichroic mirror and does, therefore, not interfere with the detection system. The fluorescence light is collected by the objective and passes the dichroic mirror due to the Stokes shift, so it can be detected by a subsequent Charge Coupled Device (CCD) camera.

Instead of limiting the excitation volume, it is also applicable to limit the detection volume, as it is done in the confocal fluorescence microscope.

Confocal Fluorescence Microscopy

Figure 2.11 shows a schematic drawing of a standard confocal microscope. The collimated laser beam is reflected on a dichroic mirror and focused by the objective. Therefore, a comparably wide area in the sample is excited. The resulting fluorescence is collected by the objective and passes the dichroic mirror due to the Stokes shift. A convex lens focuses exactly that part of the fluorescence light that was emitted at the laser focus position into the aperture of a pinhole. Any other fluorescence light origin is focused ahead or after this position, so that only a small fraction of defocused light passes the pinhole. The divergent fluorescence light is then focused onto a sensitive detector. With a movable specimen stage or a maneuverable optical path, samples can be scanned laterally and axially, yielding a pointwise detected 3-dimensional image of the sample.

The utilization of this confocal principle enhances the resolution, given by equation (2.14) and equation (2.15), by a factor of 1.41. This results in a lateral resolution of 210 nm and an axial resolution o 728 nm, respectively, for a objective with a numerical aperture of 1.4 and a fluorescence wavelength of 680 nm. A still distinctly higher resolution can be obtained with *superresolution techniques*.

2.3.2 Superresolution Techniques

The specimen, that need to be sampled quite often in fluorescence microscopy, are usually labeled with a high number of emitters. Two fluorophores in close distance to each other can only be resolved in conventional microscopy, if their distance is approximately the same as the wavelength of light they emit, though, while a single fluorophore can be resolved with a much higher accuracy, because the obtained intensity distribution in the Airy disk can be deconvolved with a two-dimensional Gaussian function.

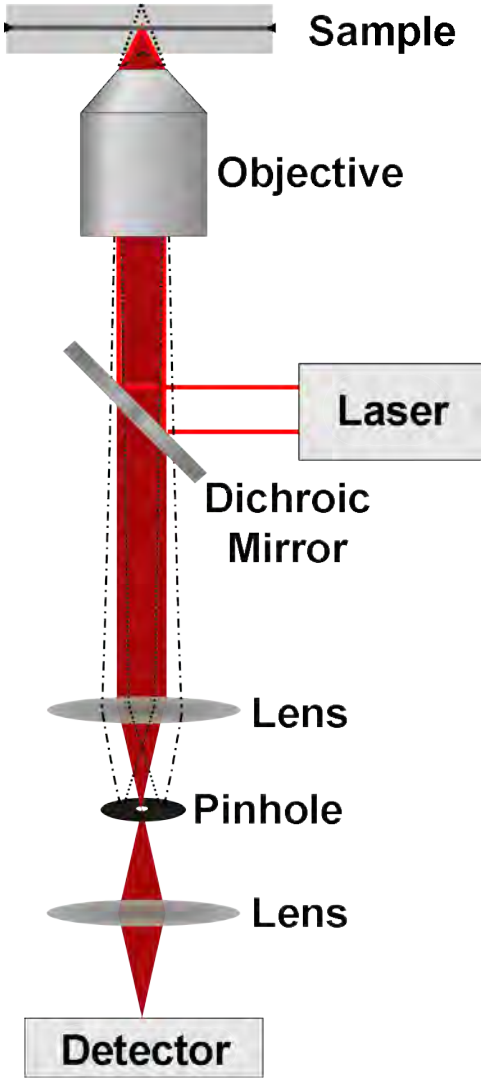

Figure 2.11: Standard confocal microscope.

Within the last years, there have been many efforts to detect single molecules in a highly labeled sample by taking advantage of photoswitching properties. Generally, there are two main directions for this, the spatial limitation of fluorescent molecules and the temporally limited emission of single fluorophores.

The most prominent spatially limiting high resolution method has been introduced by Hell *et al.* in 1994 [75]. This *Stimulated Emission Depletion* (STED) Microscopy is based on a standard confocal microscope. After the standard excitation, a secondary donut-shaped beam illuminates the very same spot, leading to the stimulated emission of the excited fluorophores in this area. Therefore, only a small volume of excited fluorophores is left to spontaneously fluoresce. This method leads to a strong resolution enhancement of down to 5.8 nm laterally [98].

The most popular method for resolution enhancement by temporally limited fluorophore emission is represented by the (direct) Stochastic Optical Reconstruction Microscopy (*d*)STORM.

(*direct*) Stochastic Optical Reconstruction Microscopy

In 2006, Bates *et al.* published a method that takes advantage of a stochastic photoswitching of all present fluorophores in a sample [76]. The deconvolution of the fluorescent signals can be used for a reconstruction the fluorophore positions and, therefore, yield an imaging resolution of 20 nm.

While the stochastic switching is achieved with an activator fluorophore in close proximity to the detected fluorophores in STORM, *d*STORM only utilizes an organic chromophore such as Cy5 or Alexa 647, as published by Heilemann *et al.* [35, 99].

The sample of interest can, therefore, be labeled with only a single fluorophore and imaged on a TIRF microscope. For the efficient photoswitching, quenching processes need to be inhibited. Therefore, oxygen has to be efficiently removed from the sample. By applying a strong laser power to read out the fluorophores, they are efficiently deexcited, which can be reversed with an additional irradiation at 514 nm with a comparably low intensity. This way, only a subset of molecules fluoresce simultaneously. The computational localization of a set of subsequent images then leads to a reconstructed *d*STORM image, as depicted in figure 2.12.

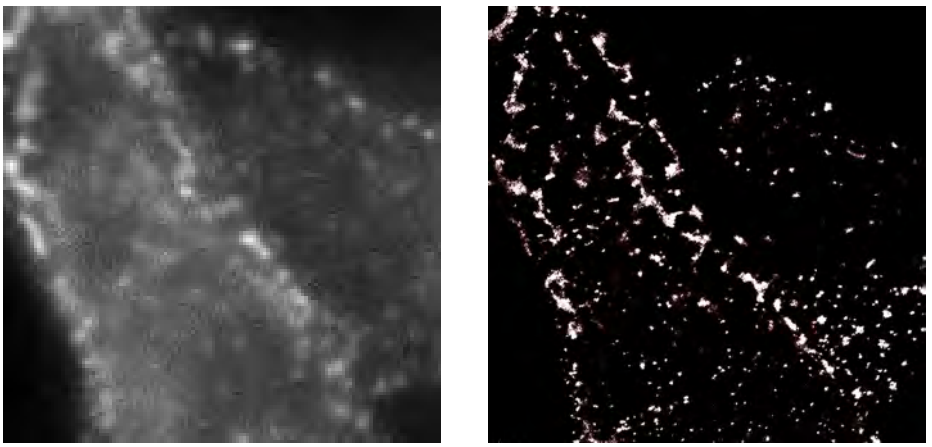

a) TIRF **b)** *d*STORM

Figure 2.12: Resolution enhancement by *d*STORM. The cell membrane is indirectly labeled with Alexa 647 and irradiated with 647 nm. While the TIRF image shows a blurry image of an overlap of two cell shapes, the dSTORM image reveals fluorophore agglomerations and hidden structures.

2.4 Enzymes

Enzymes are catalysts, which means that they accelerate reactions, that would mostly not happen on their own even within years.

As depicted in figure 2.13, a conversion from substrate to product requires a certain energy that has to be surpassed in order to take place (ΔE_A), while an enzyme lowers this required energy (to ΔE_C).

Most occurring reactions are catalyzed by a specially designated enzyme. The total number of existing enzymes can only be guessed. In the bacterium *Escheria coli* (*E. coli*), 1701 enzymes have been found, which represents two thirds of the proteins, that have been characterized for this organism so far [100]. Since *E. coli* are rather simple in contrast to any eukariotic organism, it can be assumed, that the number of enzymes is a lot bigger there.

Enzymes generally consist of chained α - amino acids, building secondary and tertiary structures, which results in the formation of the active site. These can most efficiently be determined by X-ray crystallography, where enzymes are mostly static due to the crystallization process. However, struc-

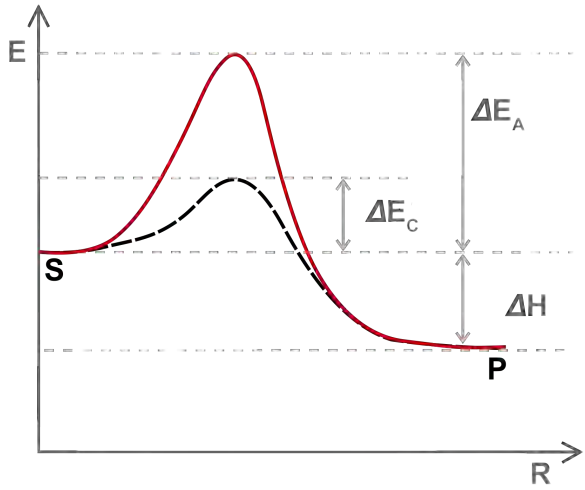

Figure 2.13: Energy barriers that have to be surpassed for a specific reaction from substrate (S) to product (P) with (black) and without (red) enzyme.

tural analysis by Nuclear Magnetic Resonance (NMR) revealed, that enzymes are rather flexible in solution [100], which is essential for the binding of substrates [101] (see section 2.4.1). The compact folded form of an enzyme is thermodynamically only a little more stable than the unfolded form [102]. Therefore, they can be easily unfolded ('denatured') via strong heat, extreme pH, detergents or high concentrations of urea or guanidium chloride [103–105] with a mostly sharp transition range [102, 106]. This enzyme unfolding process is mostly reversible on a very short time scale and has been widely studied in protein folding research [107].

However, an enzyme molecule does not act forever. In a living organism, each protein is continuously replaced as part of an intrinsic control mechanism. These enzyme 'turnovers' take place in a wide range of time scales and are, therefore, a characteristic feature for each specific enzyme. While the mechanisms of enzyme synthesis have been well understood, enzyme degradation is still a flowering aspect in research [100].

Enzymes have found a wide utilization in clinical and industrial aspects. Food, pharmaceutical and chemical industries utilize enzymes so naturally,

that mankind does not even take great notice anymore[4].

2.4.1 Interactions between Enzyme and Substrate

As individual as enzymes are, as individual are their substrates. There are enzymes, that can only catalyze one single reaction with a specific natural substrate, e.g. Caspase 1, that solely cleaves peptides carrying the recognition sequence Trp - Glu - His - Asp [110]. Other enzymes process huge varieties of substrates, for example those utilized in this work (see section 2.4).

An appropriate substrate needs to be noncovalently bound by the enzyme at its active site in order to be catalyzed. The easiest model for this binding is the *lock-and-key model*, where the substrate and eventual cofactors precisely fit in a provided binding pocket (see figure 2.14 a)). Mostly, enzymes undergo formational changes upon substrate binding though, which is called the *induced fit model* (see figure 2.14 b)).

The induced fit model supports the formation of catalytic intermediate states, because it alters the substrate conformation. An irreversible reaction scheme with a single intermediate is generally described as in equation (2.19).

$$E + S \underset{k_{-1}}{\overset{k_1}{\rightleftharpoons}} ES \xrightarrow{k_2} E + P \tag{2.19}$$

Here, E is the enzyme, S the substrate and P the product. The rate for the formation of the enzyme-substrate complex is expressed by k_1, k_{-1} expresses the dissociation rate and k_2 stands for the product formation rate.

In a kinetic process, these compounds vary in their concentrations over time, as depicted in figure 2.15.

In the beginning of the reaction, it needs a certain time for the enzymes to bind substrates. This first reaction phase is called *pre steady state*. After all enzyme molecules have bound a substrate molecule, the concentration of free enzyme is constantly negligible in the *steady state* phase, if two prerequisites are fulfilled:

- The overall substrate concentration is high in comparison to enzyme concentration.

[4]There is a high number of chapters and whole books dedicated to either of these aspects (e.g. [100, chapters 10 and 11], [108], [109] and many more) which should be referred to for further reading.

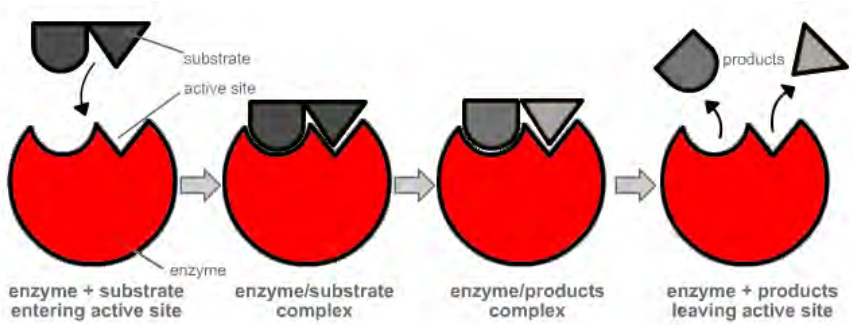

a) lock-and-key model

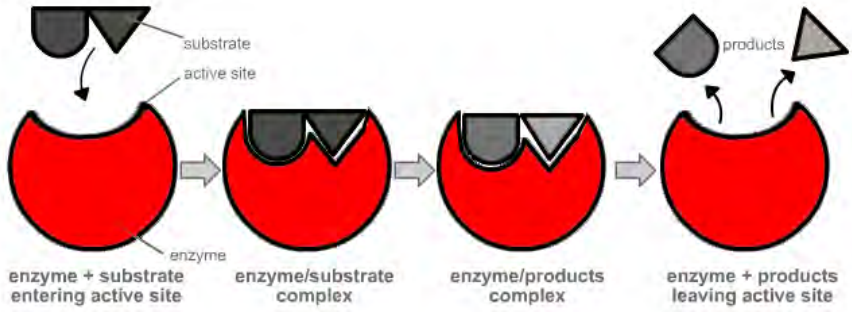

b) induced fit model

Figure 2.14: Standard models for the description of enzyme substrate complex conformation.

- The complex formation (k_1) is much faster than the complex decomposition ($k_{-1} + k_2$).

As soon as there is no more substrate available to instantly supply each freshly released enzyme molecule, the ES complex concentration slowly decreases until all enzyme molecules exist in the initial form.

Regarding the product formation in this course, the pre steady state phase only shows a little increase, while a linear increase is obtained in the steady state phase, before a saturation value is approached in the last reaction phase. A mathematical description of the temporal development of all components looks as follows:

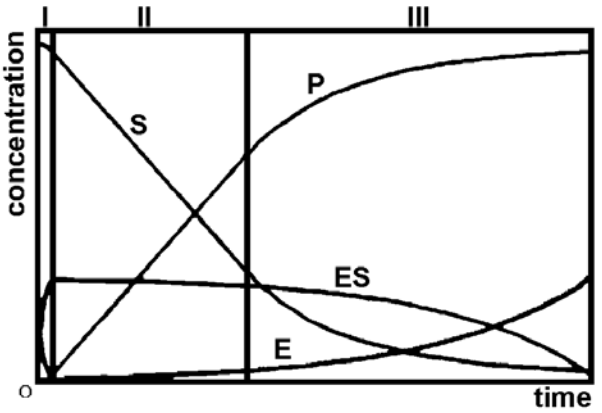

Figure 2.15: Temporal variations of substrate (S), product (P), enzyme (E) and enzyme substrate complex (ES) concentrations in an enzymatic reaction.

$$\frac{\delta[S]}{\delta t} = -k_1 \cdot [S] \cdot [E] + k_{-1} \cdot [ES] \tag{2.20}$$

$$\frac{\delta[E]}{\delta t} = -k_1 \cdot [S] \cdot [E] + (k_{-1} + k_2) \cdot [ES] \tag{2.21}$$

$$\frac{\delta[ES]}{\delta t} = k_1 \cdot [S] \cdot [E] - (k_{-1} + k_2) \cdot [ES] \tag{2.22}$$

$$\frac{\delta[P]}{\delta t} = k_2 \cdot [ES] =: v, \tag{2.23}$$

where v is the velocity of the reaction.
Employing the steady state prerequisites, equation (2.21) and equation (2.22) simplify to

$$\frac{\delta[E]}{\delta t} = 0 \tag{2.24}$$

and

$$\frac{\delta[ES]}{\delta t} = 0. \tag{2.25}$$

Therefore, this gives

$$0 = -k_1 \cdot [S] \cdot [E] + (k_{-1} + k_2) \cdot [ES]. \tag{2.26}$$

Since $[E] + [ES]$ equals the initial enzyme concentrations $[E_0]$, it follows from equation (2.26):

$$[ES] = \frac{k_1 \cdot [S] \cdot [E_0]}{k_1 \cdot [S] + k_{-1} + k_2} \tag{2.27}$$

The *maximum velocity* v_0 can be described with

$$v_0 := k_2 \cdot [ES]. \tag{2.28}$$

Setting the *Michaelis-Menten constant* K_M

$$K_M := \frac{k_{-1} + k_2}{k_1}, \tag{2.29}$$

it follows from equation (2.27) after multiplication with k_2 and insertion of v_0 and K_M:

$$v = \frac{v_0 \cdot [S]}{K_M + [S]} \tag{2.30}$$

which is called the *Michaelis-Menten equation*. K_M can be described as the substrate concentration, at which half the maximum speed of the reaction is obtained. Therefore, each combination of substrate and enzyme has its specific K_M value. It can be determined by measurement of starting velocities v_0 in individual kinetics of constant enzyme concentration but varying substrate concentrations. Plotting the determined starting velocities against

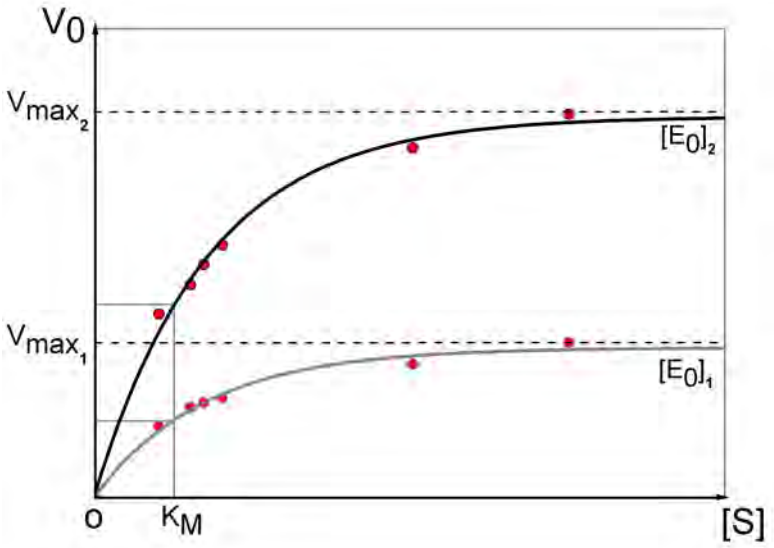

Figure 2.16: Theoretical Michaelis-Menten plot with two different enzyme concentrations.

the applied substrate concentrations, results in one hyperbola for each tested enzyme concentration, as presented in figure 2.16.

Here, v_{max} represents the maximum velocity for the observed reaction, which obviously corresponds to the enzyme concentration. The asymptote and therefore also K_M can be easily fit, if there is a distinct gradient.

If the gradient is missing, however, there are linearization methods, that still allow the determination of K_M and v_{max}. The most popular linearization types are shown in figure 2.17.

The linearization equations follow directly from the Michaelis-Menten evaluation (equation (2.30)).

$$\frac{1}{v_0} = \frac{K_M}{v_{max}} \cdot \frac{1}{[S]} + \frac{1}{v_{max}} \qquad \text{Lineweaver Burke} \tag{2.31}$$

$$v_0 = -K_M \cdot \frac{v_0}{[S]} + v_{max} \qquad \text{Eadie Hofstee} \tag{2.32}$$

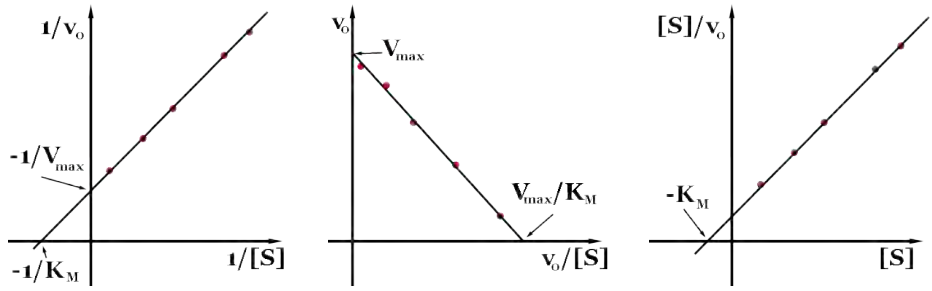

a) Lineweaver-Burke plot **b)** Eadie-Hofstee plot **c)** Hanes plot

Figure 2.17: Linearization methods for the determination of K_M and v_{max}.

$$\frac{[S]}{v_0} = \frac{1}{v_{max}} \cdot [S] + \frac{K_M}{v_{max}} \qquad \text{Hanes} \tag{2.33}$$

These linearizations are very sensitive to measurement deviations though, and should, therefore, not be applied if possible otherwise.

The parameters K_M and v_{max} are commonly used for a characterization of enzyme-substrate reactions, where low K_M values indicate a high affinity of the enzyme substrate complex [100, 111].

Michaelis-Menten constants for enzyme catalyzed reactions range from 0.2 nM, for the DNA-(apurinic or apyrimidinic site) lyase on DNA containing thymine glycol [112], up to 10 M, for the glucose 1-dehydrogenase on D-Galactose [113]. However, common constants are in the micro- to milli-Molar regime.

Enzyme kinetics are not always this easy to describe. Generally, enzyme catalysis can consist of more than a single step and, therefore, more than these three rate constants. Also, reactions can be dependent on multiple substrates or constraint to the presence of cofactors and inhibitors [100, 111].

2.4.2 Enzyme Characterization

Enzymes are categorized into main classes by *Enzyme Commission numbers* due to their catalyzed reactions as presented in table 2.2 [114].

Table 2.2: Enzyme main classes as categorized by the Enzyme Commission [115–122]

main class number	main class name	catalyzed reaction
EC 1	Oxidoreductases	redox reactions
EC 2	Transferases	intermolecular transfer of functional groups
EC 3	Hydrolases	hydrolytic cleavage
EC 4	Lyases	breaking of chemical bonds other than hydrolysis and oxidation
EC 5	Isomerases	conversion to isomeric structures
EC 6	Ligases	binding of two molecules by Adenosine-5'-triphosphate consumption

Within these main classes, enzymes are further categorized into subclasses. For the class of hydrolases, for example, there are 13 subclasses that specify the kind of bond the hydrolase works on. Any nuclease is therefore gathered in subclass 3.1, while subclass 3.4 describes all characterized peptidases [115–122]. Enzyme commission numbers consist of two more digits, providing information about required cofactors, substrate preferences or catalyzed products, which does not follow any universal method, though.

2.4.2.1 Peptidases

The subclass of peptidases, EC number 3.4, is further divided into 19 different categories, containing 1161 different enzymes [116–122], which is both subject to regular changes. Highly popular substitutes are the Cathepsines, Collagenases, HIV-1 Protease, Pepsin, Thrombin and Trypsin.

Carboxypeptidase A

Another popular and well studied peptidase is the Carboxypeptidase A. It is registered with the EC number 3.4.17.1 and was, therefore, the first metallocarboxypeptidase to be categorized. Carboxypeptidase A from bovine

pancreas (*Bos taurus*) is a globular monomer with a molecular weight of 34.49 kDa, consisting of 300, 305 or 307 amino acids and is exocytosed from the secretory granule [64, 123]. Its active site is built by five amino acids, which is stabilized by a zinc ion [124]. The amount of zinc excreted by the pancreas is related to enzyme output [125], but amounts to 0.98 - 1.03 mol Zn2+ per mol enzyme [123]. The zinc ion position in the native Carboxypeptidase A molecule is depicted in the crystal structure in figure 2.18.

Figure 2.18: Crystal structure of Carboxypeptidase A, determined by X-ray diffraction with a resolution of 1.25 Å [126, 127]. Zinc ion depicted as grey sphere.

Carboxypeptidase A has a pH optimum in the neutral range [64] and an optimum temperature for kinetic assays at 25°C [123, 128]. The optimum temperature for immobilized enzymes is published to be at 50°C [129].

This peptidase does not have a specific substrate, but cleaves any peptide bond except for those to proline, arginine and hydroxyproline. It shows only little action on glycine, lysine, aspartic acid and glutamic acid. Peptide bonds linking amino acids that contain aromatic rings are preferred [65, 130]. Carboxypeptidase A is an exopeptidase and produces mono-, di- and tripeptides beginning from the C-terminus of the substrate [64–68]. Furthermore, Carboxypeptidase A can also cleave esters, some even faster than their analogue peptide bonds [68]. Typical K_M - values for natural peptide bonds are in the range of 1 mM [64].

Carboxypeptidase A can be inhibited by a variety of chemical compounds, most interestingly also by D-Cys [131], L-Cys [132], D-Phe [123], L-Phe [64]

and D-His [123].

2.4.2.2 Nucleases

Nucleases are categorized into the subclass of *Hydrolases acting on ester bonds* (EC number 3.1) and can be further classified by their cleavage site behavior. There are five sub-subclasses describing exonucleases and eight describing endonucleases [116–122]. The most common of these nucleases are DNaseI and DNaseII.

DNaseI

Deoxyribonuclease I (EC number 3.1.21.1) is the first described endodeoxyribonuclease producing 5'-phosphomonoesters [116–122]. It is derived from the bovine pancreas (*Bos taurus*). DNaseI is also a globular monomer with a molecular weight of 31 kDa and a peptide length of 282 amino acids [133]. This enzyme naturally occurs in the cytoplasm of cells [134].

Its activity is dependent upon magnesium and calcium ions at a milli-Molar concentration [135, 136]. Deoxyribonuclease I can be inhibited by a Ca^{2+} concentration above 1 mM [137] and by G-Actin [135]. A G-Actin inhibited DNaseI is depicted in the crystal structure in figure 2.19.

Figure 2.19: Crystal structure of DNaseI bound to Actin, determined by X-ray diffraction with a resolution of 1.85 Å [138].

The optimum pH value for DNaseI activity is 7 - 7.5 [136] and the optimum temperature has been published to be at 37°C [139]. Beginning from 65°C, the enzyme gets inactivated [140].

DNaseI can hydrolyze both, double and single stranded DNA [136], but has a preference for double-stranded DNA [133,135], where it produces nicks on one strand in preference to scission of both strands. Autoretardation then causes the continuous formation of products, which are poorer substrates, than those from which they are derived [133]. There is no preference for any specific nucleotide [135].

DNaseX

Deoxyribonuclease X (EC number 3.1.22.5) is an endodeoxyribonuclease, producing 3'-phosphomonoesters. Therefore, this enzyme belongs to another sub-subclass of enzymes than DNaseI [116–122].

This enzyme is still mostly unknown. DNaseX from *E. coli* preferentially cleaves supercoiled plasma DNA at a pH optimum of 8, absolutely requires Mg^{2+} and Ca^{2+} ions, but is also inhibited by them at concentrations above 5 mM respectively 1.5 mM [141].

Human DNaseX, has a coding sequence on the human X chromosome and was the first detected gene to encode a DNaseI homologous protein [37,142,143]. The enzyme is located on the cell surface by its glycosylphosphatidylinositol (GPI) - anchor, where it is supposed to hydrolyze endocytosed extracellular DNA [43]. DNaseX is highly expressed in cardiac and skeletal muscles and has an extra hydrophobic stretch at its C-terminus [39]. It has a peptide length of 285 amino acids and a molecular weight of 35 kDa. As DNaseI, this enzyme is dependent on Ca^{2+} and Mg^{2+} ions and inhibited by G-Actin, but only at higher inhibitor concentrations. Its ideal pH has been roughly determined to be at 6.8 [39,42,43]. Crystal structures are not yet available for this enzyme.

DNaseII

Deoxyribonuclease II (EC number 3.1.22.1) is the first described endodeoxyribonuclease [144] that produces 3'-phosphomonoesters [116–122]. The enzyme from bovine spleen (*Bos taurus*) has a molecular weight of 41 kDa [145] and is found in the nucleus [146] and in the lysozome [100]. It functions best at a pH value of 4.8 on ds DNA [145]. DNaseII is inhibited by Mg^{2+} at a concentration above 10mM [145]. Most surprisingly, there is only little information as well as no crystal structure available for DNaseII.

S1-Nuclease

S1-Nuclease belongs to the sub-subclass of *endoribonucleases that are active with either ribo- or deoxyribonucleic acids and produce 5'-phosphomonoesters* and has the EC number 3.1.30.1 [116–122].

It occurs extracellular [147] in the sprout of *Aspergillus oryzae* [148]. S1-Nuclease consists of a single peptide chain of 270 amino acids [149], resulting in a molecular weight of 36 kDa [150]. The crystal structure is shown in figure 2.20.

Figure 2.20: Crystal structure of S1-nuclease with a substrate analog, determined by X-ray diffraction with a resolution of 1.8 Å [149].

S1-Nuclease requires zinc for its activity [147]. Its optimum pH is at 4.5 - 4.6 [151, 152]. The published optimum temperatures vary immensely from 37°C [153,154] to 65°C (for immobilized enzymes) [155]. The enzyme is 75000 times more active on single-stranded than on native DNA [156] and shows a five fold more activity on DNA than on RNA [152]. Published K_M - values are 0.0142 mM for DNA and 0.144 mM for RNA [151].

2.5 Fluorescence based Enzyme Research

Enzyme research can be accomplished with various methods, like X-ray Crystallography, NMR, AFM, Scanning Electron Microscopy (SEM) and TEM.

The specimen preparation for these methods, however, is mostly complex, time-consuming and invasive to the samples.

Fluorescence based methods are generally non-invasive and are, therefore, ideally suited for the research on any living material. Thus, fluorescence has been employed very early for enzyme research, first represented by ELISAs, that started in the 1970s [70, 71], and western blots, which began in the 1980s [157].

Both methods employ antibodies, which are specifically directed against the antigen of interest. In a standard ELISA, the antigens are bound to a surface, incubated first with a specific primary antibody and then with a secondary antibody, carrying an enzyme like Horse Radish Peroxidase (HRP). For the detection of antigen, therefore, specific HRP substrate is added, which gives a colorimetric information about the presence of antigen down to a concentration of 10^{-13} M [74]. Due to unspecific antigen adsorption, ELISAs bear a high risk of false positive signals.

The western blot method is a lot more confident in this concern, since proteins are initially unraveled by gel-electrophoresis in respect to their three dimensional structure or their protein length. The purified proteins are then transferred to a membrane and detected by incubation with specific primary, consecutive secondary enzyme-linked antibody and the addition of appropriate enzyme substrate.

These fluorescent methods, thus, are only capable of the detection of dissolved enzymes. The specific interaction between antibodies and their antigens can also be utilized, though, for the detection of proteins for immunolabeling in their native environments [158,159]. Thus, enzymes, that are linked to a cell compartment, e.g. the outer membrane, can be bound by their specific antibody, which is then bound by a secondary labeled antibody, directed against the primary antibody. This scheme is depicted in figure 1.4.

Such a specimen, therefore, allows the examination of the native occurrence of enzymes. However, the tissue mostly gets fixed in the sample preparation.

The fluorescence based research on living enzymes utilizes natural enzyme substrates that are bound to one or more fluorophores, that either yield a FRET or a PET pair (see section 2.2.2). In both ways, the fluorescent substrate needs to show a change in fluorescence signal upon the specific enzymatic reaction. For hydrolases, therefore, the cleavage generally results in a spatial contact loss, which restores fluorescence of an initially quenched

fluorophore via FRET [47, 160, 161] or PET [31–33, 54, 55, 162]. The design of those fluorescent substrates, that take advantage of intrinsic electron donating properties of tryptophan and guanosine residues (cf. section 2.2.2), is exemplarily depicted for nucleotides and peptides in figure 1.2 and figure 1.3. This method can also be adapted to any other substrate with an extra attachment of these natural compounds, if they are not already incorporated.

The fluorescence signal of the modified substrate can be read out with any fluorescence detector based device, beginning from a fluorescence spectrometer over wide field microscopes to confocal and TIRF microscopes, including 'super-resolution' techniques such as STED and *d*STORM. Therefore, fluorescent substrates offer a wide range of applications for the analysis of enzyme activity.

Autofluorescence

When dealing with biological samples for any fluorescence based method, the specific autofluorescence of the specimens have to be regarded. Figure 2.21 shows the yield of intrinsic fluorescence of two different mammalian cells upon an irradiation with 488 nm.

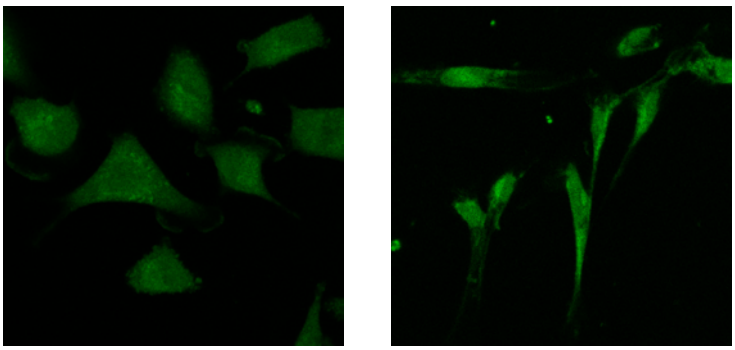

a) A - 549 **b)** HEK 293T

Figure 2.21: Autofluorescence of different cell types at excitation with 488 nm.

The molecule of interest should, therefore, be examined employing a fluorophore in the spectral range of least autofluorescence intensity. Naturally, this range varies with the utilized application. Whereas plant cells show a high autofluorescence in the red spectral range due to lignins, such

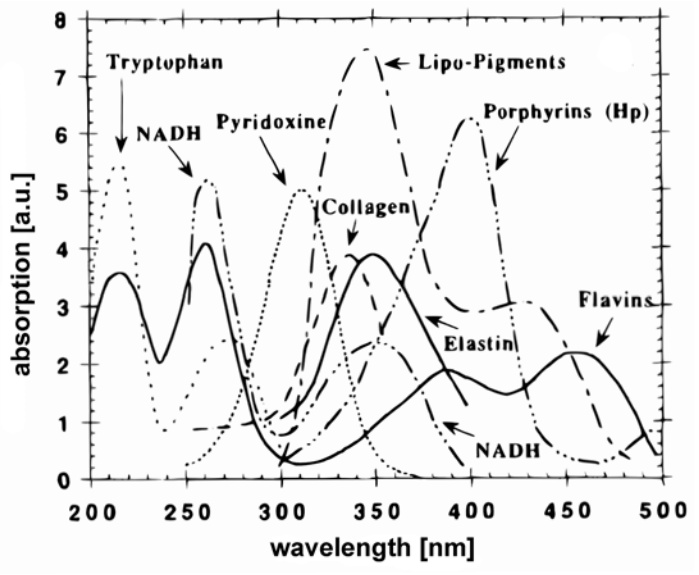

a) absorption

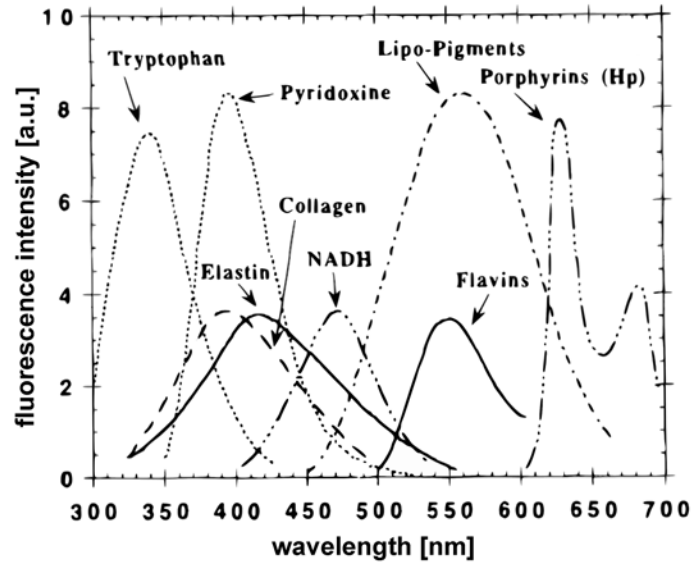

b) fluorescence

Figure 2.22: Absorption (a)) and fluorescence (b)) spectra of different natural compounds in the visible spectrum [163].

as chlorophylls, the intrinsic fluorescence of mammalian cells is rather low at these wavelengths. In mammalian cells, autofluorescence is mostly due to flavin coenzymes (FAD[5] and FMN[6]) and reduced pyridine nucleotides (NADH[7]) [164, 165].

Figure 2.22 shows the spectrally dependent absorption and fluorescence intensities of these and other important fluorescent compounds in mammalian organisms. Only the blood component porphyrin shows a noteworthy fluorescence intensity above 650 nm [163]. Sample examination in these cells, therefore, mostly utilizes red fluorescing fluorophores.

[5] flavin adenine dinucleotide
[6] flavin mononucleotide
[7] nicotinamide adenine dinucleotide

3 Materials and Methods

In this section all utilized hardware devices and microscopic setups, samples and their preparations as well as their measurements and data evaluation will be described.

3.1 Hardware Devices and Setups

The presented work was carried out on several ready-to-use hardware devices like the absorption and the fluorescence spectrometer, a multiplate reader and a high performance liquid chromatograph. Furthermore, an easy to handle confocal microscope and a custom made total internal reflection fluorescence microscope were used. This section will describe the equipment, components and configurations of these instruments.

3.1.1 Absorption Spectrometer

Absorption spectra were measured with a Perkin Elmer Lambda 25 UV/VIS Spectrometer at room temperature. For a zero balance, the measurement buffer was used in the applied cuvettes. Spectral ranges were adjusted to each fluorophore, while the scan speed remained constant at 240 nm/min. Each ensemble measurement was performed in quartz SUPRASIL®precision cells (Hellma®).

3.1.2 Fluorescence Spectrophotometer

Emission spectra measurements, enzyme kinetics and thermal stability measurements were carried out with a Cary Eclipse Fluorescence Spectrophotometer. In all measurements, emission light was collected for 0.1 s. Each ensemble measurement was performed in quartz SUPRASIL®precision cells (Hellma®). Up to 4 concurrent measurements can be realized in the tempered cuvette holder. Emission spectra were acquired in the scan-mode of

this device at 25°C, excited and detected at individual, appropriate spectral ranges (see section 3.3). Measurements on thermal characteristics were carried out with custom excitation wavelengths for each fluorophore and a detection wavelength, destined by the appropriate spectral emission maximum. Temperatures varied from a minimum of 15°C to a maximum of 90°C or less, dependent upon the examined sample. Temperature variations were chosen to be as slowly as possible to guarantee a thermal balance between sensor and sample, but still fast enough to minimize side effects like evaporation of sample liquids. Typical velocities were in the range of 1°C/min. Kinetic measurements were accomplished at 25°C for CPA experiments, at 37°C for DNaseI, DNaseII and DNaseX experiments and at 20°C for S1-Nuclease measurements. Temporal measurement intervals were adjusted to each reaction, but took place in a maximum frequency of 4 times a minute for fast kinetics up to a waiting time of 30 minutes for very slow kinetics.

3.1.3 Multiplate-Fluorescence Reader

Multiplate based experiments were carried out on a FLUOStar Optima (BMG LABTECH) at the Laser Research Laboratory (LFL) in Munich. The gain was set to 2500. Every 10 minutes one data point can be collected for each sample with an excitation wavelength of 650 nm and and emission wavelength of 680 nm.

3.1.4 High Performance Liquid Chromatograph - HPLC

The High Performance Liquid Chromatograph by Agilent Technologies (1100 series) was used for separation of labeled oligonucleotide for CPA single molecule measurements as well as for the analysis of cleaving sites in peptidase substrates. In every case, the two eluents (0.1 M Tetraethylammoniumacetat in water (A) and 0.1 M Tetraethylammoniumacetat in acetonitrile and water (3:1) (B)) were run with a gradient from 100% A to 100% B in 20 minutes. Absorption was observed for 260 nm and 630 nm and emission for 360 nm and 680 nm.

3.1.5 Zeiss Laser Scanning Microscope 710 - LSM

The LSM 710 is a confocal microscope (see section 2.3) by Carl Zeiss AG, Germany. It is equipped with a Helium Neon (HeNe) Laser and an Argon Ionen

(Ar^+) Laser. Therefore, it provides five wavelengths to work with: 458 nm (Ar^+), 488 nm (Ar^+), 514 nm (Ar^+), 543 nm (HeNe) and 633 nm (HeNe). Laser powers can only be governed by a remote control dial (only in case of Ar^+) with arbitrary units and the software in relative units. Furthermore, due to the optical path and security mechanisms it is not possible to measure applied laser powers with an external device. At instrument setup the original powers for each line were measured to 1.42 mW for 458 nm, 7.18 mW for 488 nm, 5.76 mW for 514 nm, 0.56 mW for 543 nm and 1.71 mW for 633 nm. Since Ar^+ remote control dial is adjusted to maximum power it can be assumed that 100 % laser power roughly correlates with the original absolute power.

Two independent galvanometric scan mirrors lead the laser focus through a Plan-Apochromat 63x/1.40 Oil objective (Zeiss) into the sample. The fluorescent answer is collected by the same objective, passes a filter and is directed to the master pinhole. The fluorescent light is then spectrally separated by a grid and nanometer-wise directed into three different paths. Here, the spectral ranges are reduced to the desired detection range by adjustable blockades. With this a resolution of 3 nm on the three QUASAR photomultiplier tubes (PMTs) can be reached.

The LSM 710 is, furthermore, supplied with an 'Axio Observer' z-drive to scan various specimen samples with a minimum step size of below 25 nm.

The standard software 'Zen' that is supplied with the LSM 710 allows a high number of individual settings and automation procedures. The most interesting for this work is the z-stack function, that after setting a center, number of layers and step size automatically produces a 3D-image of the defined region of interest. This image can be further depicted as simple (xy) and orthogonal cut (xy, xz, yz) for any given layer, maximum intensity projection and 3d animation. For any of these functions there are different design elements like depth coding, brightness, gamma and contrast settings, color table selection and modification and drawing tools. Derived images can also be analyzed with colocalization, histogram and measurement tools. Any produced image can be saved as .lsm with the according measurement parameters and be exported with more than 20 data formats (PNG , TIF, BMP, JPG, PSD, PCX, GIF, AVI, Quicktime ...) for further processing and presentation.

3.1.6 Total Internal Reflection Fluorescence Microscope

Single molecule measurements on CPA activity were accomplished on a TIRF microscope setup based on an Olympus inverted research microscope IX71. A collimated laser beam (531 nm/647 nm, selected by an acousto-optical tunable filter (AOTF)) of an Ar^+Kr^+ mixed gas laser (Innova 70 C by Coherent) with a power of 0.1 mW is totally reflected at its focus on the bottom of a cover slide after being reflected at a dichroic mirror (AHF Analysentechnik) and passing a plan apo N oil immersion objective (Olympus 60x, NA 1,45). Fluorescence signal is collected by the same objective, passes the dichroic mirror, filtered by an appropriate fluorescence light filters (700DF75, AHF Analysentechnik) and is collected by an electron-multiplying CCD (EMCCD) camera (iXon DV887DCS-BV, Andor Technologies). Experiments on live cells with modified substrate are also carried out at this setup, incorporating a telescope to magnify the derived image and without the use of the 531 nm excitation. For *d*STORM measurements an equivalent setup was used with additional laser irradiation at 514 nm and a polychromic beamsplitter (532/647, AHF Analysentechnik).

3.2 Samples and their Preparation

Biological samples constitute the key element of this work. Here, the examined enzymes, their buffers, substrates and their arrangement for ensemble and single molecule measurements are described. Furthermore, all examined cell lines are presented and the immunostaining of these cells is described.

3.2.1 Enzymes and corresponding Buffers

Carboxypeptidase A (EC no. 3.4.17.1, CAS no. 11075-17-5) from bovine pancreas was obtained from Sigma Aldrich (Cat.no. C-0261) in aqueous solution with a molecular weight of 35 kDa.

DNaseI (EC no. 3.1.21.1, CAS no. 9003-98-9) from bovine pancreas was obtained by Ambion Europe (Cat.no. 2224) in storage buffer (20 mM Hepes pH 7.5, 10 mM CaCl2, 10 mM MgCl2, 1 mM DTT, 50% (v/v) glycerol) with a molecular weight of 31 kDa. Human DNaseI was greatly gifted by R-Biopharm AG in Darmstadt and is derived from the commercially available medicine Pulmozyme® (Roche) upon description. DNaseII (EC no. 3.1.22.1,

CAS no. 9025-64-3) from bovine spleen was obtained by SIGMA (Cat.no. D8764) as lyophilized powder, essentially salt free with a molecular weight of 41 kDa. S1-Nuclease (EC no. 3.1.30.1, CAS no. 37288-25-8) from *Aspergillus oryzae* was obtained by SIGMA (Cat.no. N5661) in storage buffer (30 mM sodium acetate, 50 mM NaCl, 1 mM ZnCl2, 50% glycerol) with a molecular weight of 36 kDa. DNaseX (EC no. 3.1.22.1, CAS no. 97002-82-9) was greatly provided by R-Biopharm AG, produced by CRELUX in a stem concentration of 1 mg/ml with a C-terminal 6 x His-Tag.

DNaseI and DNaseX measurement buffer is as follows: 50 mM MOPS-NaOH pH 6.8, 3 mM $MgCl_2$ and 0.25 mM $CaCl_2$. DNaseII and S1-Nuclease measurement buffer consist of 30 mM SodiumAcetat, pH 4.6, 1 mM ZinkAcetat and 5%(v/v) Glycerol. All buffer components were obtained from Sigma.

3.2.2 (Fluorescent) Substrates and Modifications

Peptide probes for CPA analysis were linked to MR121 and purified via HPLC by ATTO-TEC GmbH Siegen and Biosynthan GmbH, Berlin. Unlabeled Gly-Trp was obtained from Bachem GmbH, Weil am Rhein (ordering number G-2220). Labeled and unlabeled DNA Hairpins as well as 3'-thiol-modified $SP2^{CM}$ (all double HPLC purification grade) were supplied by IBA GmbH, Goettingen. DNaseAlert™ - substrate was retained from DNaseAlert™QC System, obtained from Ambion Europe (ordering number AM1970) and dissolved in 20 µl TE buffer (DNaseAlert™QC System) to yield a 0.1 mM stock solution before further dilution. The Cystein-modified cell-penetrating peptide Antennapedia (Antp, RQIKIWFQNRRMKWKK-C) was synthesized by Biolux GmbH, Stuttgart. The thiol-modified DNA Hairpins were incubated with Antp at equimolar concentration in 100 mM phosphate buffer pH 7.0 (SIGMA, ordering number S8282) and 3 mM TCEP (Aldrich, ordering number C4706) for 6 hours at 35°C and purified via centrifugal filtering.

3.2.3 CPA Single Molecule-Localization

For single molecule measurements with Carboxypeptidase A the enzyme molecules were bound to the surface as follows: I) CPA was added to a 2.5 fold molar excess of N-Succinimidyl 4-(maleimidomethyl) cyclohexanecaboxylate (SMCC, Sigma-Aldrich) and a 2000 fold molar excess of sodium bicarbonate (Molecular Probes) to react for one hour at room temperature. Af-

terwards the solution was purified from unbound SMCC using a Sephadex G-25 column and reduced in volume by centrifugal filtering (Microcon YM-50). II) Cy3b-NHS (Amersham Biosciences Europe, Freiburg, Germany) was bound to an internal C6-amino linker and 3'-modified (Biotin) oligonucleotide (IBA GmbH, Göttigen, Germany) following a standard protocol, purified by HPLC and reduced in volume. III) A 10 fold molar excess of Tris(2-carboxyethyl)phosphine hydrochlorid (TCEP, Sigma-Aldrich) was added to a 10 mM solution of product II. After adding a 10 fold molar excess of CPA to the solution the mixture reacted over night at 4°C and was then stopped by addition of mercaptoethanol (Fluka) and purified using a Sephadex G-25 column. IV) After adding the product to a modified (biotin-streptavidin conjugation) surface, the complementary oligonucleotide (IBA GmbH, Göttingen, Germany) was added to avoid folding of the complex. As enzyme substrate, MR 121 - Gly - Trp was added during acquisition in a concentration of $5 \cdot 10^{-10}$ M.

3.2.4 Cell Cultures

All cell lines used for immunostaining and enzyme detection in living cells were cultivated in the Applied Laser Physics and Laser Spectroscopy work group in the faculty for physics in Bielefeld University. Chemicals for cell culturing were ordered at 'PAA: The Cell Culture Company' if not mentioned differently. Ordering numbers are given in brackets. For any of these experiments cells were grown in Lab-Tek II chambered coverglasses (Nunc). Those cells used for ensemble measurements on the multiplate fluorescence reader arose from cell lines cultured in the Laser Research Laboratory in Munich. Measurements in the fluorescence spectrophotometer incorporated lysed cells from R-Biopharm AG in Darmstadt.

Neuroblastoma Cell Line - SK-N-MC

SK-N-MC cell line was gratefully gifted by J. Kopitz from Applied Tumorbiology at University Hospital Heidelberg. This epithelial brain neuroblastoma cell line was derived from the supra-orbital area from a 14 year old female Caucasian [166].

Adherent SK-N-MC are cultured in RPMI 1640 (PAA ordering number E15-840) medium containing 10% FCS (ordering number A15-105) at 37°C in 5% CO_2. Two to three times a week at a confluency of 80 -90% cultures are

split with 0.05% Trypsin containing 0.02% EDTA in PBS (L11-004) following a standard cell splitting protocol to a subcultivation ratio of 1:6 to 1:12.

Human Lung Carcinoma Cell Line - A-549

A-549 cells were provided by R-Biopharm AG in Darmstadt. The cell line was isolated from the lung carcinogen tissue of a 58 year old Caucasian man in 1972 [167].

These epithelial cells grow adherently in monolayer in DMEM high glucose (4.5 g/l) (E15-843) with 10% FCS (A15-105) and 50 µg/ml Gentamicin (P11-004) at 37°C in 5% CO_2. Twice a week confluent cultures are split 1:5 to 1:10 with 0.05% Trypsin containing 0.02% EDTA in PBS (L11-004) following a standard cell splitting protocol.

Human Bladder Carcinoma Cell Line - ECV-304

The human urinary bladder carcinoma cell line ECV-304, supplied by R-Biopharm AG in Darmstadt, is a derivative of human urinary bladder carcinoma cell line T-24 [168–170].

The cells adherently grow as cobblestone monolayers in RPMI 1640 (E15-840) with 10% FCS (A15-105) and 50 µg/ml Gentamicin (P11-004) at 37°C in 5% CO_2. Every two to three days cultures are conventionally split in a ratio of 1:6 to 1:10 with 0.05% Trypsin containing 0.02% EDTA in PBS (L11-004).

Human Cervix Adenocarcinoma Cell Line - HeLa

The 31 year old black Female Henrietta Lacks was treated due to her epitheloid cervical adenocarcinoma in 1951. From this treatment the first aneuploid, continuously cultured human cell line arose [171–173], gratefully gifted by Prof. Hans-Georg Kräusslich from the Department of Virology in the University Hospital Heidelberg.

These cells grow in DMEM high glucose (4.5 g/l) (E15-843) with 10% FCS (A15-105) at 37°C in 5% CO_2 and are split twice a week with 0.05% Trypsin containing 0.02% EDTA in PBS (L11-004) following a standard cell splitting protocol with a dilution of 1:2 to 1:6.

Human Colon Carcinoma Cell Line - LS-174T

LS-174T represents a colon cell line obtained from a colorectal adenocarcinoma of a 58 year old Caucasian woman. This line is a variant of cell line LS 180 [174] and was gratefully gifted by R-Biopharm AG in Darmstadt.

The adherent epithelial cells grow in DMEM high glucose (4.5 g/l) (E15-

843)with 10% FCS (A15-105) plus 50 µg/ml Gentamicin (P11-004) at 37°C in 5% CO_2. Two to three times weekly the cells are split with a ration of 1:2 to 1:5 with 0.05% Trypsin containing 0.02% EDTA in PBS (L11-004) following a standard cell splitting protocol.

Human Colon Carcinoma Cell Line - SW-837

R-Biopharm AG in Darmstadt also provided SW-837, the rectum adenocarcinoma cell line of a 53 year old male Caucasian [175].

In RPMI 1640 (E15-840) with 10% FCS (A15-105) plus 50 µg/ml Gentamicin (P11-004), 37°C and 5% CO_2 the cultured cells are split with 0.05% Trypsin containing 0.02% EDTA in PBS (L11-004) once or twice a week with a subcultivation ratio of 1:2 to 1:5 in a conventional splitting manner.

HT-29 - Human Colon Carcinoma Cell Line

Established from the primary tumor of a 44 year old Caucasian woman with colorectal adenocarcinoma in 1964, these adherent, epitheloid cells, gifted by R-Biopharm AG, Darmstadt, grow as monolayers and in large colonies [176, 177].

Culture conditions are DMEM low glucose (1 g/l) (E15-806) with 10% FCS (A15-105) and 1% non-essential amino acids (M11-003) supplemented with 50 µg/ml Gentamicin (P11-004) at 37°C and 5% CO_2. Confluent cultures are split every three to six days using 0.05% Trypsin containing 0.02% EDTA in PBS (L11-004) to a ratio of 1:3 to 1:8 following a standard splitting protocol.

Flp-In™ T-REX™ Human Embryonic Kidney (HEK) 293T Cell Line

The human embryonic kidney cell line HEK 293T grows generally adherently as monolayer [178]. The cells need to be cultivated in 37°C and 5% CO_2 and split 3 times a week with a ratio of 1:3 to 1:4 with 0.05% Trypsin containing 0.02% EDTA in PBS (L11-004). This cell line served as transfection host for the commercially available transfection system Flp-In™ T-REX™ (invitrogen, ordering number K6500-01). The **control cell line** is the Zeocin™ and blasticidin-resistant Flp-In™ T-REX™ host cell line produced in the DNaseX transfection protocol. Therefore, the culture medium consists of DMEM high glucose (4.5 g/l) (E15-810) with 10% tetracycline negative FCS (A15-109), 15 µg/ml Blasticidin (P05-017) and 100 µg/ml Zeocin™ (invitrogen, ordering number 45-0430). If the host cell line is further transfected with a vector containing DNaseX DNA a **stable transfected Flp-In™ T-REX™ HEK 293T cell line** can be obtained. These cells constantly transcribe DNaseX

gene and, therefore, produce DNaseX. Here, DMEM high glucose (4.5 g/l) (E15-810) with 10% tetracycline negative FCS (A15-109) and 150 µg/ml Hygromycin B (P15-014) is used as medium. Alternatively, the host cell line can be modified with the gene of interest and a Tet repressor to form a **stable transfected and inducable Flp-In™ T-REX™ HEK 293T cell line** containing an additional Tet repressor. In the absence of tetracycline this repressor inhibits the transcription of DNaseX, while upon addition of tetracycline binds to this repressor, leading to the DNaseX transcription. This repressor also reacts to doxicycline. Tetracycline (SIGMA, ordering number T7660-5G) and Doxicycline (SIGMA, ordering number D9891-1G) were both used in a final concentration of 1 µg/ml. The medium for this cell line variant generally consists of DMEM high glucose (4.5 g/l) (E15-810) with 10% tetracycline negative FCS (A15-109), 150 µg/ml Hygromycin B (P15-014), 15 µg/ml Blasticidin (P05-017) and 50µ g/ml Gentamicin (P11-004). All HEK 293T cell lines were provided by R-Biopharm AG, Darmstadt.

3.2.5 Chemicals for Immunostaining

The immunostaining procedure incorporates the following chemicals: Phosphate Buffered Saline (PBS) was obtained from Sigma Aldrich (ordering number P4417). Hanks' Balanced Salt Solution (HBSS) was ordered from invitrogen (ordering number 14025). Triton® X-100 solution is supplied by Sigma Aldrich (ordering number 93443). Normal Goat Serum (NGS) is available at invitrogen (ordering number PCN5000), as well as RNase A (ordering number 12091-039). Primary Antibody 'DNAX', Protein G purified with a stock concentration of 0.912 mg/ml + 0.1% NaN_3, Primary Antibody '148', Protein G purified with a stock concentration of 0.707 mg/ml and pre-immune serum (rabbit) with 0.35mg/ml + 0.1% NaN_3 are gratefully gifted by R-Biopharm AG, Darmstadt. Secondary Antibody - Alexa Fluor®647 goat anti-rabbit IgG (H+L) (ordering number A-21244), Rhodamin-Phalloidin (ordering number R415) and Sytox® Green Nucleic Acid Stain (ordering number S7020) are available at invitrogen. The mounting medium components Mowiol® 4-88 and DABCO were obtained from Sigma Aldrich (ordering number 81381) respectively Carl Roth (ordering number: 0718.1).

The protocol for the production of the complete mounting medium can be found in section B.1. This medium not only preserves the samples for a longer use but also amplifies their fluorescence intensity which is proven in

section C.1. In case of *d*STORM measurements also Glucoseoxidase (Sigma Aldrich), Catalase (Roche Applied Science) β -Mercaptoethylamine (Sigma Aldrich) and Glucose (Sigma Aldrich) are used.

3.2.6 Labeling Protocol for LSM and *d*STORM-Measurements

For immunostaining experiments different protocols were applied. The standard protocol starts with a fixation of the cells followed by membrane permeabilization. Before primary antibody respectively control protein incubation, the samples are incubated with blocking buffer to saturate all possible unspecific binding sites for the secondary antibody. Afterwards, the primary antibody / antibodies are added to the blocking buffer. Then, labeled secondary antibody and labeled phalloidin are added to selectively label the primary antibody and the cytoskeleton. As a last step the nuclear stain is incubated. Finally, the samples are covered with mounting medium to prolong the stability of the samples.

To minimize DNA staining outside the nucleus, RNase A is added to blocking buffer, primary antibody and secondary antibody incubation. Therefore, these incubation periods are arranged to take place at 37°C to activate the enzyme. Starting from secondary antibody incubation the samples are, furthermore, continuously covered with aluminum foil to prevent fluorophores from photo-bleaching. The presented succession is surrounded by a high number of washing steps to minimize any cross reactivity. The complete and detailed labeling protocol is presented in section B.4.

For the examination of labeling efficiencies in different cell viabilities the standard protocol was modified in three different ways. Generally, one approach incorporates cell fixation before primary antibody incubation, another approach schedules it in between primary and secondary antibody and the third approach has the cell staining after secondary antibody incubation. Apart from that, these three approaches need to be as similar as possible to each other to allow any comparison of result. Therefore, a permeabilization and the labeling with the toxic phalloidin had to be spared. Furthermore, RNase A was left out in each approach to prevent any side effects in the living cells. Those samples being labeled alive obviously needed to be surrounded with usual culture conditions. Thus, fixed samples were also kept at 37°C at equivalent labeling steps. The exact labeling protocols for this experiment can be found in section B.3.

In enzyme quantification measurements on the TIRF setup (section 3.1.6) only the membrane-bound enzymes on different samples were relevant. Therefore, the standard protocol was applied with only little changes. Cytoskeletal and nuclear counterstaining were spared. Thus, also RNase A was unnecessary. Since the *d*STORM technique (see section 2.3.2) requires oxygen removal and the addition of Mercaptoethylamine (MEA), no mounting medium was used. The cells were stored in PBS until used and changed to measuring buffer shortly ahead of the experiment. The complete protocol can be found in section B.5.

3.3 Measurements and Data Evaluation

To understand and analyze the (biological) meaning of an experiment, it is important to know the measurement details and the data evaluation methods. In this section the computation of hairpins for nuclease research, the ensemble measurements and evaluations of these hairpins and other fluorescent substrates and a single molecule measurement of enzyme kinetics is described. Also, measurements of live cells with modified substrate and of mostly fixed immunostained cells on a confocal and a super-resolution microscope are described.

3.3.1 Hairpin Computation

Calculations for DNA hairpins were done by mfold web server (version 3.2) [179–181]. The settings were adjusted to linear DNA sequences in a mM concentration. Folding temperatures and ionic conditions were adjusted to the corresponding buffers.

3.3.2 Ensemble Measurements and Data

Absorption and emission spectra of each substrate were measured in PBS. For MR 121 and Atto 655 carrying substrates, absorption was observed from 400 nm to 800 nm at 240 nm/min and fluorescence was excited with 630 nm and detected from 650 nm to 800 nm. $SP2^{CM}$-FRET was examined with the same parameters, while DNaseAlert was excited with 535 nm and detected from 540 nm to 700 nm in fluorescence spectrum observation. Hydrolysis experiments were set to an excitation wavelength of 630 nm respectively 535 nm

and an observation wavelength at the determined emission maximum of each sample. The enzyme was added to the substrate solution not until a constant fluorescence signal was observed. Substrate concentration was sustained below 5 µM to avoid reabsorption and reemission effects. All measurements for CPA analysis were carried out in PBS at 25°C. Measurements for DNaseI activity were accomplished in a DNaseI reaction buffer at 37°C if not mentioned differently, measurements for DNaseII activity were carried out in a DNaseII reaction buffer at 37°C. Measurements for S1-Nuclease activity took place in a DNaseII reaction buffer at 20°C.

Data of absorption measurements were exported from UV Winlab (version 2.85.04) as ASCII files. All data collected by the Cary Eclipse Fluorescence Spectrophotometer were saved as ASCII file (scan application, version 1.1(132); thermal application, version 1.1(133); kinetics application, version 1.1(133)). ASCII files were imported into Origin 8 for further analysis. Spectra were normalized to their maxima. Hydrolysis data was normalized to the fluorescence intensity at the beginning of hydrolysis and adjusted in starting time to the moment of enzyme addition. Velocities were determined using an exponential fit $I(t) = I_{sat} \cdot (1 - exp(-\tau \cdot t)) + I_{start} \cdot exp(-\tau \cdot t)$, with I_{sat} representing the fluorescence intensity at saturation and I_{start} the fluorescence intensity before addition of enzyme for single step kinetics. Multiple step kinetics were mathematically adjusted with additional exponential terms. Data of thermal measurements was normalized to the fluorescence intensity at 20°C. Melting temperatures were determined with the Boltzmann fit $y = \frac{A_1 - A_2}{1 + exp(\frac{x - x_0}{dx})} + A_2$, where A_1 corresponds to the initial value, A_2 to the final value, x_0 to the center and dx to the time constant.

Spectral information for the calculation of relative fluorescence quantum yields were examined in PBS. Values were determined by $\Phi_{rel} = \frac{Abs_{ref}}{Abs_{sample}} \times \frac{Em_{sample}}{Em_{ref}}$, where the absorption values at 630 nm and the emission values at each maximum were considered. Free corresponding fluorophore served as reference for Abs_{ref} and Em_{ref}.

3.3.3 Single Molecule Measurements and Data

After localization of enzyme molecules by detection of Cy3b fluorescence in a series of 30 consecutive images with an integration time of 0.1 s the substrate was added and the probe was permanently excited at 647 nm. The

resulting fluorescence signals were collected in multiple series of consecutive images in the frame transfer mode using an integration time of 0.1 s. Data from single molecule experiments was gathered with provided software by iXon EMCCD camera and analyzed with a customized LabVIEW software to export fluorophore positions in an ASCII file and correlate the channels. ASCII files were further processed by Origin 8 for visualization.

3.3.4 Live Cell Measurements and Data

A-549 cells were grown in a chambered cover glass 24 h prior to use. 4 hours before the experiment, cells were washed twice with PBS and changed to colorless L-15 medium with FCS. Cells were than incubated for 4 hours at 37°C. Shortly before use, L-15 plus FCS was removed and replaced by L-15 plus Pyrenebutyrate (SIGMA, ordering number 257354-1G) respectively G-Actin (invitrogen, ordering number A12375) to yield final concentrations of $7 \cdot 10^{-7}$ M respectively $5 \cdot 10^{-5}$ M.

Cell images were acquired with Andor iXon software version 1.3.1.2 respectively Andor Solis software version 4.8.30003.0. Further analysis was done with these Andor versions and WinSpec version 2.5.16.4. All incident light images as well as all TIRF images were scaled equally to another and exported for a further graphical processing in ImageJ [182]. For incident light and TIRF image overlays, a threshold was applied to the TIRF image to not cover the cell contours completely.

3.3.5 LSM Measurements and Data

In LSM measurements Sytox® Green Nucleic Acid Stain was excited with 488 nm (Ar^+) at 0.3 % (see section 3.1.5) and detected in the range of 496 nm to 540 nm. Rhodamin-Phalloidin was excited with 543 nm (HeNe) at 7 % (see section 3.1.5) and detected in the range of 584 nm to 628 nm. Alexa Fluor®647 was excited with 633 nm (HeNe) at 20 % (see section 3.1.5) and detected in the range of 650 nm to 747 nm. The applied wavelengths and fluorophore spectra are presented in figure 3.1.

Furthermore, all excitations were carried out in individual tracks to prevent crosstalk. The master pinhole was set to a 140 µm section and as filter 'MBS 488/543/633' was used. The region of interest was individually set to match the object size. Pixel dwell time was kept as equally as possible with the

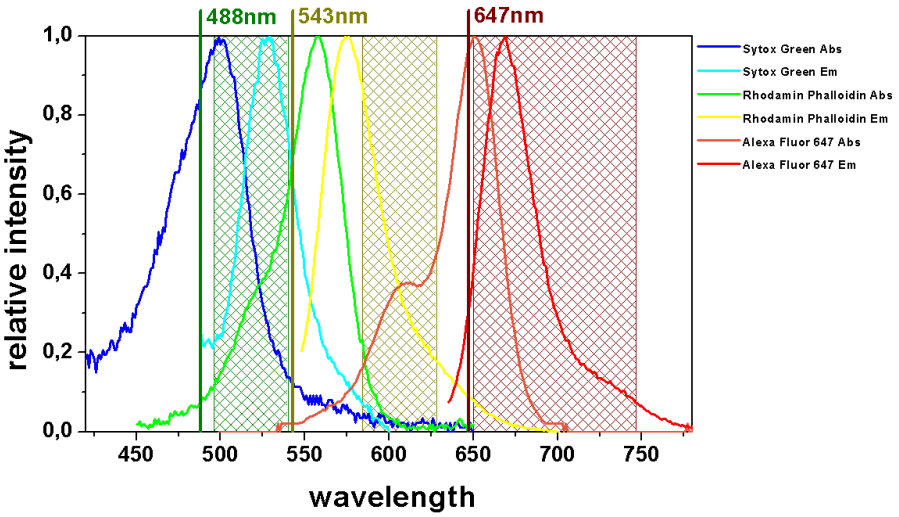

Figure 3.1: Spectral ranges in measurements on LSM 710. The three utilized laser lines and according detection ranges are shown, as well as the fluorophore absorption and emission spectra in PBS.

'Zen' Software (Zeiss) at around 2 to 2.6 µsec. The number of layers was also set individually for each object and ranged from 40 to 100. The step size was kept constant at 0.3 µm. Mastergain was set to 580 and digital gains were 6, 4 and 5 for 488 nm, 543 nm and 633 nm respectively.

Data Processing was done with 'Zen' Software (Zeiss). After applying desired color schemes and adding a scalebar the 3D image was projected onto one layer with a maximum intensity projection. These images were then exported as png files. ImageJ [182] was used to replace the black background by white color for a printer friendly version of the images and minor modifications on figure panels for better visibility.

3.3.6 *d*STORM Measurements and Data

Immunolabeled cells as described in section 3.2.6 are changed to PBS pH7.4 containing oxygen scavenger (0.5 mg/mL glucose oxidase, 40 µg/mL catalase, 10% w/v glucose) and 50 mm β -mercaptoethylamine (MEA) and sealed with an adhesive silicon sheet to cover sample from fresh oxygen. For *d*STORM

measurements the samples are excited with 647 nm with a power of 100 mW for readout and 514 nm with a power of 0.9 mW for switching the fluorophores back to the on-state. Movies of 10 000 128 x 128 pixel frames with an integration time of 10 msec at frame transfer with a read-out rate of 10 000 Hz were acquired for 3 cells a sample with Andor iXon software. For TIRF and for autofluorescence control images the samples were irradiated with 3.2 mW of 647 nm respectively with 0.9 mW of 514 nm at an integration time of 100 msec on the full chip (512 x 512) as well as on the chosen *d*STORM area only.

For data analysis the acquired movies were evaluated frame by frame with the 'rapid STORM' software, now distributed by PicoQuant GmbH Berlin and as previously described by Heilemann *et al.* [35, 183]. Fluorophore spots exceeding a defined threshold of 700 and an allowed deviation of 0.1 from an absolutely circular shape were fitted with a two-dimensional Gaussian function. Its center of mass was defined to be the fluorophores exact position. The raw picture derived by rapid STORM analysis is given with an intensity coding, ranging from red over yellow to white with either black background (figure 4.62) or gray background (section C.3), accomplished by color substitution in ImageJ [182] for a printer friendly version. Furthermore, raw rapid STORM pictures are presented with a white background (accomplished with ImageJ [182]) and a spectral color scale, encoding either intensities (figure 4.66) or the frame in which respectively the time at which the spot was detected (figure 4.67).

For further evaluation each list of spot coordinates was imported to Origin8, converted into a 128 x 128 matrix with a one-fold binning and equally depicted as color contour plot, showing the amount of hits for each pixel (cf. figure 4.63). Then a 40 x 40 submatrix of an area clearly filled with membrane was chosen. From this area the total number of hits was counted and plotted against the doxicycline induction time for every sample. Out of three samples per value the mean and standard deviation were calculated and used for either linear fits (controls) or the sigmoidal fit $f(t) = I_0 + (I_\infty - I_0) \cdot \frac{t^n}{k^n + t^n}$ for the positive sample, where I_0 represents the start value, I_∞ the saturation value, n is the Hill coefficient [184], k the time at which half the maximum value is reached and t the doxicycline induction duration.

Images showing TIRF illumination and autofluorescence at 514 nm were only adjusted in brightness and contrast with Andor iXon software individually to show best visibility of the cells.

4 Results and Discussion

In this chapter the major results obtained in this work will be presented and discussed in two main sections.

First, results derived via enzyme investigations with fluorescent substrates are depicted. As a prerequisite the utilized fluorescent substrates are carefully examined before being used for enzyme kinetics, the determination of the label effect on substrate acceptance by the enzymes and the examination of ideal temperatures and buffers for specific enzyme kinetics with fluorescent substrates. Fluorescent substrates can not only be used in ensemble measurements but also on a single molecule scale, which will be exemplarily shown with surface immobilized enzymes, followed by investigations with fluorescent substrates in living cells.

In the second section the results obtained by enzyme immunostaining are presented. Here, the prerequisite of a suitable staining method has to be examined, before the enzyme occurrence in native and transfected mammalian cell lines can be analyzed with different microscopy methods.

4.1 Enzyme Investigations with fluorescent Substrates

Fluorescent substrates have become a standard method in enzyme research, because they allow the examination of a multitude of questions in a multitude of different approaches and measurement setups [47, 161, 185–192, amongst others].

Two different enzyme subclasses - peptidases and nucleases - are investigated with miscellaneous fluorescent substrates. Therefore, all of these substrates are characterized in the first subsection, split by their assigned enzyme subclass. The following single enzyme kinetics are also split into enzyme attributed subsections, while Michaelis-Menten kinetics are only shown exemplary for one nuclease. For any of the utilized enzymes it is possible to determine the effect of an attached fluorophore to the substrate acceptance, nonetheless, this is neither possible nor reasonable for every utilized

substrate. Therefore, of each enzyme subclass, only one substitute was chosen to be presented in chapter section 4.1.4. In contrast, the investigation of ideal temperature settings is useful for any utilized combination of enzyme and substrate. However, this would elongate this work substantially and is, therefore, only presented for one peptidase and two nucleases. Also exemplary, the localization of Carboxypeptidase A on a single molecular scale is presented, before the occurrence of nucleases in cells is examined with fluorescent substrates.

4.1.1 Substrate Characterization

When incorporating fluorescent substrates for the research on enzyme activities, it is essential to characterize these substrates in the absence of enzymes. This includes their absorption and emission spectra, their stability in various conditions and their relative signal yield before enzyme procession. The results of these measurements are of highest importance when judging on a substrates potency for enzyme research. Therefore, this data is shown in the following chapter. Since substrates for peptidases and substrates for nucleases differ from each other due to their purposes, both kinds are presented in individual sections.

Substrates for Peptidases

Generally, substrates for peptidases consist of peptides[1]. Depending on the specific enzyme, these peptides can range from only a few amino acids to long chains building tertiary structures. For the exopeptidase Carboxypeptidase A six different substrates were tested, two of which only have a single amino acid attached to the oxazine derivative MR 121, as schematically shown in figure 4.1. Therefore, they only offer one possible cleavage site.

It has been described, that tryptophan efficiently quenches the red-absorbing oxazine derivative MR 121 due to its strong electron donating properties, while phenylalanine only shows little quenching efficiency on MR 121 [28–31]. As visible in the normalized spectra in figure 4.2, the attachment of a single amino acid also results in small spectral shifts. While the absorption spectrum of free MR 121 fluorophore shows a maximum at 660 nm, MR 121 -

[1] Enzymes are usually classified upon their major or first detected substrate specificity. Nonetheless enzymes can also show activity on substrates that do not belong to their assigned substrate class (cf. section 2.4.1 and section 2.4.2.1).

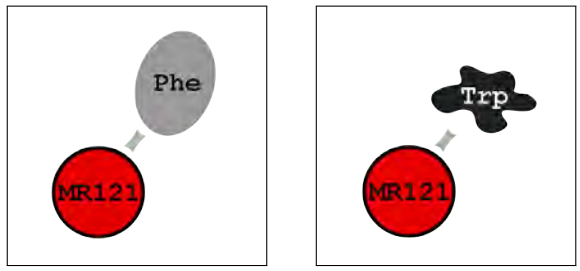

a) MR 121 - Phe **b)** MR 121 - Trp

Figure 4.1: MR 121 - Phenylalanine (Phe) and MR 121 - Tryptophan (Trp) schemes. Both substrates only offer one cleavage site.

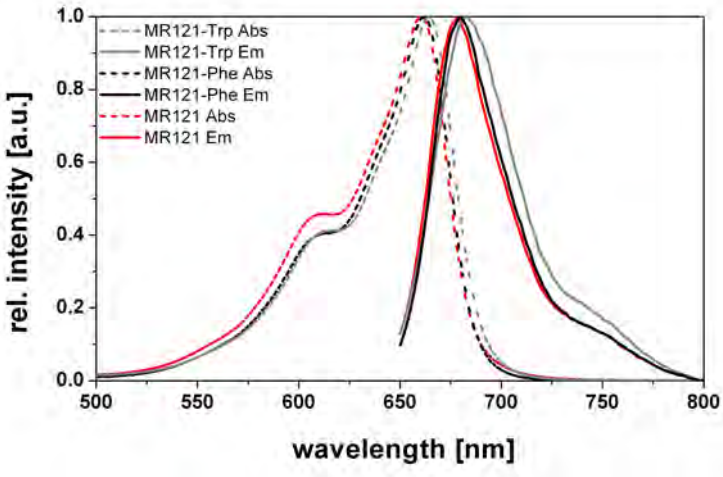

Figure 4.2: Normalized MR 121, MR 121 - Phe and MR 121 - Trp absorption and emission spectra.

Phenylalanine absorbs most at 662 nm and MR 121 - Tryptophan at 664 nm. The emission spectra of both substrates are equally shifted by 2 nm and 4 nm from the emission maximum of MR 121 at 678 nm, respectively.

Another two of the six substrates are dipeptides, each carrying one tryptophan residue at the C-terminus (see figure 4.3). Between MR 121 and tryptophan either phenylalanine or glycine, the smallest natural amino acid, was incorporated.

In the normalized spectra both substrates show a 5 nm red-shift of the absorption maximum while the emission maximum is almost the same compared to that of free MR 121 (see figure 4.4).

The last two of the six substrates incorporated for peptidase research consist of a MR 121 attached phenylalanine, followed by either two or three consecutive tryptophan residues (see figure 4.5).

These substrates, therefore, already offer a variety of cleavage sites. Again, the normalized substrate spectra are shifted in comparison to those of the free chromophore (see figure 4.6). While MR 121 - Phe - $(Trp)_2$ and MR 121 - Phe - $(Trp)_3$ have an identical fluorescence maximum blue-shift of two to three nanometers, their absorption spectra differ very strongly. MR 121 - Phe - $(Trp)_2$ shows a familiar spectrum which is red-shifted by 6 nm. MR 121 - Phe - $(Trp)_3$ though shows a red-shift of 9 nm. Furthermore, the plateau in the absorption spectrum at around 615 nm is not only equally red-shifted, but immensely increased from 46% of the total absorption to 75%. That can only be assigned to the third consecutive tryptophan in this oligopeptide.

The raw absorption spectra are also used for the calculation of relative quantum yields as described in section 3.3.2. The results are presented in table 4.1. MR 121 fluorescence yield is increased by 50% if phenylalanine is attached to the dye. As expected [30], tryptophan quenches the fluorescence very efficiently. The incorporation of a spacer results in a distinctly less efficient quenching, because the distance of electron donor and electron acceptor increases, which leads to less quenching events. The big difference between MR 121 - Gly - Trp and MR 121 - Phe - Trp is caused by the fluorescence increasing effect of phenylalanine on the one hand and the less size of glycine on the other hand. Increasing the number of C-terminal tryptophan residues amplifies the quenching efficiency, thus these oligopeptides are flexible and, therefore, allow 'far' tryptophan residues to come in close proximity with MR 121.

Peptide bonds are known to be rather stable even at high temperatures

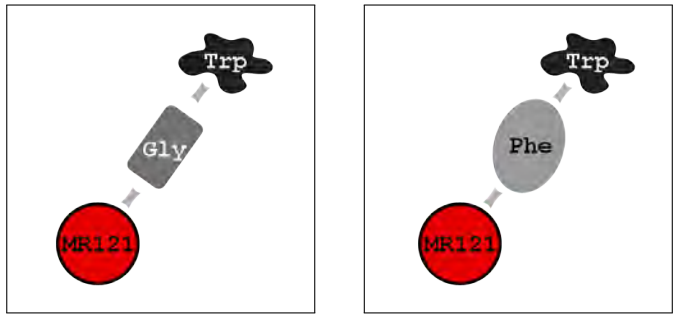

a) MR 121 - Gly - Trp **b)** MR 121 - Phe - Trp

Figure 4.3: MR 121 - Glycine - Tryptophan and MR 121 - Phenylalanine - Tryptophan schemes. Both substrates offer two cleavage sites, one of which each is a true peptide bond.

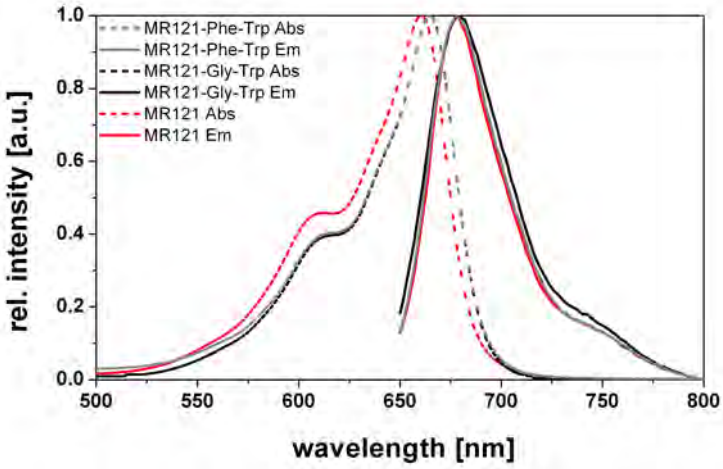

Figure 4.4: Normalized MR 121, MR 121 - Glycine - Tryptophan and MR 121 - Phenylalanine - Tryptophan absorption and emission spectra.

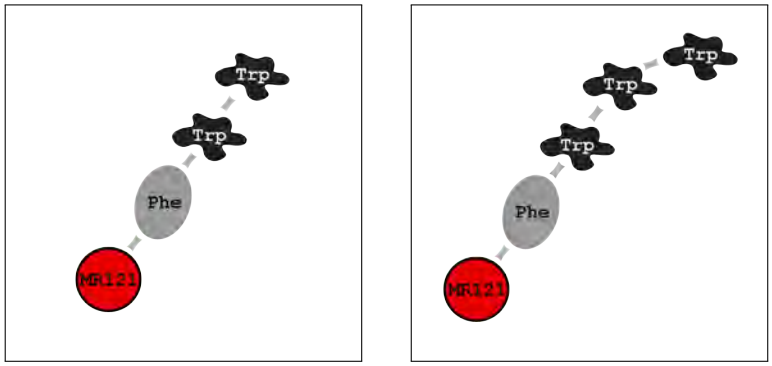

a) MR 121 - Phe - $(Trp)_2$ **b)** MR 121 - Phe - $(Trp)_3$

Figure 4.5: MR 121 - Phe - $(Trp)_2$ and MR 121 - Phe - $(Trp)_3$ schemes. MR 121 - Phe - $(Trp)_2$ offers three cleavage sites, two of which are true peptide bonds, MR 121 - Phe - $(Trp)_3$ offers four cleavage sites with three true peptide bonds.

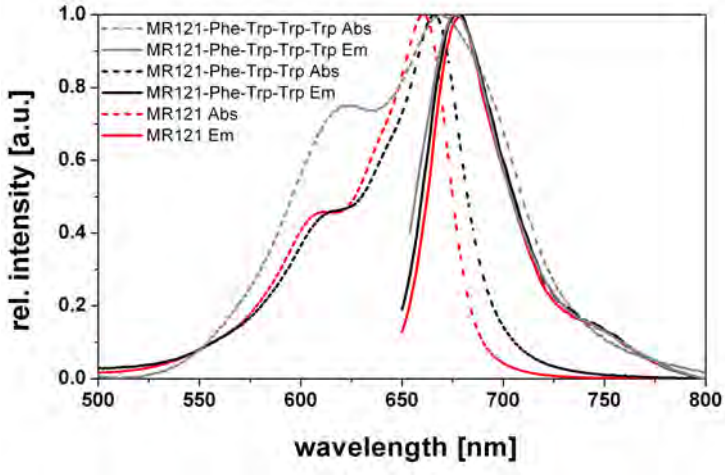

Figure 4.6: Normalized MR 121 - Phe - $(Trp)_2$ and MR 121 - Phe - $(Trp)_3$ absorption and emission spectra.

Table 4.1: Relative quantum yields of labeled peptides.

substrate	Φ_{rel}
MR 121 - Phe	1.52
MR 121 - Trp	0.01
MR 121 - Gly - Trp	0.18
MR 121 - Phe - Trp	0.33
MR 121 - Phe - $(Trp)_2$	0.17
MR 121 - Phe - $(Trp)_3$	0.09

[193,194]. This also applies for the peptide substrates utilized in this work as can be seen in the normalized temperature graphs in figure 4.7. Obviously, the thermal behavior of MR 121 - Trp results from MR 121 itself over the whole applied thermal range, while MR 121 - Phe shows a stronger decrease of fluorescence intensity than the free chromophore, starting at a temperature of about 40°C. This indicates, that the fluorescence increasing effect of phenylalanine declines with rising temperatures.

MR 121 - Phe - Trp shows a similar decrease in fluorescence intensity at temperatures higher than 40-50°C, which, therefore, must be dominated by the same effect. Since, MR 121 - Gly - Trp also shows a decrease in fluorescence intensities in the same range, there must also be an improved quenching due to the spacer amino acid. Thus the higher the temperature, the higher the molecular movements and, therefore, the flexibility of a single peptide [195], it can be assumed, that these short substrates are more efficiently quenched at high temperatures due to an increased number of contact events. MR 121 - Phe - $(Trp)_2$ and MR 121 - Phe - $(Trp)_3$ on the other hand ultimately show increases in fluorescence intensities at rising temperatures. MR 121 - Phe - $(Trp)_2$ already shows this increase beginning at 30°C, but reaches a plateau with a 10% higher intensity at 55°C. MR 121 - Phe - $(Trp)_3$ shows a rather stable fluorescence intensity up to 60°C and then rises distinctly. Despite this small number of substrate components there can already be a lot of alternative interactions and a formation of a spatial structure denaturing at higher temperatures, which would lead to this ambiguous behavior [196,197].

Still, all these fluorescence intensity changes due to thermal variations are

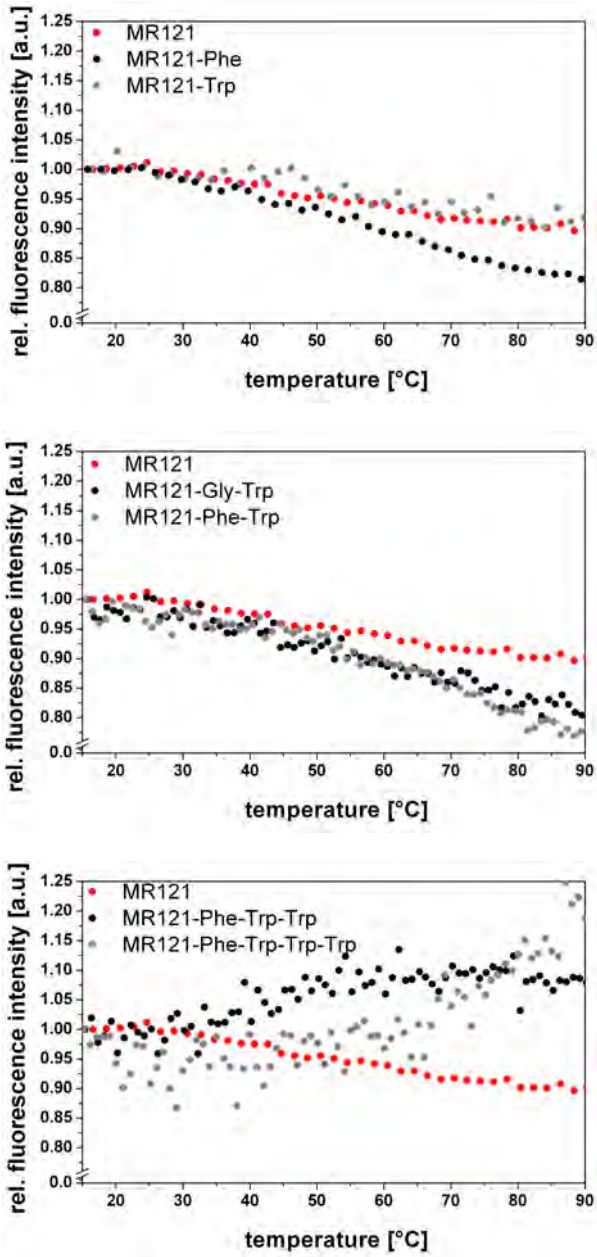

Figure 4.7: Thermal behavior of peptide substrates and free MR 121. Graphs are normalized to fluorescence intensities at 15°C.

rather small, allowing the use of peptide substrates even at very high temperatures. It has to be regarded though, that a high working temperature will change the determined relative quantum yields. Measurements in the range of 15-30°C are entirely feasible without further alterations or additional computations.

Substrates for Nucleases

Nucleases generally hydrolyze DNA[2]. Most nucleases process DNA in its naturally most often occurring form of a double helix. Still, there are nucleases that cleave single stranded DNA or complex forms like supercoiled plasmid DNA (cf. section 2.4.2.2). When designing fluorescent substrates consisting of DNA, these preferences should be considered and therefore appropriate domains should be provided. Given, that the design of a supercoiled plasmid DNA substrate with single and double stranded regions, that can be efficiently quenched and instantly fluoresces upon any scission, is hardly possible, DNA hairpins constitute a fairly good substitute.

In this work several DNA hairpins were utilized for the research on DNase I and DNase II, both preferring double stranded DNA, S1-Nuclease, preferring single stranded DNA and the barely familiar DNase X, known to prefer supercoiled plasmid DNA (cf. section 2.4).

The designed hairpins can be summarized to two sets of highly related structures. The first set of ten hairpins and their connections to each other are presented in figure 4.8.

SP1 and SP2 only differ by minor sequence variations. A modification of two nucleic acids changes SP2 to SP3, while a variable stem to loop ratio and an according slight sequence variation distinguishes SP2 and SP4. SP2 was furthermore modified by two different methylation patterns and a substitution of loop bases to yield $SP2^{CM}$, $SP2^{AM}$ and $SP2_{AL}$. A methylation of $SP2_{AL}$ yields ${SP2_{AL}}^{AM}$ and a further methylation ${SP2_{AL}}^{mM}$. This substrate is still closely related to $SP2^{CM}$, which is also further modified by a variation of the quenching mechanism.

Figure 4.9 shows the detailed structures of SP1, SP3 and SP4. These DNA hairpins are not directly related to each other (cf. figure 4.8) but to a favorable substitute which will be presented later on. Still, this subset yields

[2]Enzymes are usually classified upon their major or first detected substrate specificity. Nonetheless enzymes can also show activity on substrates that do not belong to their assigned substrate class.

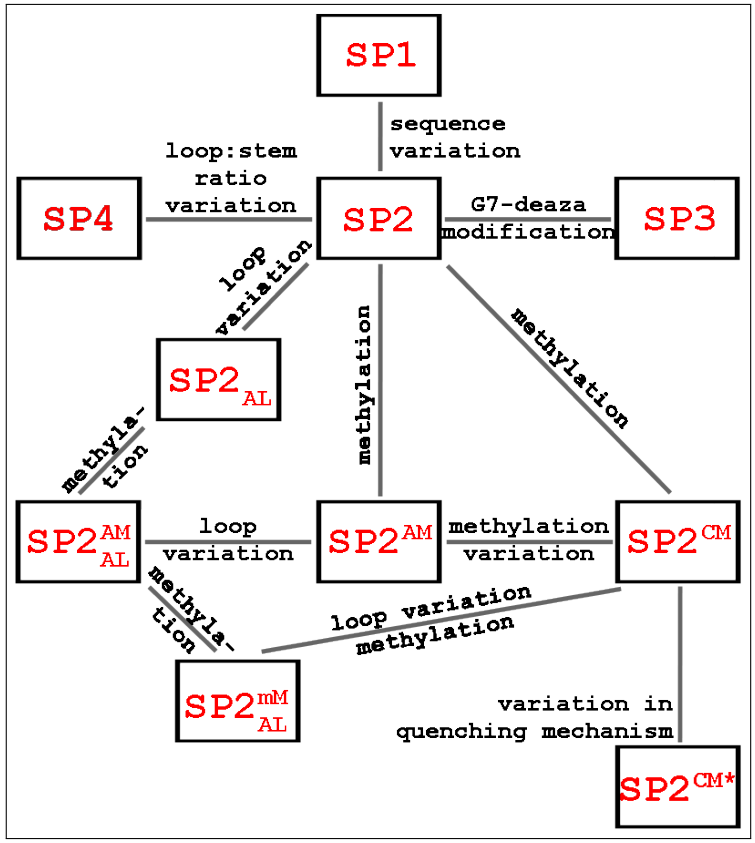

Figure 4.8: Concept map of the set of ten DNA hairpins called *SmartProbes* (SP).

an efficient introduction into DNA hairpin discussion, since it offers a comparably strong structure variation and, therefore, a rapid and early overview on structural effects. SP1, SP3 and SP4 all carry an Atto 655 fluorophore at the 5'-end of the nucleic acid sequence. Each 3'-end consists of several guanosine residues, which are known to efficiently quench Atto 655 [30,32–34]. DNA hairpins built in this manner are generally called *Smart Probes* (in the following abbreviated with 'SP').

The nucleic acid sequence of SP1 is designed to form a double stranded region forming the hairpin stem of eight base pairs and a single stranded

region of 6 bases to form the hairpin loop. The loop only consists of thymine residues due to its small shape which allows a high loop flexibility and, therefore, a short loop sequence. Furthermore, neither thymine nor its association partner adenine effect Atto 655 fluorescence due to their high oxidation potentials [30, 32]. The stem region comprises adenine - thymine and cytosine - guanine pairs in a succession that allows only one distinct folding structure [179]. Furthermore, guanine is placed sequentially far away from Atto 655 and as close as possible at hairpin formation. Since guanine positions have an important effect on fluorophore quenching [198, 199], they are consequently presented differently than the other nucleotide bases.

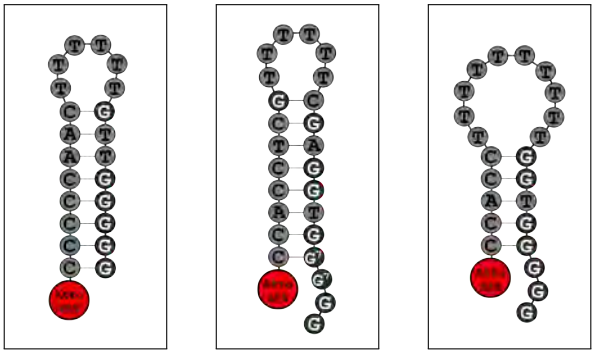

a) SP1 **b)** SP3 **c)** SP4

Figure 4.9: SP1, SP3 and SP4 structures.

SP3 also has a stem of 8 base pairs and a loop of six thymine residues. Furthermore, there is an overlap of three bases at the 3' - end. Those three bases, approximated to be closest to Atto 655 in a hairpin formation, consist of 7-Deaza-2'-deoxyguanosine (G^7) [200], which has even higher electron donating properties than guanosine itself [32]. To allow only one folding structure [179] and still incorporate as many guanines as possible, the double stranded sequence alternates stronger between base pairs than SP1 stem sequence.

SP4 consists of a five base pair long stem and a ten thymines long loop. It also has an overlap of three guanines at the 3' - end of the sequence and can only form one structure [179].

As figure 4.10 shows, the attachment of nucleotide sequences changes the

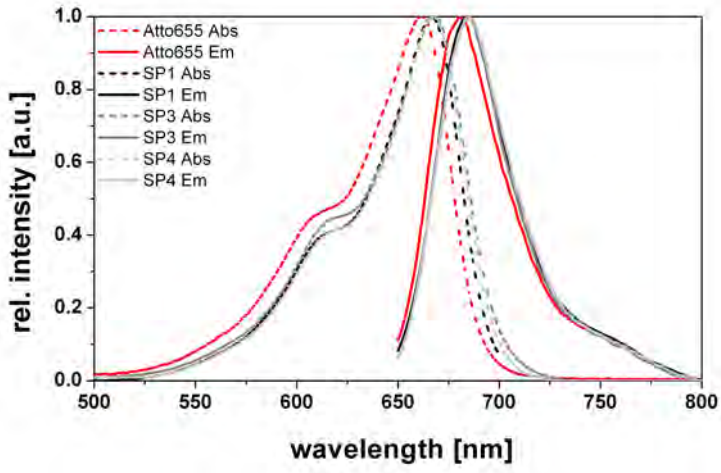

Figure 4.10: Absorption and emission spectra of SP1, SP3 and SP4 compared to those of free Atto 655.

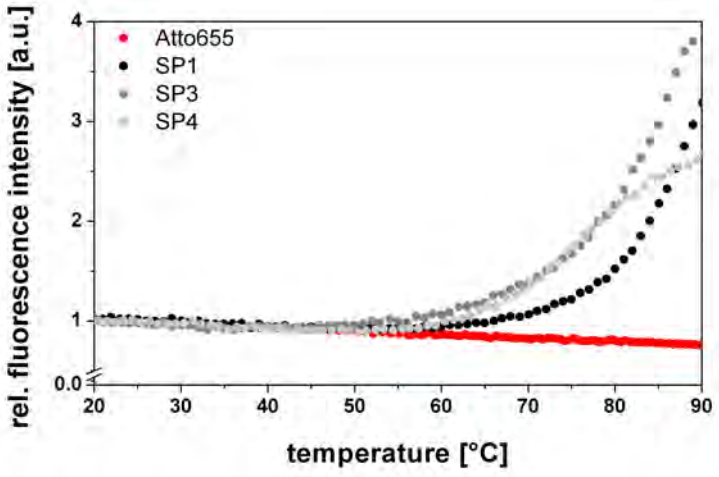

Figure 4.11: Thermal stability of SP1, SP3 and SP4 compared to that of free Atto 655.

absorption and emission spectra to longer wavelengths. While Atto 655 has an absorption maximum at 662 nm, all three smart probes reveal an absorption maximum at around 667 nm. The emission maximum also shifts by 5 nm from 680 nm for Atto 655 to 685 nm for SP1, SP3 and SP4.

Phosphodiester bonds in a DNA strand are very stable even at high temperatures. Base pairing hydrogen bonds, though, are only stable up to a specific temperature, destined by the buffer composition and the amount of surrounding base pairs [201, 202]. Once hydrogen bonds break, the hairpin formation denatures and guanosine residues lose spatial contact to Atto 655, which results in decreasing quenching efficiencies. This can be observed in figure 4.11. Up to 50°C the normalized fluorescence intensities of SP1, SP3 and SP4 follow the intensity of free Atto 655. Between 50°C and 90°C Atto 655 fluorescence intensity continuously decreases, while SP1 fluorescence intensity slightly rises up to 70°C, where a much stronger increase in intensity begins. A saturation value is not reached until 90°C, therefore, a melting temperature cannot be distinctly determined, a Boltzmann fit, though, suggests 91.9 °C ± 1.3 °C. SP3 normalized fluorescence intensity distinctly rises between 50°C and 90°C, indicating a saturation value at very high temperatures. Here, the determined melting temperature amounts to 96 °C ± 1.6 °C. SP4 fluorescence intensity stays rather constant up to 60°C before rising up to 90°C. Despite there is no distinct saturation plateau, a melting temperature can be determined to 76.3 °C ± 0.2 °C.

Table 4.2: Calculated melting temperatures, Gibbs free energy and evaluated relative quantum yields of SP1, SP3 and SP4.

substrate	**calculated melting temperature** [°C]	**Gibbs free energy** [kcal/mol]	**evaluated** Φ_{rel}
SP1	82.9	-7.48	0.22
SP3	80.9	-8.01	0.15
SP4	65.3	-3.15	0.28

All determined melting temperature top the calculated values [179] as presented in table 4.2 by 10°C and more. Since calculations are made for indi-

vidual DNA strands and an intramolecular binding is comparably stronger, it can be assumed that actual melting temperatures indeed meet the determined values better than the calculated ones, which is already indicated by the temperature dependency graphs in figure 4.11.

Zuker also provides calculations of the free Gibbs energy of the utilized smart probes [179]. These energies mostly correlate with stem to loop length ratio as can be seen in table 4.2. This ratio, the melting characteristics and the amount of guanine respectively 7-Deaza-2'-deoxyguanosine determine the relative quantum yield of the *smart probes* in comparison to Atto 655. While SP1 fluoresces with 22% of the intensity free Atto 655 shows, the attachment of a guanine overlap and the incorporation of modified guanine in SP3 lowers the relative quantum yield to 0.15. The variation of stem to loop length ratio results in less efficient quenching despite the utilization of a 3-mer guanine overlap in SP4.

Concerning quenching efficiency and melting characteristics, SP1 and SP3 clearly dominate over SP4. Their evolutionary intermediate SP2 and five modifications of it are presented in figure 4.12. SP2 has the very same nucleic acid sequence as SP3, except for the two guanine modifications at position 22 and 23. Here, SP2 has standard guanine bases. Therefore, SP2 differs from SP1 only by small sequence variations and the 3-mer guanine overlap[3]. SP2 was modified by methylations to yield $SP2^{AM}$, which carries a N6-Methyl-2'-deoxyadenosine (N6-Methyl-2'-dA) at position 17 and $SP2^{CM}$, which incorporates N4-Methyl-deoxycytidine (N4-Methyl dC) at position 2. A further modification of SP2 is the substitution of all thymines in the hairpin loop by adenosine residues, yielding $SP2_{AL}$. This smart probe was again methylated with N6-Methyl-2'-dA at position 17 and additionally at position 12 to yield ${SP2_{AL}}^{AM}$. A supplementary modification with N4-Methyl dC at position 2 finally yields ${SP2_{AL}}^{mM}$.

As can be seen in figure 4.13 and figure 4.14, SP2 and all its variations show the same 5 nm redshift of absorption and emission maxima, compared to free Atto 655 as SP1, SP3 and SP4.

Figure 4.15 shows the melting characteristics of SP2, $SP2^{AM}$ and $SP2^{CM}$ compared to that of free Atto 655. These hairpins reveal a lower normalized fluorescence intensity than Atto 655 up to 60°C for SP2 and $SP2^{AM}$ and 70°C for $SP2^{CM}$. The hairpin stem in this sequence obviously contracts in this tem-

[3]For the connections between any of these *smart probes* also see figure 4.8.

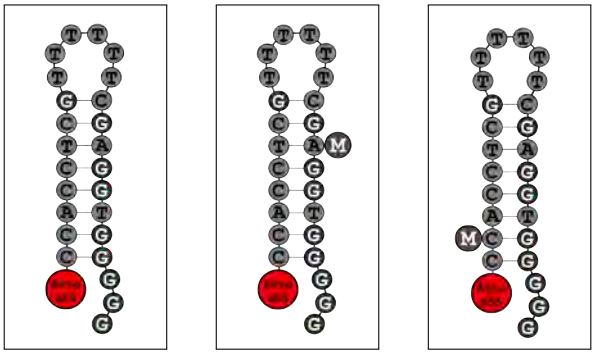

a) SP2 **b)** $SP2^{AM}$ **c)** $SP2^{CM}$

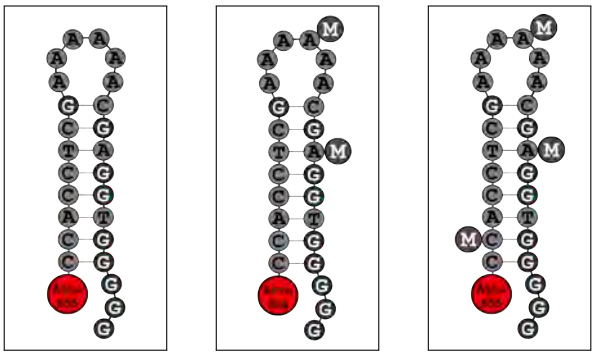

d) $SP2_{AL}$ **e)** $SP2_{AL}{}^{AM}$ **f)** $SP2_{AL}{}^{mM}$

Figure 4.12: SP2, $SP2^{AM}$, $SP2^{CM}$, $SP2_{AL}$, $SP2_{AL}{}^{AM}$ and $SP2_{AL}{}^{mM}$ structures.

perature range, increasing the quenching efficiency. Around 65°C both SP2 and $SP2^{AM}$ show a strong increase in fluorescence, which demonstrates that the hairpin structure denatures, preventing efficient quenching. Since $SP2^{CM}$ carries the very same nucleic acid sequence but shows the same fluorescence intensity effects each at a ten degrees higher temperature, it can be assumed that the hairpin does not actually denature at higher temperatures, but that the N4-Methyl dC modification in such a constantly close distance to the fluorophore also has a quenching effect. Determined melting temperatures are 88.3 °C ± 1.2 °C for SP2, 87.5 °C ± 1.3 °C for $SP2^{AM}$ and 88.9 °C ± 1.7 °C for $SP2^{CM}$, which yields 88.2 °C ± 0.8 °C for all.

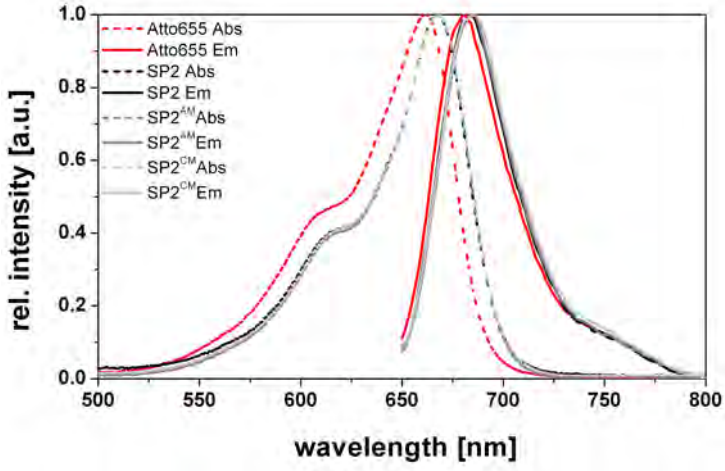

Figure 4.13: Absorption and emission spectra of SP2, $SP2^{AM}$ and $SP2^{CM}$ compared to those of free Atto 655.

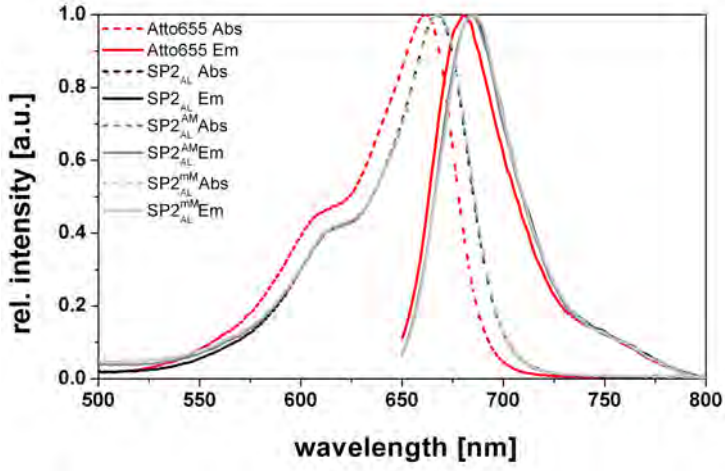

Figure 4.14: Absorption and emission spectra of $SP2_{AL}$, $SP2_{AL}{}^{AM}$ and $SP2_{AL}{}^{mM}$ compared to those of free Atto 655.

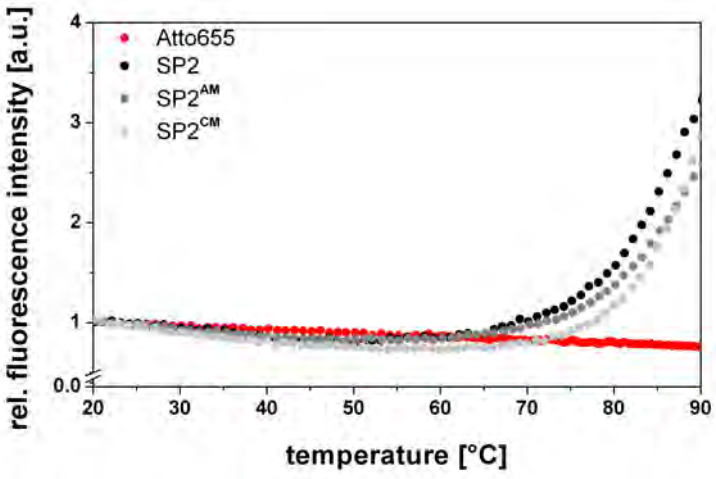

Figure 4.15: Thermal stability of SP2, SP2$^{\mathrm{AM}}$ and SP2$^{\mathrm{CM}}$ compared to free Atto 655.

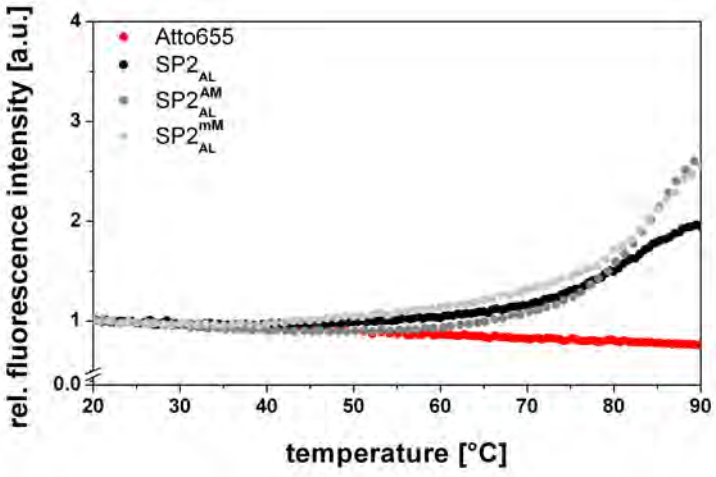

Figure 4.16: Thermal stability of SP2$_{\mathrm{AL}}$, SP2$_{\mathrm{AL}}{}^{\mathrm{AM}}$ and SP2$_{\mathrm{AL}}{}^{\mathrm{mM}}$ compared to free Atto 655.

Melting characteristics of $SP2_{AL}$, $SP2_{AL}{}^{AM}$ and $SP2_{AL}{}^{mM}$ compared to free Atto 655 are presented in figure 4.16. These three *smart probes* show a normalized fluorescence intensity which equals that of Atto 655 only up to 40°C after which the hairpins start a slow increase in fluorescence up to 75°C. The twofold N6-Methyl-2'-dA modified $SP2_{AL}{}^{AM}$ shows a lower fluorescence intensity than the unmethylated $SP2_{AL}$, while the multiple methylated $SP2_{AL}{}^{mM}$ shows the highest fluorescence intensity over a wide thermal range. Melting temperatures could be determined to 84 °C ± 0.5 °C for $SP2_{AL}$ and 86.6 °C ± 0.7 °C for $SP2_{AL}{}^{AM}$. For $SP2_{AL}{}^{mM}$ no reasonable melting temperature could be determined by Boltzmann fits.

Table 4.3: Calculated melting temperatures, Gibbs free energy and evaluated relative quantum yields of SP2, $SP2^{AM}$, $SP2^{CM}$, $SP2_{AL}$, $SP2_{AL}{}^{AM}$ and $SP2_{AL}{}^{mM}$.

substrate	**calculated melting temperature**[4] [°C]	**Gibbs free energy**[4] [kcal/mol]	**evaluated** Φ_{rel}
SP2	80.2	-7.91	0.19
$SP2^{AM}$	68.5	-4.46	0.24
$SP2^{CM}$	78.1	-5.26	0.14
$SP2_{AL}$	80.9	-8.01	0.37
$SP2_{AL}{}^{AM}$	69.2	-4.56	0.23
$SP2_{AL}{}^{mM}$	59.6	-1.91	0.20

The determined melting temperatures for SP2 and its modifications also override the computed melting temperatures by several degrees [179]. SP2, $SP2^{AM}$ and $SP2^{CM}$ showed a higher melting temperature than $SP2_{AL}$ and its methylated version although computationally expected differently. This indicates on the one hand, that methylated bases pair ordinarily with their nucleic acid matches, and on the other hand, that a hairpin with a 6-mer loop, consisting only of adenines, is indeed not as stable as a hairpin with a

[4]Since the effect of N6-Methyl-2'-dA and N4-Methyl dC are not predictable with 'mfold' [179], methylated bases were stated as non-pairing bases.

6-mer loop of only thymines. The calculated melting temperatures and Gibbs free energies should, therefore, only be conditionally regarded for hairpin structures.

Comparing SP2 with SP1 and SP3 in regard to structures and melting temperatures, one should expect nearly identical melting temperatures, since the base pairs are nearly identical as well. Computed melting temperatures (see table 4.2 and table 4.3), indeed, only show slight deviations. Determined melting temperatures though vary between 88.3 °C ± 1.2 °C for SP2 and 96.0 °C ± 1.6 °C for SP3. It should be assumed, that SP3 and possibly also SP1 determined melting temperatures are not realistic due to the unconfident Boltzmann fit, and should ,therefore, be in the range of the SP2 melting temperature.

Temperature profiles (figure 4.15, figure 4.16) have already indicated relative quantum yields of SP2 and its direct relatives. SP2 has a relative quantum yield of 0.19 compared to free Atto 655, which averages SP1 and SP3 relative quantum yields (cf. table 4.2). N6-Methyl-2'-dA at position 17 ($SP2^{AM}$) decreases the quenching efficiency considerably. To the same extent N4-Methyl dC at position 2 ($SP2^{CM}$) increases the quenching efficiency as has been expected by temperature profiles (figure 4.15). Thus, $SP2^{CM}$ represents the best quenched *smart probe* in this set. The $SP2_{AL}$ relative quantum yield of 0.37 again proves the reduced stability of the hairpin by a deoxynucleoside substitution in the loop. Here, both methylation variations increase the quenching efficiency, not reaching an efficiency as good as that of the unmethylated SP2.

The favored fluorescent substrates for enzyme research have been FRET systems over PET systems, because FRET is easily to incorporate in any sample and accessible at any desired wavelength. Also, FRET usually has a very high quenching efficiency, since it works at distances one order of magnitude higher than PET [47, 150, 203–205]. On the other hand, FRET systems carry several disadvantages over PET systems. Due to the necessity of two modifications (e.g. either two fluorophores or one fluorophore and a dark quencher) the synthesis consumes a longer time, results in higher costs and, statistically, the amount of not properly labeled substrates is higher than in a process that only involves one modification. Furthermore, the probability for the natural substrate to be accepted by an enzyme, especially for very small substrates, is much higher if there is only one foreign substance attached to it.

Therefore, FRET systems should only be used if their advances rule out the intrinsic drawbacks. To evaluate this ratio, SP2^{CM} was modified by a substitution of photo-induced electron transfer quenching to fluorescence resonance energy transfer to a dark quencher (cf figure 4.8). Therefore, Atto 655 was displaced by Dy 631 and the appropriate quencher DyQ 660 was attached to the 3'-end of the nucleotide sequence. The structure of this molecular beacon[5], SP2^{CM}-FRET, is presented in figure 4.17.

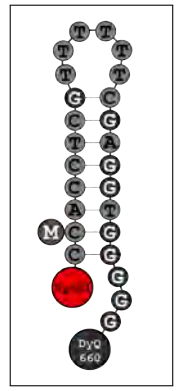

Figure 4.17: SP2^{CM}-FRET structure.

Naturally, this substrate shows absorption and emission spectra that are different to the *smart probes*, because it carries another fluorophore. The derived spectra are presented in figure 4.18.

Dy 631 shows an emission maximum at 654 nm. The absorption spectrum of this molecular beacon shows two peaks, resulting from the absorption maximum of the fluorophore and the dark quencher. The absorption maximum, which corresponds to fluorophore absorption, is at 610 nm. Melting characteristics of this molecular beacon are similar to those of the corresponding *smart probe*, except for slight differences influenced by varied fluorophores and the additional thermal influence of the dark quencher. The relative quantum yield of SP2^{CM}-FRET[6] amounts to 0.17 at neutral pH.

In this case, FRET quenching obviously cannot compete with PET quench-

[5]DNA hairpins, carrying a FRET pair, are called *molecular beacons* instead of *smart probes*.

[6]Here, the intact molecular beacon is related to an enzyme-processed beacon, so a part of the nucleotide sequence is most likely still attached to the fluorophore.

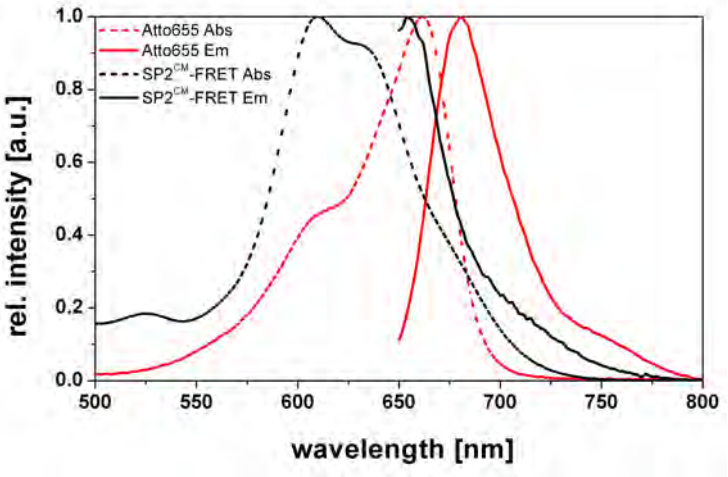

Figure 4.18: Absorption and emission spectra of $SP2^{CM}$ - FRET compared to those of free Atto 655.

ing and would have to be optimized by different quenching FRET pairs and positions. Also, a combination of FRET and PET could be utilized. Since the presented *smart probes* already deliver very satisfactory quenching efficiencies, the intrinsic drawbacks of *molecular beacons* do not need to be risked, so a further quenching modification can be abandoned.

The second set of *smart probes* only consists of three pieces, named VIP[7], depicted in figure 4.19. VIP control consists of a 17 base pair long hairpin stem and a nine bases long loop, formed only of adenine residues. The complete nucleotide sequence carries solely three guanines, in order to avoid quenching of Atto 655 attached to the 5'-end of this hairpin. Therefore, this *smart probe* merely has a control function, as the name indicates.

VIP ds carries a 14 base pair stem, a nine guanine loop and a three guanine overlap at the 3'-end of the sequence. In total, 19 out of the 40 bases are guanosine residues, indicating a strong quenching potential on the attached Atto,655. This *smart probe* is called VIP ds, since only upon a double stranded (ds) scission it would immediately start fluorescing. Upon single stranded (ss) scission, it would either keep its double stranded region, or

[7]In analogy to the *smart probes*, these substrates were called *very intelligent probes*, abbreviated VIP.

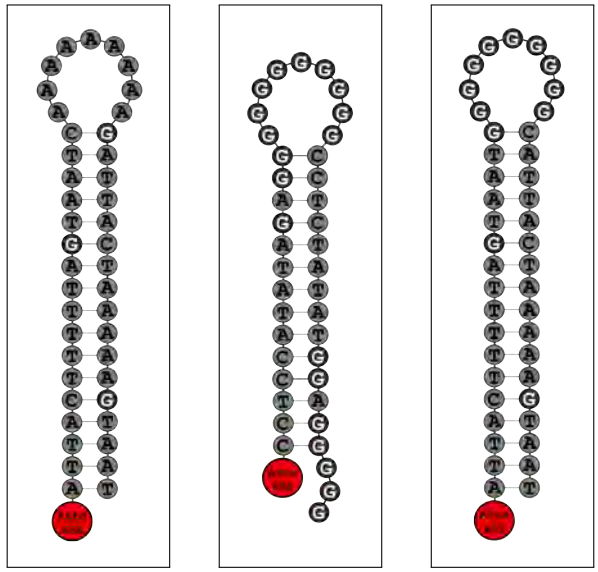

a) VIP control **b)** VIP ds **c)** VIP ss

Figure 4.19: VIP control, VIP ds and VIP ss schemes.

fold into a smaller hairpin, again positioning guanines in close proximity to Atto 655 [179]. VIP ss on the other hand functions as a single stranded scission marker. This *smart probe* carries a 17 base pair stem with only three guanines and a nine guanosine residues loop. Therefore, its Atto 655 is not quenched initially and will not be upon ds scission. Upon ss scission though, the remaining nucleotide forms a new, smaller hairpin, bringing the guanosine residues into close proximity to Atto 655 [179].

Regarding the absorption and emission spectra, which are presented in figure 4.20, all VIP probes show a slight red shift of absorption maximum by 6 - 8 nm and an emission maxima red shift by 4 - 6 nm. The absorption spectrum, furthermore, shows, that the Atto 655 absorption plateau at around 615 nm with a normalized absorption intensity of 0.47 is also red shifted by 5 - 7 nm for all VIP probes, but shows a difference in absorption intensities. While the non quenched VIP control even shows a slightly higher normalized absorption of 0.48, VIP ds has a normalized absorption intensity of 0.41 and VIP ss a value of 0.44. Thus, it can be assumed, that this value corresponds

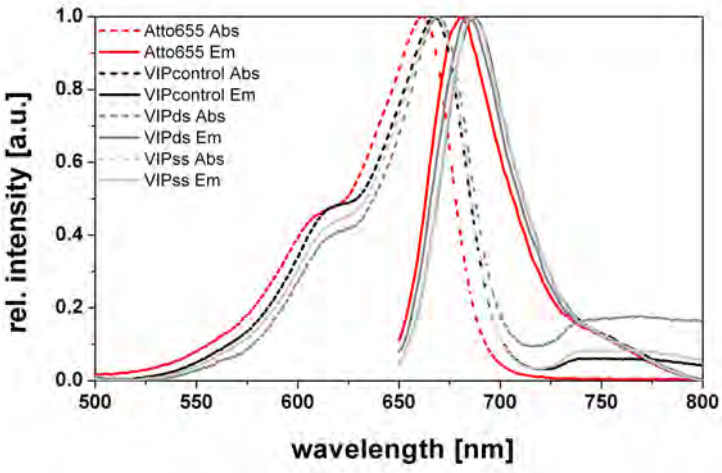

Figure 4.20: Absorption and emission spectra of VIP control, VIP ds, VIP ss compared to those of free Atto 655.

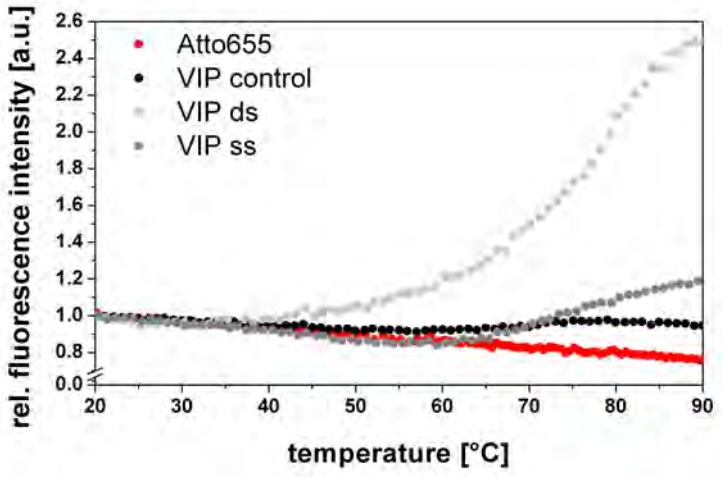

Figure 4.21: Thermal stability of VIP control, VIP ds, VIP ss compared to free Atto 655.

to the amount of guanosine residues in the nucleotide sequence of the *smart probe*.

Figure 4.21 presents the thermal characteristics of the VIP probes in comparison to free Atto 655. Although VIP control was designed to be unquenched, its fluorescence intensity does not overlay the free chromophores thermal fluorescence characteristics. Instead, beginning around 43 °C, VIP control shows a higher normalized fluorescence intensity, meaning there is a nucleotide effect on Atto 655, despite its very small amount of guanines. A melting temperature cannot be fitted for this course, though. VIP ds, thus initially quenched, shows a strong thermal fluorescence intensity dependency, beginning at 40 °C. A Boltzmann fit determines the melting temperature to 79.3 °C ± 0.6 °C. VIP ss, initially non-quenched, also shows a characteristic increase in fluorescence intensity, starting not until 60 °C. The determined melting temperature is 76.7 °C ± 1.2 °C. Since VIP ss and VIP control carry almost identical nucleotide sequences and, therefore, show nearly identical base pairing (cf. figure 4.19), it can be assumed, that VIP control has a similar melting temperature as VIP ss.

This guesswork is supported by computed melting temperatures and the Gibbs free energies [179], given in table 4.4.

Table 4.4: Calculated melting temperatures, Gibbs free energy and evaluated relative quantum yields of VIP control, VIP ds and VIP ss.

substrate	**calculated melting temperature** [°C]	**Gibbs free energy** [kcal/mol]	**evaluated** Φ_{rel}
VIP control	71.8	-11.1	0.95
VIP ds	79.1	-12.23	0.26
VIP ss	71.4	-11.23	0.79

VIP ss and VIP control show nearly identical computed values. VIP ss determined melting temperature tops the computed value by several degrees (cf. table 4.2), while VIP ds determined melting temperature perfectly matches the calculated value. Evaluated relative quantum yields given in this table

prove the assumption made above. VIP control is very slightly quenched, but VIP ss, carrying the same amount of guanines in the nearly identical hairpin stem, is quenched a lot more. This can only be assigned to the guanosine loop despite its distance from the chromophore, suggesting long range energy transfer [88, 199, 206]. As expected, VIP ds is efficiently quenched to yield only 26% of the fluorescence intensity free Atto 655 shows, which is not as good as could have been expected by a comparison to SP2 and SP4 structures and their relative quantum yields.

To investigate the advantage of *smart probes* over other substrates, also the commercially available nuclease substrate 'DNaseAlert' was examined. DNaseAlert is published to be a synthetic oligonucleotide, carrying a HEX™ reporter dye. The normalized spectra of this substrate are depicted in figure 4.22. The absorption maximum is around 537 nm and the emission maximum at 553 nm. Therefore, this fluorescein based substrate has a very small Stokes shift at a spectral range that is not ideally suited for biological samples.

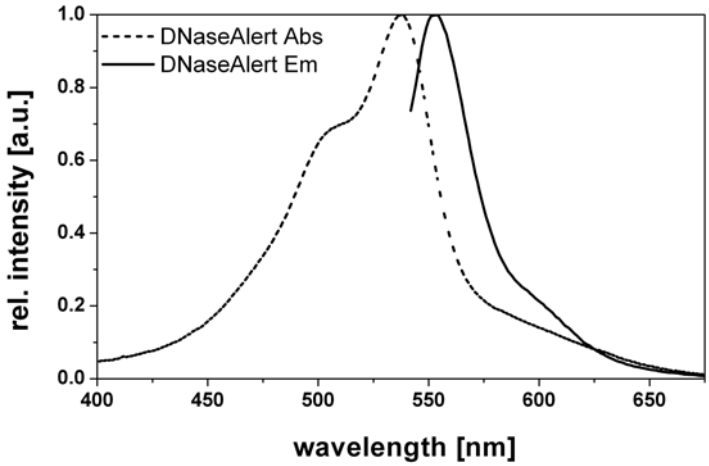

Figure 4.22: Absorption and emission spectra of DNaseAlert substrate.

DNaseAlert shows a constantly rising fluorescence intensity with rising temperature, as presented in figure 4.23. Since the detailed structure of this substrate is not published, this cannot be further interpreted. Still, DNaseAlert

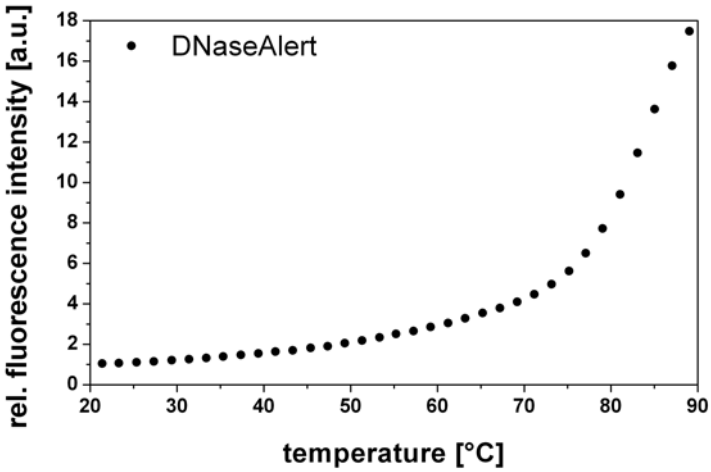

Figure 4.23: Thermal stability of DNaseAlert substrate.

has a major advantage over all presented *smart probes*: This substrate has a relative fluorescence intensity in its initial state[8] of 0.03 at neutral pH - about a fifth of the best quenched examined *smart probe*.

4.1.2 Enzyme Kinetics

The fluorescent substrates, that have so far only been tested for temporal and spectral characteristics, need to be examined in the presence of an enzyme to judge on their suitability for their assigned research. The results of these measurements are presented in this chapter, which again is divided into enzyme subclass assigned sections.

Peptidases and their Substrates

The peptide substrates, introduced in section 4.1.1, were designed for the use with Carboxypeptidase A. This enzyme is known to process peptide bonds between nearly every amino acids by C-terminally releasing mono-, di- or tripeptides [65–68, 207] (cf. section 2.4.2.1). Therefore, in any utilized peptide substrate the C-terminal tryptophan residues can be stripped, which would then diffuse away from the fluorophore, disabling the quenching mech-

[8] related to its enzyme processed state

anism. Thus, a strong increase in fluorescence should be obtained upon enzyme addition to a substrate, while the substrate itself ideally shows a constant fluorescence intensity during the complete measurement time scale.

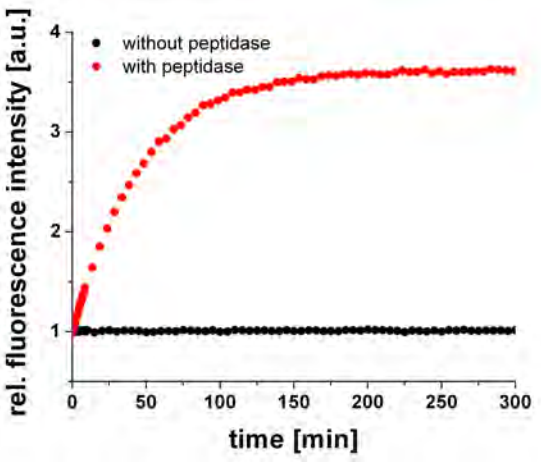

Figure 4.24: Fluorescence intensity variation of MR 121 - Phe - Trp in absence and in presence of Carboxypeptidase A.

Figure 4.24 shows MR 121 - Phe - Trp fluorescence intensity over time in presence and in absence of Carboxypeptidase A. After enzyme addition, the fluorescence intensity immediately rises, while it stays absolutely constant for six hours, if no enzyme is present. The same behavior occurs with any other utilized peptide substrates (data not shown).

Figure 4.25 shows a set of comparable measurements with all introduced peptide substrates. MR 121 - Phe shows a slight decrease in fluorescence intensity, reaching a 0.98 fold initial intensity after 6 hours. Thus, it is not possible to make a statement about an enzyme procession of this substrate. MR 121 - Trp shows a very slow increase in fluorescence upon Carboxypeptidase A addition. 6 hours after addition , the intensity has only reached a signal that is 1.7 fold as high as the starting intensity. After 45 hours, the signal reached a 5.5 fold starting intensity. Regarding the relative quantum yield of 0.01 (cf. table 4.1) a signal 100 fold as high as that at the beginning of the reaction should be possible. MR 121 - Gly - Trp and MR 121 - Phe - Trp both show a comparably fast increase in fluorescence intensity. After 2.5

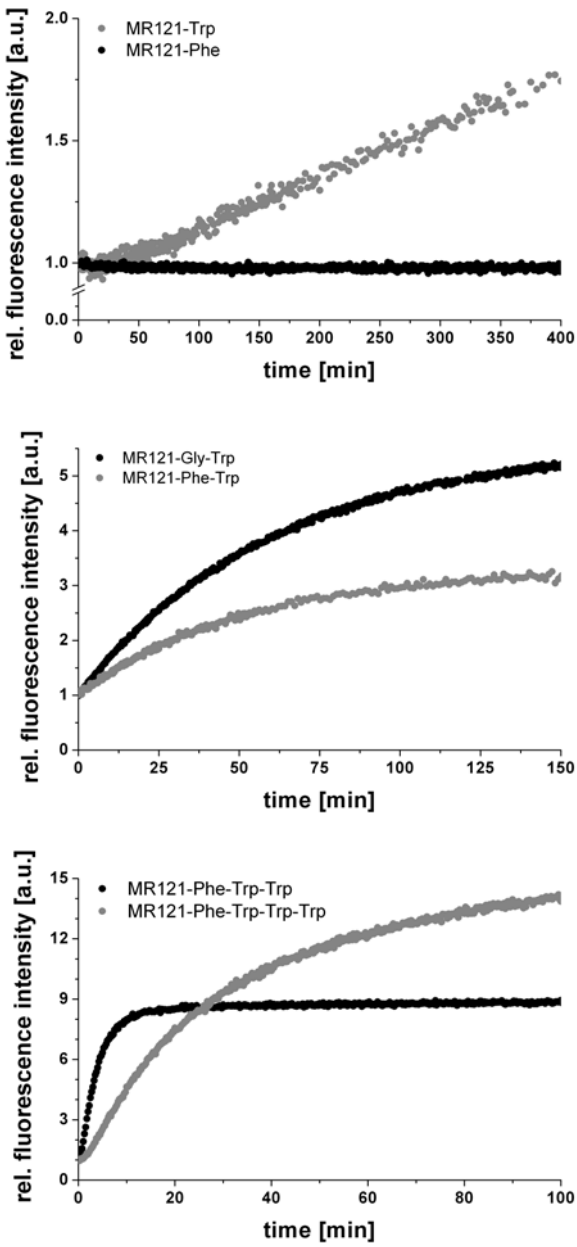

Figure 4.25: Normalized fluorescence intensity plots of all utilized peptide substrates upon addition of Carboxypeptidase A.

hours the saturation of a 5.6 respectively to a 3.3 fold initial intensity is almost reached, which is in perfect accordance to the examined relative quantum yields. MR 121 - Phe - $(Trp)_2$ approximates its saturation intensity of a 9.0 fold starting intensity already 20 minutes after enzyme addition, while MR 121 - Phe - $(Trp)_3$ takes more than 2 hours to reach a 17.3 fold starting intensity. Multiplied by their relative quantum yields, both substrates reveal a final intensity, that is 1.5 fold the signal shown by free MR 121, similar to MR 121 - Phe relative quantum yield. This indicates, that both of these substrates are relieved from all tryptophans they carried, but mostly keep their attached phenylalanine for the complete observation time of 100 minutes. Since MR 121 - Phe - Trp is obviously processed into free MR 121 without any attached phenylalanine, this could indicate a general preference of Carboxypeptidase A for producing dipeptides over monopeptides. Furthermore, the question whether MR 121 - Phe is processed at all needs to be asked.

HPLC measurements were used to address these problems. MR 121 - Phe and Carboxypeptidase A were incubated for 24 hours before HPLC analysis started. A distinct MR 121 signal elevated next to a high peak of unprocessed MR 121 - Phe. MR 121 - Phe - Trp, equally treated, was found to be processed at both possible cleavage sites, mostly though stepwise. Therefore, a stepwise scission of MR 121 - Phe - $(Trp)_2$ and MR 121 - Phe - $(Trp)_3$ is very likely, which would be more slowly and, therefore, possibly not be finished in the presented observation time of 100 minutes, due to the higher amount of amino acids.

Most intriguing in HPLC measurements was the measurement on MR 121 - Gly - Trp. Even after four days of incubation with Carboxypeptidase A, when both slowly processed substrates MR 121 - Phe and MR 121 - Trp had been completely converted into amino acids and free fluorophore, MR 121 - Gly - Trp was solely cleaved into MR 121 - Gly and free tryptophan. MR 121 - Gly was not processed by this enzyme by any means, implying there is no hidden competitive inhibition in this reaction.

MR 121 - Gly - Trp, therefore, represents the ideal fluorescent substrate for Carboxypeptidase A research, because it is efficiently quenched in its intact state with a relative quantum yield of 0.18, it is rapidly processed by the enzyme and the only process that can occur between these two reactants is clearly visible.

Nucleases and their Substrates

Most nucleases do not only work on specific sequences. Therefore, it has to be expected that the designed *smart probes* are accepted by several nucleases. Still, DNA sequences can be modified in order to optimize the desired acceptance and downgrade others. The presented *smart probes* were customized to allow a discrimination between DNaseI and the very similar DNaseX. Most important for *smart probe* functionality is a nucleolytic cleavage, that results in a breakage of the DNA backbone. At an appropriate combination of cleavage position, double stranded region size and sample temperature, base pairs detach from each other, ultimately resulting in the degradation of the double stranded region. By diffusion fluorophore and quenchers lose contact, yielding an increase in fluorescence. On the time scale and measurement settings of such a reaction, the *smart probe* needs to stably fluoresce, if there is no enzyme present. Figure 4.26 representatively proves with SP1 and DNaseI

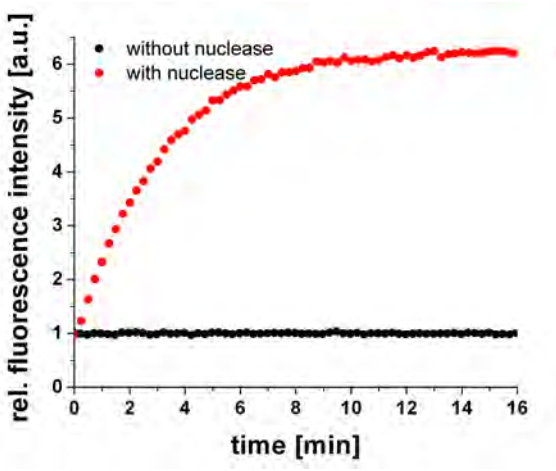

Figure 4.26: Fluorescence intensity variation of SP1 in absence and in presence of bovine DNaseI.

presence and its absence, that this demand can be answered.

Since a noteworthy number of *smart probes* was examined with DNaseI, DNaseII, S1-Nuclease and DNaseX in this work, the results are reasonably split into several graphs. Figure 4.27 shows the normalized fluorescence intensity plots of SP1 and its successors SP2 and SP3 (cf. figure 4.8) upon addition of bovine DNaseI. 10 minutes after enzyme addition, SP1 approx-

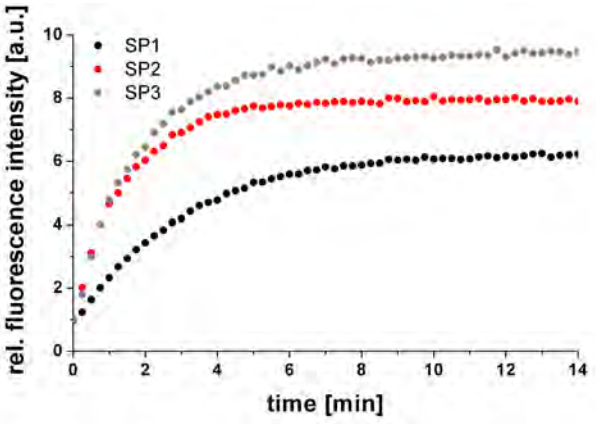

Figure 4.27: Normalized fluorescence intensity plots of all SP1, SP2 and SP3 upon addition of bovine DNaseI in DNaseI-buffer.

imates its saturation intensity, which is 6.3 fold higher than the starting intensity. SP2 is processed in around 5 minutes to yield a 8.1 fold intensity and for SP3 it takes 7 minutes to reach a 9.6 fold intensity as that at the beginning of the process. The comparison of examined fluorescence increase with relative quantum yields (table 4.2, table 4.3) reveals, that these samples actually show a stronger increase than they should be able to. This must be accounted to the effect of the specific DNaseI buffer on the fluorophore and the quenching mechanism[9].

Thus SP2 is processed the fastest and shows a strong increase in fluorescence intensity upon DNaseI addition without any high-cost 3'-modifications, it offers a good basis for nuclease comparison. For the best contrast in *smart probe* structure, SP4 is integrated into this arrangement, which is depicted in figure 4.28.

For this measurement, each enzyme was tested in an appropriate environment (cf. section 2.4 and section 3.2.1) and equivalent substrate concentrations. Enzyme concentrations were adjusted to show sufficient results within

[9]Relative quantum yields in DNaseI-buffer are generally at around 70% of those in PBS.

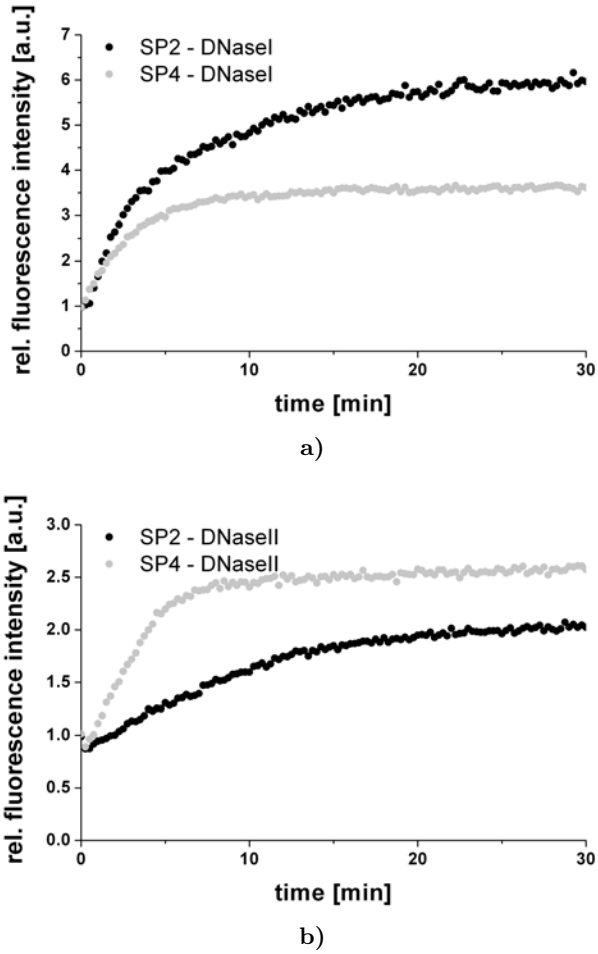

Figure 4.28: Normalized fluorescence intensity plots of SP2 and SP4 upon addition of bovine DNaseI (a)), DNaseII (b)), S1-Nuclease (c)) and DNaseX (d)).

30 minutes[10,11]. While SP2 is completely processed by DNaseI in 25 minutes,

[10]This results in a stretched increase in normalized fluorescence increase of SP2 in presence of DNaseI of figure 4.28 a) in comparison to that one shown in figure 4.27.

[11]This adjustment could not be realized for DNaseX without accepting very high dilution effects on fluorescence signals due to its little activity. Therefore DNaseX measurements were allowed to result in remarkable signals within 80 minutes.

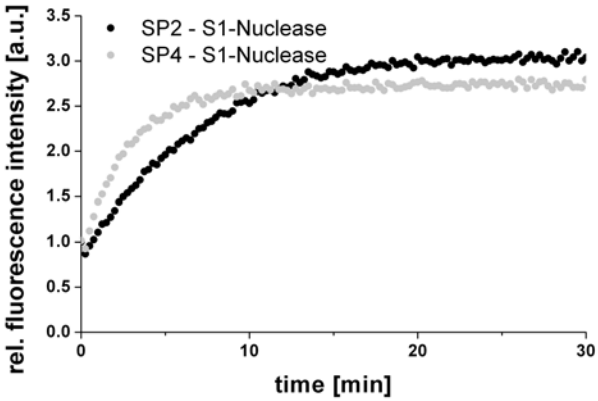

c)

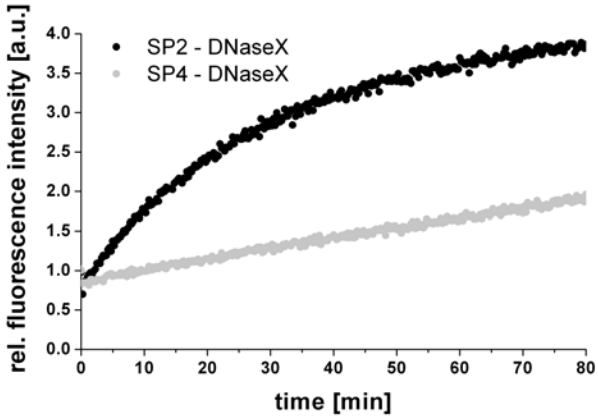

d)

Figure 4.28: Normalized fluorescence intensity courses of SP2 and SP4 upon addition of bovine DNaseI (a)), DNaseII (b)), S1-Nuclease (c)) and DNaseX (d)).

SP4 already approximates its maximum fluorescence intensity after 12 minutes. As expected by relative quantum yields, the signal that is obtained by SP4 is not as high as that of SP2. DNaseII processes SP2 and SP4 in similar time scales, whereas SP4 actually yields a stronger increase in fluorescence intensity than SP2. Generally, the achieved signal increase by DNaseII is very

low compared to the signal obtained by DNaseI, because DNaseII requires a buffer at much lower pH value, which negatively effects initial quenching efficiencies. Next to the same pH value reduction, *smart probes* in S1-Nuclease research also meet a temperature decrease by 17°C, which suits initial quenching efficiencies better. As anticipated due to S1-Nuclease specificity for single stranded DNA [156, 208], SP4 reaches its saturation value faster than SP2, because it offers a larger hairpin loop. Unlike the other tested nucleases, DNaseX clearly shows that it processes SP2 faster than SP4. While the SP2 sample reaches its saturation 100 minutes after enzyme addition, the normalized fluorescence intensity graph showing SP4 signal, does not indicate any saturation. For a discrimination of DNaseX from other nucleases, SP2 constitutes an optimal basis.

Since DNaseX is suggested to detect and destroy foreign DNA [43], it can be assumed, that this enzyme might be sensitive to methylation patterns which contribute to the epigenetic code [209]. Therefore, SP2 was methylated in different ways. The methylation effects on substrate acceptance for DNaseX and its homologue DNaseI are presented in figure 4.29.

The increase in fluorescence intensity of SP2 upon DNaseI cleavage is determined to 7.8 fold compared to the intensity before enzyme addition (cf. figure 4.27). Half of this increase is reached after 11 minutes. $SP2^{AM}$ shows the same velocity as SP2, but a different maximum intensity of only 5.9 fold the starting intensity in accordance to relative fluorescence quantum yields (cf. table 4.3). A methylation of adenine at position 17 does, therefore, not effect the procession of this *smart probe* by DNaseI. A methylation of cytosine at position 2 on the other hand, reaches half of its maximum increase to a 9.5 fold starting intensity already at 7.5 minutes, meaning that DNaseI is strongly attracted by $SP2^{CM}$. The substitution of all loop inherited thymines to adenines does not only affect the relative quantum yield and, therefore, the fluorescence increase that is obtained upon cleavage by DNaseI, but also its attraction to this enzyme. Half of the increase $SP2_{AL}$ shows, has only happened 13 minutes after nuclease addition. Again, the methylation of adenines, that was applied in $SP2_{AL}{}^{AM}$, does not change its procession velocity by DNaseI, because half of its fluorescence increase has happened at 13 minutes as well. The additional methylation of cytosine at position 2, that yields $SP2_{AL}{}^{mM}$, decelerates the observed kinetics. 18 minutes after DNaseI addition, half of the determined maximum signal increase is reached.

Summing up DNaseI kinetics, N6-Methyl-2'-dA does not effect *smart probe*

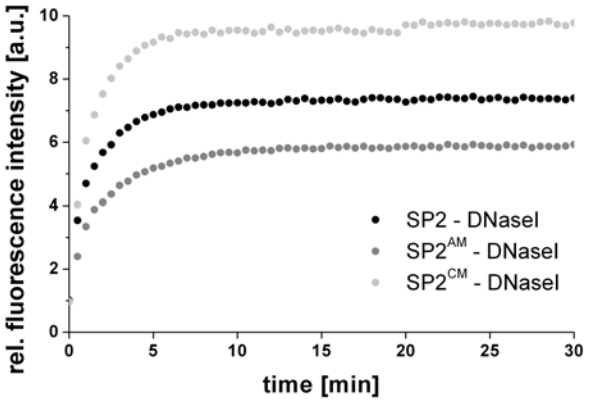

a)

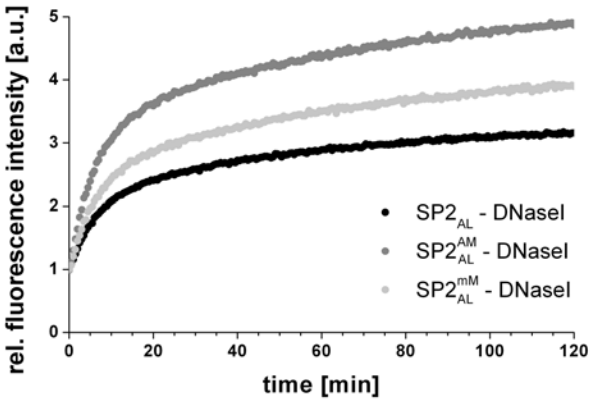

b)

Figure 4.29: Normalized fluorescence intensity plots of SP2, $SP2^{AM}$, $SP2^{CM}$, $SP2_{AL}$, $SP2_{AL}{}^{AM}$ and $SP2_{AL}{}^{mM}$ upon addition of bovine DNaseI (a) and b)).

digestion, let it be in the hairpin loop or stem region, while N4-Methyl dC at position 2 distinctly induces changes to DNaseI kinetics. Here, it can only be assumed, that DNaseI only prefers the cytosine methylation, as long as there are little or no other methylations present or close by. Furthermore, the wider structure, induced by $SP2_{AL}$, decreases the digestion velocity, which can be

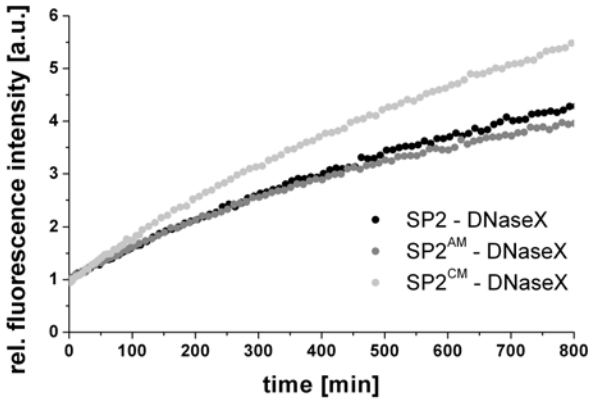

c)

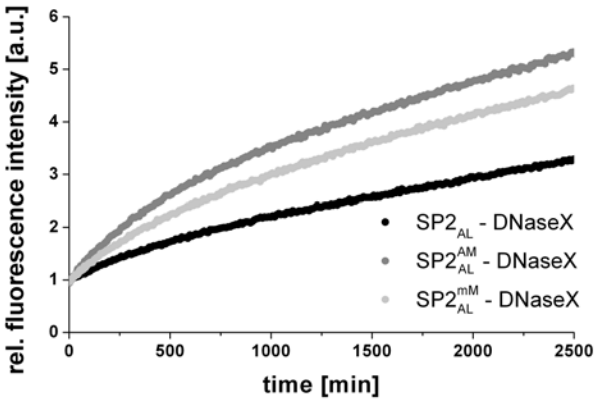

d)

Figure 4.29: Normalized fluorescence intensity plots of SP2, $SP2^{AM}$, $SP2^{CM}$, $SP2_{AL}$, $SP2_{AL}{}^{AM}$ and $SP2_{AL}{}^{mM}$ upon addition of DNaseX (c) and d))

accounted to the reduced preferred double stranded region. For DNaseI research, therefore, $SP2^{CM}$ generates the ideal *smart probes*, because it provides the fastest and strongest feedback of all examined hairpin substrates.

The equivalent measurements, carried out with DNaseX, do not reveal or even indicate a fluorescence intensity saturation value, despite their long

observation times of up to 42 hours. Therefore, a detailed evaluation is hardly possible. Presuming a similar behavior of all examined *smart probes* in these comparable measurements[12], the following precarious conclusions can be drawn: Half of the supposed maximum fluorescence increase is reached for $SP2^{AM}$ after 590 minutes, followed by $SP2^{CM}$ with 745 minutes. Then, SP2, ${SP2_{AL}}^{mM}$ and ${SP2_{AL}}^{AM}$ show their half maximum fluorescence increase at 840 minutes, 845 minutes, and 875 minutes, respectively. Finally, $SP2_{AL}$ reaches its half maximum value at 940 minutes. Thus, it can be assumed, that DNaseX indeed prefers a methylation pattern, especially of N6-Methyl-2'-dA at position 17, and totally neglects an adenine loop, particularly if the sequence does not carry any methylation. This ranking list[13] clearly distinguishes DNaseX from DNaseI and could be taken into account for a further adaption of *smart probes* for research on either one of these nucleases. The DNaseI favorite $SP2^{CM}$ also displays a fair candidate for DNaseX research, because of its good compromise between velocity and quenching efficiency.

Therefore, $SP2^{CM}$ was modified to $SP2^{CM}$-FRET (cf. figure 4.17) for a balance of quenching mechanisms. Both hairpin versions were then examined in presence of all introduced nucleases, as presented in figure 4.30.

$SP2^{CM}$ shows a familiar increase in fluorescence intensity upon addition of DNaseI, while the equivalent FRET quenched hairpin shows a different course and, most interestingly, a lower relative increase in fluorescence intensity. This indicates, that FRET quenching of this hairpin is not as efficient as PET quenching of the *smart probe*. With DNaseII at acidic pH value, this behavior tilts over. Here, $SP2^{CM}$-FRET clearly dominates over $SP2^{CM}$. Remarkably, both observed fluorescence kinetics show a characteristic increase shape, that can also be found for SP2 and SP4 in DNaseII presence in figure 4.28. This clearly proves that DNaseII processes the hairpins differently than DNaseI. In S1-Nuclease presence $SP2^{CM}$ shows a quite common fluorescence intensity plot with a low saturation intensity due to the acidic pH value. $SP2^{CM}$-FRET on the other hand reveals a peculiar development. After a maximum value has been reached, the fluorescence intensity distinctly decreases. Since all measurements were equally accomplished, this cannot be accounted to

[12]DNaseI and DNaseX were examined in the same buffer, at the same temperature and with equal substrate concentrations.

[13]This ranking list is only presumed, because it resulted from the assumption, that the utilized *smart probes* reach saturation values upon DNaseX scission, that are similar to those yielded by DNaseI cleavage.

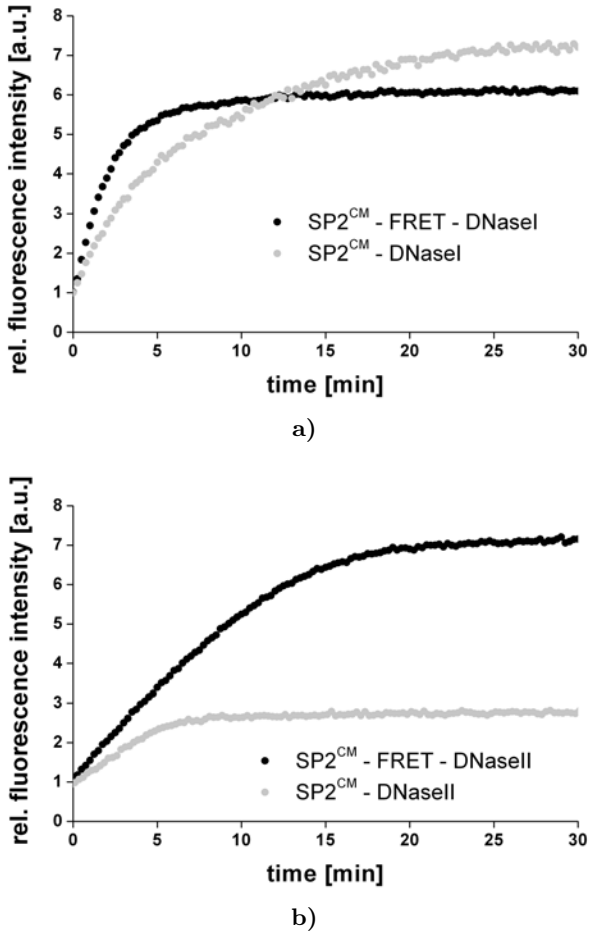

Figure 4.30: Normalized fluorescence intensity courses of $SP2^{CM}$ and $SP2^{CM}$-FRET upon addition of bovine DNaseI (a)), DNaseII (b)), S1-Nuclease (c)) and DNaseX (d)).

any photophysical process and must, therefore, be associated with the S1-Nuclease itself. Possible explanations for this are a nicking of the attached fluorophore by S1-Nuclease or a cleavage of the label bond, which itself could have amplified the fluorescence yield.

Both hairpin variations show a familiar shape of fluorescence intensity in-

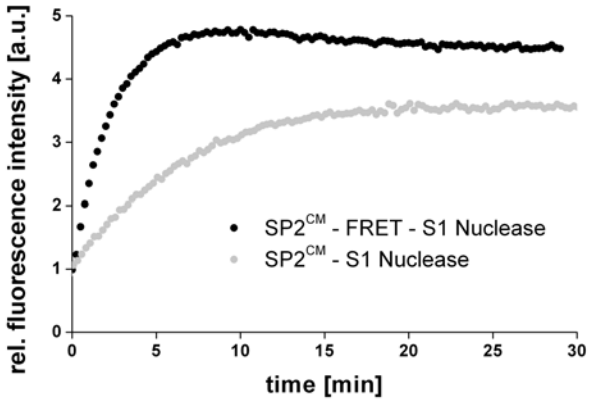

c)

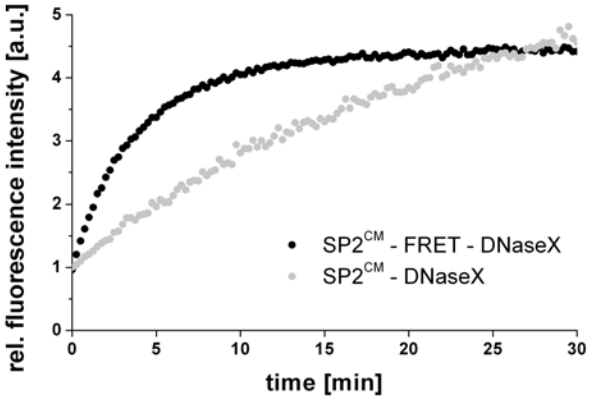

d)

Figure 4.30: Normalized fluorescence intensity plots of $SP2^{CM}$ and $SP2^{CM}$-FRET upon addition of bovine DNaseI (a)), DNaseII (b)), S1-Nuclease (c)) and DNaseX (d)).

crease in presence of DNaseX, where again $SP2^{CM}$ reveals a higher relative saturation intensity. Comparing the applied quenching mechanisms, it can be summarized that at neutral pH the PET quenched $SP2^{CM}$ gives better results, while at acidic pH, $SP2^{CM}$-FRET enables a higher increase in fluorescence intensities.

In presence of DNaseI, $SP2^{CM}$ reveals a half maximum time of 5 minutes. $SP2^{CM}$-FRET shows a completely different fluorescence intensity plot with a half maximum time of only 1.5 minutes. In the DNaseII sample, $SP2^{CM}$ reaches half of its determined fluorescence intensity gain 7 minutes after enzyme addition and $SP2^{CM}$-FRET in only 3.25 minutes. Due to the $SP2^{CM}$-FRET fluorescence decrease in presence of S1-Nuclease, a half maximum time cannot be determined. Apparently though, it also seems to occur earlier than that of $SP2^{CM}$ 4.75 minutes after enzyme addition. Since $SP2^{CM}$ does not reach a fluorescence intensity saturation in DNaseX sample within the observation time, the half maximum time of $SP2^{CM}$ clearly exceeds 2.75 minutes, which is the duration it takes DNaseX to convert $SP2^{CM}$-FRET to show half of its maximum signal increase. Therefore, with every examined nuclease, $SP2^{CM}$-FRET is processed distinctly faster than $SP2^{CM}$. Since the sequences of these hairpins are identical, this means that the attachments greatly affect enzyme affinities to specific substrates. Most remarkably, the utilized double modification suits all nucleases better than a single labeling of Atto 655. It should be assumed, though, that this is attributed to the specific utilized fluorophores or dark quenchers more than to the number of chemical modifications (cf. section 4.1.4).

The second set of *smart probes*, designed for allowing a discrimination between double and single stranded scission of nucleases, was examined with DNaseI, known to preferentially process ds DNA and S1-Nuclease, preferring ss DNA. The results were then used to characterize DNaseX scission. The normalized fluorescence intensity profiles are presented in figure 4.31.

VIP control is hardly quenched due to its lack of guanosine residues (cf. figure 4.19, table 4.4) and should, therefore, not show any variation in fluorescence intensity upon nuclease addition[14]. After a distinct dilution effect VIP control does show an increase in fluorescence during the observation time of 100 minutes upon double stranded nickage by DNaseI and single stranded scission by S1-Nuclease. This affirms the theory of long range energy transfer that has been discussed before.

VIP ds, efficiently quenched in its initial state (cf. table 4.4), is designed to show a distinct increase upon any ds cleavage. If this *smart probe* is cut in the single stranded loop domain, the remaining nucleotide sequence, theoretically, readopts a hairpin structure, independent of the exact cutting position [179].

[14] except for a small dilution effect

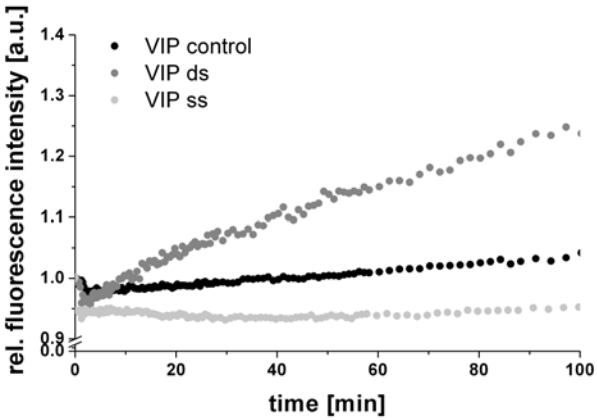

a) DNaseI

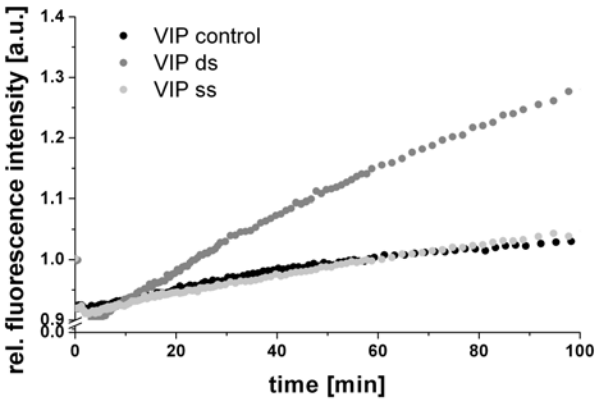

b) S1-Nuclease

Figure 4.31: Normalized fluorescence intensity plots of VIP control, VIP ds and VIP ss upon addition of bovine DNaseI (a)), S1-Nuclease (b)) and DNaseX (c)).

This hairpin is then again efficiently quenched, due to a minimum amount of two guanines, pairing with the 5'-adenines before being processed again. In case the ss domain at the 3'-end is cleaved, the smart probe should show an increase in fluorescence, not restoring the full signal yield, though (cf. figure 4.19). Therefore ideally, this hairpin shows an immediate result upon

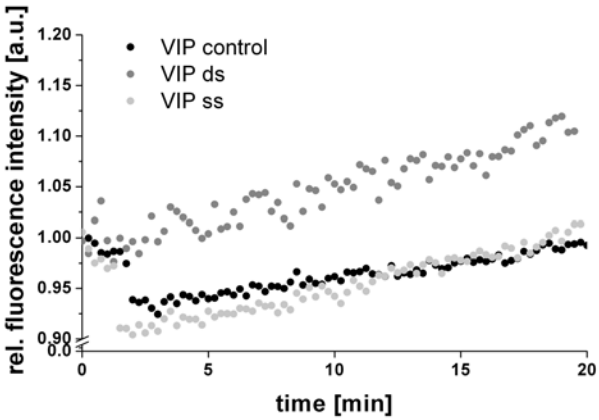

c) DNaseX

Figure 4.31: Normalized fluorescence intensity courses of VIP control, VIP ds and VIP ss upon addition of bovine DNaseI (a)), S1-Nuclease (b)) and DNaseX (c)).

ds scission and a delayed increase upon any ss scission.

VIP ss is slightly quenched (cf. table 4.4), due to long range electron transfer to loop inherited guanosine residues (cf. figure 4.19). Upon double stranded scission this *smart probe* is supposed to fully fluoresce, because there are none but as most one guanine left in the remaining Atto 655 attached nucleotide sequence. Upon single stranded DNA scission, which is only possible in the hairpin loop, the remaining nucleotide sequence forms a smaller hairpin structure, independent of the exact cleavage site, bringing a nucleotide overlap of at least one guanosine residue into close contact with Atto 655. Therefore, this substrate should show a decrease in fluorescence intensity upon ss scission, before the established overlap can be cleaved and fluorescence is restored.

Figure 4.31 shows, that the theoretical considerations do not completely meet the observed kinetics, though. As anticipated, VIP ds shows an increase in fluorescence in presence of DNaseI, while VIP ss mostly abides its initial value, instead of slightly increasing. In presence of S1-Nuclease, VIP ds, supposed to slightly increase in fluorescence intensity, shows a remarkable slope, which does not reveal any delay in kinetics and can only be attributed to a fast procession of the 3'-guanosine overlap. VIP ss shows the

same fluorescence intensity characteristic as VIP control, without the supposed fluorescence decrease. A conceivable excision of the fluorophore alone would result in an immediate, stronger increase. Therefore, the formation and degradation of the supposed intermediate hairpin structure must occur concurrently and well-balanced.

Because of the aberration of obtained fluorescent courses from expected characteristics, that are even hard to interpret for enzymes with known substrate preferences, it is impossible to use these *smart probes* for the determination of an unknown preference, as can be observed in figure 4.31 c). Here, all hairpins reveal a slight increase in fluorescence intensity upon DNaseX addition, which would, in case of VIP ds, indicate a single stranded scission, and a double stranded scission in case of VIP ss.

The last kinetic characterization was performed with the commercially available nuclease substrate 'DNaseAlert'. These normalized fluorescence intensity profiles are presented in figure 4.32.

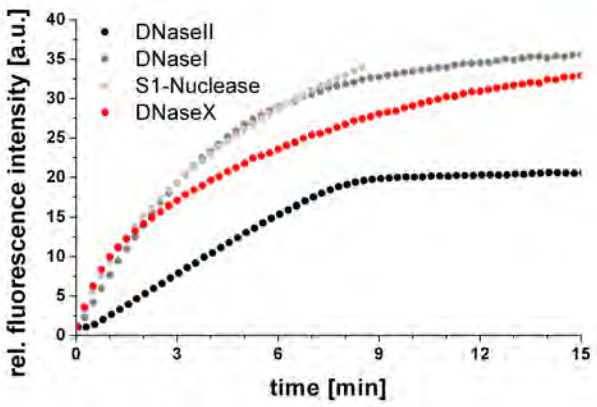

Figure 4.32: DNaseAlert upon addition of DNaseI, DNaseII, S1-Nuclease and DNaseX.

Clearly, DNaseAlert is processed by all examined nucleases, yielding a remarkable signal increase of up to 37.5 fold. As for *smart probes*, the maximum signal and the fluorescence intensity courses are strongly dependent on the specific nuclease and its required measurement settings. For general nuclease detection and for most descriptive research on isolated nucleases, this substrate is fairly applicable. When it comes to the question of sequence

specificity and fluorophore assigned conversion effects, it is futile, though. Furthermore, an adaption of this substrate to other spectral ranges, as easily adjustable with *smart probes* and especially molecular beacons, is simply impossible. Therefore, if not in need of an immense signal increase[15], labeled hairpins are to be preferred.

4.1.3 Michaelis-Menten Kinetics

Next to singular kinetics, as presented in section 4.1.2, smart probes can be utilized for the research of Michaelis-Menten parameters (see section 2.4.1), which will exemplarily be shown for S1-Nuclease on SP4. Here, three different enzyme concentrations were used with several substrate concentrations each. Of each combination, three samples were examined. Plotting the determined starting velocities against the determined substrate concentrations results in the graph, depicted in figure 4.33.

The higher the substrate concentrations, the more the data points seem to mismatch the general course, beginning from $4 \cdot 10^{-6}$ M smart probe concentration. There, the fluorophore density is high enough to allow reabsorption effects, hampering the acquisition of true starting velocities.

Still, a numerical evaluation of these plots leads to the values presented in table 4.5.

Table 4.5: Enzyme concentrations, corresponding maximum velocities (v_{max}) and Michaelis-Menten constants (K_M) of S1-Nuclease with SP4.

	enzyme concentration	v_{max} **[a.u.]**	K_M **[µM]**
$[E]_1$	0.100 U/ml	$(2.5 \pm 0.3) \cdot 10^{-6}$	1.0 ± 0.4
$[E]_2$	0.020 U/ml	$(5.3 \pm 0.8) \cdot 10^{-8}$	0.4 ± 0.4
$[E]_3$	0.005 U/ml	$(3.8 \pm 1.2) \cdot 10^{-6}$	29.7 ± 11.3

Low enzyme concentrations obviously result in doubtful Michaelis-Menten

[15] There are several molecular beacons with immense possible signal increases, as have been described by Li *et al.* [46]. Furthermore, smart probe quenching can most likely be improved by several, small variations.

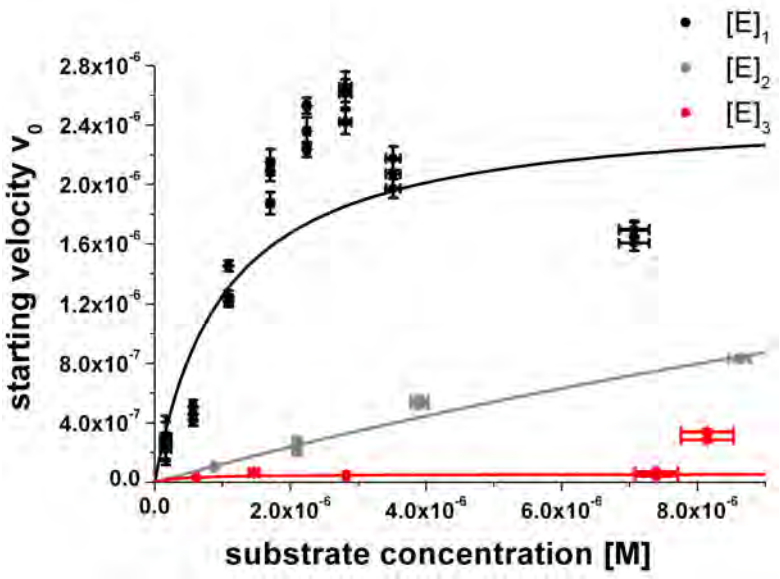

Figure 4.33: Michaelis-Menten kinetics of S1-Nuclease with SP4 with 3 different enzyme concentrations.

parameters. $[E]_1$ on the other hand, results in the need of high substrate concentrations as well, leading to interactions between the high number of fluorophores. Despite the reasonability of the determined K_M by $[E]_1$, the variations of parameters for high substrate concentrations, which mostly determine the Michaelis-Menten parameters, are too big to rely on the determined values.

A lower enzyme concentration does not avoid these problems until a concentration is reached, where new problems[16] occur. Therefore, Michaelis-Menten parameters can only be determined for low Michaelis-Menten constants of up to $2 \cdot 10^{-6}$, which are rare for hydrolases in general and could not be observed for any of the utilized enzymes.

The *smart probe* concentration can be increased without reabsorption effects though, if only a subset of the substrates were fluorescently labeled.

[16]These account the lack of reproducibility due to very small sample amounts and very long reaction times, that tend to hide side effects like cuvette wall adsorption and concentration variations due to evaporation.

This implies, however, that labeled hairpins are equally processed as unlabeled substrate, which will be examined in section 4.1.4.

4.1.4 Determination of Label Effect to Substrate Acceptance

A general concern in enzyme research based on fluorescent substrates is the question, whether the attached modification effects the acceptance and velocities, an enzyme shows on a specific substrate. To address this task, MR 121 - Gly - Trp and unlabeled Gly - Trp were mixed in different ratios, before Carboxypeptidase A was added identically to each sample. As before, fluorescence intensity profiles were normalized to their starting intensities. A selection of these are presented in figure 4.34.

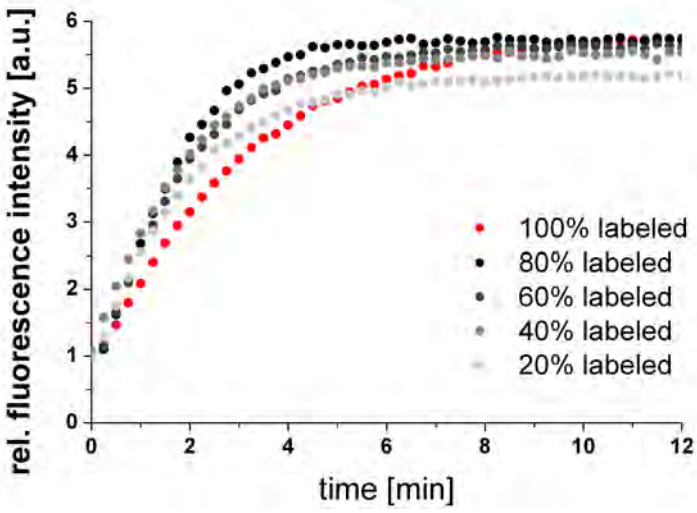

Figure 4.34: Normalized fluorescence intensity profiles of MR 121 - Gly - Trp and Gly - Trp in different ratios upon addition of Carboxypeptidase A.

Clearly, there are only small variations of velocities and saturation values. A numerical evaluation of these courses results in the graph depicted in figure 4.35.

The higher the degree of labeled substrates, the lower the time constant of the reaction gets. Since it was proven that MR 121 - Gly - Trp is only pro-

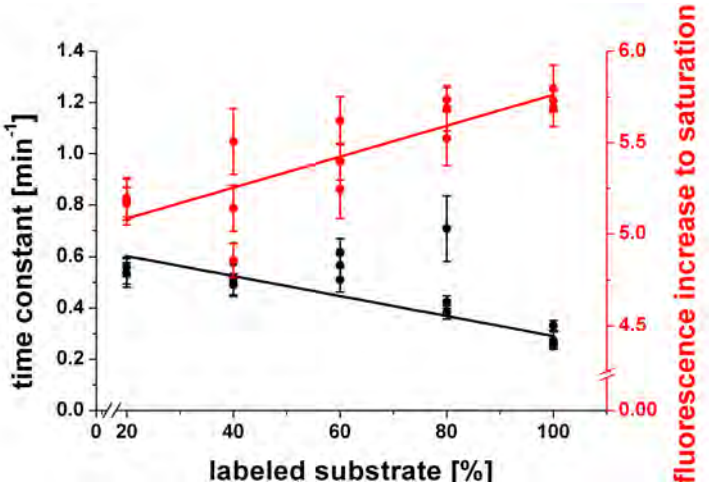

Figure 4.35: Time constants and maximum fluorescence increase of different ratios of labeled MR 121 - Gly - Trp to unlabeled Gly - Trp upon addition of Carboxypeptidase A.

cessed between glycine and tryptophan (cf. section 4.1.2), both constituents offer exactly the same cleaving possibility. Therefore, Carboxypeptidase A distinctly favors the unlabeled Gly - Trp. Most remarkably, also the fluorescence increase to saturation changes with the ratio of labeled substrate. The original data[17] reveals, that absolute starting and saturation intensities do not head into a distinct direction but fluctuate statistically.

An equivalent measurement with bovine DNaseI and SP2, labeled and unlabeled, is presented in figure 4.36.
Again, only slight variations of velocities and saturation values can be seen. Evaluating the normalized fluorescence profiles numerically, results in a similar picture as with Carboxypeptidase A, depicted in figure 4.37. Here, the time constants only slightly decrease with increasing labeling percentage of the substrate, proving the preference of DNaseI to process unlabeled substrate just a little better.

With increasing labeling ratio of the examined hairpin, the fluorescence increase to saturation also rises. The original data[17]of this measurements also shows an increase of absolute starting and saturation intensities with

[17]Data not shown.

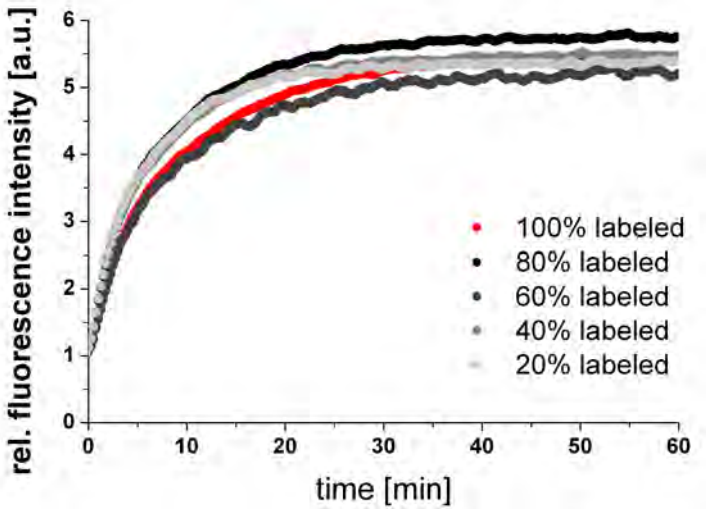

Figure 4.36: Normalized fluorescence intensity profiles of labeled and unlabeled SP2 in different ratios upon addition of DNaseI.

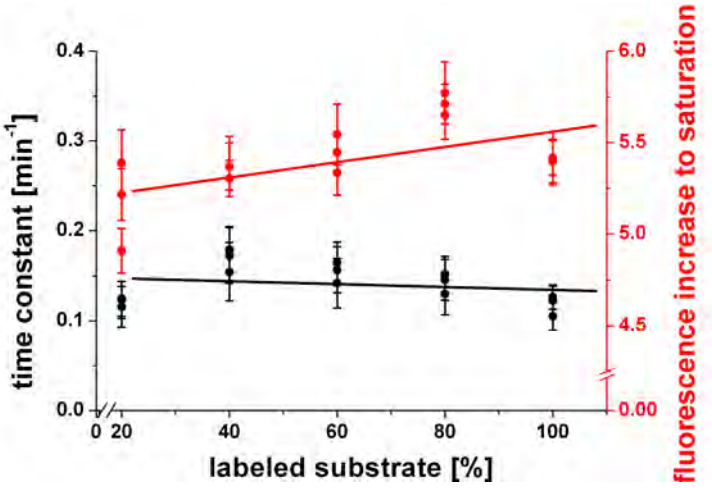

Figure 4.37: Time constants and maximum fluorescence increase of different ratios of labeled SP2 to unlabeled SP2 upon addition of bovine DNaseI.

the ratio of labeled hairpin. This indicates, that the labeling degree of the *smart probes* is most likely to be higher than 1, which would explain the correlation of the ratio between saturation and initial fluorescence intensity with the percentage of labeled hairpin.

Since both examined hydrolases are definitely slowed down by labeled enzyme substrates, the predominance of the two fold labeled $SP2^{CM}$-FRET over $SP2^{CM}$, as presented in section 4.1.2, is even more remarkable. Regarding these two effects, this leads to the consideration that Atto 655 could be a fluorophore that is not specifically favored by any nuclease, which possibly also accounts for its peptide homologue MR 121 in Carboxypeptidase A acceptance.

4.1.5 Evaluation of ideal Temperature Settings

Fluorescent peptidase substrates are rather thermally stable (cf. figure 4.7). Therefore, they can also be used for kinetic measurements at various temperatures, thus, for measurements concerning temperature preferences of an enzyme.

MR 121 - Gly - Trp samples were equally measured with Carboxypeptidase A at different temperatures. Plotting the computationally determined time constants of the reaction against the applied temperatures, reveal the thermal preferences of this enzyme. These can be seen in figure 4.38.

Clearly, Carboxypeptidase A shows a stronger activity on MR 121 - Gly - Trp at higher temperatures. Still, no distinct course is observable. There appear to be local activity maxima at 25°C, 40°C and around 60°C. The published activity maximum of 25°C [68, 210] could, therefore, be locally affirmed, but any reaction occurring at 35°C and above is distinctly faster. Regarding the fact that Carboxypeptidase A is a pancreatic enzyme, this and the local maximum at 40°C are indeed very reasonable[18]. Since the determined time constants at 45°C, 50°C and 65°C are very similar to each other, and only 60°C strongly peaks out, an error could be assumed for this high value. However, in further measurements this high activity could be reproduced. Therefore, it has to be approved, that, indeed, Carboxypeptidase A shows an unexpected maximum activity on MR 121 - Gly - Trp around 60°C.

[18] This Carboxypeptidase A is from a bovine source and the paunch temperature is around 39°C.

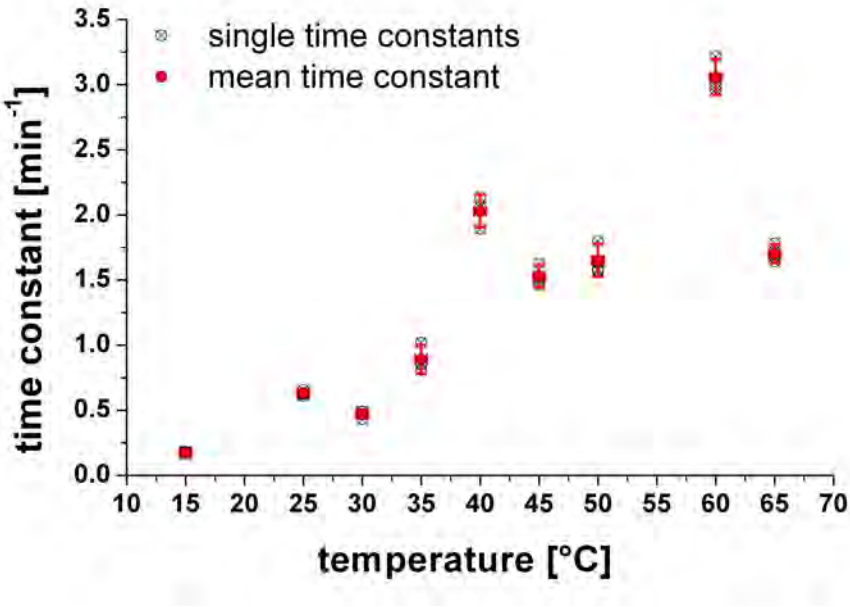

Figure 4.38: Time constants of kinetic measurements with Carboxypeptidase A and MR 121 - Gly - Trp, plotted against applied measurement temperatures. The single time constants (grey), derived from three individual measurements, were additionally averaged (red).

A different plotting type was chosen to analyze the maximum activity of DNaseI[19] and DNaseX on SP2 and SP4, respectively. SP2 has calculated melting temperature of 80.2°C (cf. table 4.3). As figure 4.15 shows, *this smart probe* does not lose its hairpin formation up to 70°C. Therefore, SP2 is still ideally suited for measurements at high temperatures. If SP2 was cleaved in the single stranded loop domain, which could generally occur for DNaseI and DNaseX, a very stable product would result. The highest conceivable product melting temperature would be 40.3°C [179]. Therefore, this *smart probe* can only be utilized for thermal preference measurements between 40°C and 70°C. For temperatures below 40°C, a hairpin with shorter stem length has to be utilized. Here, SP4 with a calculated melting temperature of 65.3°C (cf. table 4.2), a very constant fluorescence intensity up to 55°C (cf. figure 4.11)

[19]Here, human DNaseI was utilized.

and a highest conceivable product melting temperature of 14.9°C [179], is ideally suited.

To be able to see nuclease activities as well as possible enzyme denaturation at higher temperatures, figure 4.39 shows the relative fluorescence intensities, normalized to each starting temperature at 5, 10 and 15 minutes after DNaseI addition. Regarding the fluorescence intensities 5 minutes after substrate addition, the activities increase up to a temperature of 50°C. After that, the fluorescence intensities decrease again. Generally the fluorescence intensities 10 minutes after enzyme addition reveal the same result. At 60°C and 70°C, though, they have not increased any further, despite not having reached the maximum possible intensity. This shows an inactivation of DNaseI at these temperatures after approximately 5 minutes. Since 15 minutes after DNaseI addition, fluorescence intensities at these temperatures have not changed unlike 20°C to 50°C. Analyzing the gain height at each temperature and temporal interval, it is possible to read out the progress of each reaction. At 50°C the reactions with both SP4 and SP2 nearly reached a saturation after 15 minutes, whereas at 40°C and 30°C the reactions are consecutively slowing down. At 20°C the gain height of each temporal interval looks quite identical, revealing, that this reaction is still working in its steady state.

From this measurement the maximum activity of DNaseI is observed with SP2 at 50°C. However, this measurement technique generally only observes single data points and misses intermediate temperatures. A refining measurement in the range of 40°C to 60°C should follow after this crude approximation of an ideal measurement temperature.

The same measurement yields a different picture, when applied to DNaseX, as visualized in figure 4.40. Generally, the fluorescence intensity gain upon DNaseX scission between 20°C and 40°C is very low with both *smart probes*. The maximum intensity gain occurs at 56°C. At 66°C a denaturation of DNaseX can be observed 5 minutes after enzyme addition, while at 70°C an instant denaturation occurs. Again, this type of measurement misses intermediate temperatures and should, therefore, be refined especially around 56°C.

To circumvent the need of a set of individual measurements for each applied temperature, a new experimental approach was utilized for refined thermal activity maxima research that takes advantage of the steady state in the beginning of enzyme kinetics. By adjusting the concentrations of the substrate and the enzyme, the steady state phase of a reaction can be prolonged to an

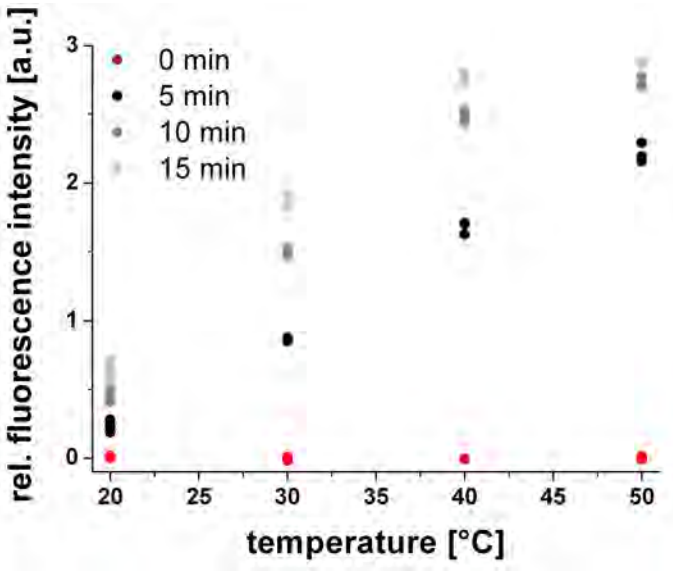

a) SP4

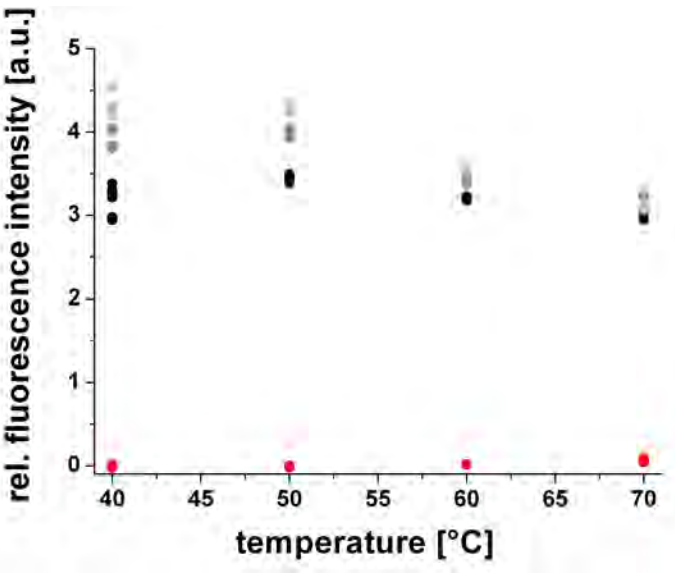

b) SP2

Figure 4.39: Normalized fluorescence intensities of SP4 (a)) and SP2 (b)) at different temperatures 5, 10 and 15 minutes after addition of DNaseI.

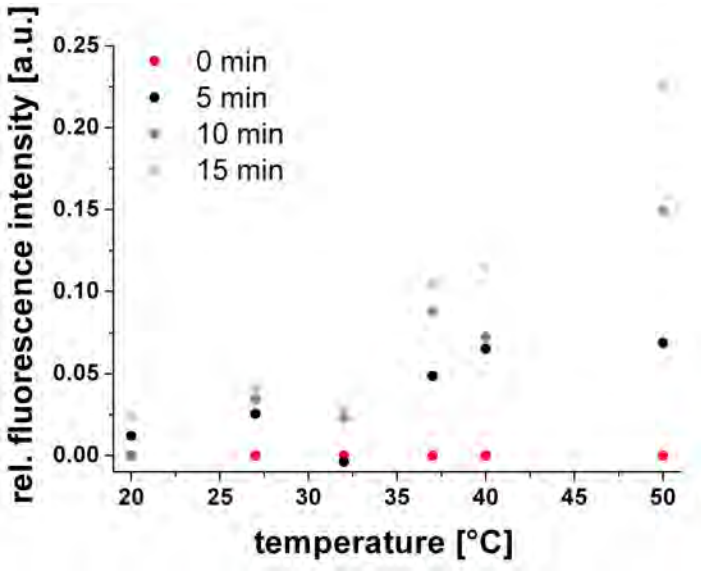

a) SP4

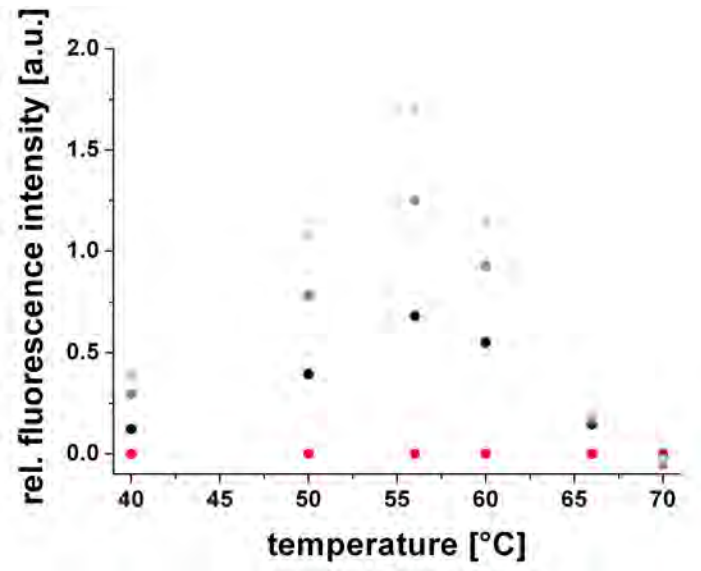

b) SP2

Figure 4.40: Normalized fluorescence intensities of SP4 (a)) and SP2 (b)) at different temperatures 5, 10 and 15 minutes after addition of DNaseX.

appropriate duration. If the reaction temperature is varied constantly during this steady state phase, the initially linear fluorescence intensity course, will change, revealing temperature preferences. An example of how such a steady state phase looks like at varying temperatures is given in figure 4.41.

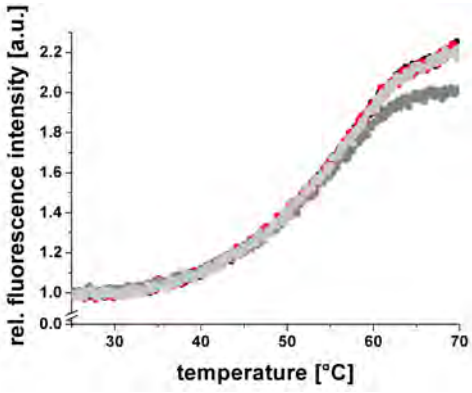

Figure 4.41: Steady state fluorescence intensity measurements of DNaseX and SP4 at varying temperature.

As can be seen, the four individual samples perfectly match each other with only one aberration at high temperature. The observed fluorescence intensity profiles reflect the activity preferences of the enzyme and the thermal fluorescence intensity variations of intact *smart probes*[20], which can be easily subtracted. Derivations of the resulting graphs, therefore, directly reveal continuous thermal enzyme activities for a wide range of temperatures in a minimum of time.

Due to a thermal overlap of SP4 and SP2 graphs by some degrees, both obtained activity graphs can even be normalized to another. Complete DNaseI and DNaseX graphs were then adjusted to hit at 45°C yielding a perfect comparison of nuclease activities in figure 4.42. As shown in figure 4.41, DNaseX shows a maximum velocity at 56°C. If the temperature gets higher than that, the velocity drastically decreases, mostly due to denaturation. DNaseI, on the other hand, still increases in its activity up to 70°C, which is still in

[20] A prerequisite for steady state phases is a huge amount of unprocessed substrate, thus a negotiable amount of fluorescent product. Therefore, the influence of this constituent can be disregarded.

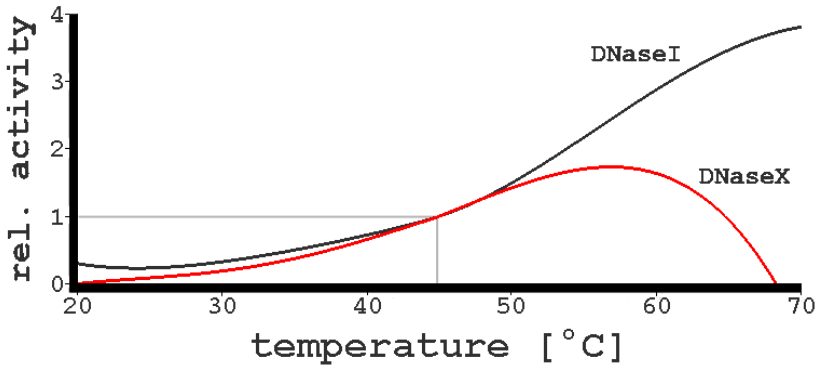

Figure 4.42: Normalized activities of DNaseI and DNaseX over varying temperatures.

perfect accordance to figure 4.39, where a five minutes increase hides initial slopes that occur before a likely inactivation.

The introduced experimental approach for temperature preferences proved to result in satisfactory results in accordance to single kinetic measurements with a high accuracy. Therefore, this method can generally be applied for any enzyme with its appropriate fluorescent substrate, as exclusive measurement, as a verification for single kinetic measurements or for an initial setting of temperatures to be sampled with single kinetic measurements.

Unfortunately, temperature is the only measurement parameter that can constantly be changed during a measurement in a standard fluorescence spectrometer. In a flow device, this method can also be used with fluorescent substrates for the examination of buffer preferences like pH values and activator concentrations. Furthermore, inhibition processes can be examined.

4.1.6 Single Molecule Enzyme Localization

In this section the suitability of PET quenched fluorescent substrates for enzyme investigations on a single molecular level is briefly documented.

Carboxypeptidase A is indirectly bound to a 16-mer double stranded DNA, which itself is labeled with a fluorophore, spectrally separated from MR 121 and bound to bovine serum albumin (BSA) molecules, attached to a surface (see figure 4.43 b)). Therefore, CPA is surface bound and its position is easily detected upon appropriate illumination.

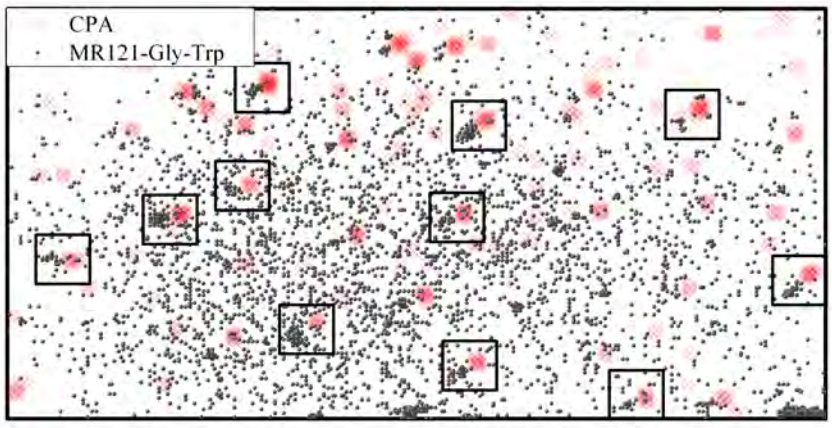

a) CPA (red) and substrate (black) localizations in a 137 µm x 68.5 µm section. Black squares represent correlated localizations.

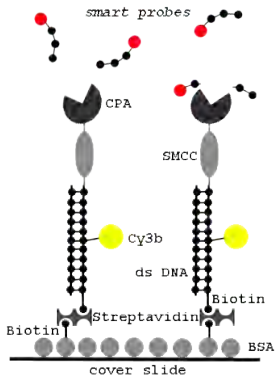

b) sample assembly

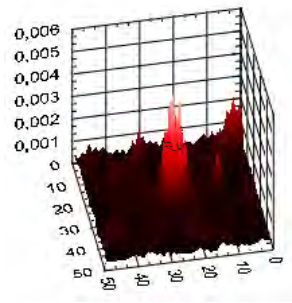

c) localization correlation

Figure 4.43: Single molecule Carboxypeptidase A and substrate localizations, sample assembly scheme and localization correlation result.

During illumination that irradiates MR 121 by total internal reflection, the addition of MR 121 - Gly - Trp (see section 4.1.1) leads to short fluorescence signal bursts in close proximity to the coverslide. This happens each time a substrate is processed by a Carboxypeptidase A molecule, because this substrate requires only one incision to fully fluoresce (cf. section 4.1.2). Col-

lecting the position of hits over time and plotting them with all localized CPA molecules results in figure 4.43 a).

Obviously, there is a wide distribution of substrate localizations, that do not necessarily cover CPA spots. It is striking though, that there are several accumulations of substrate spots, slightly left and downwards shifted to enzyme localizations. This could first of all indicate a spectral detection channel shift. Figure 4.43 c) shows the result of a line- and row-wise adjustment of one frame to the other. Here, a distinct correlation peak is reached when the substrate localizations are shifted by 7 nm to the right and up. In this general, big shift still smaller variations take place due to different orientations the CPA molecules can take, because of its flexible surface attachment.

Still, there are CPA localizations without any substrate localizations close by, as well as MR 121 - Gly - Trp localizations without any neighbored enzyme hits. For this, there is a variety of explanations. A destined Carboxypeptidase A position can, first of all, not bear an enzyme due to miscarried labeling or a detachment in later processing. Furthermore, an attached enzyme can be inactive. Both scenarios would result in missing substrate localizations at supposed enzyme position. Analogous, there can be surface attached CPA molecules, that are not fluorescently labeled. This would result in MR 121 - Gly - Trp localizations without any enzyme localization near by and should mostly account for unassigned substrate localization accumulations. Furthermore, there are single substrate localizations without corresponding enzyme localizations. Generally, there can be freely diffusing enzyme due to miscarried synthesis and purification, yielding fluorescent products over the complete sample. Fluorescent peptide probes were found to interact with BSA in enzyme kinetics though (data not shown), which is, therefore, also most likely to occur in this sample, because the complete surface is covered with BSA molecules (cf. figure 4.43 b)).

This sample assembly is, therefore, only conditionally suitable for investigations on Carboxypeptidase A due to the interaction between BSA and peptide substrates. Furthermore, this assembly is not at all transferable to nuclease investigations, because in sample synthesis the nuclease would degrade any incorporated DNA spacer, breaking the surface attachment system. Nonetheless, this measurement countervails to proof the general suitability of fluorescent substrates for enzyme research on a single molecule scale.

4.1.7 Enzymes in Cells

Enzymes do not naturally occur in purified environments, that have so far been employed for any measurement presented in this work. To examine on the usefulness of fluorescent substrates in natural environments, several *smart probes* were tested on different cell types in various ways.

SP2, SP3 and SP4 were added to a constant number of LS-174T cells (see section 3.2.4) and their fluorescence intensity was monitored over time. The normalized fluorescence intensity progression is presented in figure 4.44.

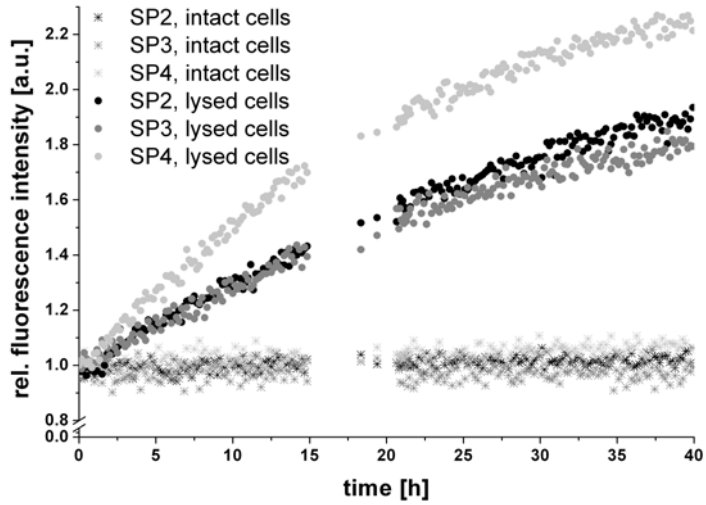

Figure 4.44: Normalized fluorescence intensity progressions over time of SP2, SP3 and SP4 in samples with either intact, living (crosses) or lysed (circles) LS-174T cells.

Neither of the utilized *smart probes* shows any remarkable variation in fluorescence intensity in samples with intact, living cells over 40 hours. *Smart probes* incubated with lysed cells, though, show distinct increases in fluorescence intensity, which still haven't reached saturation values after 40 hours. Here, at first sight, SP4 shows the strongest increase in the shortest time, followed nearly equivalently by SP2 and SP3. Regarding the fact, that these substrates are quenched differently efficiently and, therefore, yield diverse relative saturation values, this appearance needs to be evaluated further. SP4, with a relative quantum yield of 0.28, can generally reach an intensity that is

3.57 fold higher than the starting intensity. Here, after 40 hours, 63% of the possible increase are reached. SP2 reaches only 36% of its potential relative fluorescence intensity and SP3 only arrives at 27%. So, first sight estimation already gave the right impression, that enzymes revealed by lysis of LS-174T cells preferably process SP4 over the *smart probes* with a longer stem and a shorter loop. When risking a closer look to the *smart probes* fluorescence intensities, incubated with living cells, one can notice, that final values reflect the same substrate order as in lysed cells. The final SP4 fluorescence intensity is slightly higher than that of SP2, followed by SP3. This might indicate a little action on intact cells as well. Regarding the measurement time scale though, it is most likely, that these signals derive from cells that died during the measurement, revealing the same enzymes as lysed cells but merely in a smaller final concentration. It has to be accepted, therefore, that *smart probes* themselves do not react with enzymes in or at intact cells, meaning that they cannot enter a cell membrane by themselves.

To utilize smart probes in cell-measurements, these substrates have to be inserted artificially. There are many approaches to this, including the slow and inefficient liposome or dendrimer based transfection techniques [211,212] or invasive methods like microinjection [213] and electroporation [214]. A promising alternative is the utilization of cell-penetrating peptides (CPPs), that generate a fast and efficient hairpin uptake, without hampering their structure and usability upon internalization [215]. Amongst the many CPPs that have been described and characterized [216–226], the 'optimal cell-penetrating peptide' Antennapedia (Antp) [222] was used due to its fine uptake characteristics in different cell types and its low toxicity. Antp was linked to $SP2^{CM}$ by a disulfide bridge, which is cleaved by the reducing environment of the cytoplasm [215], allowing the same cleavage mechanism of the *smart probe* as in artificial ensemble measurements. The Antp-linked $SP2^{CM}$ was incubated with chamber slide-grown A-549 cells in non-colored medium at room temperature and monitored over time on a total internal reflection fluorescence (TIRF) microscope. Furthermore, cells were preincubated with pyrenebutyrate to increase the Antp uptake [227]. A 90 minutes incubation results in the images depicted in figure 4.45.

While in the incident light picture a single cell is clearly visible, the TIRF image only shows nearly homogeneously distributed fluorescence signal, which does not reveal any cellular accumulation, as is clearly visible in the merged image. Since it has been reported, that DNaseI is secreted by exocrine glands

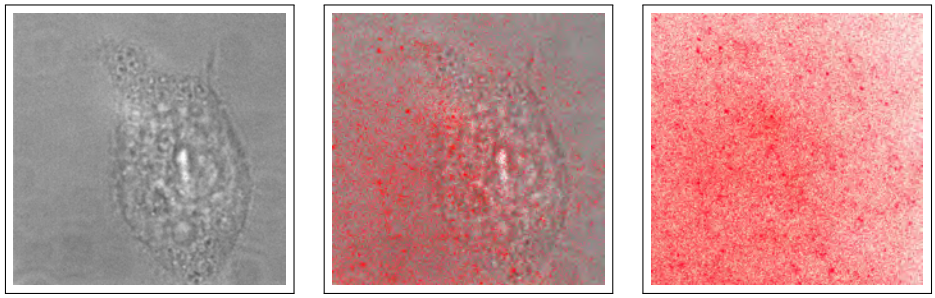

a) incident light **b)** merged image **c)** TIRF image

Figure 4.45: A-549 cells in colorless medium, preincubated with pyrenebutyrate and imaged on a TIRF microscope, 90 minutes after Antp-linked $SP2^{CM}$ addition. a) shows a 32 µm x 32 µm incident light image, c) shows the corresponding raw TIRF image and b) shows a merged picture in which the TIRF signal was threshold selected for enhanced visibility.

[228], there must be a cell release mechanism for DNaseI. Therefore, DNaseI existing in the medium can process the *smart probes* before they can enter the cell. Since Antp is bound to the 3'-end of the sequence, Atto 655, attached to the 5'-end, is not capable of entering the cell anymore. This scenario would, therefore, lead to a small fraction of fluorescence intensity assigned to Atto 655 inside the cell via properly endocytosed Antp-linked $SP2^{CM}$ and another fraction of fluorescence, resulting from DNaseI activity outside the cell.

An addition of $7 \cdot 10^{-7}$M G-Actin, which selectively inhibits DNaseI [39] , results in the images depicted in figure 4.46.

The cell shape that can be seen in the incident light picture is also indicated in the TIRF image. The fluorescence signal clearly accumulates in the cell after 90 minutes, while there is only little signal outside the cells as the merged picture proves. Thus, the signals in figure 4.45 result from DNaseI procession outside the cells, which are efficiently reduced by G-Actin addition.

To examine the supposed uptake increasing effect of pyrenebutyrate [227], a further measurement with G-Actin, without pyrenebutyrate was accomplished in the same manner. The result is shown in figure 4.47.

Clearly, there is fluorescence signal within the cell, but there is also a high amount of signal outside of it. This can only be attributed to a decreased

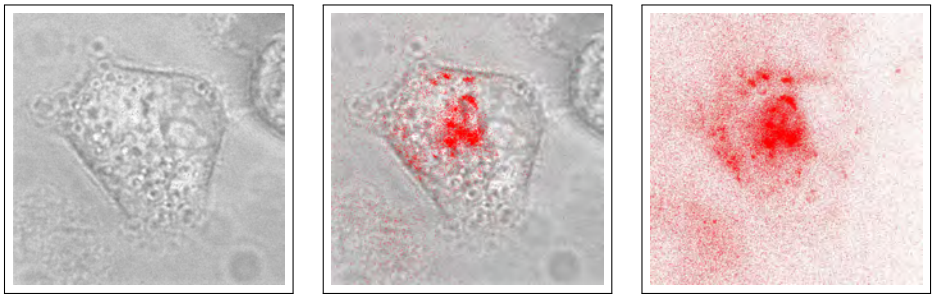

a) incident light **b)** merged image **c)** TIRF image

Figure 4.46: A-549 cells in colorless medium containing G-Actin, preincubated with pyrenebutyrate and imaged on a TIRF microscope, 90 minutes after Antp-linked $SP2^{CM}$ addition. a) shows a 32 µm x 32 µm incident light image, c) shows the corresponding raw TIRF image and b) shows a merged picture in which the TIRF signal was threshold selected for enhanced visibility.

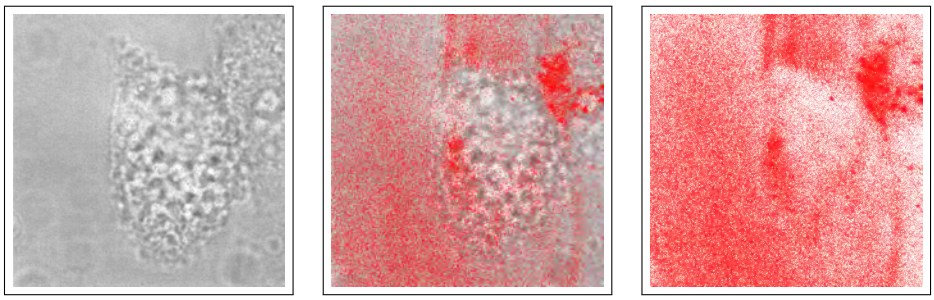

a) incident light **b)** merged image **c)** TIRF image

Figure 4.47: A-549 cells in colorless medium containing G-Actin, imaged on a TIRF microscope, 90 minutes after Antp-linked $SP2^{CM}$ addition. a) shows a 32 µm x 32 µm incident light image, c) shows the corresponding raw TIRF image and b) shows a merged picture in which the TIRF signal was threshold selected for enhanced visibility.

uptake kinetics, because DNaseI activity is inhibited.

In general, *smart probes* can pass cell membranes by the attachment of the cell-penetrating peptide Antennapedia. This uptake is distinctly increased by pyrenebutyrate, but can be deteriorated by destruction of the modified *smart*

probe outside of the cell, e.g. a procession by DNaseI, which can be inhibited by G-Actin addition. Once the modified *smart probe* has entered the cell, the successive processes are totally ambiguous, though. There might not be any *smart probe* action at all, there might be a scission by any present nucleases or any other enzyme, capable of DNA degradation, there might also be enzymatic action other than hydrolysis or also hybridization to complementary DNA.

Therefore, Antp-linked *smart probes* are suited for intracellular investigations that are harmless to the cells at relatively low concentrations, but at best only those, that encounter only one or very few possible processes in the cell. Cellular nuclease research should thus be addressed differently, as done in section 4.2 for example.

4.2 Enzyme Investigations via Immunostaining

Immunostaining constitutes a universal tool for the investigation of any bound antigen. Therefore, also fixed enzymes in cells can be examined with the appropriate specific antibody. This primary antibody is then labeled specifically with a chromophore attached to a secondary antibody directed against the primary antibody.

In this section the effect of different labeling strategies for an immunostaining of DNaseX is examined. The best labeling method is then used to depict the occurrence of DNaseX in divers native mammalian cell types with two different specific primary antibodies. Furthermore, the DNaseX expression of a cell line in its native and at different expression states after transfection with two different DNaseX transfection mechanisms is shown and numerically evaluated via single molecule based localization microscopy.

4.2.1 Labeling Methods

There is a multitude of different protocols for labeling mammalian cells, incorporating various chemicals, temperatures and incubation times. Nonetheless, immunostaining experts use very similar successions of labeling steps. Therefore, the standard protocol in this work (see section 3.2.6) evolved from a highly tested protocol, published by microscopic experts [229] (see Appendix B.2). The standard protocol consists of six main steps, surrounded by a high number of washing cycles. The cells are first fixed and their membranes are

permeabilized. After a saturation of potent unspecific binding sites the cells are incubated with primary antibody or negative control proteins, followed by secondary antibody and finally nuclear counterstaining incubation.

However, some experimenters claim the importance of living cells during antibody incubation. To investigate on this effect the chosen standard protocol was further modified into three different protocols (see section 3.2.6), scheduling the cell fixation once before primary antibody (I)), once between primary and secondary antibody (II)) and once after secondary antibody incubation (III)). Since a permeabilization of living cells hampers their viability, this step was left out for the first protocol as well. Primary antibody 'DNAX' dissolved in PBS, respectively accustomed cell culture medium, was incubated at 37 °Celsius in all samples. For a negative control, protein preimmune serum, derived from the same source as the primary antibody before immunization, was used in the same way as primary antibody. Alexa Fluor® 647 labeled secondary antibody was processed equally. The nuclear counterstaining with Sytox® Green Nucleic Acid Stain was applied as the last step at fixed cells equally in all protocols. Despite the different proceedings all cells were treated as equally as possible and can, therefore, be considered comparable to each other.

After labeling the samples were embedded in antifading mounting medium and measured likewise on a confocal microscope in several vertical layers. For a manageable demonstration these layers are projected onto one single plane that shows the maximum intensity derived for that coordinate. Figure 4.48 shows the main results of this measurement, while the complete set of images is depicted in Appendix C.2.

Despite the unique cell shapes I) and II) show very similar looking cells in respect to both the samples (a)) and the controls (b)). Since the cells in I) were fixed before and the cells in II) fixed after primary antibody incubation, the viability of the cell during primary antibody incubation does not alter the labeling efficiency. Figure 4.48 III) clearly shows a different result. Here secondary antibody attachment onto the living cell took place, but obviously the membrane was damaged due to this treatment. Also the counterstaining result in the control samples looks different to those of I) and II), although the cells were already fixed at this point in every labeling protocol. This indicates that the incubation with secondary antibody on living cells not only affects the membrane, but also other cell compartments and, therefore, the viability of the complete cell. These results demand a cell

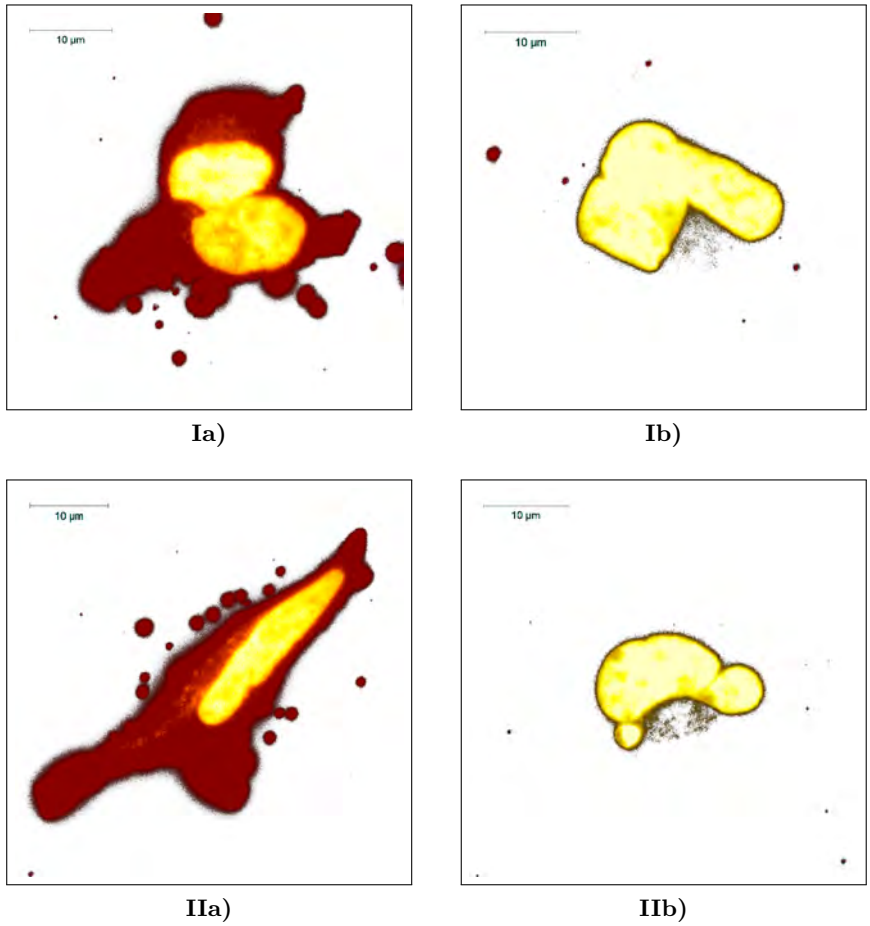

Figure 4.48: Examination of different labeling procedures. I) Cell fixation before incubation with primary antibody, II) Cell fixation between primary and secondary antibody incubation, III) Cell fixation after incubation with secondary antibody. a) incubated with primary antibody and Alexa Fluor®647 linked secondary antibody (red), b) incubated with preimmune serum and Alexa Fluor®647 linked secondary antibody (red). Both samples counterstained with Sytox® Green Nucleic Acid Stain (yellow) after fixation. Cells confocally scanned in several layers and projected onto one plane showing the maximum intensity per pixel.

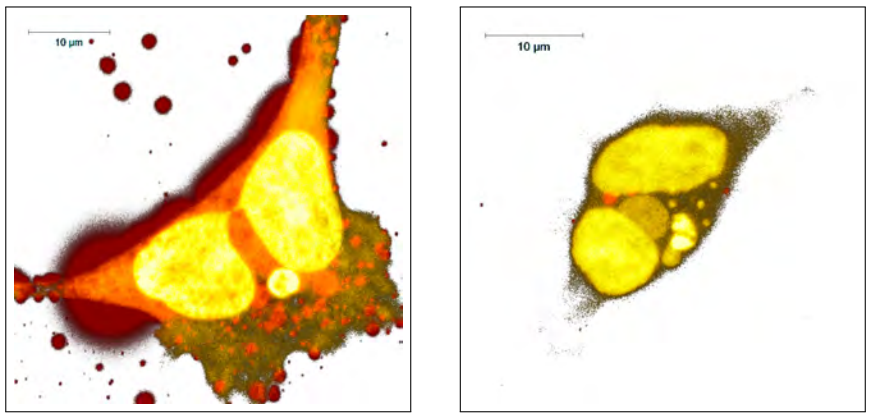

IIIa) **IIIb)**

Figure 4.48: Examination of different labeling procedures. Description see second picture part.

fixation between primary and secondary antibody at the latest. To keep the cell stress level as low as possible and, furthermore, allow a penetration of primary and secondary antibody into the cell, a fixation at the very beginning of the labeling protocol should generally be favored and was applied to any other immunostaining that is shown in this work.

4.2.2 DNaseX occurrence in native mammalian Cell Lines

In 2001 Shiokawa *et al.* published DNaseX transcript concentrations in different tissues compared to DNaseI mRNA amount in human pancreas [39]. Only heart and skeletal muscle revealed a higher amount than 30 % to the reference value in the applied RNA dot blots. Lung, bladder, uterus and colon showed an amount of up to 30 % while no DNaseX transcript could be detected in the whole human brain.

In their European patent application from 2002 Coy *et al.* described their research and prediction on the biological importance of DNaseX [40]. According to them this enzyme appears in cells which have a high turnover and plays an important role in apoptosis, whereas the absence of DNaseX might, therefore, be connected with diseases like AIDS, systemic lupus erythematodes, cystic fibrosis and cancer.

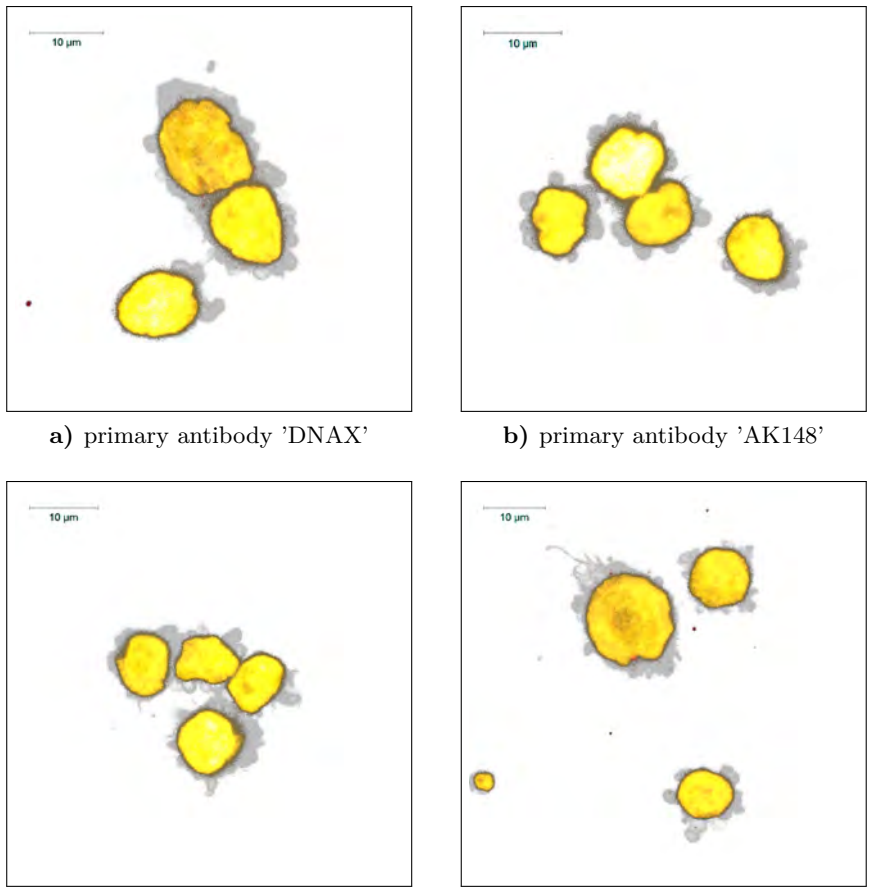

a) primary antibody 'DNAX'

b) primary antibody 'AK148'

c) negative control

d) pre-immune serum

Figure 4.49: Maximum intensity projections of confocally derived z-stacks of SK-N-MC cells. Nucleus labeled with Sytox® Green Nucleic Acid Stain (yellow), cytoskeleton labeled with rhodamine-phalloidin (grey), DNaseX immunostained with Alexa Fluor®647 (red). Samples equally measured and scaled. a) and b) show the effect of different primary antibodies, c) incubated with primary antibody 'DNAX' and counterstained, without secondary antibody, d) shows the outcome by utilization of pre-immune serum instead of a primary antibody.

Due to these facts the knowledge about DNaseX occurrence in tumorigenic cell lines of different tissues constitutes new evidence for the biological relevance of DNaseX, which is until now suggested to hinder foreign DNA from entering the cell [43]. Cells of one brain, one lung, one bladder, one uterus and three colon tissue cell lines were, therefore, fixed and permeabilized. Four samples of each cell line were prepared for two different primary antibodies, a pre-immune serum and a blank control. During a secondary antibody incubation the cytoskeleton counterstaining reactant rhodamine phalloidin was added to all samples. Furthermore, all samples of every cell line were counterstained with Sytox® Green Nucleic Acid Stain and embedded in mounting medium. The detailed protocol is described in section 3.2.6. Afterwards, the cells were measured in different vertical layers on a confocal microscope as described in section 3.1.5. The maximum intensity projections onto single planes are presented in this chapter.

Figure 4.49 shows a set of four images of brain neuroblastoma SK-N-MC cells. These very small cells consist of a large nucleus and only little cytoplasm. Both applied primary DNaseX antibodies do not yield a fluorescent signal, but show the same pattern as the pre-immune serum and negative control upon all applied irradiation wavelengths. This cell line does obviously not express DNaseX in a concentration that can be detected despite this very sensitive method. Since neither the RNA dot blots revealed DNaseX transcript in the whole brain, it can be assumed that there is no DNaseX protein present in this tissue. Furthermore, this confirms the prediction made by Coy *et al.* [40] for neuroblastoma constitutes the most common cancer in infancy which generally has a healing prognosis of down to 30 %. Here a connection between a hampered apoptosis and the cancer affection is plausible.

The human lung carcinoma cell line A-549 (see figure 4.50) shows a completely different morphology than the previous cells. They have a lot larger cytoplasm and do not necessarily gather with other cells, but most often occur individually. The sample containing primary antibody 'DNAX' shows a distinct fluorophore signal upon illumination with the appropriate wavelength homogeneously distributed in the cytoplasm, while primary antibody 'AK148' does not lead to any positive result. Since the negative control does not show any positive signal either, it can be assumed that 'DNAX' is more sensitive than 'AK148'. This means that despite their carcinogen nature there is DNaseX protein present in A-549 cells, confirming the RNA dot blot results on lung tissue.

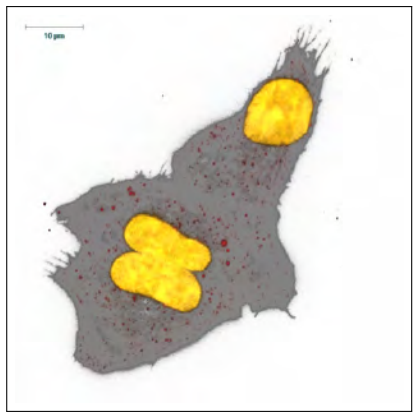

a) primary antibody 'DNAX'

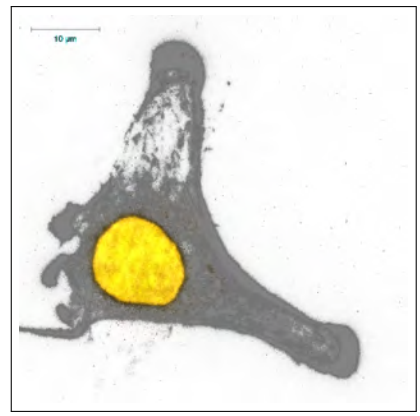

b) primary antibody 'AK148'

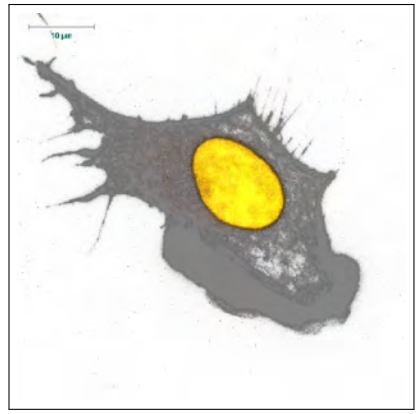

c) negative control

Figure 4.50: Maximum intensity projections of confocally derived z-stacks of A-549 cells. Nucleus labeled with Sytox® Green Nucleic Acid Stain (yellow), cytoskeleton labeled with rhodamine-phalloidin (grey), DNaseX immunostained with Alexa Fluor®647 (red). Samples equally measured and scaled. a) and b) show the effect of different primary antibodies, c) incubated with primary antibody 'DNAX' and counterstained, without secondary antibody. For this experiment no pre-immune serum was available.

Human urinary bladder carcinoma cell line ECV-304 (see figure 4.51) shows a morphology and growth behavior similar to that of A-549 cells. Only little antigen can be detected with 'DNAX' primary antibody, while an incubation with pre-immune serum results in a comparable signal. 'AK148' yields even lower secondary antibody binding events. The derived signal is likewise homogeneously distributed within the cytoplasm. Due to this low signal and the contradictory data it is not possible to postulate a conclusion about the DNaseX occurrence in ECV-304 cells despite their bladder carcinoma origin.

The well established HeLa cell line samples represent uterine tissue and show accumulations of several cells (see figure 4.52). Here both primary antibodies result in similar secondary antibody signals, while the strongest signal is obtained in the pre-immune serum sample. Again the signal is distributed homogeneously in the cytoplasm and a distinct statement about DNaseX expression is not feasible despite their carcinogen origin and positive RNA dot blot results.

The fifth tissue species examined in this work is depicted by three different substitutes. LS-174T, SW-837 and HT-29 represent human colon carcinoma cell lines. The typical conglomerations of LS-174T cells (see figure 4.53) show a fluorescent signal after incubation with secondary antibody upon appropriate irradiation for both primary antibodies and the pre-immune serum. As in ECV-304 the strongest signal is obtained in the 'DNAX' sample, followed by pre-immune serum. Both show a homogeneous distribution of secondary antibody. 'AK148' again only yields little signal, mostly in the nuclei.

The same distributions and measures of 'AK148' and pre-immune serum can be found in SW-837 cells (see figure 4.54). Primary antibody 'DNAX', though, leads to a remarkable signal in this cell type. DNaseX is localized in the nucleus, in the cytoplasm and on the membrane. Furthermore, there are comparably large areas completely stained with secondary antibody fluorophore. The reason for these agglomerations and the type of compartment carrying this signal remains unknown, but could be linked to the exceptional tight compositions built by several individuals in this cell line though.

The conglomerations of HT-29 cells (see figure 4.55) finally reveal a situation that was described by literature [43] and expected by theory: While there are only few spots in the pre-immune serum sample both 'AK148' and 'DNAX' show distinct secondary antibody signals, which seem to be located on the cell membrane with a high ratio. To verify this assumption a cross section of a small agglomeration of immunostained HT-29 cells is shown in

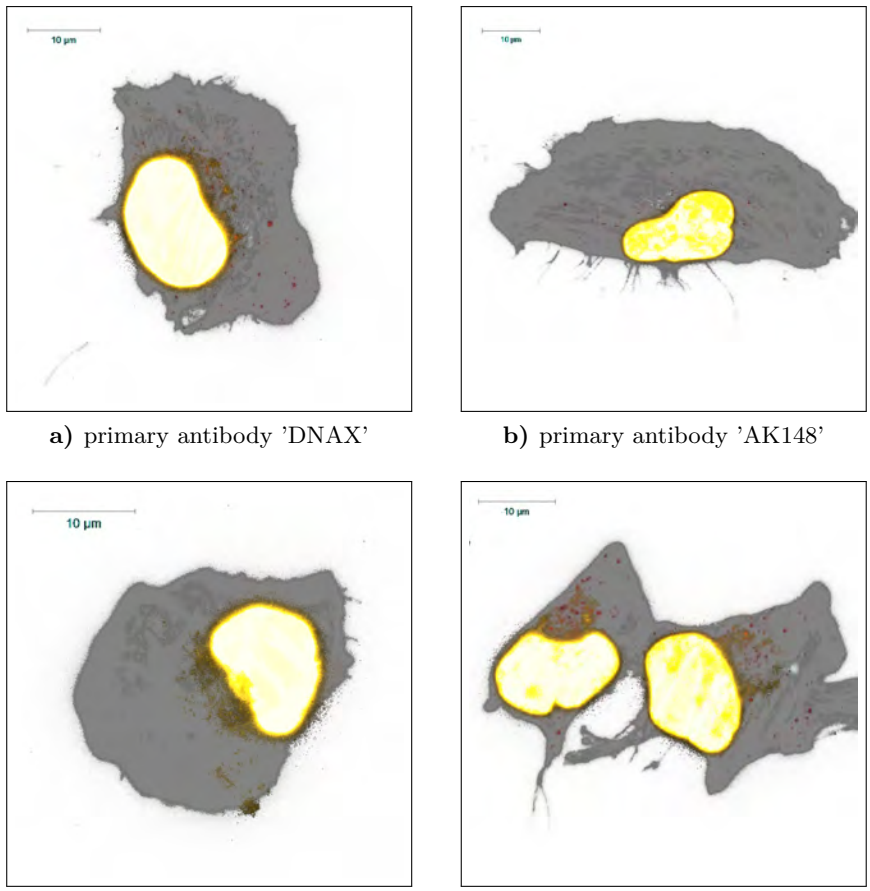

a) primary antibody 'DNAX'

b) primary antibody 'AK148'

c) negative control

d) pre-immune serum

Figure 4.51: Maximum intensity projections of confocally derived z-stacks of ECV-304 cells. Nucleus labeled with Sytox® Green Nucleic Acid Stain (yellow), cytoskeleton labeled with rhodamine-phalloidin (grey), DNaseX immunostained with Alexa Fluor®647 (red). Samples equally measured and scaled. a) and b) show the effect of different primary antibodies, c) incubated with primary antibody 'DNAX' and counterstained, without secondary antibody, d) shows the outcome by utilization of pre-immune serum instead of a primary antibody.

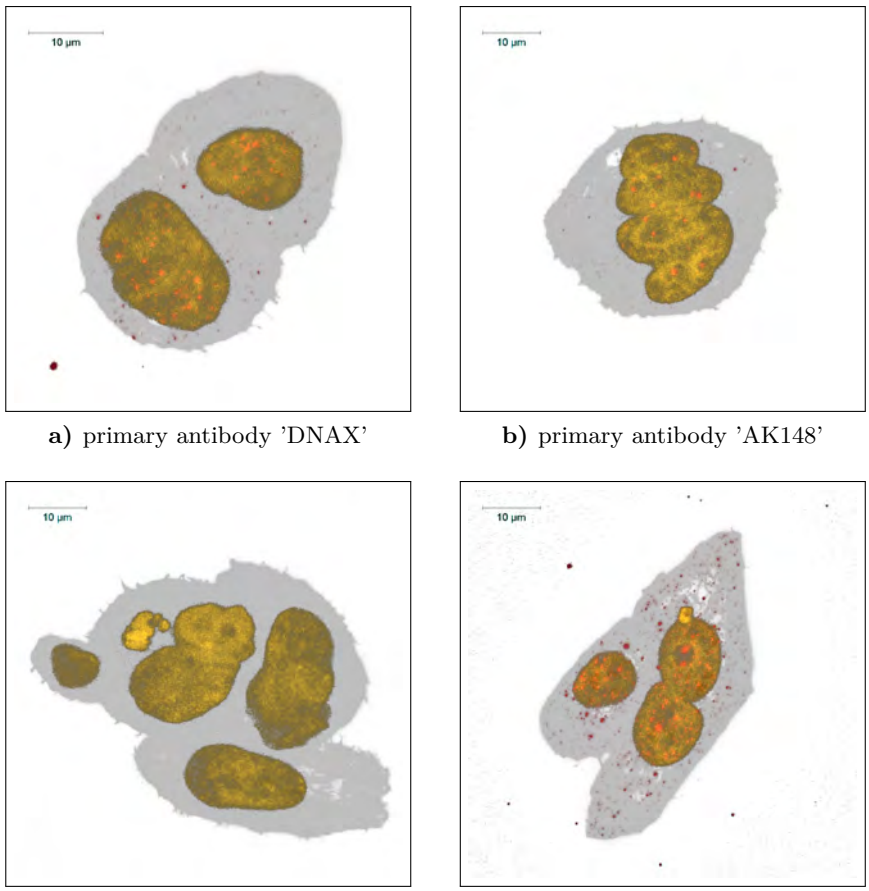

a) primary antibody 'DNAX' **b)** primary antibody 'AK148'

c) negative control **d)** pre-immune serum

Figure 4.52: Maximum intensity projections of confocally derived z-stacks of HeLa cells. Nucleus labeled with Sytox® Green Nucleic Acid Stain (yellow), cytoskeleton labeled with rhodamine-phalloidin (grey), DNaseX immunostained with Alexa Fluor®647 (red). Samples equally measured and scaled. a) and b) show the effect of different primary antibodies, c) incubated with primary antibody 'DNAX' and counter-stained, without secondary antibody, d) shows the outcome by utilization of pre-immune serum instead of a primary antibody.

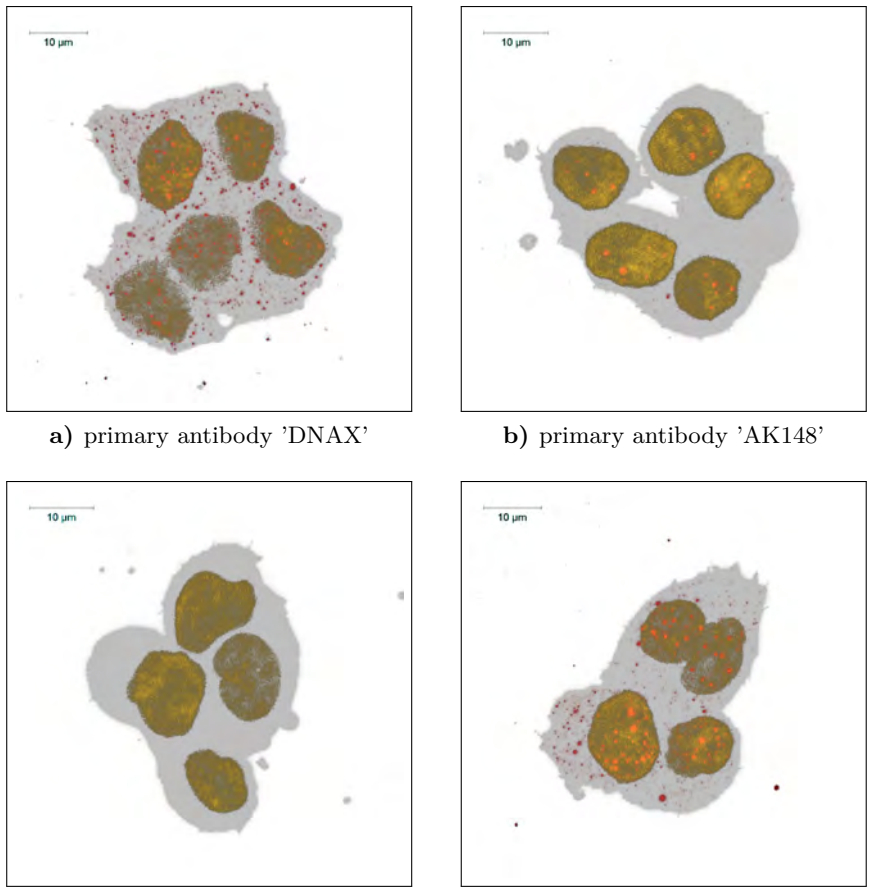

a) primary antibody 'DNAX'

b) primary antibody 'AK148'

c) negative control

d) pre-immune serum

Figure 4.53: Maximum intensity projections of confocally derived z-stacks of LS-174T cells. Nucleus labeled with Sytox® Green Nucleic Acid Stain (yellow), cytoskeleton labeled with rhodamine-phalloidin (grey), DNaseX immunostained with Alexa Fluor®647 (red). Samples equally measured and scaled. a) and b) show the effect of different primary antibodies, c) incubated with primary antibody 'DNAX' and counter-stained, without secondary antibody, d) shows the outcome by utilization of pre-immune serum instead of a primary antibody.

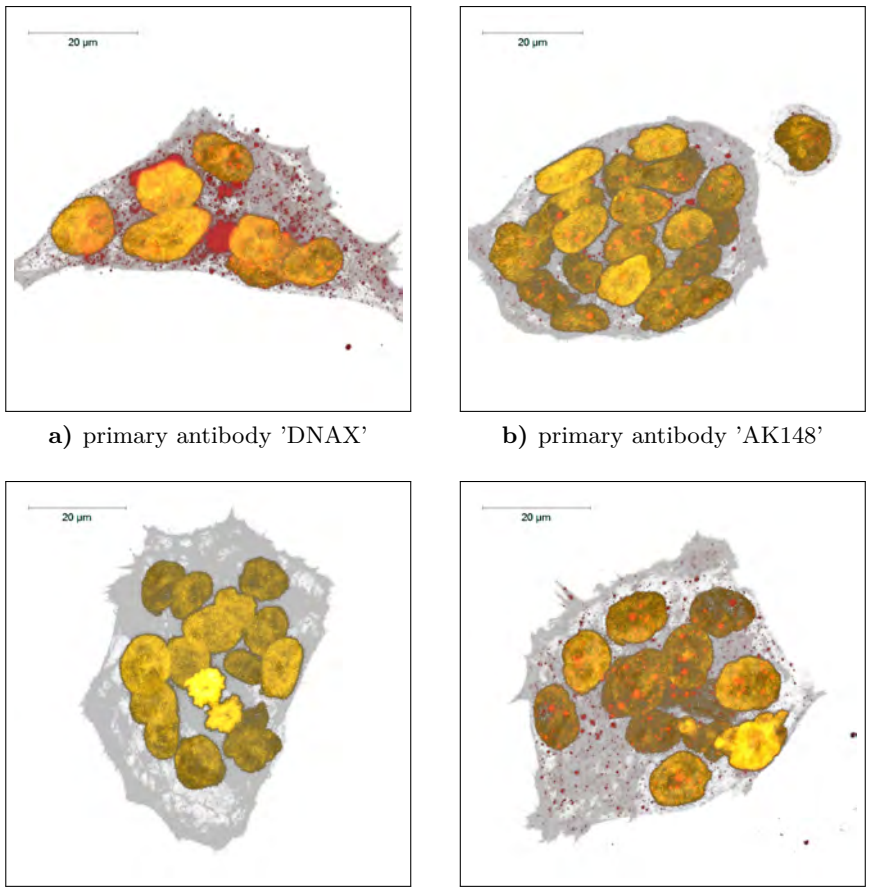

a) primary antibody 'DNAX' **b)** primary antibody 'AK148'

c) negative control **d)** pre-immune serum

Figure 4.54: Maximum intensity projections of confocally derived z-stacks of SW-837 cells. Nucleus labeled with Sytox® Green Nucleic Acid Stain (yellow), cytoskeleton labeled with rhodamine-phalloidin (grey), DNaseX immunostained with Alexa Fluor®647 (red). Samples equally measured and scaled. a) and b) show the effect of different primary antibodies, c) incubated with primary antibody 'DNAX' and counter-stained, without secondary antibody, d) shows the outcome by utilization of pre-immune serum instead of a primary antibody.

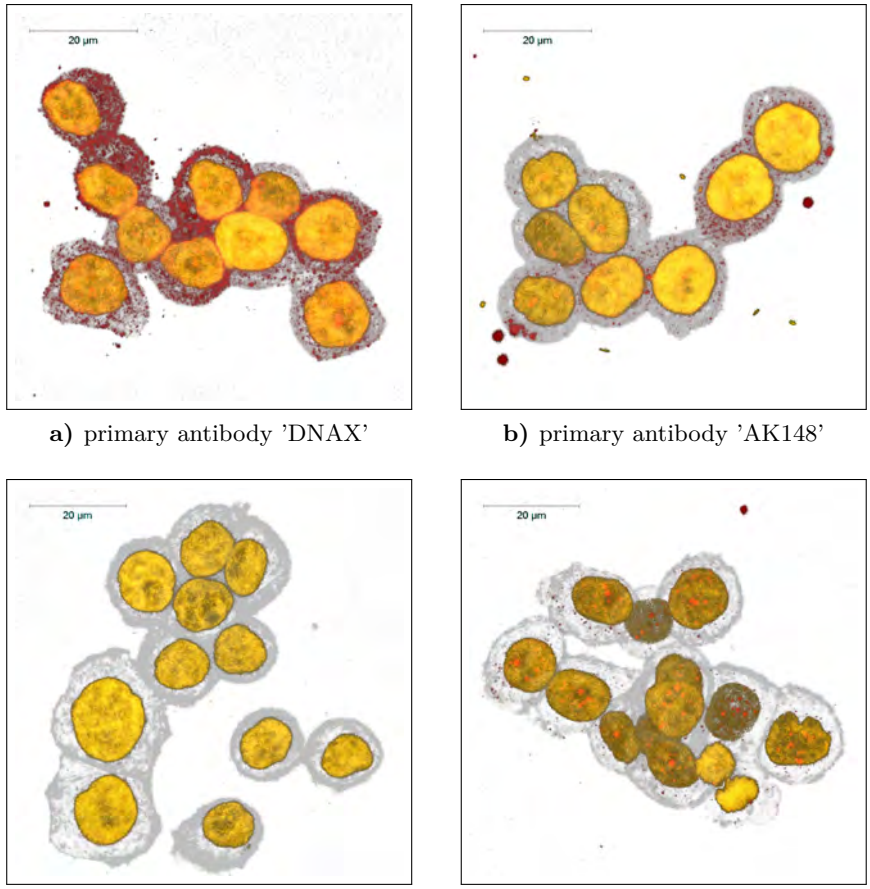

a) primary antibody 'DNAX'

b) primary antibody 'AK148'

c) negative control

d) pre-immune serum

Figure 4.55: Maximum intensity projections of confocally derived z-stacks of HT-29 cells. Nucleus labeled with Sytox® Green Nucleic Acid Stain (yellow), cytoskeleton labeled with rhodamine-phalloidin (grey), DNaseX immunostained with Alexa Fluor®647 (red). Samples equally measured and scaled. a) and b) show the effect of different primary antibodies, c) incubated with primary antibody 'DNAX' and counter-stained, without secondary antibody, d) shows the outcome by utilization of pre-immune serum instead of a primary antibody.

figure 4.56.

The lower surface of HT-29 cells (figure 4.56 (blue frame)) reveals a high density of DNaseX signals. Also the membranes in between cells as well as the membrane on top and on the side of single cells (figure 4.56 (red frame)) contain DNaseX. Figure 4.56 (green frame), furthermore, exposes DNaseX accumulations at or inside the nucleus.

A central layer of these HT-29 cells was used to evaluate the colocalization of DNaseX with the membrane and with the nucleus computationally. Figure 4.57 shows the chosen layer with complete staining (a)) and those signals correlated to each other (b)). When a background excluding threshold is applied to this correlation, the remaining DNaseX localizations can be divided into those hitting a left over cytoskeleton localization and those placed somewhere else. This distribution is shown in figure 4.57 c), where the black dots code the colocalized DNaseX spots with the membrane. The applied threshold and signal distributions are presented in d). Figure 4.58 represents the same method for the colocalization of DNaseX and nucleus with the same threshold and color codings. These graphs show, that the largest proportion of detected DNaseX molecules in HT-29 cells is indeed located on the membrane. Only a few DNaseX spots are not colocalized with the membrane. Most of those though are colocalized with the nucleus. This evaluation indicates that the appearance of DNaseX containing nuclei in other cell lines also holds. The biological relevance for this enzyme distribution has only partly been described [43]. If the only task fulfilled by DNaseX was to provide a barrier for foreign DNA for entering the cell, a localization on the membrane and also in the cytoplasm during protein expression or vesicle transport would be plausible. The reason for DNaseX occurrence in a nucleus is highly remarkable though, given that DNaseX does not follow strong substrate preferences and can therefore process cell associated DNA, compromising the cell metabolism and induce apoptosis. This could, therefore, indicate the precise connection between DNaseX occurrence and those diseases with a disturbed apoptose mechanism (cf. [40]). Nonetheless, it is astonishing, that DNaseX is imported into the nucleus, not carrying a nuclear localization signal [41].

A specialty of HT-29 cells is the heterogeneous distribution of DNaseX over the membrane. Generally the enzyme seems to be concentrated on membrane sections neighboring other cells (cf. figure 4.55). Also the bottom surface of the cell building the interface to the chamber slide seems to contain more

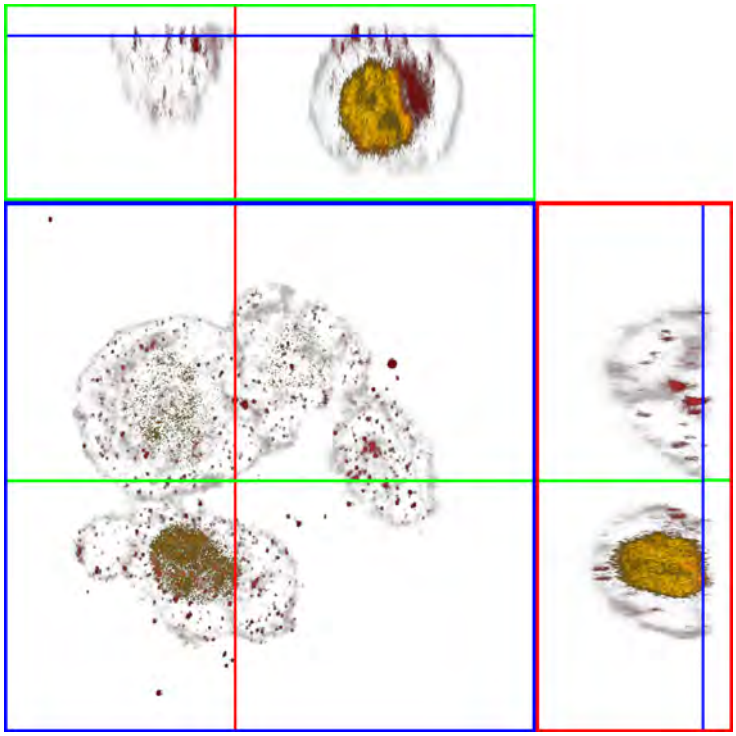

Figure 4.56: Orthogonal cut through HT-29 cells. Nucleus labeled with Sytox® Green Nucleic Acid Stain (yellow), cytoskeleton labeled with rhodamine-phalloidin (grey), DNaseX immunostained with 'DNAX' primary antibody and Alexa Fluor®647 labeled secondary antibody (red). The large section (blue frame) shows a 57 µm x 57 µm section of the lower surface of the cell. The red and green lines indicate the sections depicted in the red and green framed areas (right and top pictures). The blue lines in these frames represent the lower cell surface depicted in the main frame.

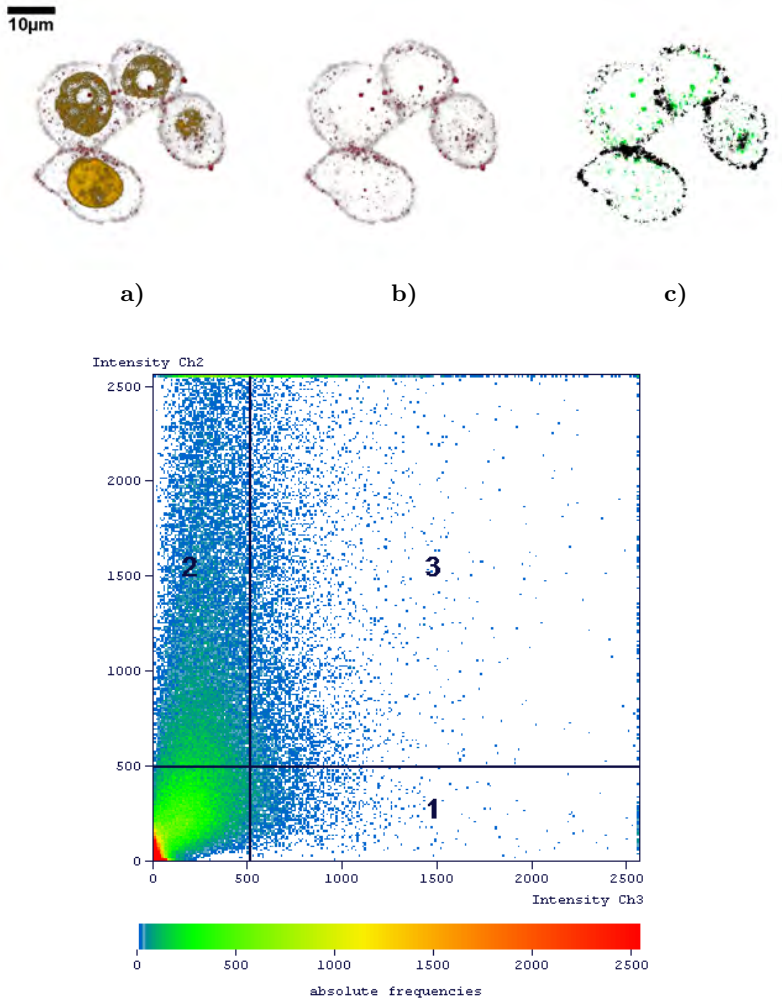

Figure 4.57: Colocalization of DNaseX and membrane signal in HT-29 central layer. a) Central layer of HT-29 cells. Nucleus labeled with Sytox® Green Nucleic Acid Stain (yellow), cytoskeleton labeled with rhodamine-phalloidin (grey), DNaseX immunostained with 'DNAX' primary antibody and Alexa Fluor®647 labeled secondary antibody (red). b) Central layer of HT-29 cells as in a) without nucleus visualization. c) Colocalization image of b). Black represents colocalized spots, green represents DNaseX spots not localized on the membrane. d) colocalization graph: 1 represents DNaseX signals, 2 represents membrane signals and 3 represents colocalized spots.

DNaseX than equivalently large areas at top or side membrane sections (cf. figure 4.56). Following Shiokawa [43], this could indicate the individual cells potential to recognize neighbored cells as likely invasion sites and their ability to establish a defense alignment. Furthermore, the greatly various DNaseX concentrations of individual cells are highly remarkable (cf. especially figure 4.55 b)). Here no distinct pattern is apparent. The allocation might, therefore, be dependent upon a huge number of factors, most likely though the cell age or its viability.

All three examined colon cell lines revealed a distinct DNaseX occurrence, despite their tumorigenic nature, fortified by the RNA dot blots (cf. [39]). Still, there is a high diversity of DNaseX expression between the different cell lines. Except for the SK-N-MC brain neuroblastoma cell line all presented cell lines were tested to carry a DNaseX transcript concentration of up to 30% of the DNaseI gene found in adult pancreas. Since the signals that could be detected in different tissues with immunostaining are highly divergent, the range given by Shiokawa *et al.* ([39]) is not ideally suited for DNaseX expression quantification in native mammalian cells and tissues.

There is still one unanswered question that emerged from these measurements. In every cell line carrying DNaseX the pre-immune serum yielded a high signal in DNaseX detection, although it was meant to serve as a negative control. This signal was mostly even higher than that of primary antibody 'AK148'. This is quite unsettling at first sight. Since the employed pre-immune serum samples in these experiments yielded a signal that corresponds to the signal obtained by the primary antibodies respectively the supposed DNaseX amounts, the negative control does not nearly show a similar result, and, furthermore samples with only secondary antibody[21] do not show any similar signal, it is most likely that there is no unspecific binding in the pre-immune serum samples. Hence, this signal must result from a component only present in these samples, which solely is the pre-immune serum itself. The utilized pre-immune serum originates from the same animal individuum as 'DNAX'. In a standard procedure an immunization success is determined by the ratio of desired antibody in antisera to that of the pre-immune serum. Possibly, the 'negative' serum does contain an intrinsic DNaseX antibody in a concentration, that can almost saturate the DNaseX present in the depicted cell lines. If so, a measurement with different concentrations of pre-immune

[21] These samples can be seen in section C.2, figure 4.65 and section C.3.

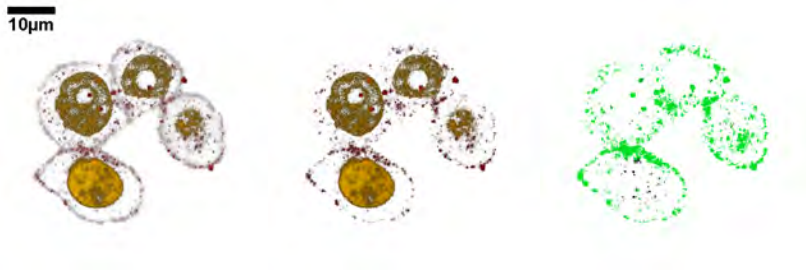

a) b) c)

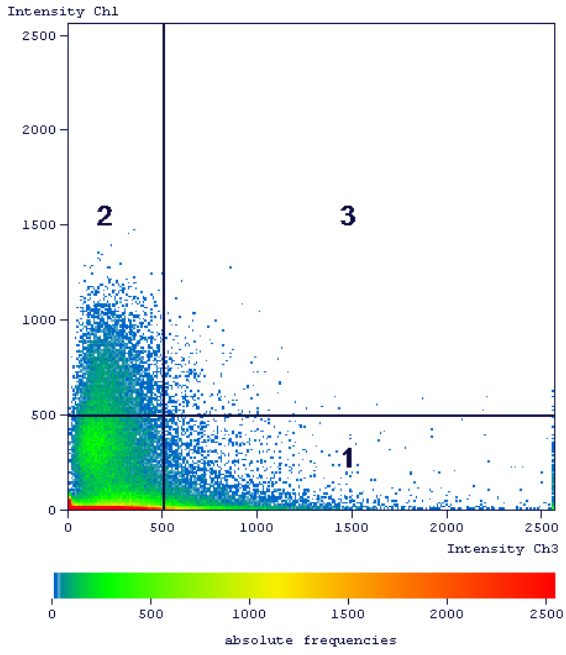

d)

Figure 4.58: Colocalization of DNaseX and nucleus signal in HT-29 central layer. a) Central layer of HT-29 cells. Nucleus labeled with Sytox® Green Nucleic Acid Stain (yellow), cytoskeleton labeled with rhodamine-phalloidin (grey), DNaseX immunostained with 'DNAX' primary antibody and Alexa Fluor®647 labeled secondary antibody (red). b) Central layer of HT-29 cells as in a) without membrane visualization. c) Colocalization image of b). Black represents colocalized spots, green represents DNaseX spots not localized in the nucleus. d) colocalization graph: 1 represents DNaseX signals, 2 represents nucleus signals and 3 represents colocalized spots.

serum would show.

4.2.3 DNaseX occurrence in transfected HEK cells

The generally minor expression of DNaseX in native mammalian cell lines hampers the research on DNaseX characteristics in a native environment. Therefore, the simulation of a native environment at a high expression level can be favorable for research on DNaseX characteristics like its localization for instance.

There are cell lines that are specially adapted for gene transfections. One of these is the tumorigenic human embryonic kidney cell line called Flp-In™-293 or HEK 293T [178]. This cell line was labeled with two different primary antibodies and a blank control as described in section 3.2.6. All samples were measured on a confocal microscope (see section 3.1.5) in different layers and projected onto a single one showing the maximum intensity derived for each coordinate.

In their non-transfected form these cells show only little DNaseX expression confirmed by a similar DNaseX gene expression level as in lung, urine bladder, uterus and colon tissue (cf. section 4.2.2) [39]. This expression is depicted in figure 4.59 a) with primary antibody 'DNAX'. Primary antibody 'AK148' yields a lot less secondary antibody signal, while the negative control proves that there is no unspecific binding of the fluorescent label. These human embryonic kidney cells have very unique shapes which can be seen due to the cytoskeleton staining. However, in these cells the habitual concentration of rhodamine-phalloidin generates a staining efficiency, which is a lot smaller than in other labeled cells (cf. section 4.2.2).

If the very same cell line is steadily transfected with a DNaseX coding plasmid, the cells are to constantly express DNaseX. After following the same labeling and measuring method as described above, highly immunolabeled cells are obtained, as can be seen in figure 4.60. As in HT-29 cells (cf. section 4.2.2) the enzyme is especially located on the cell membrane here. A very high amount of DNaseX is expressed upon transfection, recognized and bound by primary antibody 'DNAX' as well as by 'AK148'. The stronger signal yielded by 'DNAX' over 'AK148' yet conceals the likewise weak cytoskeletal fluorescent label and supports the results presented in section 4.2.2.

An overexpression of the DNaseX gene is not necessarily advantageous in

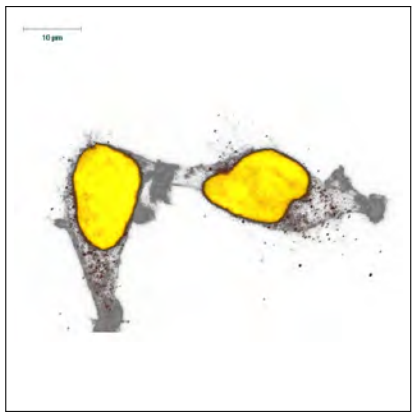

a) primary antibody 'DNAX'

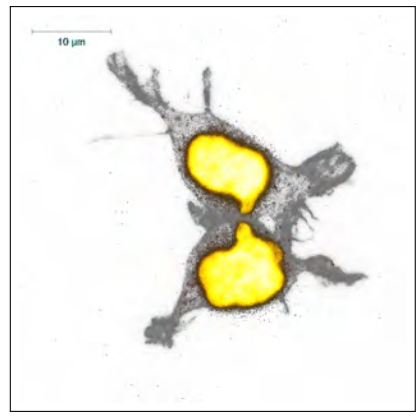

b) primary antibody 'AK148'

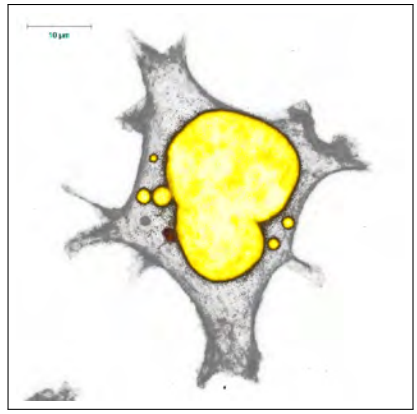

c) negative control

Figure 4.59: Maximum intensity projections of confocally derived z-stacks of non-transfected HEK 293T cells. Nucleus labeled with Sytox® Green Nucleic Acid Stain (yellow), cytoskeleton labeled with rhodamine-phalloidin (grey), DNaseX immunostained with Alexa Fluor®647 (red). Samples equally measured and scaled. a) and b) show the effect of different primary antibodies, while c) was incubated with primary antibody 'DNAX' and counterstained, without the secondary labeled antibody. For this experiment no pre-immune serum was available.

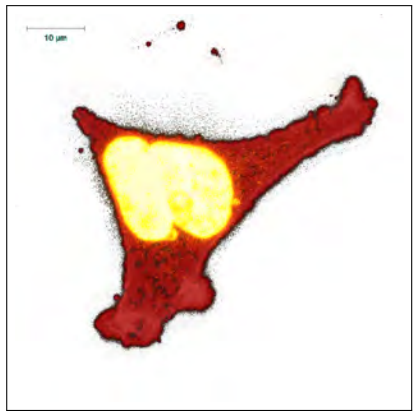

a) primary antibody 'DNAX'

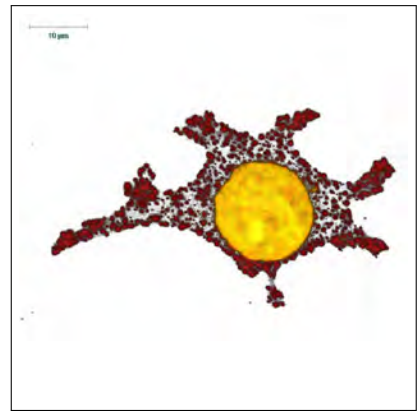

b) primary antibody 'AK148'

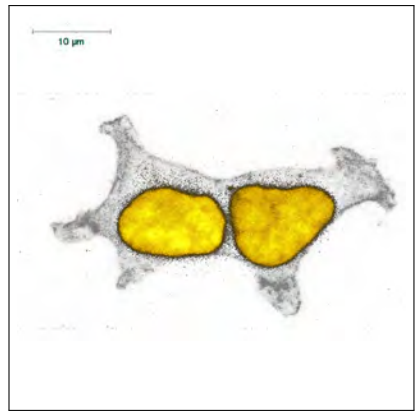

c) negative control

Figure 4.60: Maximum intensity projections of confocally derived z-stacks of steadily transfected HEK 293T cells continuously expressing DNaseX. Nucleus labeled with Sytox® Green Nucleic Acid Stain (yellow), cytoskeleton labeled with rhodamine-phalloidin (grey), DNaseX immunostained with Alexa Fluor®647 (red). Samples equally measured and scaled. a) and b) show the effect of different primary antibodies, while c) was incubated with primary antibody 'DNAX' and counterstained, without the secondary labeled antibody. For this experiment no pre-immune serum was available.

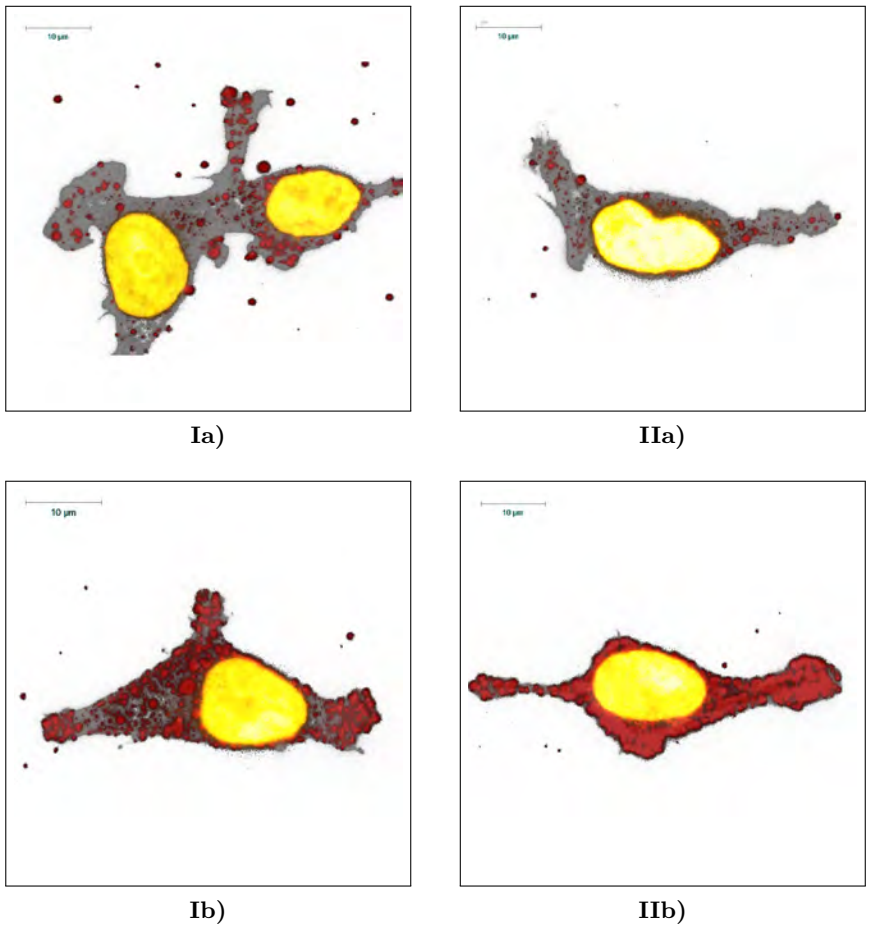

Figure 4.61: Maximum intensity projections of confocally derived z-stacks of steadily transfected HEK 293T cells expressing DNaseX upon antibiotic induction. Description see second image part.

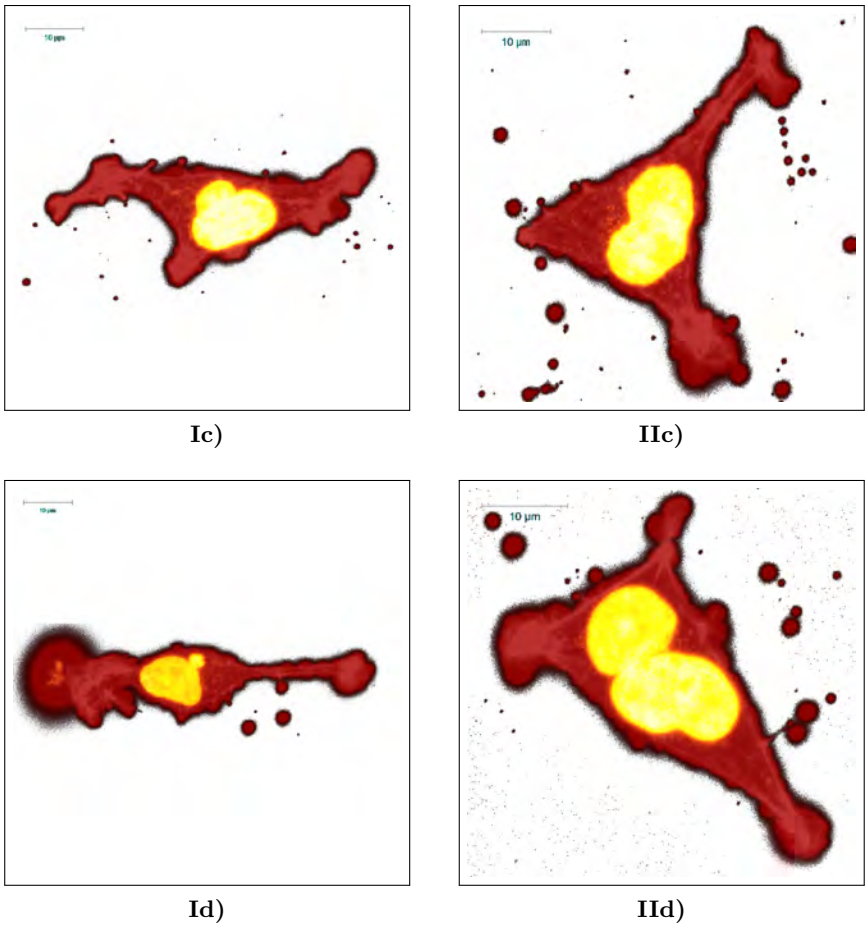

Ic) **IIc)**

Id) **IId)**

Figure 4.61: Maximum intensity projections of confocally derived z-stacks of steadily transfected HEK 293T cells expressing DNaseX upon antibiotic induction. Nucleus labeled with Sytox® Green Nucleic Acid Stain (yellow), cytoskeleton labeled with rhodamine-phalloidin (grey), DNaseX immunostained with Alexa Fluor®647 (red). I) shows cells induced with tetracycline, II) with doxicycline induction for 2.5 (a)), 5 (b)), 24 (c)) and 48 hours (d)). Samples equally measured and scaled.

all cases. When studying membrane assembly for instance, an adjustable amount of DNaseX is preferable. This can be achieved by a transfection with a modified DNaseX gene, that is only transcribed upon an antibiotic trigger. Altering the duration of trigger incubation, therefore, should result in adjusted DNaseX amounts. Figure 4.61 shows a set of images of those modified cells that were equally labeled with 'DNAX' following the standard protocol (see section 3.2.6), except for an order of magnitude higher concentration of cytoskeletal label. Here a wide incubation duration range with two different antibiotics was applied. Obviously a maximum expression level is already reached after 24 hours of both tetracycline and doxicycline induction. While the DNaseX amounts of the two 2.5 hours induction durations appear very similar to each other, at 5 hours induction duration the doxicycline sample seems to contain more enzyme than the corresponding tetracycline sample. Nonetheless, a strong correlation between antibiotic induction duration and DNaseX is clearly visible for both triggers.

4.2.4 High Resolution Measurements and Quantification of Membrane-bound DNaseX

The temporal dependency between Doxicycline induction and DNaseX expression provides an ideal query for superresolution microscopy. DNaseX inducable HEK293T cells of different Doxicycline induction durations were stained (see section 3.2.6) and examined on a TIRF setup (see section 3.1.6). Due to autofluorescent properties of mammalian cells at short wavelengths (cf. figure 2.21) cells of all labeling degrees could be detected via illumination with 514 nm. Figure 4.62 a) shows an autofluorescence picture of HEK293T cells, with the typical low signal to background ratio and the defocused profile.

Figure 4.62 b) shows the very same spot with total internal reflection illumination at 647 nm, focused onto the surface of the cell, yielding a high signal to background ratio. A small part of this area is chosen (see figure 4.62 c)) to be examined via *d*STORM. Whereas c) shows a blurry picture of the junction of the two cells the picture that is reconstructed from the *d*STORM movie (d)) reveals distinct spots and the true assembly of the two cells.

For a post-processing of the *d*STORM data it has to be taken into account that only part of the surface is actually covered with membrane. Therefore an individual 40 x 40 pixels area of each sample and spot is defined for further

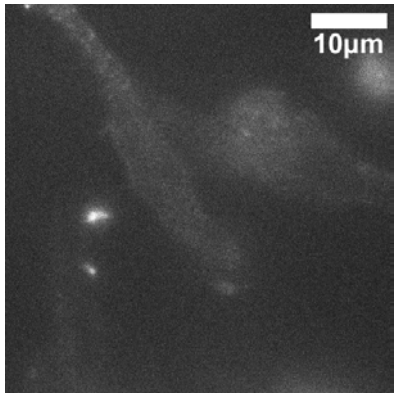

a) Autofluorescence at 514 nm

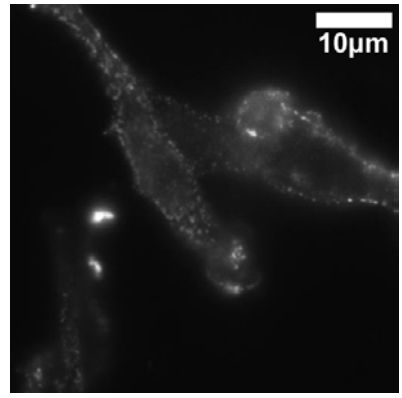

b) TIRF illumination at 647 nm, 512x512 pixels

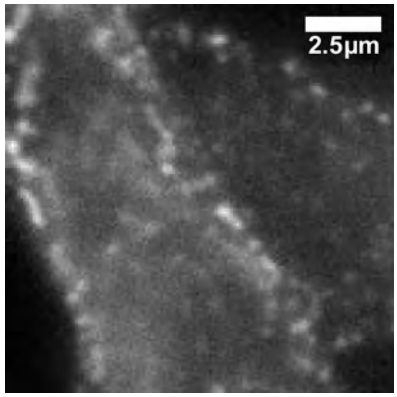

c) TIRF illumination at 647 nm, 128 x 128 pixels

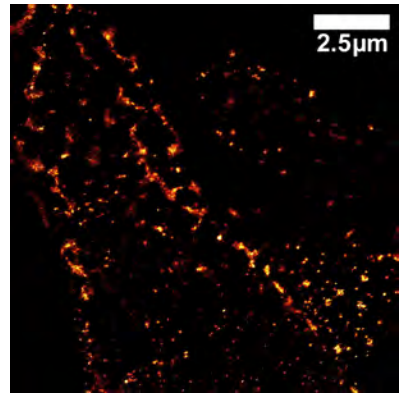

d) Computed *d*STORM picture

Figure 4.62: Set of derived images for the example of one spot of the 32 h Doxicycline induction sample

evaluation (see figure 4.63).

Some examined spots of different tested doxicycline induction durations are presented in figure 4.64. Clearly, the number of hits in a defined area increases with the duration of induction. Counting the number of hits in these areas for three spots per sample, and plotting this over induction duration, results in the graph shown in figure 4.65. Also negative controls with only primary

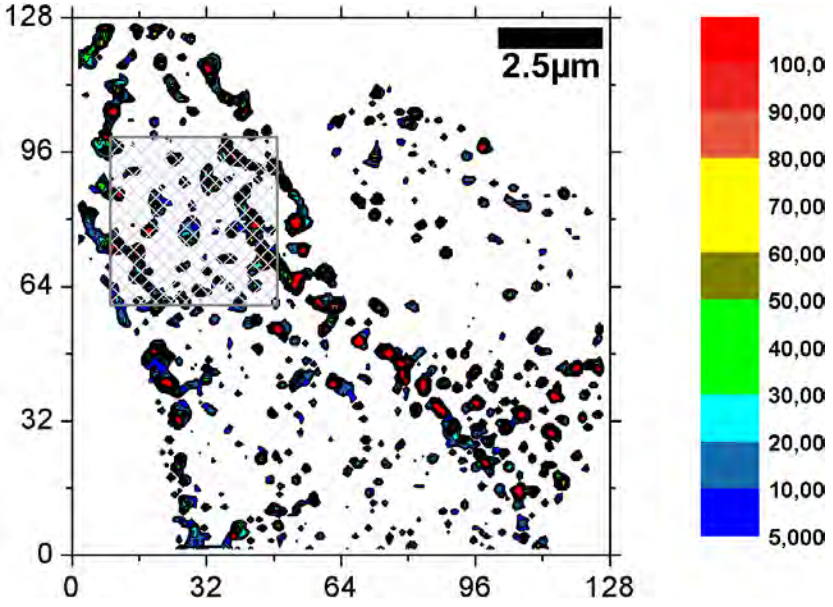

Figure 4.63: Numerical data processing of the 128 x 128 pixels area with a one fold binning. The color bar shows the number of hits.

respectively and only secondary antibody, respectively, were measured. The complete set of images can be found in Appendix C.3.

In the completely immunostained samples a distinct correlation between doxicycline induction duration and DNaseX expression can be confirmed numerically, although in most cases there is a remarkable strong variation of hits between the examined spots of one doxicycline induction duration sample. After 4.11 ± 0.47 hours of induction half of the maximum DNaseX expression is reached already. The maximum number of counts adds up to 22667.8 ± 2131.9 for an averaged 1600 pixels area of membrane and is almost reached after 6 hours of doxicycline induction.

The averaged total number of hits at no doxicycline induction amounts to 6585.7 ± 1261.7 , representing 30% of the maximum value. This value is significantly higher than that of the control sample with only primary antibody, which sums up to 452.8 ± 106 at no doxicycline induction, representing only 7% of the corresponding sample value. The control sample with only secondary antibody shows 2024.7 ± 519.2 hits at no doxicycline induction,

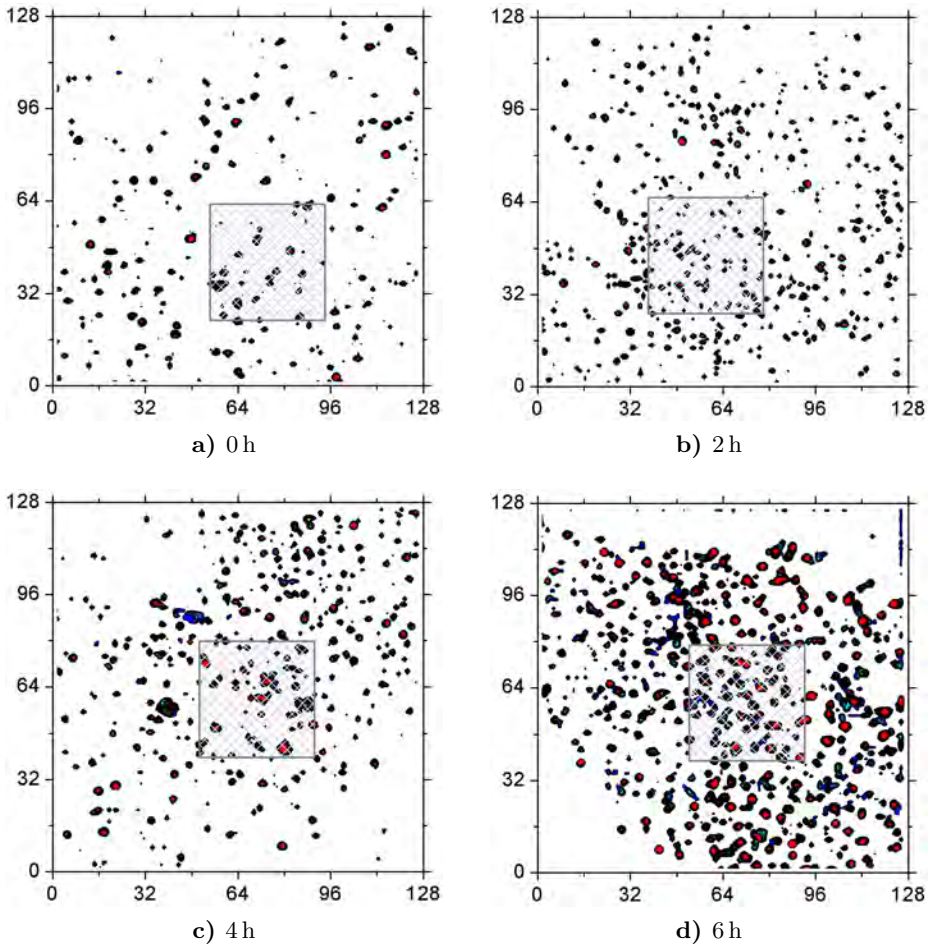

a) 0 h **b)** 2 h

c) 4 h **d)** 6 h

Figure 4.64: Numerical data processing of 128 x 128 pixels areas with a one fold binning for different Doxicycline induction durations.

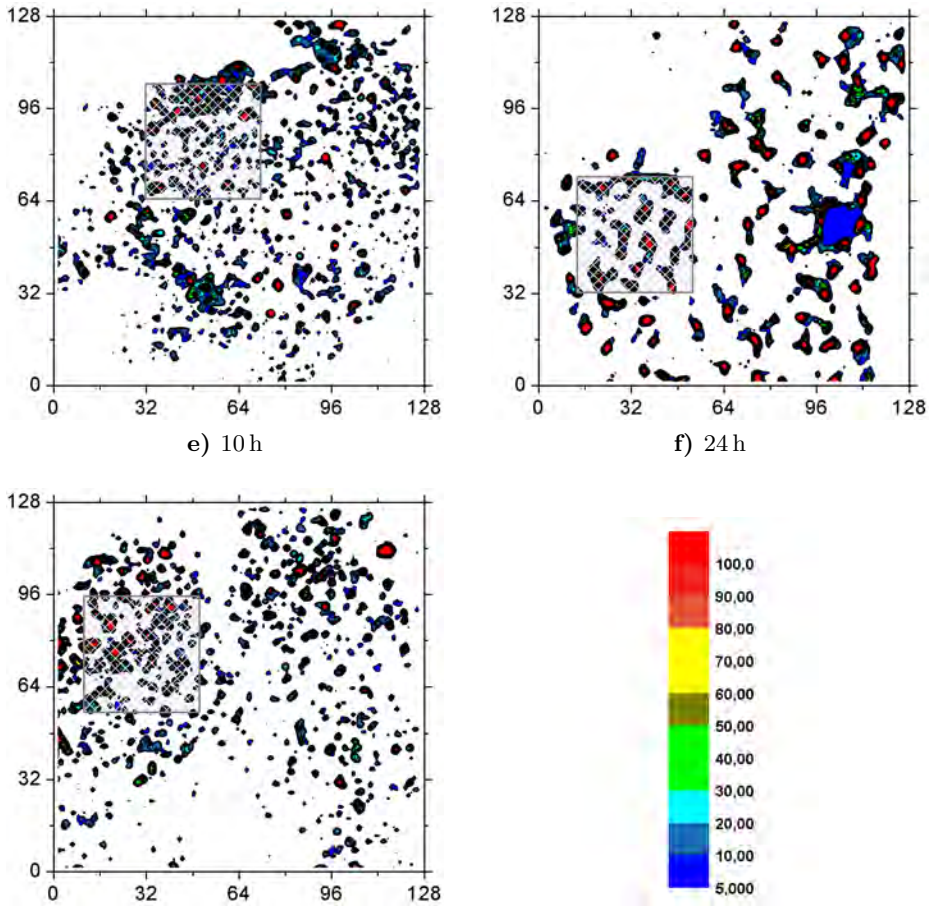

e) 10 h **f)** 24 h

g) 32 h **h)** calibration bar

Figure 4.64: Numerical data processing of 128 x 128 pixels areas with a one fold binning for different Doxicycline induction durations. h) shows the calibration bar that applies for all graphs.

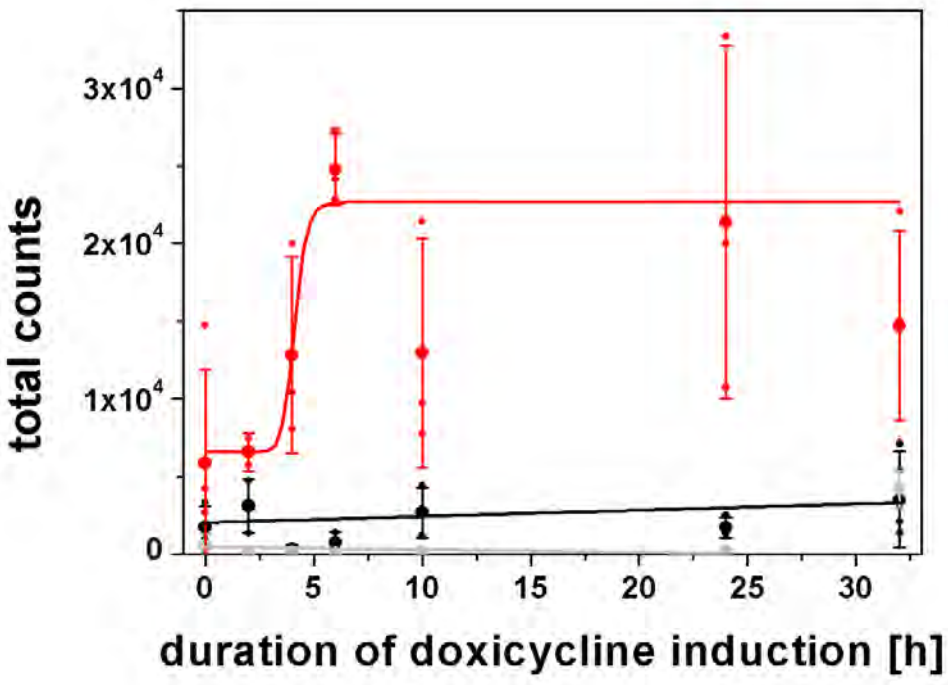

Figure 4.65: DNaseX expression over Doxicycline induction duration. Each Doxicycline induction period was examined with primary and secondary antibody (blue), only primary antibody (green) and only secondary antibody (red) with three spots in each sample (small dots). The big dots represent the mean values.

representing 31% of the corresponding sample value. This means there is a constant level of DNaseX in the DNaseX inducable HEK293T cells, which could be determined by either the expression mechanism or the cell line itself.

When looking at the computed *d*STORM pictures of the samples it is obvious, that the total hits are not homogeneously distributed over the membrane, but gathered in clusters. Figure 4.66 shows a frequency coded, computed membrane image of a 24 hours doxicycline induced cell. Most of the easily to distinguish accumulations show a maximum of hit in the center of the cluster.

Coding the same color bar of this picture differently, results in figure 4.67.

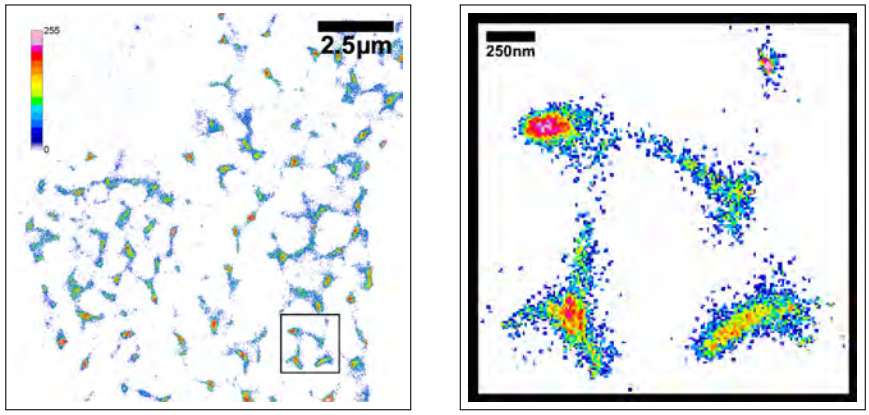

Figure 4.66: Computed *d*STORM image of a HEK 293T cell, Doxicycline induced for 24 h. Clusters are frequency coded. Left: complete area, right: enlarged area of four clusters.

Here, the computed DNaseX locations are coded for their appearance within the *d*STORM movie, thus temporally.

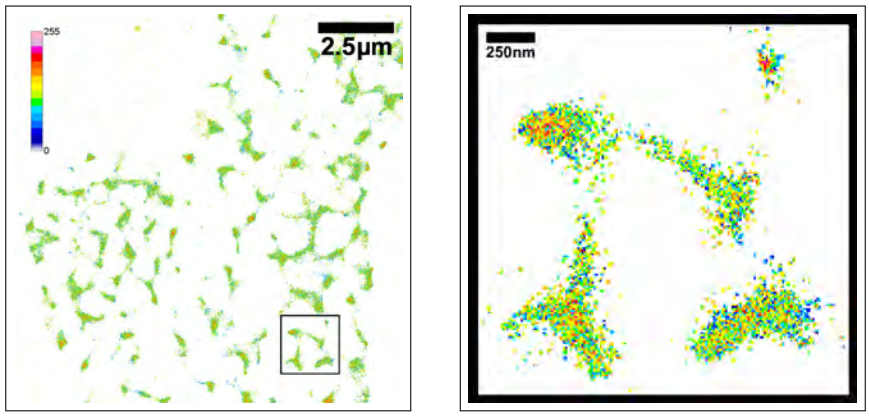

Figure 4.67: Computed *d*STORM image of a HEK 293T cell, Doxicycline induced for 24 h. Clusters are temporally coded. Left: complete area, right: enlarged area of four clusters.

The homogeneous distribution of calibration bar colors in the familiar clus-

ters proves the stability of the microscopic setup, the fixed position of the molecules and therefore the true existence of these clusters. The size of these clusters ranges from about 100 to 500 nm in this example, while they tend to be a lot smaller in other samples (cf. Appendix C.3). Bearing the GPI-anchor and biological relevance of DNaseX in mind, this could be a first evidence for a DNaseX localization in lipid rafts [230] and their suggested task to hinder foreign DNA from entering the cell membrane [43, 231, 232].

5 Conclusion and Outlook

Next to their important tasks in many aspects of every day life and their role in the functioning of any biological process, enzymes have been associated with an immense number of severe diseases within the past decades, including the most harmful sanitary harassments of HIV infection, stroke, heart disease and cancer [1–27]. The important, complex and versatile research field of enzymology, therefore, has keenly been approached with a high number of investigation techniques. Amongst many conventional methods, the fluorescence based approach is least invasive to the enzymes. Most common methods in this field include the rather insensitive Western Blot [157, 233] and the intensity amplified ELISA [234–236]. These approaches suit well for the simple detection of an enzyme up to a quantification of different enzyme concentrations. However, very small amounts of enzyme, that most often suffice to cause physical and medical reactions in biological systems, cannot be detected with these approaches. Furthermore, an examination of enzyme activities, that can be used as information about disease severeness and treatment success, is not feasible. In this work, two promising approaches of fluorescence based enzyme research to these tasks were presented and evaluated for several members of the enzyme class of hydrolases.

Carboxypeptidase A, acting on peptide bonds, except to those bridging arginine, proline and hydroxyproline [65], is a pancreatic enzyme, that is widely known and incorporated in enzyme research [57, 65, 237–242]. Furthermore, Carboxypeptidase A can be used as supplement in specific enzyme detection systems, taking advantage of its particular amino acid disfavor and its exopeptidic characteristics [31] (see section 2.4.2.1).

DNaseI and its close relative DNaseX have been widely associated with diseases like systemic lupus erythematosus and various cancer types [3–24]. For medical analyses it can be crucial, to discriminate these nucleases from each other. This is not easily possible, because they share a lot of characteristics [39]. For a detailed differentiation, also DNaseII and S1-Nuclease were accounted into this study (see section 2.4.2.2).

The first presented fluorescence based enzyme research approach utilized special **fluorescent substrates**, which differ from established colorimetric substrates [47,161,185–192, amongst others] by their exploitation of intrinsic electron donating properties of the naturally occurring amino acid tryptophan and the nucleic acid guanosine (see section 2.2.2) [28–34].

Six different peptide substrates for Carboxypeptidase A research were examined, which all carry MR 121 at the N-terminus. C-terminally, up to three tryptophans were attached, resulting in different fluorescence intensities. Labeled monopeptides showed relative fluorescence quantum yields of 1.52 for MR 121 - Phe and 0.01 for MR 121 - Trp. Spacing the fluorophore and the quencher by one amino acid, raised the quantum yield to 0.18 for MR 121 - Gly - Trp and 0.33 for MR 121 - Phe - Trp. Additional tryptophans reduced this yield to 0.17 for MR 121 - Phe - $(Trp)_2$ and 0.09 for MR 121 - Phe - $(Trp)_3$. All peptide probes showed an absorption maximum around 664 nm and an emission maximum around 684 nm. These maxima were slightly red-shifted to those of free MR 121. Additionally, MR 121 - Phe - $(Trp)_3$ showed a distinctly increased absorption around 615 nm. The attachment of amino acids to MR 121 also resulted in differing variations of thermal characteristics. While MR 121 - Trp equaled free MR 121 thermal behavior, MR 121 - Phe, MR 121 - Gly - Trp and MR 121 - Phe - Trp showed decreases in fluorescence intensity with rising temperatures. MR 121 - Phe - $(Trp)_2$ and MR 121 - Phe - $(Trp)_3$ ultimately showed strong increases in fluorescence intensities (see section 4.1.1).

Once, the peptide substrates were processed by Carboxypeptidase A, the cleaved tryptophan residues diffused away from the fluorophore, disabling the quenching mechanism. The fluorescence intensity immediately rose, while it stayed constant in samples without enzyme. The observed increase in fluorescence intensity mostly correlated directly with the examined relative fluorescence quantum yields. MR 121 - Trp was processed too slowly to finish observation within a reliable measurement period. MR 121 - Gly - Trp and MR 121 - Phe - Trp procession was overrun by MR 121 - Phe - $(Trp)_3$ hydrolysis. The fastest signal that could be obtained was achieved by cleavage of MR 121 - Phe - $(Trp)_2$. Kinetic measurements on MR 121 - Phe did not show any remarkable variation in fluorescence intensity. HPLC measurements revealed, though, that MR 121 - Phe could indeed be cleaved very slowly by Carboxypeptidase A. MR 121 - Phe - Trp was found to be processed at both possible cleavage sites in an essentially stepwise manner. MR 121 - Gly - Trp, though, was solely cleaved into MR 121 - Gly and free tryptophan. This sub-

strate, therefore, represents the ideal Carboxypeptidase A peptide probe (see section 4.1.2).

Thus, MR 121 - Gly - Trp was utilized to examine, whether the attached fluorophore hampers the acceptance by the enzyme and its velocity. The time constants of Carboxypeptidase A on samples with different ratios of MR 121-labeled and unlabeled Gly - Trp revealed, that the enzyme indeed favored the unlabeled Gly - Trp (see section 4.1.4).

Reaction kinetics of MR 121 - Gly - Trp and Carboxypeptidase A at different temperatures displayed the thermal preferences of this peptidase. The higher the temperature, the faster the substrate was processed. In this general course, several local activity maxima were found at 25°C, 40°C and around 60°C. The high activity at 25°C affirmed the published enzyme preference [68,210], while an activity maximum at 40°C could be explained by the bovine pancreatic enzyme source. Since further measurements confirmed the unexpected local maximum around 60°C, a new optimum reaction temperature for bovine Carboxypeptidase A on MR 121 - Gly - Trp has to be approved (see section 4.1.5).

A last application of MR 121 - Gly - Trp on Carboxypeptidase A qualitatively proved the general suitability of fluorescent substrates for enzyme research on a single molecular scale. Enzymes were bound to a BSA-covered surface and localized by their linker label. As soon as the substrate was added to the sample, fluorescence signal bursts in correlation to the Carboxypeptidase A positions occurred (see section 4.1.6).

For nuclease research, several *smart probes* were developed. These DNA hairpins carry Atto 655 fluorophores at the 5'-end and several guanosine residues at the 3'-end of their nucleotide sequence. By examination of the commercially available substrate 'DNaseAlert' the general predominance of the *smart probes* was shown, since this substrate was processed by all examined nucleases and can not be modified in its acceptance nor its spectral range (see section 4.1.2).

The first set of *smart probes* was dedicated to the research on the effect of sequence variations, stem-to-loop-ratio differences and changes in the methylation patterns. All examined DNA hairpins showed a 5 nm red-shift in absorption and emission maxima to free Atto 655. The computationally determined melting temperatures of 59.6°C ($SP2_{AL}{}^{mM}$) to 82.9°C (SP1) were generally found to be lower than the experimentally examined values by sev-

eral degrees. Relative quantum yields of these substrates varied from 0.14 for the best quenched *smart probe*, $SP2^{CM}$, to 0.37 for $SP2_{AL}$, proving that a N4-Methyl dC modification in close proximity to Atto 655 has an additional quenching effect. Furthermore, the ordinary base pairing of methylated bases with their nucleic acid matches, and a decreased stability of a hairpin with an adenine loop in contrast to an equivalent loop of only thymines was shown (see section 4.1.1).

The utilized *smart probes* were proved to stably fluoresce in absence of enzyme, while they distinctly rose immediately upon the addition of a nuclease. Small sequence variations, thereby, efficiently changed enzyme velocities, uniquely for each specific nuclease. While DNaseI, DNaseII and S1-Nuclease preferred a DNA hairpin with a comparably large loop and small stem (SP4), DNaseX processed a *smart probe* with small loop and long stem (SP2) fastest. The applied modifications on this *smart probe* revealed a preferation of DNaseX for methylation patterns and a disfavor for adenine loops. DNaseI on the other hand revealed a differentiated reaction to methylations. It was specifically attracted to a single N4-Methyl dC and completely disregarded single N6-Methyl-2'-dA modifications. Several methylations in one *smart probe* were not favored by this nuclease. For DNaseI research, $SP2^{CM}$ generates the ideal substrate, while $SP2^{AM}$ represents the optimal candidate for DNaseX investigations (see section 4.1.2).

Since $SP2^{CM}$ is the most efficiently quenched *smart probe* utilized in this work and it is simultaneously greatly processed and accepted by all nucleases, it was used as a model substrate for the examination of quenching variation consequences. The substitution of Atto 655 and the additional attachment of a dark quencher yielded a FRET quenched hairpin ($SP2^{CM}$-FRET), which was efficiently quenched and faster processed by every examined nuclease. This behavior led to the assumption, that Atto 655 is specifically unfavored by all utilized enzymes. S1-Nuclease kinetics, furthermore, revealed a procession of the attached fluorophore or a cleavage of the label bond. In general, $SP2^{CM}$-FRET could not compete with the according PET probe, because it offered only little advantages but bore a high number of disadvantages that FRET samples commonly suffer from (see section 4.1.1 and section 4.1.2).

The second set of utilized *smart probes* consisted of an assembly of three substrates, designed to reveal cleavage site preferences in respect to double and single stranded domains. These *smart probes* showed long range energy transfer as detected by their relative quantum yields of 0.26 to 0.95 and their

thermal fluorescence dependencies (see section 4.1.1). Fluorescence kinetics upon known double and single stranded scissions displayed the complexity of nucleolytic processes, because the substrates did not show exactly the expected fluorescence intensity profile. Therefore, it turned out that this set of *smart probes* is not feasible for the determination of an unknown reaction preference (see section 4.1.2).

Smart probes were shown to be widely applicable in a high number of various enzyme research tasks. The general feasibility of these substrates for Michaelis-Menten examinations was presented with SP4, processed by S1-Nuclease. The evaluation with three different enzyme concentrations revealed, that there are global difficulties at the fluorescence based determination of Michaelis-Menten constants higher than $2 \cdot 10^{-6}$ M, (see section 4.1.3).

The exemplary investigation on the effect of the attached fluorophore to acceptance and kinetics of an enzyme, which could be utilized to circumvent the problems in the determination of Michaelis-Menten constants, was accomplished with DNaseI and SP2. Time constants, that were derived from enzyme kinetics on samples of various ratios of labeled to unlabeled hairpin, proved that DNaseI favors unlabeled substrates (see section 4.1.4).

SP2 and its counterpart SP4 served for an evaluation of ideal working temperatures of DNaseI and DNaseX. Single enzyme kinetics at various temperatures offered maximum substrate conversion at 50°C for DNaseI and at 56°C for DNaseX. A new approach for the investigation of ideal temperatures, that was presented in this work, covered a wide thermal range in a minimum of time by utilization of the steady state kinetics only. By this means, the temperature optimum for DNaseX was approved, while it could be more closely defined for DNaseI. The introduced steady state method was successfully used for the determination of ideal temperature settings with fluorescent substrates and can also be used for the examination of buffer preferences, activator concentrations and inhibition processes (see section 4.1.5).

The suitability of *smart probes* in complex environments was shown in living cells with several DNA hairpins. These substrates did not pass cell membranes themselves, but showed distinct activities on lysed cells. When attached to a cell-penetrating peptide, $SP2^{CM}$ was capable of entering the cell, and the uptake was accelerated by pyrenebutyrate and aided by G-Actin, which inhibits extracellular DNaseI.

In a nutshell, *smart probes* proved to be a highly versatile, efficient and

adjustable tool for the research on enzyme activities. The only drawback of this approach occurs for non-specifically working enzymes in heterogeneous environments, because there, increases in fluorescence intensity do not necessarily reveal enzyme activities. The general predominance of unlabeled substrate for Carboxypeptidase A as well as for DNaseI and the preference of $SP2^{CM}$-FRET over $SP2^{CM}$ for any nuclease, suggested a broad animosity of hydrolases against the utilized oxazine derivatives, which can be easily examined by testing the acceptance of DNA hairpins, carrying other fluorophores for either FRET or PET quenching.

The presented second approach for fluorescence based enzyme research was completely focused on DNaseX detection. The **immunostaining** method utilized specific primary antibodies, that were bound to intracellular DNaseX. The incubation with labeled secondary antibody resulted in the efficient detection of DNaseX.

In a first examination it was found, that the cell viability at primary antibody incubation does not have an effect on labeling efficiency. The secondary antibody staining worked with live as well as fixed cells, but harmed several compartments of live cells (see section 4.2). To avoid this problem and to allow intracellular accumulation of primary and secondary antibody, the fixation was, furthermore, destined to the very beginning of the labeling protocol.

This optimized labeling strategy was then used for a variety of native cells (see section 4.2.2). The brain neuroblastoma cell line SK-N-MC was not found to carry DNaseX. A-549 (lung carcinoma), ECV-304 (urinary bladder carcinoma) and HeLa (cervix carcinoma) cell lines only showed little signal correlated to DNaseX presence. Three individual colon cancer cell lines (LS-174T, SW-837 and HT-29) revealed distinct DNaseX signal.

The largest proportion of detected DNaseX molecules was generally membrane bound, affirming the assumed task to provide a barrier for foreign DNA to enter the cell [43]. Other localizations of DNaseX were concentrated in the nucleus, which is astonishing due to its missing nuclear localization signal [41] and its revealed unspecific DNA degradation. This could therefore indicate the precise connection between DNaseX occurrence and those diseases with a disturbed apoptose mechanism. Furthermore, large areas completely filled with DNaseX and very heterogeneous distributions on the membranes and in between individual cells were found.

Specially transfected human embryonic kidney cell lines were shown to

carry a DNaseX level that correlates with the expression trigger induction duration (see section 4.2.3). This connection was further evaluated with the high resolved *d*STORM method (see section 4.2.4). Here, an intrinsic enzyme level was revealed for the transfected HEK cells. Furthermore, the examined enzyme was disclosed to form clusters with a diameter up to 500 nm on the membrane, that built a first hint for DNaseX localization in lipid rafts [232].

Enzyme research based on immunostaining was shown to constitute an efficient labeling strategy for DNaseX, which can be applied on any immobilized enzyme and investigated by a variety of different microscopy methods, e.g. high resolution techniques. The latter application will be of highest impact to microscopic as well as enzymatic research, because cellular structures like lipid rafts are too small to be observed with a standard microscope. With a counterstaining of cholesterol [232], colocalizations of DNaseX and lipid rafts could be easily revealed. Furthermore, localization patterns of DNaseX on native cell lines can be highly resolved and examined for colocalizations.

Due to their nature, the two presented fluorescent approaches for enzyme research highly differ in their preparation, suitability and obtainable results. While an active enzyme is crucial for the utilization of fluorescent substrates, no activity can be visualized by immunostaining. On the other hand, an enzyme localization, which is easily possibly with labeled detection antibodies, is not feasible with fluorescent substrates in heterogeneous environments. Therefore, these approaches perfectly complement each other.

An ideal, universal solution would combine these two features into a single method without their intrinsic disadvantages. This, indeed, can be achieved by the incorporation of streptavidin coated, magnetic beads. These can efficiently bind biotinylated, specific antibody. The enzymatic antigen can then be captured in heterogeneous samples like blood or cell lysis. In a washing step, the magnetic properties of the bead can be used to efficiently remove unbound capture antibodies and enzyme. Now, a labeled and specific detection antibody can be added to the sample, which allows the quantification of the protein of interest in a specific volume [243–245]. Instead of a detection antibody addition, also fluorescent substrates can be added to the sample. These are then processed if the enzyme is still active when bound to the

antibody[1]. Consequently, the concentration as well as the specific activity of the enzyme in question, 'fished' out of a heterogeneous sample, can be easily monitored on a standard widefield fluorescence microscope, yet even a fluorescence microplate reader.

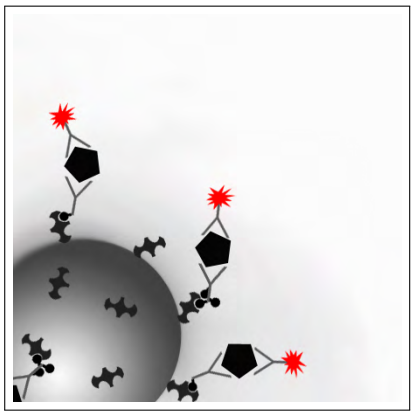

a) Enzyme quantification with detection antibodies

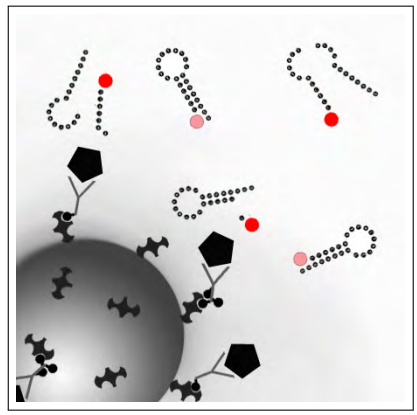

b) Enzyme activity analysis with fluorescent substrates

Figure 5.1: Schematic structure of bead based enzyme research. Specific enzyme antibodies are captured onto a bead due to the strong Biotin-Streptavidin affinity. After the antibody-antigen coupling, either labeled detection antibody (a)) is added for a sensitive enzyme quantification or fluorescent substrates (b)) are added for the investigation on enzyme activities.

[1]This activity has indeed been examined for antibody bound DNaseX.

Bibliography

[1] Sarkar I. et al. HIV-1 proviral DNA excision using an evolved recombinase. *Science (New York, N.Y.)*, 2007. 316(5833):1912–1915.

[2] Hanna R.A. et al. Calcium-bound structure of calpain and its mechanism of inhibition by calpastatin. *Nature*, 2008. 456(7220):409–412.

[3] Avall Lundqvist E.H. et al. Initial experiences with serum alkaline DNase activity in monitoring the effects of therapy for carcinoma of the uterine cervix. *Eur J Cancer*, 1991. 27(10):1313–1315.

[4] Basso D. et al. Serum deoxyribonuclease and ribonuclease in pancreatic cancer and chronic pancreatitis. *Tumori*, 1985. 71(6):529–532.

[5] Basso D. et al. Deoxyribonuclease I serum activity in pancreatic cancer. *Bull Cancer*, 1990. 77(4):385–387.

[6] Chan K.C. et al. Molecular characterization of circulating EBV DNA in the plasma of nasopharyngeal carcinoma and lymphoma patients. *Cancer Res*, 2003. 63(9):2028–2032.

[7] Del Favero G. et al. Ribonucleases and deoxyribonucleases in pancreatic cancer: clinical value and pathophysiological interrelationships. *Int J Pancreatol*, 1988. 3:107–112.

[8] Dewez B. et al. Serum alkaline deoxyribonuclease activity, a sensitive marker for the therapeutic monitoring of cancer patients: methodological aspects. *Eur J Clin Chem Clin Biochem*, 1993. 31(11):793–797.

[9] Economidou-Karaoglou A. et al. Variations in serum alkaline DNase activity in rats during growth and treatment of tumors sensitive or resistant to therapy. *Int J Cancer*, 1989. 43(5):956–959.

[10] Economidou-Karaoglou A. et al. Variations in serum alkaline DNase activity. A new means for therapeutic monitoring of malignant lymphomas. *Cancer*, 1988. 61(9):1838–1843.

[11] Fraser M.J. et al. Endo-exonuclease of human leukaemic cells: Evidence for a role in apoptosis. *Journal of Cell Science*, 1996. 109:2343–2360.

[12] Larmonier N. et al. An atypical caspase-independent death pathway for an immunogenic cancer cell line. *Oncogene*, 2002. 21(39):6091–6100.

[13] Linardou H. et al. Deoxyribonuclease I (DNase I). A novel approach for targeted cancer therapy. *Cell Biophys*, 1994. 24-25:243–248.

[14] Lykourinas M. et al. The role of acid and alkaline DNases as tumour markers in cancer of the genitourinary tract. *Urol Res*, 1982. 10(2):67–70.

[15] Patel P.S. et al. Evaluation of serum alkaline DNase activity in treatment monitoring of head and neck cancer patients. *Tumour Biol*, 2000. 21(2):82–89.

[16] Ramandanis G. et al. Correlation between serum and tissue deoxyribonuclease levels in breast cancer patients. *Anticancer Res*, 1982. 2(4):213–218.

[17] Raval G.N. et al. Role of sialic acid and alkaline DNase in breast cancer. *Int J Biol Markers*, 1997. 12(2):61–67.

[18] Roullet B. et al. Possible value of variations in the serum alkaline DNAse activity in the prognosis of cancers of the upper respiratory-digestive tract treated by chemotherapy. *Bull Cancer*, 1990. 77(7):675–680.

[19] Scully C. et al. Serum alkaline deoxyribonuclease in oral cancer and premalignant lesions. *Biomedicine*, 1981. 35(6):179–180.

[20] Spandidos D.A. et al. Serum deoxyribonucleases in patients with breast cancer. *Eur J Cancer*, 1980. 16(12):1615–1619.

[21] Sulitzeanu D. et al. Immune complex-like materials in sera of patients with breast cancer: detection by complement-consumption assay. *Isr J Med Sci*, 1981. 17(9-10):869–873.

[22] Taper H. et al. Variations in serum alkaline DNase activity: a possible clinical test for therapeutic prognosis of human tumors. *Anticancer Res*, 1986. 6(5):949–956.

[23] Tsou K.C. et al. Nucleases and adenosine 3',5'-cyclic monophosphate phosphodiesterase activities in murine sarcoma virus (Moloney)-infected mice. *J Natl Cancer Inst*, 1978. 61(4):1077–1083.

[24] Watanabe H. et al. Apoptosis of a fibrosarcoma induced by protein-free culture involves DNA cleavage to large fragments but not internucleosomal fragmentation. *Int J Cancer*, 1995. 62(2):191–198.

[25] Gillis A.J. et al. Structure of the Tribolium castaneum telomerase catalytic subunit TERT. *Nature*, 2008. 455(7213):633–637.

[26] Lee K.N. et al. A novel plasma proteinase potentiates {alpha} 2-antiplasmin inhibition of fibrin digestion. *Blood*, 2004. 103(10):3783–3788.

[27] Lu X. et al. The Wip1 phosphatase acts as a gatekeeper in the p53-Mdm2 autoregulatory loop. *Cancer Cell*, 2007. 12(4):342–354.

[28] DeFilippis et al. Electrochemical properties of tyrosine phenoxy and tryptophan indolyl radicals in peptides and amino acid analogues. *J Phys Chem*, 1991. 93:3416–3419.

[29] Wagenknecht H.A. Evidence of electron transfer from peptides to DNA: Oxidation of DNA-bound tryptophan using the flash-quench technique. *Journal of the American Chemical Society*, 2000. 122(1):1–7.

[30] Marme N. et al. Inter- and intramolecular fluorescence quenching of organic dyes by tryptophan. *Bioconjug Chem*, 2003. 14(6):1133–1139.

[31] Marme N. et al. Highly sensitive protease assay using fluorescence quenching of peptide probes based on photoinduced electron transfer. *Angew Chem Int Ed Engl*, 2004. 43(29):3798–3801.

[32] Heinlein T. et al. Photoinduced electron transfer between fluorescent dyes and guanosine residues in DNA-hairpins. *Journal of Physical Chemistry B*, 2003. 107(31):7957–7964.

[33] Piestert O. et al. A Single-Molecule Sensitive DNA Hairpin System Based on Intramolecular Electron Transfer. *Nano Lett*, 2003. 3:979–982.

[34] Buschmann V. et al. Spectroscopic study and evaluation of red-absorbing fluorescent dyes. *Bioconjugate Chemistry*, 2003. 14(1):195–204.

[35] Heilemann M. et al. Subdiffraction-resolution fluorescence imaging with conventional fluorescent probes. *Angew. Chemie. Int. Ed*, 2008. 47:6172–6176.

[36] Altermark B. et al. The structure of Vibrio cholerae extracellular endonuclease I reveals the presence of a buried chloride ion. *Acta Crystallographica Section D: Biological Crystallography*, 2006. 62(11):1387–1391.

[37] Coy J.F. et al. Isolation, differential splicing and protein expression of a DNase on the human X chromosome. *Cell death and differentiation*, 1996. 3(2):199–206.

[38] Los M. et al. Functional characterization of DNase X, a novel endonuclease expressed in muscle cells. *Biochemistry*, 2000. 39(25):7365–7373.

[39] Shiokawa D. and Tanuma S. Characterization of human DNase I family endonucleases and activation of DNase gamma during apoptosis. *Biochemistry*, 2001. 40(1):143–152.

[40] Poustka A. and Coy J.F. Murine DNase X, pharmaceuticals containing thereof and non-human mammal with modified DNase X-gene, 2002. URL `http://www.freepatentsonline.com/EP1249495A1.html`.

[41] Shiokawa D. et al. Identification of two functional nuclear localization signals in DNase gamma and their roles in its apoptotic DNase activity. *The Biochemical journal*, 2003. 376(Pt 2):377–381.

[42] Shiokawa D. et al. Physical and biochemical properties of mammalian DNase X proteins: non-AUG translation initiation of porcine and bovine mRNAs for DNase X. *Biochemical Journal*, 2005. 392:511–517.

[43] Shiokawa D. et al. DNaseX is a glycosylphosphatidylinositol-anchored membrane enzyme that provides a barrier to endocytosis-mediated transfer of a foreign gene. *Journal of Biological Chemistry*, 2007. 282(23):17132–17140.

[44] Beck T. et al. Quantitative fluorescence spectroscopy for the detection of cancer-specific enzymatic activity. *Medical Laser Application*, 2009. 24(2):126.

[45] Minta A. et al. Fluorescent indicators for cytosolic calcium based on rhodamine and fluorescein chromophores. *Journal of Biological Chemistry*, 1989. 264(14):8171.

[46] Li J.J. et al. Molecular beacons: a novel approach to detect protein-DNA interactions. *Inorg. Chem*, 1994. 33:4370–4375.

[47] Li J.J. et al. Using molecular beacons as a sensitive fluorescence assay for enzymatic cleavage of single-stranded DNA. *Nucleic acids research*, 2000. 28(11):E52.

[48] Monici M. Cell and tissue autofluorescence research and diagnostic applications. *Biotechnol Annu Rev*, 2005. 11:227–256.

[49] Lakowicz J.R. *Principles of fluorescence spectroscopy*. SPRINGER, New York, NY, 3. ed. edn., 2006.

[50] Sauer M. et al. New fluorescent dyes in the red region for biodiagnostics. *Journal of Fluorescence*, 1995. 5(3):247–261.

[51] Knemeyer J.P. et al. Probes for detection of specific DNA sequences at the single-molecule level. *Anal Chem*, 2000. 72(16):3717–3724.

[52] Marmé N. et al. A fluorescence-based assay for exopeptidases using self-quenching peptide probes with single-molecule sensitivity.

[53] Neuweiler H. and Sauer M. Using photoinduced charge transfer reactions to study conformational dynamics of biopolymers at the single-molecule level. *Curr Pharm Biotechnol*, 2004. 5(3):285–298.

[54] Henkenjohann S. et al. Photoinduced electron transfer (PET)-probes for the study of enzyme activity at the ensemble and single molecule level. *Proceedings of SPIE*, 2007. 6633(1):663323–663323–10.

[55] Henkenjohann S. and Sauer M. Photoinduced electron transfer probes for the observation of enzyme activities. *Proceedings of SPIE*, 2009. 7185(1):718503–718503–10.

[56] Doose S. et al. Fluorescence quenching by photoinduced electron transfer: a reporter for conformational dynamics of macromolecules. *Chemphyschem*, 2009. 10(9-10):1389–1398.

[57] Allan B.J. et al. Procedures for the Isolation of crystalline bovine pancreatic Carboxypeptidase A. Isolation from acetone from acetone powders of pancreas glands. *Biochemistry*, 1964. 3:40–44.

[58] Davies D.R. The Structure and Function of the Aspartic Proteinases. *Annual Review of Biophysics and Biophysical Chemistry*, 1990. 19(1):189–215.

[59] Brik A. and Wong C.H. HIV-1 protease: mechanism and drug discovery. *Organic & biomolecular chemistry*, 2003. 1(1):5–14.

[60] Jaskolski M. et al. Structure at 2.5-A resolution of chemically synthesized Human Immunodeficiency Virus Type 1 protease complexed with a hydroxyethylene-based inhibitor. *Biochemistry*, 1991. 30(6):1600–1609.

[61] Stebbins J. and Debouck C. Expression systems for retroviral proteases. *Methods in enzymology*, 1994. 241:3–16.

[62] Tomasselli A.G. and Heinrikson R.L. Specificity of retroviral proteases: an analysis of viral and nonviral protein substrates. *Methods in enzymology*, 1994. 241:279–301.

[63] Ozer N. et al. Substrate specificity in HIV-1 protease by a biased sequence search method. *Proteins: Struct Func Bioinfor*, 2006. 64:444–456.

[64] Ludwig M.L. and Lipscomb W.N. Carboxypeptidase A and other peptidases. *Inorganic Biochemistry*, 1973. 1:438–487.

[65] Christianson D.W. and Lipscomb W.N. Carboxypeptidase A. *Acc. Chem. Res.*, 1989. 22:62–69.

[66] Petra P.H. Bovine procarboxypeptidase and Carboxypeptidase A. *Acc. Chem. Res.*, 1970. 19:460–503.

[67] Lipscomb W.N. Enzymatic Activities of Carboxypeptidase A's in Solution and in Crystals. *Proc. Natl. Acad. Sci. USA*, 1973. 70(12, Part II):3797–3801.

[68] Lipscomb W.N. Carboxypeptidase A mechanisms. *Proceedings of the National Academy of Sciences of the United States of America*, 1980. 77(7):3875–3878.

[69] Sternberger L.A. Immunhistochemistry, 1979.

[70] van Weeman B.K. and Schuurs A. Immunoassay using antigen-enzyme conjugates. *FEBS Letter*, 1971. 15:232–235.

[71] Engvall E. and Perlmann P. Enzyme-linked immunosorbent assay (ELISA). Quantitative assay of immunoglobulin G. *Immunochemistry*, 1971. 8(9):871–874.

[72] Lequin R.M. Enzyme immunoassay (EIA)/enzyme-linked immunosorbent assay (ELISA). *Clinical Chemistry*, 2005. 51(12):2415–2418.

[73] Voller A. et al. Enzyme immunoassays in diagnostic medicine. *Bull. WHO*, 1976. 53:55–65.

[74] O'Connor T. and Gosling J.P. The dependence of radioimmunoassay detection limits on antibody affinity. *Journal of immunological methods*, 1997. 208(2):181–189.

[75] Hell S.W. and Wichmann J. Breaking the diffraction resolution limit by stimulated emission: stimulated-emission-depletion fluorescence microscopy. *Optics Letters*, 1994. 19(11):780–782.

[76] Rust M.J. et al. Sub-diffraction-limit imaging by stochastic optical reconstruction microscopy (STORM). *Nature methods*, 2006. 3(10):793–795.

[77] Bayliss N.S. and McRae E.G. Solvent Effects in Organic Spectra: Dipole Forces and the Franck Condon Principle. *The Journal of Physical Chemistry*, 1954. 58(11):1002–1006.

[78] Haken H. and Wolf H.C. *Molekülphysik und Quantenchemie: Einführung in die experimentellen und theoretischen Grundlagen*. Springer-Lehrbuch. Springer-Verlag, Berlin, Heidelberg, fünfte auflage. edn., 2006.

[79] Tsien R.Y. The green fluorescent protein. *Annu Rev Biochem*, 1998. 67:509–544.

[80] Tsien R.Y. Die Farbpalette der fluoreszierenden Proteine (Nobel-Vortrag). *Angew. Chem.*, 2009. 121:5721–5736.

[81] Morise H. et al. Intermolecular energy transfer in the bioluminescent system of Aequorea. *Biochemistry*, 1974. 13(12):2656–2662.

[82] Morin J.G. and Hastings J.W. Energy transfer in a bioluminescent system. *Journal of cellular physiology*, 1971. 77(3):313–318.

[83] Kautsky H. Quenching of luminescence by oxygen. *Transactions of the Faraday Society*, 1939. 35:216–219.

[84] Zander C. et al. Detection and characterization of single molecules in aqueous solution. *Applied Physics B: Lasers and Optics*, 1996. 63(5):517–523.

[85] Sauer M. et al. Dynamics of the electron transfer reaction between an oxazine dye and DNA oligonucleotides monitored on the single-molecule level. *Chemical Physics Letters*, 1998. 284(3-4):153–163.

[86] DeFelippis et al. Pulse radiolytic measurement of redox potentials: the tyrosine and tryptophan radicals. *Biochemistry*, 1989. 28(11):4847–4853.

[87] Torimura M. et al. Fluorescence-quenching phenomenon by photoinduced electron transfer between a fluorescent dye and a nucleotide base. *Analytical Sciences*, 2001. 17(1):155–160.

[88] Lewis F.D. et al. Dynamics of photoinduced charge transfer and hole transport in synthetic DNA hairpins. *Acc. Chem. Res*, 2001. 34(2):159–170.

[89] Dietrich A. et al. Fluorescence resonance energy transfer (FRET) and competing processes in donor–acceptor substituted DNA strands: a comparative study of ensemble and single-molecule data. *Reviews in Molecular Biotechnology*, 2002. 82(3):211–231.

[90] Neuweiler H. et al. Measurement of submicrosecond intramolecular contact formation in peptides at the single-molecule level. *Journal of the American Chemical Society*, 2003. 125(18):5324–5330.

[91] Kavarnos G.J. and H. H. *Fundamentals of Photoinduced Electron Transfer*. VCH, New York, 1993.

[92] Pina F. et al. Fluorescent chemosensors containing polyamine receptors. *European Journal of Inorganic Chemistry*, 2000. 2000(10):2143.

[93] de Silva A.P. et al. Signaling recognition events with fluorescent sensors and switches. *Chem. Rev*, 1997. 97(5):1515–1566.

[94] de Silva A.P. et al. The development of molecular fluorescent switches. *Trends in Biotechnology*, 2001. 19(1):29–34.

[95] Czarnik A.W. et al. Fluorescent chemosensors for ion and molecule recognition. *Instrumentation Science & Technology*, 1994. 22(4):405–406.

[96] Stryer L. Fluorescence energy transfer as a spectroscopic ruler. *Annual Review of Biochemistry*, 1978. 47(1):819–846.

[97] Campbell I.D. The Croonian lecture 2006. Structure of the living cell. *Philosophical transactions of the Royal Society of London. Series B, Biological sciences*, 2008. 363(1502):2379–2391.

[98] Rittweger E. et al. STED microscopy reveals crystal colour centres with nanometric resolution. *Nature Photonics*, 2009. (3):144–147.

[99] Heilemann M. et al. Carbocyanine dyes as efficient reversible single-molecule optical switch. *J. Am. Chem. Soc*, 2005. 127(11):3801–3806.

[100] Price N.C. and Stevens L. *Fundamentals of enzymology: The cell and molecular biology of catalytic proteins*. Oxford Univ. Press, Oxford, 3. ed., reprinted (twice) 2006. edn., 2006.

[101] Citri N. Conformational adaptability in enzymes. *Advances in enzymology and related areas of molecular biology*, 1973. 37:397.

[102] Pace C.N. Measuring and increasing protein stability. *Trends in biotechnology(Regular ed.)*, 1990. 8(4):93–98.

[103] Nozaki Y. and Tanford C. The solubility of amino acids and related compounds in aqueous urea solutions. *J. biol. Chem*, 1963. 238(12):4074–4081.

[104] Pace C.N. and Vanderburg K.E. Determining globular protein stability: guanidine hydrochloride denaturation of myoglobin. *Biochemistry*, 1979. 18(2):288–292.

[105] Roseman M. and Jencks W.P. Interactions of urea and other polar compounds in water. *J. Am. Chem. Soc.*, 1975. (97):631–640.

[106] Pace C.N. Determination and analysis of urea and guanidine hydrochloride denaturation curves. *Methods in enzymology*, 1986. 131:266–280.

[107] Jaenicke R. Folding and association of proteins. *European Biophysics Journal*, 1982. 8(4):231–256.

[108] Polaina J. and MacCabe A.P. *Industrial Enzymes: Structure, Function and Applications*. Springer Verlag, 2007.

[109] Loesche K. Enzymatic food preservation. *Lebensmitteltechnik (Germany, FR)*, 1991. 23(1-2):43–49.

[110] Fassy F. et al. Enzymatic activity of two caspases related to interleukin-1 beta-converting enzyme. *European Journal of Biochemistry*, 1998. 253(1):76–83.

[111] Bisswanger H. et al. *Enzyme kinetics: Principles and methods*. Wiley-VCH, Weinheim, 1. ed., 1. reprint. edn., 2004.

[112] Kow Y.W. and Wallace S.S. Mechanism of action of Escherichia coli endonuclease III. *Biochemistry*, 1987. 26(25):8200–8206.

[113] Shatton J.B. et al. Glucose (hexose 6-phosphate) dehydrogenase in liver of rainbow trout. *Journal of Biological Chemistry*, 1971. 246(15):4878–4885.

[114] Apweiler R. et al. UniProt: the Universal Protein knowledgebase. *Nucleic Acids Res.*, 2004. 32:D115–D119.

[115] Chang A. et al. BRENDA, AMENDA and FRENDA the enzyme information system: new content and tools in 2009. *Nucleic Acids Research*, 2008. (37):D588–D592.

[116] Barthelmes J. et al. BRENDA, AMENDA and FRENDA: the enzyme information system in 2007. *Nucleic Acids Research*, 2007. 35:D511–D514.

[117] Schomburg I. et al. BRENDA, the enzyme database: updates and major new developments. *Nucleic Acids Research*, 2004. 32:D431–D433.

[118] Pharkya P. et al. Review of the BRENDA Database. *Metabolic Engineering*, 2003. 5(2):71–73.

[119] Schomburg I. et al. BRENDA: a resource for enzyme data and metabolic information. *Trends in Biochemical Sciences*, 2002. 27(1):54–56.

[120] Schomburg I. et al. BRENDA, enzyme data and metabolic information. *Nucleic Acids Research*, 2002. 30(1):47–49.

[121] Schomburg D. et al. *Springer handbook of enzymes*. SPRINGER, Berlin, 2. ed. edn., 2004.

[122] Schomburg I. et al. Enzyme data and metabolic information: BRENDA, a resource for research in biology, biochemistry, and medicine. *Gene Function & Disease*, 2000. 1(3-4):109–118.

[123] Petra P.H. Bovine procarboxypeptidase and carboxypeptidase A. *Methods Enzymol*, 1970. 19:460–503.

[124] Park J.D. and Kim D.H. Sulfamide derivatives as transition state analogue inhibitors for carboxypeptidase A. *Bioorganic & medicinal chemistry*, 2004. 12(9):2349–2356.

[125] Dominguez-Muñoz J.E. et al. Quantification of pancreatic zinc output as pancreatic function test: making the secretin-caerulein test applicable to clinical practice. *Pancreatology*, 2004. 4(1):57–62.

[126] Kim D.H. Chemistry-based design of inhibitors for carboxypeptidase A. *Current Topics in Medicinal Chemistry*, 2004. 4(12):1217–1226.

[127] Kilshtain-Vardi A. et al. Refined structure of bovine carboxypeptidase A at 1.25 A resolution. *Acta Crystallographica Section D: Biological Crystallography*, 2003. 59(2):323–333.

[128] Hennig A. et al. Design of peptide substrates for nanosecond time-resolved fluorescence assays of proteases: 2,3-diazabicyclo[2.2.2]oct-2-ene as a noninvasive fluorophore. *Anal Biochem*, 2007. 360(2):255–265.

[129] Vertesi A.e.a. Preparation, characterization and application of immobilized carboxypeptidase A. *Enzyme and Microbial Technology*, 1999. 25:73–79.

[130] Ambler R.P. Carboxypeptidases A and B. *Methods Enzymol*, 1967. 11:436–445.

[131] Aalten D.M.F. et al. Crystal Structure of Carboxypeptidase A Complexed with D-Cysteine at 1.75 A-Inhibitor-Induced Conformational Changes. *Biochemistry-Columbus*, 2000. 39(33):10082–10089.

[132] Chong C.R. and Auld D.S. Inhibition of Carboxypeptidase A by d-Penicillamine: Mechanism and Implications for Drug Design. *Biochemistry*, 2000. 39(25):7580–7588.

[133] *Desoxyribonuclease I in: The Enzymes.* Academic Press, New York, 1971.

[134] de Maria A. and Arruti C. DNase I and fragmented chromatin during nuclear degradation in adult bovine lens fibers. *Mol Vis*, 2004. 10:74–82.

[135] Kreuder V. et al. Isolation, characterisation and crystallization of deoxyribonuclease I from bovine and rat parotid gland and its interaction with rabbit skeletal muscle actin. *Eur J Biochem*, 1984. 139(2):389–400.

[136] Cobianchi F. and Wilson S.H. Enzymes for modifying and labeling DNA and RNA. *Methods Enzymol*, 1987. 152:94–110.

[137] Moore S. Pancreatic DNase. *The enzymes*, 1981. 14:281–296.

[138] Chereau D. et al. Actin-bound structures of Wiskott–Aldrich syndrome protein (WASP)-homology domain 2 and the implications for filament assembly. *Proc Natl Acad Sci*, 2005. 102(46):16644–16649.

[139] Iwamori M. et al. Shedding of sulfated lipids into gastric fluid and inhibition of pancreatic DNase I by cholesterol sulfate in concert with bile acids. *BBA-Molecular and Cell Biology of Lipids*, 2000. 1487(2-3):268–274.

[140] Chen W.J. et al. Biological functions of the disulfides in bovine pancreatic deoxyribonuclease. *Protein Science: A Publication of the Protein Society*, 2004. 13(4):875–883.

[141] Ghosh S. and DasGupta U. Studies with endonuclease X: a new deoxyendonuclease of E. coli that preferentially cleaves supercoiled plasmid DNA. *Curr. Trends Life Sci*, 1984. 12:79–88.

[142] Appierto V. et al. Functional characterization of a human DNase-like protein encoded by a gene positioned in Xq28. *Gene*, 1997. 188(1):119–122.

[143] Parrish J.E. et al. Chen. E., and Nelson. DL (1995) A muscle-specific DNase I-like gene in human Xq28. *Hum. Mol. Genet.* 4:1557–1564.

[144] Bernardi G. Spleen acid deoxyribonuclease. *The enzymes*, 1971. 4:271–287.

[145] Keys D.S. and Zbarsky S.H. Isolation of deoxyribonuclease II from bovine intestinal mucosa. *Biochemistry and Cell Biology*, 1980. 58(9):749–753.

[146] Slor H. and Lev T. Acid deoxyribonuclease activity in purified calf thymus nuclei. *Biochemical Journal*, 1971. 123(5):993–995.

[147] Desai N.A. and Shankar V. Single-strand-specific nucleases. *Fems microbiology reviews*, 2002. 26(5):457–492.

[148] Till B.J. et al. Mismatch cleavage by single-strand specific nucleases. *Nucleic Acids Research*, 2004. 32(8):2632–2641.

[149] Romier C. et al. Recognition of single-stranded DNA by nuclease P1: high resolution crystal structures of complexes with substrate analogs. *Proteins: Structure, Function, and Bioinformatics*, 1998. 32(4):414–424.

[150] Lee S.P. et al. Characterization of endonucleolytic activity of HIV-1 integrase using a fluorogenic substrate. *Analytical Biochemistry*, 1995. 227(2):295–301.

[151] Bochkov D.V. et al. Hydrolytic approach for production of deoxyribonucleoside-and ribonucleoside-5 8242-monophosphates and enzymatic synthesis of their polyphosphates. *Biochemistry-New York-English Translation of Biokhimiya*, 2006. 71(1):79–83.

[152] Lehman R.I. Endonucleases specific for single-stranded polynucleotides. *The enzymes*, 1981. 4:193–201.

[153] Tang Y. et al. Direct visualization of enzymatic cleavage and oxidative damage by hydroxyl radicals of single-stranded DNA with a cationic polythiophene derivative. *Journal of the American Chemical Society*, 2006. 128(46):14972–14976.

[154] Sasaki Y. et al. Regulation of DNA nucleases by molecular crowding, 2007.

[155] Reddy L.G. and Shankar V. Immobilization of single-strand specific nuclease (S1 nuclease) from Aspergillus oryzae. *Applied biochemistry and biotechnology*, 1987. 14(3):231–240.

[156] Wiegand R.C. et al. Specificity of the S1 nuclease from Aspergillus oryzae. *The Journal of biological chemistry*, 1975. 250(22):8848–8855.

[157] Burnette W.N. 'Western Blotting': Electrophoretic transfer of proteins from sodium dodecyl sulfate-polyacrylamide gels to unmodified

nitrocellulose and radiographic detection with antibody and radioiodinated protein A. *Analytical Biochemistry*, 1981. 112(2):195–203.

[158] Cooper G.M. and Hausman R.E. *The cell: A molecular approach.* ASM Press [u.a.], Washington, DC, 3. ed. edn., 2004.

[159] Spector D.L. and Goldman R.D. *Basic methods in microscopy: Protocols and concepts from cells: a laboratory manual ; [basic light microscopy, confocal microscopy, deconvolution microscopy, multiphoton microscopy, labeling organelles, immunofluorescence, in situ hybridization, transmission electron microscopy, immunoelectron microscopy].* Cold Spring Harbor Laboratory Press, Cold Spring Harbor, NY, 2006.

[160] Bissell R.A. et al. Fluorescent PET (photoinduced electron transfer) sensors. *Topics in Current Chemistry*, 1993. 168:223–223.

[161] Medintz I.L.e.a. Proteolytic activity monitored by fluorescence resonance energy transfer through quantum-dot-peptide conjugates. *nature materials*, 2006. 5:581–589.

[162] Beck T. et al. A fluorescence diagnostic system detecting cancer-specific enzymatic activities: preliminary results. *Proceedings of SPIE*, 2009. 7169(1):71691G–71691G–6.

[163] Wagnieres G.A. et al. In vivo fluorescence spectroscopy and imaging for oncological applications. *Photochemistry and photobiology*, 1998. 68(5):603–632.

[164] Aubin J.E. Autofluorescence of viable cultured mammalian cells. *Journal of Histochemistry and Cytochemistry*, 1979. 27(1):36–43.

[165] Benson R.C. et al. Cellular autofluorescence–is it due to flavins? *The journal of histochemistry and cytochemistry: official journal of the Histochemistry Society*, 1979. 27(1):44–48.

[166] Biedler J.L. et al. Morphology and growth, tumorigenicity, and cytogenetics of human neuroblastoma cells in continuous culture. *Cancer research*, 1973. 33(11):2643–2652.

[167] Giard D.J. et al. In vitro cultivation of human tumors: establishment of cell lines derived from a series of solid tumors. *Journal of the National Cancer Institute*, 1973. 51(5):1417–1423.

[168] Takahashi K. et al. Spontaneous transformation and immortalization of human endothelial cells. *In vitro cellular & developmental biology : journal of the Tissue Culture Association*, 1990. 26(3 Pt 1):265–274.

[169] Takahashi K. and Sawasaki Y. Human endothelial cell line, ECV304, produces pro-urokinase. *In vitro cellular & developmental biology: journal of the Tissue Culture Association*, 1991. 27(10):766–768.

[170] Takahasi K. and Sawasaki Y. Rare spontaneously transformed human endothelial cell line provides useful research tool. *In Vitro Cellular & Developmental Biology-Animal*, 1992. 28(6):380–382.

[171] Gey G.O. et al. Tissue culture studies of the proliferative capacity of cervical carcinoma and normal epithelium. *Cancer Research*, 1952. 12(4):264–265.

[172] Scherer W.F. et al. Studies on the propagation in vitro of poliomyelitis viruses IV. Viral multiplication in a stable strain of human malignant epithelial cells (strain HeLa) derived from an epidermoid carcinoma of the cervix. *Journal of Experimental Medicine*, 1953. 97(5):695–710.

[173] Masters J.R. HeLa cells 50 years on: the good, the bad and the ugly. *Nature Reviews Cancer*, 2002. 2(4):315–319.

[174] Tom B.H. et al. Human colonic adenocarcinoma cells. *In Vitro Cellular & Developmental Biology-Plant*, 1976. 12(3):180–191.

[175] Leibovitz A. et al. Classification of human colorectal adenocarcinoma cell lines. *Cancer Research*, 1976. 36(12):4562–4569.

[176] Fogh J. et al. One hundred and twenty-seven cultured human tumor cell lines producing tumors in nude mice. *Journal of the National Cancer Institute*, 1977. 59(1):221–226.

[177] Fogh J. et al. Absence of HeLa cell contamination in 169 cell lines derived from human tumors. *Journal of the National Cancer Institute*, 1977. 58(2):209–214.

[178] Graham F.L. et al. Characteristics of a human cell line transformed by DNA from human adenovirus type 5. *The Journal of general virology*, 1977. 36(1):59–74.

[179] Zuker M. Mfold web server for nucleic acid folding and hybridization prediction. *Nucleic Acids Research*, 2003. 31(13):3406–3415.

[180] SantaLucia J. A unified view of polymer, dumbbell, and oligonucleotide DNA nearest-neighbor thermodynamics. *Proceedings of the National Academy of Sciences of the United States of America*, 1998. 95(4):1460–1465.

[181] Peyret N. Prediction of nucleic acid hybridization: parameters and algorithms, 2000.

[182] Abramoff M.D. et al. Image processing with ImageJ. *Biophotonics International*, 2004. 11(7):36–43.

[183] van de Linde S. et al. Subdiffraction-resolution fluorescence imaging of proteins in the mitochondrial inner membrane with photoswitchable fluorophores. *Journal of structural biology*, 2008. 164(3):250–254.

[184] Yifrach O. Hill coefficient for estimating the magnitude of cooperativity in gating transitions of voltage-dependent ion channels. *Biophysical journal*, 2004. 87(2):822–830.

[185] Moreau R.A. Regulation of phospholipase activity in potato leaves by calmodulin and protein phosphorylation dephosphorylation. *Plant science(Limerick)*, 1986. 47(1):1–9.

[186] Duque M. et al. New fluorogenic triacylglycerol analogs as substrates for the determination and chiral discrimination of lipase activities. *The Journal of Lipid Research*, 1996. 37(4):868–876.

[187] Izquierdo M.S. and Henderson R.J. The determination of lipase and phospholipase activities in gut contents of turbot (Scophthalmus

maximus) by fluorescence-based assays. *Fish Physiology and Biochemistry*, 1998. 19(2):153–162.

[188] Beisson F. et al. Use of naturally fluorescent triacylglycerols from Parinari glaberrimum to detect low lipase activities from Arabidopsis thaliana seedlings. *The Journal of Lipid Research*, 1999. 40(12):2313–2321.

[189] Samet D. and Barenholz Y. Characterization of acidic and neutral sphingomyelinase activities in crude extracts of HL-60 cells. *Chemistry and physics of lipids*, 1999. 102(1-2):65–77.

[190] Loidl A. et al. High-precision fluorescence assay for sphingomyelinase activity of isolated enzymes and cell lysates. *The Journal of Lipid Research*, 2002. 43(5):815–823.

[191] de Cremer G. et al. Dynamic disorder and stepwise deactivation in a chymotrypsin catalyzed hydrolysis reaction. *Journal of the American Chemical Society*, 2007. 129(50):15458–15459.

[192] Blank K. et al. Fluorescence-based analysis of enzymes at the single-molecule level. *Biotechnology journal*, 2009. 4(4):465–479.

[193] Shock E.L. Stability of peptides in high-temperature aqueous solutions. *Geochimica et Cosmochimica Acta*, 1992. 56:3481–3491.

[194] Chi E.Y. Physical stability of proteins in aqueous solution: Mechanism and driving forces in nonnative protein aggregation. *Pharmaceutical Research*, 2003. 20(9):1325–1336.

[195] Atkins P.W. et al. *Physikalische Chemie*. VCH Weinheim, 1990.

[196] Bryngelson J.D. et al. Funnels, pathways and the energy landscape of protein folding: a synthesis. *Journal reference: Proteins-Struct. Func. and Genetics*, 1995. 21:167–220.

[197] Onuchic J.N. et al. Theory of protein folding: the energy landscape perspective. *Annual review of physical chemistry*, 1997. 48(1):545–600.

[198] Rehm D. and Weller A. Kinetics of Fluorescence Quenching by Electron and H-Atom Transfer. *Israel Journal of Chemistry*, 1970. 8(2):259–272.

[199] Gray H.B. and Winkler J.R. Long-range electron transfer. *Biophysical journal*, 2005. 102(10):3534–3539.

[200] Fernandez-Rachubinski F. et al. Incorporation of 7-deaza dGTP during the amplification step in the polymerase chain reaction procedure improves subsequent DNA sequencing. *Mitochondrial DNA*, 1990. 1(2):137–140.

[201] Dimitrov R.A. and Zuker M. Prediction of hybridization and melting for double-stranded nucleic acids. *Biophysical journal*, 2004. 87(1):215–226.

[202] Markham N.R. and Zuker M. DINAMelt web server for nucleic acid melting prediction. *Nucleic Acids Research*, 2005. 33:W577–W581.

[203] Ghosh S.S. et al. Real time kinetics of restriction endonuclease cleavage monitored by fluorescence resonance energy transfer. *Nucleic Acids Research*, 1994. 22(15):3155–3159.

[204] Lee S.P. et al. A fluorometric assay for DNA cleavage reactions characterized with BamHI restriction endonuclease. *Analytical Biochemistry*, 1994. 220(2):377–383.

[205] Lee S.P. and Han M.K. Fluorescence assays for DNA cleavage. *Methods in enzymology*, 1997. 278:343–363.

[206] Jones G. et al. Intramolecular Electron Transfer across Amino Acid Spacers in the Picosecond Time Regime. Charge-Transfer Interaction through Peptide Bonds. *Journal of Physical Chemistry B*, 1999. 103:572–581.

[207] Bradshaw R.A.e.a. The Amino Acid Sequence of Bovine Carboxypeptidase A. *Biochemistry*, 1969. 63:1389–1394.

[208] Ren B.Z. et al. Straightforward detection of SNPs in double-stranded DNA by using exonuclease III/nuclease S1/PNA system. *Nucleic Acids Research*, 2004. 32(4):e42.

[209] Jaenisch R. and Bird A. Epigenetic regulation of gene expression: how the genome integrates intrinsic and environmental signals. *Nature genetics*, 2003. 33:245–254.

[210] Auld D.S. and Vallee B.L. Kinetics of Carboxypeptidase A. pH and Temperature Dependence of Tripeptide Hydrolysis. *Biochemistry*, 1971. 10(15):2892–2897.

[211] Barton G.M. and Medzhitov R. Retroviral delivery of small interfering RNA into primary cells. *Proceedings of the National Academy of Sciences*, 2002. 99(23):14943–14945.

[212] Cheung C.Y. et al. A pH-sensitive polymer that enhances cationic lipid-mediated gene transfer. *Bioconjugate Chem*, 2001. 12(6):906–910.

[213] Sokol D.L. et al. Real time detection of DNA - RNA hybridization in living cells. *Proceedings of the National Academy of Sciences of the United States of America*, 1998. 95(20):11538–11543.

[214] Yin D. and Tang J.G. Gene therapy for streptozotocin-induced diabetic mice by electroporational transfer of naked human insulin precursor DNA into skeletal muscle in vivo. *FEBS letters*, 2001. 495(1-2):16–20.

[215] Nitin N. et al. Peptide-linked molecular beacons for efficient delivery and rapid mRNA detection in living cells. *Nucleic Acids Research*, 2004. 32(6):e58.

[216] Lindgren M. and H\Ü. Cell-penetrating peptides. *Trends in Pharmacological Sciences*, 2000. 21(3):99–103.

[217] Wadia J.S. and Dowdy S.F. Protein transduction technology. *Current opinion in biotechnology*, 2002. 13(1):52–56.

[218] Derossi D. et al. Cell internalization of the third helix of the Antennapedia homeodomain is receptor-independent. *Journal of Biological Chemistry*, 1996. 271(30):18188–18193.

[219] Derossi D. et al. Trojan peptides: the penetratin system for intracellular delivery. *Trends in cell biology*, 1998. 8(2):84–87.

[220] Pooga M. et al. Cellular translocation of proteins by transportan. *The FASEB Journal*, 2001.

[221] Matsui H. et al. Protein Therapy: in vivo protein transduction by polyarginine (11R) PTD and subcellular targeting delivery. *Current Protein and Peptide Science*, 2003. 4(2):151–157.

[222] Jones S.W. et al. Characterisation of cell-penetrating peptide-mediated peptide delivery. *British Journal of Pharmacology*, 2005. 145(8):1093–1102.

[223] Rhee M. and Davis P. Mechanism of uptake of C105Y, a novel cell-penetrating peptide. *The Journal of biological chemistry*, 2006. 281(2):1233–1240.

[224] Kerkis A. et al. Crotamine is a novel cell-penetrating protein from the venom of rattlesnake Crotalus durissus terrificus. *Faseb Journal*, 2004.

[225] Thorén P.E.G. et al. Uptake of analogs of penetratin, Tat(48-60) and oligoarginine in live cells. *Biochemical and biophysical research communications*, 2003. 307(1):100–107.

[226] Yandek L.E. et al. Mechanism of the cell-penetrating peptide transportan 10 permeation of lipid bilayers. *Biophysical journal*, 2007. 92(7):2434–2444.

[227] Takeuchi T. et al. Direct and rapid cytosolic delivery using cell-penetrating peptides mediated by pyrenebutyrate. *ACS chemical biology*, 2006. 1(5):299–303.

[228] Takeshita H. et al. Mammalian deoxyribonucleases I are classified into three types: pancreas, parotid, and pancreas–parotid (mixed), based on differences in their tissue concentrations. *Biochemical and Biophysical Research Communications*, 2000. 269(2):481–484.

[229] Claxton N.S. et al. Staining Adherent Cells with Intermediate Filament Primary Antibodies and Synthetic Fluorophores, 2009. URL `http://www.olympusfluoview.com/applications/protocols/cellsintermediatefilaments.html`.

[230] Brown D.A. and Rose J.K. Sorting of GPI-anchored proteins to glycolipid-enriched membrane subdomains during transport to the apical cell surface. *Cell*, 1992. 68(3):533–544.

[231] Pike L.J. The challenge of lipid rafts. *Journal of lipid research*, 2009. 50 Suppl:323–328.

[232] Korade Z. and Kenworthy A.K. Lipid rafts, cholesterol, and the brain. *Neuropharmacology*, 2008. 55(8):1265–1273.

[233] Burnette W.N. Western blotting (Citation Classic). *Curr Contents*, 1991. 34(8).

[234] Engvall E. and Perlmann P. Enzyme-Linked Immunosorbent Assay, Elisa: III. Quantitation of Specific Antibodies by Enzyme-Labeled Anti-Immunoglobulin in Antigen-Coated Tubes. *J Immunol*, 1972. 109(1):129–135.

[235] Keren D.F. Enzyme-linked immunosorbent assay for immunoglobulin G and immunoglobulin A antibodies to Shigella flexneri antigens. *Infection and Immunity*, 1979. 24(2):441–448.

[236] Goldsby R.A. et al., eds. *Enzyme-linked immunosorbent assay.* 2003.

[237] Auld D.S. and Vallee B.L. Kinetics of Carboxypeptidase A. II. Inhibitors of the Hydrolysis of Oligopeptides. *Biochemistry*, 1970. 9(3):602–609.

[238] Chai J.J. et al. Crystal structure of carboxypeptidase A complexed with an inactivator in two crystal forms. *Protein Eng*, 1998. 11(10):841–845.

[239] Beck I.T. The role of pancreatic enzymes in digestion. *The American journal of clinical nutrition*, 1973. 26(3):311–325.

[240] Capocchi A. et al. Degradation of gluten by proteases from dry and germinating wheat (Triticum durum) seeds: An in vitro approach to storage protein mobilization. *Journal of agricultural and food chemistry*, 2000. 48(12):6271–6279.

[241] Lee M. et al. A mechanism-based inhibitor targeting the DD-transpeptidase activity of bacterial penicillin-binding proteins. *Journal of the American Chemical Society*, 2003. 125(52):16322–16326.

[242] Mesters J.R.e.a. Structure of glutamate Carboxypeptidase II, a drug target in neuronal damage and prostate cancer. *EMBO*, 2006. 25:1375–1384.

[243] N. B. Liabakk et al. A rapid and sensitive immunoassay for tumor necrosis factor using magnetic monodisperse polymer particles. *J Immunol Methods*, 1990. 134(2):253–259.

[244] Agrawal A. et al. Single-bead immunoassays using magnetic microparticles and spectral-shifting quantum dots. *J. Agric. Food Chem*, 2007. 55(10):3778–3782.

[245] Birtwell S. and Morgan H. Microparticle encoding technologies for high-throughput multiplexed suspension assays. *Integrative Biology*, 2009. 1(5-6):345–362.

Appendix A - Publications

Publications

- Sigrun Henkenjohann, Sebastian van de Linde, Sören Doose, Philip Tinnefeld, Markus Sauer; Photoinduced electron transfer (PET)-probes for the study of enzyme activity at the ensemble and single molecule level. Proc. SPIE, Vol. 6633, 663323 (2007)
- Sigrun Henkenjohann and Markus Sauer; Photoinduced electron transfer probes for the observation of enzyme activities. Proc. SPIE, Vol. 7185, 718503 (2009)
- Tobias Beck, Herbert Stepp, Rainer Wittig, Markus Böhl, Peter Schubert, Sigrun Henkenjohann, Markus Sauer, Christian S. Betz, Ann Johanson; A fluorescence diagnostic system detecting cancer-specific enzymatic activities: preliminary results. Proc. SPIE, Vol.7169, 71691G (2009)
- Tobias Beck, Herbert Stepp, Rainer Wittig, Markus Böhl, Markus Sauer, Sigrun Henkenjohann, Axel Dürkop, Christian S. Betz, Ann Johanson; Quantitative fluorescence spectroscopy for the detection of cancer-specific enzymatic activity, Medical Laser Application 24 (2), 126, 2009

Oral Presentations

- 14^{th} Internatinal Workshop on "Single Molecule Spectroscopy and Ultrasensitive Analysis in Life Sciences", 2008, Berlin. "Monitoring Enzyme Activities by Photoinduced Electron Transfer Probes"
- BiOS Conference at SPIE Photonics West 2009, San Jose, CA, USA, 'Single Molecule Spectroscopy & Imaging' Session. "Photoinduced electron transfer probes for the observation of enzyme activities"

- Invited Talk at the Biophysics Graduate Seminar, Arizona State University, Phoenix, Arizona, 2009. "Monitoring Enzyme Activities by Photoinduced Electron Transfer Probes"
- 15^{th} International Workshop on "Single Molecule Spectroscopy and Ultrasensitive Analysis in Life Sciences", 2009, Berlin. "Fluorescent Approaches to Enzyme Detection, Quantification and Analysis"

Poster Prensentations

- 18^{th} International Congress on Photonics in Europe - SPIE/OSA - ECBO, 2007, Munich. "Photoinduced electron transfer (PET)-probes for the study of enzyme activity at the ensemble and single molecule level"
- 17^{th} Annual Conference of the German Society for Cytometry, 2007, Regensburg. "Photoinduced electron transfer (PET)-probes for the detection of cancer related nucleases"
- BiOS Conference at SPIE Photonics West 2009, San Jose, CA, USA. "A fluorescence diagnostic system detecting cancer-specific enzymatic activities: preliminary results"

Scientific Award

- 'Young Investigator Award' at 'Single Molecule Spectroscopy & Imaging' Session, BiOS Conference at SPIE Photonics West 2009, San José, CA, USA

Appendix B - Protocols

B.1 Protocol for Preparation of Mowiol-DABCO

This recipe is deduced from a protocol published by Michael Mastrangelo and Eric Yehling from University of Rochester - Medical Center. They declare that Mowiol goes into solution with difficulty and therefore it would be best to make a large batch and freeze aliquots at -20° Celsius.

Prepare in clean 250 ml flask or beaker:

1. 24 g analytical grade glycerol
2. 9.6 g Mowiol 4-88
3. 24 ml distilled water
4. 48 ml 0.2 M Tris buffer, pH 8.5
5. Gently shake in 37° Celsius incubator for 4-5 hours until the majority of the Mowiol powder has gone into solution.
6. Aliquot into 50 ml centrifuge tubes, weigh and balance.
7. Centrifuge at 5000 g for 15 min., carefully remove the supernatant.
8. Aliquot into 0.8 ml conical tubes and freeze until use.

B.2 Original Labeling Protocol

Specimen Preparation Using Synthetic Fluorophores and Immunofluorescence

This labeling protocol is described as [229] in bibliography and only copied to this document due to possible alterations on the corresponding webpage.

Staining Adherent Cells with Intermediate Filament Primary Antibodies and Synthetic Fluorophores

A majority of the common fibroblast and epithelial cell lines derived from humans and laboratory animals produce brightly colored fluorescent specimens highlighting specific proteins in the intermediate filament network (such as vimentin and desmin) when stained with a cocktail that includes anti-intermediate filament antibodies conjugated to common low molecular weight synthetic fluorescent probes. Among the most useful fluorescent markers for visualization of intermediate filaments (as well as actin) are rhodamine, fluorescein, the Alexa Fluor series, and the cyanine dyes. Counterstaining for nuclei using a variety of popular DNA-binding dyes follows treatment with the antibodies and filamentous actin probes. This protocol details a generalized procedure for staining adherent cells.

Presented in Figure 1 [229] is a widefield fluorescence image revealing the vimentin intermediate filament and filamentous actin networks present in adherent mink uterus endometrium epithelial cells (**GMMe** line). The cells were immunofluorescently labeled with mouse anti-vimentin primary antibodies followed by goat anti-mouse secondary antibodies conjugated to Texas Red-X. In addition, the specimen was counterstained with phalloidin conjugated to Alexa Fluor 488 and DAPI, targeting the actin network and nuclei, respectively. Images were recorded in grayscale with a QImaging Retiga Fast-EXi camera system coupled to an Olympus BX-51 microscope equipped with bandpass emission fluorescence filter optical blocks provided by Omega Optical. During the processing stage, individual image channels were pseudocolored with RGB values corresponding to each of the fluorophore emission spectral profiles.

A wide variety of primary antibodies targeting other antigens can be employed in combination with anti-intermediate filament antibodies. In addition, synthetic fluorophores, such as the MitoTrackers, can also be used as counterstains. Because the mixed aldehyde and detergent fixative described

below can obscure some antigen markers, primary antibodies to other targets should first be tested alone before mixing into cocktails with intermediate filament antibodies.

Reagents

- **Cytoskeletal Buffer (CB)** - Suspend 18.14 grams of the biological buffer PIPES (free base; 60 millimolar) in one liter of double-distilled water. Add 6.50 grams of HEPES buffer (27 millimolar), 3.80 grams of EGTA (10 millimolar), and 0.99 grams of magnesium sulfate (heptahydrate; 4 millimolar). Stir and adjust the pH to 7.0 with concentrated sodium hydroxide. The PIPES buffer crystals will not completely dissolve until the buffer pH nears neutrality, but should then form a clear solution.

- **Phosphate Buffered Saline (PBS) with Calcium and Magnesium** - Dissolve 0.2 grams of potassium chloride, 0.2 grams of monobasic potassium phosphate, 8.0 grams of sodium chloride, and 1.74 grams of dibasic sodium phosphate (heptahydrate) in one liter of double-distilled water. After dissolving these reagents, add 0.132 grams of calcium chloride dihydrate and 0.10 grams of magnesium chloride hexahydrate. Adjust the pH to 7.2 with concentrated sodium hydroxide. Addition of the divalent alkaline earth metals to the buffer solution is helpful to ensure that uncondensed chromatin remains intact and contained within the nucleus during the staining procedure, dramatically decreasing background fluorescence levels when using DNA probes excited by ultraviolet irradiation (DAPI and Hoechst). This buffer should be used with cryosections.

- **Mixed Aldehyde and Detergent Fixative** - Dissolve 3 grams of electron microscope grade paraformaldehyde powder in 100 milliliters of CB with heating, and then filter when the solution appears clear. After cooling and filtering, add 1.5 milliliters of 20-percent Triton X-100 (made in CB) and 100 microliters of 50-percent glutaraldehyde. The final concentration of reagents should be 3 percent paraformaldehyde, 0.3 percent Triton X-100, and 0.05 percent glutaraldehyde. Mix the resulting solution well before use. This reagent should be made fresh daily.

- **Blocking Buffer** - 10 percent normal goat serum (**NGS**) in PBS containing 0.05 percent Triton X-100 (add 2-3 milligrams sodium azide per 100 milliliters of blocking buffer to eliminate the growth of microorganisms). If secondary antibodies to a host other than goat are being used, prepare the Blocking Buffer with normal serum from that species.
- **PBS-Triton Wash Buffer** - For wash sequences immediately before blocking and once again before staining with nuclear dyes, use PBS containing 0.05 percent Triton X-100.
- **PBS-Triton Wash Buffer with Blocking Serum** - For wash sequences between the primary and secondary antibody incubations and immediately after the secondary antibody treatment, use PBS containing 0.05 percent Triton X-100 and 1 percent normal host (goat) serum.
- **Primary Antibody Cocktail** - Add the appropriate volume of concentrated primary antibody (for example, anti-vimentin) stock solution to Blocking Buffer diluted 50-percent with PBS-Triton Wash Buffer (to yield a final concentration 5-percent normal goat serum). Several primary antibodies from different hosts can be mixed into a cocktail. Adherent cells on coverslips should be treated with 100 microliters of primary antibody cocktail.
- **Secondary Antibody/Phalloidin Cocktail** - Add the appropriate volume of secondary antibody conjugated to the selected fluorophore (for example, 8 microliters of goat anti-mouse heavy and light chain secondary IgG with Alexa Fluor 350 at 2 milligrams per milliliter) to 1 milliliter of Blocking Buffer diluted 50-percent with PBS-Triton Wash Buffer (to yield a final concentration 5-percent normal goat or other host serum). If the cells are to be simultaneously counterstained with phalloidin, add 20-40 microliters of concentrated stock solution (6.6 micromolar) to 1 milliliter of the Blocking Buffer. As with the primary antibody mixture, adherent cells on coverslips should be treated with 100 microliters of primary antibody cocktail.
- **Nuclear Dye** - Prepare fresh dilutions of the nuclear dye immediately prior to staining. When using SYTOX, DRAQ5, and the cyanine nuclear stains, background fluorescence can be significantly reduced (especially in the cytoplasm) by adding 10 milligrams of RNase to the

Blocking Buffer. In this case, block the cells or tissues at 37 degrees Celsius, rather than at room temperature, in order to activate the enzyme.

- **Nuclear Dye Wash Buffer** - Hoechst and SYTOX dyes require Hanks Balanced Salt Solution (**Hanks BSS**), while DAPI, as well as the monomeric and dimeric cyanine nuclear stains, can be used with PBS.

Nuclear Counterstain Dilutions

- **Hoechst (33342 and 33258)** - Dilute 5 microliters of 10 milligram/milliliter stock solution in 150 milliliters of Hanks BSS (treat for 30 minutes).
- **SYTOX Green and Orange** - Dilute 10 microliters of concentrated stock solution (5 millimolar in dimethyl sulfoxide) in 250 milliliters of Hanks BSS (treat for 30 minutes).
- **DAPI** - Dilute 5 microliters of 10 milligram/milliliter stock solution in 150 milliliters of PBS diluted 50-percent with double-distilled water (treat for 5 minutes).
- **Monomeric and Dimeric Cyanine Dyes** - Dilute the concentrated stock solution (for example, TO-PRO-3; usually 1 millimolar) as recommended by the manufacturer (1:20 to 1:1000) into PBS (treat for 5 to 30 minutes).
- **DRAQ5** - Dilute the concentrated stock solution (usually 1 millimolar) as recommended by the manufacturer (1:20 to 1:1000) into PBS (treat for 5 to 30 minutes).

Procedure

Aspirate the growth medium from a Petri dish containing healthy cells adhered to coverslips and replace with pre-warmed (37 degrees Celsius) CB buffer to remove medium and serum proteins (use 3 milliliters of buffer for 60-millimeter Petri dishes). Wash the cells twice for 5 minutes (each wash) with the pre-warmed CB buffer, and incubate the cells at 37 degrees Celsius during the wash cycles. Each Petri dish should be individually marked with the primary antibodies and other stains used for the coverslips in that dish.

Coverslips should remain with the original Petri dish for each step in the entire procedure.

Fix the cells by adding the appropriate volume of pre-warmed (37 degrees Celsius) mixed aldehyde fixer to each Petri dish and rapidly transfer the dishes to the incubator. Fix for 10 minutes.

Remove the Petri dishes from the incubator and wash once with CB buffer for 5 minutes and twice with PBS-Triton Wash Buffer (5 minutes each wash) before blocking.

Remove the PBS-Triton Wash Buffer and block nonspecific secondary antibody binding sites with 10-percent normal host serum Blocking Buffer. Treat the adherent cells for 60 minutes at room temperature with the Blocking Buffer and slowly rotate the Petri dishes as the cells are being blocked on an orbital shaker at 5-10 revolutions per minute. Coverslip Staining Support

During the blocking step, prepare antibody treatment supports by covering 2 x 3-inch microscope slides with Parafilm, as illustrated in Figure 2. Secure the Parafilm so that it adheres tightly and is smoothly distributed along the glass surface (no blisters). After blocking, carefully remove the coverslips from the Petri dishes and place them cell-side down on a 100 microliter drop of diluted primary antibody cocktail in 50-percent blocking buffer deposited on a Parafilm-covered slide. Between 3 and 6 coverslips (depending on size) can be placed on a single slide. Next, place the slides in a humidity chamber (see Figure 3) and incubate the coverslips in the humidity chamber for 1.5 hours at 37 degrees Celsius. If the primary antibodies are not conjugated to fluorophores, it is not necessary to protect the coverslips from light at this point.

After primary antibody treatment, return the coverslips to the original Petri dishes and wash three times at room temperature (5 to 10 minutes for each wash) with PBS-Triton Wash Buffer with Blocking Serum to remove unbound primary antibodies. Slowly rotate the Petri dishes as the cells are being washed on an orbital shaker at 5-10 revolutions per minute.

After washing, carefully remove the coverslips from the Petri dishes and place them cell-side down on a 100 microliter drop of diluted secondary antibody cocktail in 50-percent blocking buffer deposited on a Parafilm-covered slide. Once again, place the slides in a humidity chamber (see Figure 3) and incubate the coverslips in the humidity chamber for 1 hour at 37 degrees Celsius if smaller secondary antibody fragments are being used, or 1.5 hours for entire antibody molecules. It is important to cover the humidity chamber

with aluminum foil during this step to protect the fluorophores from light. Humidity Chamber Configuration

After secondary antibody treatment, return the coverslips to the original Petri dishes and wash three times at room temperature (5 to 10 minutes for each wash) with PBS-Triton Wash Buffer with Blocking Serum to remove unbound secondary antibodies. Slowly rotate the Petri dishes as the cells are being washed on an orbital shaker at 5-10 revolutions per minute.

In preparation for nuclear staining, wash the cells twice with PBS-Triton Wash Buffer for 5 minutes (each wash). Slowly rotate the Petri dishes as the cells are being washed on an orbital shaker at 5-10 revolutions per minute.

For DAPI and cyanine nuclear counterstains, add the diluted dye in PBS (dilute PBS to 50 percent with double-distilled water for DAPI) to the Petri dish and treat the coverslips for the recommended time: 5-10 minutes for DAPI; 15-30 minutes for cyanine dyes (protect from light with aluminum foil). When using Hoechst or SYTOX stains (30 minute incubation), first wash the slides in Hanks Balanced Salt Solution for two buffer exchanges prior to counterstaining.

Wash the counterstained coverslips with either PBS or Hanks Balanced Salt Solution (depending upon the nuclear dye) for three times at 5 minutes for each wash. Protect from light with aluminum foil.

In order to remove excess salt, wash the cells three times for 2 to 3 minutes (each wash) in distilled water. Note that this step is only necessary if the coverslips are to be air-dried overnight before mounting.

After the final distilled water washing step, carefully remove the coverslips from the Petri dish with tweezers and wipe excess water from the back and edges. Lean the coverslips on their sides against the labeled Petri dish cover and allow them to dry overnight. Protect the drying coverslips from light with an aluminum baking tray. After drying, mount the coverslips (cell-side down) on clean microscope slides using the appropriate mounting medium.

Contributing Authors:
Nathan S. Claxton, Gregory K. Ottenberg, Scott G. Olenych, John D. Griffin, and Michael W. Davidson - National High Magnetic Field Laboratory, 1800 East Paul Dirac Dr., The Florida State University, Tallahassee, Florida, 32310.

http://www.olympusfluoview.com/applications/protocols/cellsintermediatefilaments.html - Sep 30th 2009

B.3 Protocol for Examination of labeling Procedure

These labeling procedures evolved from the standard protocol (see page 206) and were used to examine the labeling success in respect to the cell fixation. Cells were cultivated in cells were grown in Lab-Tek II chambered coverglasses for at least 24 hours in custom culture conditions before the experiment started.

Due to its toxicity no labeled phalloidin was used. Sytox® Green Nucleic Acid Stain was incubated only after fixation. Procedures were temporally adjusted so that Sytox® Green Nucleic Acid Stain incubation took place simultaneously in every sample.

Fixation before Incubation with primary Antibody

1. Fixation
   - Take cells out of incubator.
   - Add 50µl Paraformaldehyde (20%) to 200µl medium (to yield a final concentration of 4%).
   - Incubate for 5 min.
2. Washing
   - Add PBS to each chamber while simultaneously removing solution.
   - Incubate with PBS for 5 min.
   - Repeat twice.
   - Remove solution completely.
3. Preparation with Blocking Buffer
   - Add 100µl blocking buffer (Normal Goat Serum 66% in PBS to a final concentration of 5%).
   - Incubate at 37°C for 60min.
4. Incubation with primary Antibody

- Add primary antibody respectively negative control protein dissolved in 100µl blocking buffer to yield a final amount of 1.5×10^{-12} mol/chamber.
- Incubate at 37°C for 90 min.

5. Washing
   - Add washing buffer (PBS with 0.05% TritonX-100 and 1% NGS) to each chamber while simultaneously removing solution.
   - Incubate with washing buffer for 5 min.
   - Repeat twice.
   - Remove solution completely.
6. Incubation with secondary Antibody
   - Add Alexa Fluor® 647 goat anti-rabbit IgG dissolved in 100µl blocking buffer with a final amount of 3.5×10^{-12} mol/chamber.
   - Cover cells with aluminium foil to prevent from bleaching.
   - Incubate at 37°C for 90 min.
7. Washing
   - Add PBS Triton wash buffer (PBS with 0.05% TritonX-100) to each chamber while simultaneously removing solution.
   - Incubate with washing buffer for 5 min.
   - Repeat twice.
8. Preparation for Nuclear Staining
   - Add PBS Triton wash buffer while simultaneously removing solution.
   - Incubate for 5 min.
   - Repeat once.
9. Nuclear Staining with Sytox® Green Nucleic Acid Stain
   - Add Hanks' Balanced Salt Solution while simultaneously removing solution.

- Incubate for 5 min.
- Repeat once.
- Remove solution completely.
- Add Sytox® Green Nucleic Acid Stain in HBSS to yield a final amount of 2.5×10^{-12} mol/chamber.
- Incubate for 30 min.

10. Washing
    - Add HBSS while simultaneously removing solution.
    - Incubate for 5 min.
    - Repeat once.
    - Remove solution completely.
11. Sealing
    - Add 200µl Mowiol/DABCO to each chamber.
    - Let dry over night at 4°C.

Fixation between Incubation with primary and secondary Antibody

1. Washing
    - Remove old medium.
    - Add fresh medium to each chamber.
    - Incubate at 37°C, 5% CO_2 for 15 min.
    - Remove medium.
2. Preparation with Blocking Buffer
    - Add 100µl blocking medium (Normal Goat Serum 66% in fresh medium to a final concentration of 5%).
    - Incubate at 37°C, 5% CO_2 for 60min.
3. Incubation with primary Antibody

- Add primary antibody respectively negative control protein dissolved in 100µl fresh medium to yield a final amount of 1.5×10^{-12} mol/chamber.
- Incubate at 37°C, 5% CO_2 for 90 min.

4. Fixation
   - Take cells out of incubator.
   - Add 50µl Paraformaldehyde (20%) to 200µl medium (to yield a final concentration of 4%).
   - Incubate for 5 min.
5. Washing
   - Add PBS to each chamber while simultaneously removing solution.
   - Incubate with PBS for 5 min.
   - Repeat twice.
   - Remove solution completely.
6. Incubation with secondary Antibody
   - Add Alexa Fluor® 647 goat anti-rabbit IgG dissolved in 100µl blocking buffer with a final amount of 3.5×10^{-12} mol/chamber.
   - Cover cells with aluminium foil to prevent from bleaching.
   - Incubate at 37°C for 90 min.
7. Washing
   - Add PBS Triton wash buffer (PBS with 0.05% TritonX-100) to each chamber while simultaneously removing solution.
   - Incubate with washing buffer for 5 min.
   - Repeat twice.
8. Preparation for Nuclear Staining
   - Add PBS Triton wash buffer while simultaneously removing solution.
   - Incubate for 5 min.

- Repeat once.

9. Nuclear Staining with Sytox® Green Nucleic Acid Stain
   - Add Hanks' Balanced Salt Solution while simultaneously removing solution.
   - Incubate for 5 min.
   - Repeat once.
   - Remove solution completely.
   - Add Sytox® Green Nucleic Acid Stain in HBSS to yield a final amount of 2.5×10^{-12} mol/chamber.
   - Incubate for 30 min.
10. Washing
    - Add HBSS while simultaneously removing solution.
    - Incubate for 5 min.
    - Repeat once.
    - Remove solution completely.
11. Sealing
    - Add 200µl Mowiol/DABCO to each chamber.
    - Let dry over night at 4°C.

Fixation after Incubation with secondary Antibody

1. Washing
   - Remove old medium.
   - Add fresh medium to each chamber.
   - Incubate at 37°C, 5% CO_2 for 15 min.
   - Remove medium.
2. Preparation with Blocking Buffer

- Add 100µl blocking medium (Normal Goat Serum 66% in fresh medium to a final concentration of 5%).
- Incubate at 37°C, 5% CO_2 for 60min.

3. Incubation with primary Antibody
   - Add primary antibody respectively negative control protein dissolved in 100µl fresh medium to yield a final amount of 1.5×10^{-12} mol/chamber.
   - Incubate at 37°C, 5% CO_2 for 90 min.
4. Washing
   - Add fresh medium to each chamber while simultaneously removing solution.
   - Incubate at 37°C, 5% CO_2 for 15 min.
   - Repeat twice.
   - Remove medium.
5. Incubation with secondary Antibody
   - Add Alexa Fluor® 647 goat anti-rabbit IgG dissolved in 100µl fresh medium with a final amount of 3.5×10^{-12} mol/chamber.
   - Cover cells with aluminium foil to prevent from bleaching.
   - Incubate at 37°C for 90 min.
6. Fixation
   - Take cells out of incubator.
   - Add 50µl Paraformaldehyde (20%) to 200µl medium (to yield a final concentration of 4%).
   - Incubate for 5 min.
7. Washing
   - Add PBS to each chamber while simultaneously removing solution.
   - Incubate with PBS for 5 min.
   - Repeat twice.

8. Preparation for Nuclear Staining
    - Add PBS Triton wash buffer while simultaneously removing solution.
    - Incubate for 5 min.
    - Repeat once.
9. Nuclear Staining with Sytox® Green Nucleic Acid Stain
    - Add Hanks' Balanced Salt Solution while simultaneously removing solution.
    - Incubate for 5 min.
    - Repeat once.
    - Remove solution completely.
    - Add Sytox® Green Nucleic Acid Stain in HBSS to yield a final amount of 2.5×10^{-12} mol/chamber.
    - Incubate for 30 min.
10. Washing
    - Add HBSS while simultaneously removing solution.
    - Incubate for 5 min.
    - Repeat once.
    - Remove solution completely.
11. Sealing
    - Add 200µl Mowiol/DABCO to each chamber.
    - Let dry over night at 4°C.

B.4 Standard labeling Protocol for triple stained mammalian Cells

This labeling procedure has been optimized for the employed antibodies, counterstaining chemicals and cell types (see section 3.2). Each cell type was cultivated in Lab-Tek II chambered coverglasses for at least 24 hours in custom culture conditions. The complete procedure lasts approximately 8 hours.

1. Fixation
   - Take cells out of incubator.
   - Add 50µl Paraformaldehyde (20%) to 200µl medium (to yield a final concentration of 4%).
   - Incubate for 10 min. In case of HEK 293T cells only incubate for 5 min.
2. Washing
   - Add PBS to each chamber while simultaneously removing solution.
   - Incubate with PBS for 5 min.
   - Repeat twice.
   - Remove solution completely.
3. Permeabilisation
   - Add 200µl TritonX-100 0,5% (v/v) in PBS.
   - Incubate for 10 min.
4. Washing
   - Add PBS to each chamber while simultaneously removing solution.
   - Incubate with PBS for 5 min.
   - Repeat twice.
   - Remove solution completely.

5. Preparation with Blocking Buffer
    - Add PBS Triton wash buffer (PBS with 0.05% TritonX-100).
    - Incubate for 5 min.
    - Remove solution completely.
    - Add 100µl blocking buffer (Normal Goat Serum 66% in PBS to a final concentration of 5% containing 10mg RNase (reduces background fluorescence of Sytox® Green Nucleic Acid Stain)).
    - Incubate at 37°C for 60min to activate the enzyme.
6. Incubation with primary Antibody
    - Add primary antibody respectively negative control protein dissolved in 100µl blocking buffer to yield a final amount of 1.5×10^{-12} mol/chamber.
    - Incubate for at 37°C 90 min.
7. Washing
    - Add washing buffer (PBS with 0.05% TritonX-100 and 1% NGS) to each chamber while simultaneously removing solution.
    - Incubate with washing buffer for 5 min.
    - Repeat twice.
    - Remove solution completely.
8. Incubation with secondary Antibody and labeled Phalloidin
    - Add secondary antibody cocktail (Alexa Fluor®647 goat anti-rabbit IgG with a final amount of 3.5×10^{-12} mol/chamber and rhodamine phalloidin with a final amount of 1×10^{-7} mol/chamber dissolved in 100µl blocking buffer).in
    - Cover cells with aluminium foil to prevent from bleaching.
    - Incubate for at 37°C 90 min.
9. Washing
    - Add washing buffer (PBS with 0.05% TritonX-100 and 1% NGS) to each chamber while simultaneously removing solution.

- Incubate with washing buffer for 5 min.
- Repeat twice.

10. Preparation for Nuclear Staining
    - Add PBS Triton wash buffer while simultaneously removing solution.
    - Incubate for 5 min.
    - Repeat once.
11. Nuclear Staining with Sytox® Green Nucleic Acid Stain
    - Add Hanks' Balanced Salt Solution while simultaneously removing solution.
    - Incubate for 5 min.
    - Repeat once.
    - Remove solution completely.
    - Add Sytox® Green Nucleic Acid Stain in HBSS to yield a final amount of 2.5×10^{-12} mol/chamber.
    - Incubate for 20 min.
12. Washing
    - Add HBSS while simultaneously removing solution.
    - Incubate for 5 min.
    - Repeat once.
    - Remove solution completely.
13. Sealing
    - Add 200µl Mowiol/DABCO to each chamber.
    - Let dry over night at 4°C.

Samples can also be imaged in PBS yielding lower fluorescence intensities. Sealed samples can be examined after months, not showing distinct changes in fluorescence intensities if stored in the dark at 4°C.

B.5 Labeling Protocol for *d*STORM Measurement

This labeling procedure is similar to the standard protocol (see page 206). Cells were cultivated in Lab-Tek II chambered coverglasses in custom culture conditions. Doxicycline induction took place at different points of time to achieve various induction durations but almost equal culture durations of every sample. In total cells were cultivated for 50 hours of which 32, 24, 10, 6, 4, 2 or 0 hours were Doxicycline induced.

Due to the nature of these experiments neither labeled phalloidin nor Sytox® Green Nucleic Acid Stain was used. Primary and secondary Antibody concentrations were raised to a five-fold of the standard protocol to secure the saturation of DNaseX molecules.

1. Fixation
   - Take cells out of incubator.
   - Add 50µl Paraformaldehyde (20%) to 200µl medium (to yield a final concentration of 4%).
   - Incubate for 5 min.
2. Washing
   - Add PBS to each chamber while simultaneously removing solution.
   - Incubate with PBS for 5 min.
   - Repeat twice.
   - Remove solution completely.
3. Permeabilisation
   - Add 200µl TritonX-100 0,5% (v/v) in PBS.
   - Incubate for 10 min.
4. Washing
   - Add PBS to each chamber while simultaneously removing solution.
   - Incubate with PBS for 5 min.

- Repeat twice.
- Remove solution completely.

5. Preparation with Blocking Buffer
   - Add PBS Triton wash buffer (PBS with 0.05% TritonX-100).
   - Incubate for 5 min.
   - Remove solution completely.
   - Add 100µl blocking buffer (Normal Goat Serum 66% in PBS to a final concentration of 5%).
   - Incubate at room temperature for 60min.
6. Incubation with primary Antibody
   - Add DNAX primary antibody dissolved in 100µl blocking buffer to yield a final amount of 6.5×10^{-12} mol/chamber.
   - Incubate at room temperature for 90 min.
7. Washing
   - Add washing buffer (PBS with 0.05% TritonX-100 and 1% NGS) to each chamber while simultaneously removing solution.
   - Incubate with washing buffer for 5 min.
   - Repeat twice.
   - Remove solution completely.
8. Incubation with secondary Antibody
   - Add Alexa Fluor® 647 goat anti-rabbit IgG dissolved in 100µl blocking buffer with a final amount of 1.65×10^{-11} mol/chamber.
   - Cover cells with aluminium foil to prevent from bleaching.
   - Incubate at room temperature for 90 min.
9. Washing
   - Add washing buffer (PBS with 0.05% TritonX-100 and 1% NGS) to each chamber while simultaneously removing solution.
   - Incubate with washing buffer for 5 min.

- Repeat twice.

10. Washing
    - Add PBS to each chamber while simultaneously removing solution.
    - Incubate with PBS for 5 min.
    - Repeat twice.
    - Remove solution completely.
    - Add 200µl PBS.
11. Measurement Preparation
    - Remove PBS.
    - Add switching buffer: PBS pH 7.4 containing oxygen scavenger (0.5 mg/mL glucose oxidase, 40 µg/mL catalase, 10% w/v glucose) and 50 mm β -mercaptoethylamine (MEA).
    - Seal to prevent from oxygen.

Appendix C - Additional Images

C.1 Mowiol®-DABCO Effect on Fluorescent Labels

In this measurement cells were characteristically stained and measured on a confocal mircroscop in different layers. These layers were then projected onto a single layer, showing the maximum intensity derived for each coordinate. As a first step the cells were embedded in PBS and measured. The same samples were then covered with Mowiol®-DABCO and stored overnight at 4° Celsius for the mounting medium to dry. 24 hours later the samples were equally measured and presented.

A distinct increase in fluorescence intensities is obtained for the antibody label Alexa Fluor®647 as well as for Sytox® Green Nucleic Acid Stain, while the autofluorescence seems to decrease upon Mowiol®-DABCO embedding. Therefore it is assumed that Mowiol®-DABCO generally has a positive effect on fluorescence yield over the complete range of applied fluorophores in this work.

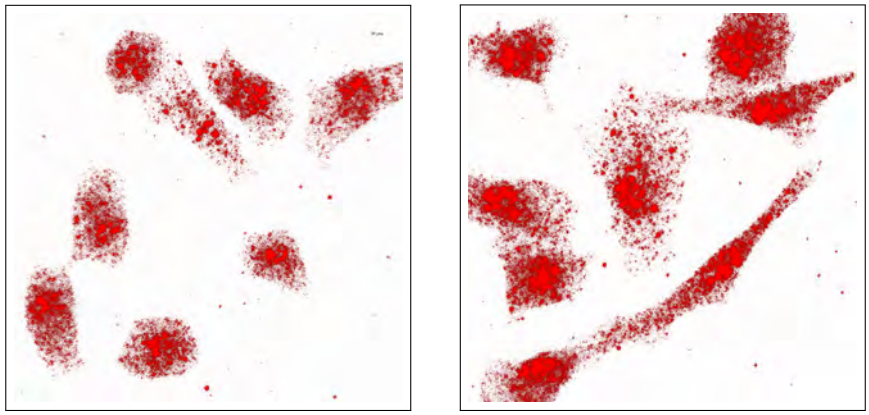

a) PBS **b)** Mowiol®-DABCO

Mounting medium effect on Alexa Fluor®647 in A-549 cells.

Ia) Autofluorescence in PBS

Ib) Autofluorescence in Mowiol®-DABCO

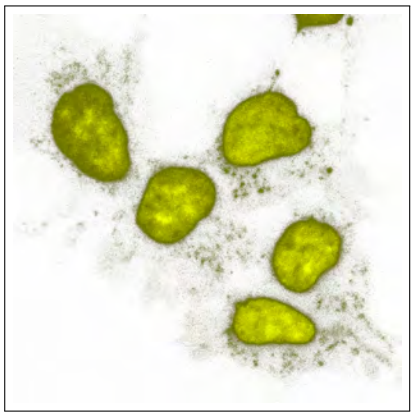

IIa) Sytox® Green in PBS

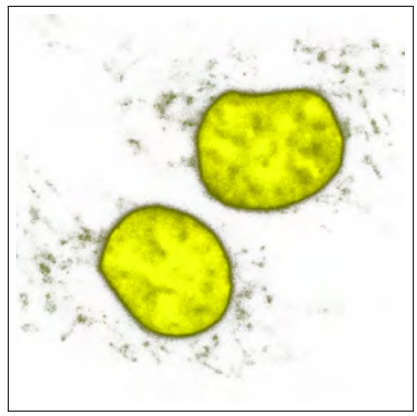

IIb) Sytox® Green in Mowiol®-DABCO

Mounting medium effect on Sytox® Green Nucleic Acid Stain (1:80000) in Cos7 (African Green Kidney) cells.

C.2 Examination of labeling Procedure - Complete Set of Images

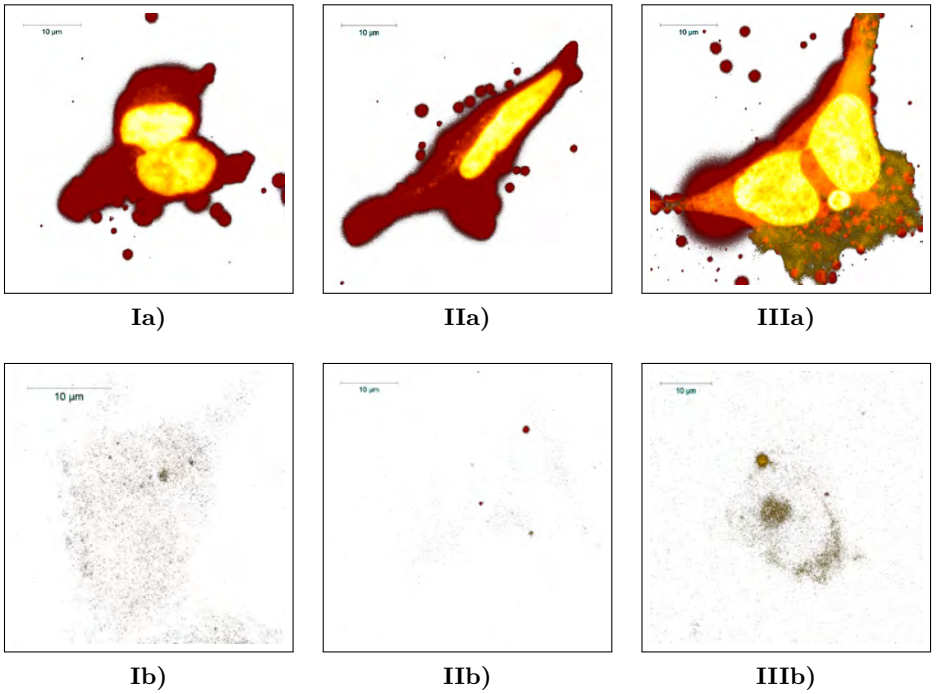

Examination of different labeling procedures. Cell fixation before incubation with primary antibody (I), between incubation with primary and secondary antibody (II) and after incubation with secondary antibody (III). a) labeled with primary and Alexa Fluor® 647 linked secondary antibody (red), b) labeled with Alexa Fluor® 647 linked secondary antibody (red) but no primary antibody, c) labeled with pre-immune serum and Alexa Fluor® 647 linked secondary antibody (red), d) labeled with primary antibody but no Alexa Fluor® 647 linked secondary antibody. All samples counterstained with Sytox® Green Nucleic Acid Stain (yellow) after fixation. Cells confocally scanned in several layers and projected onto one plane.

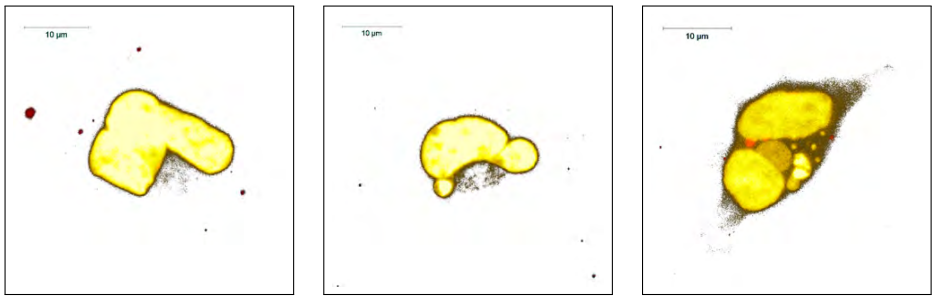

Id) **IId)** **IIId)**

Ie) **IIe)** **IIIe)**

Examination of different labeling procedures. Cell fixation before incubation with primary antibody (I), between incubation with primary and secondary antibody (II) and after incubation with secondary antibody (III). a) labeled with primary and Alexa Fluor®647 linked secondary antibody (red), b) labeled with Alexa Fluor®647 linked secondary antibody (red) but no primary antibody, c) labeled with pre-immune serum and Alexa Fluor®647 linked secondary antibody (red), d) labeled with primary antibody but no Alexa Fluor®647 linked secondary antibody. All samples counterstained with Sytox® Green Nucleic Acid Stain (yellow) after fixation. Cells confocally scanned in several layers and projected onto one plane.

C.3 Complete Set of Images from *d*STORM Measurement

As additional information here there are all samples that were taken into account for the numerical evaluation (see section 4.2.4). First all samples with primary and secondary antibody and then the controls with only primary respectively only secondary antibody are shown. For each sample there are three individual cells (I, II, III), each shown at autofluorescence at 514 nm on 512x512 pixels (a), total internal reflection at 647 nm on 512x512 pixels (b), total internal reflection at 647 nm on 128x128 pixels (c), intensity scaled hits of the same area shown in c) by *d*STORM software (d) and processed *d*STORM data showing the 40x40 pixels area used for counting the number of hits (e). a) - c) are scaled individually, d) - e) are equally processed and scaled.

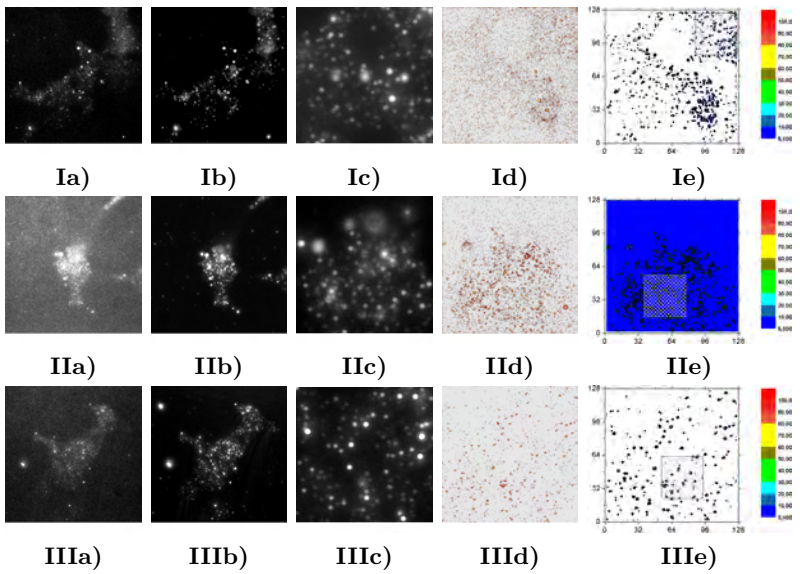

sample: 0 hours of doxicycline induction

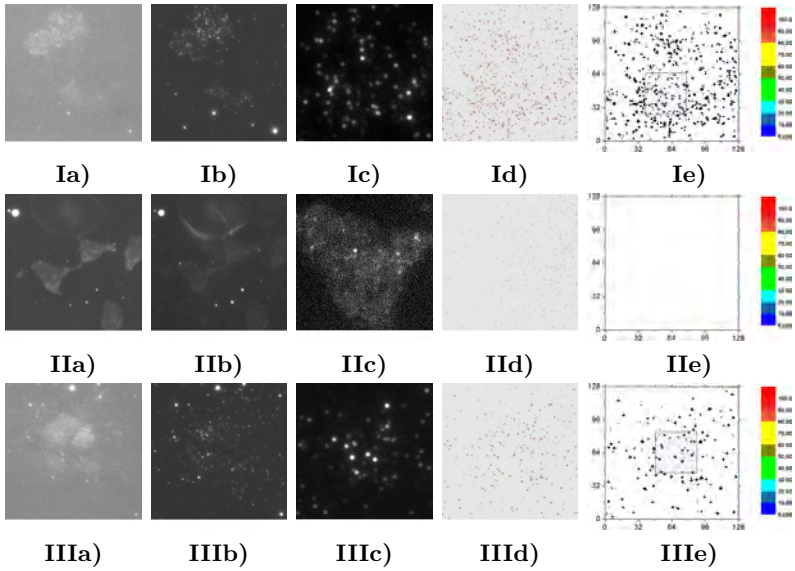

sample: 2 hours of doxicycline induction

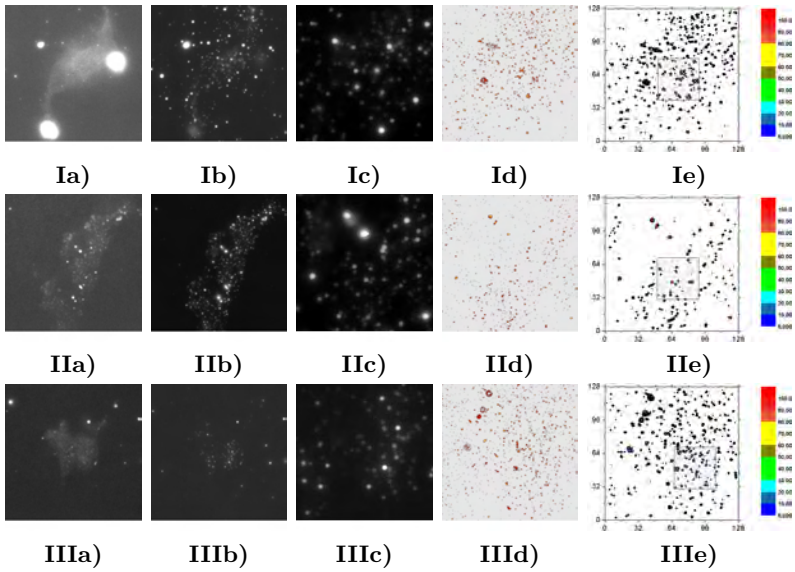

sample: 4 hours of doxicycline induction

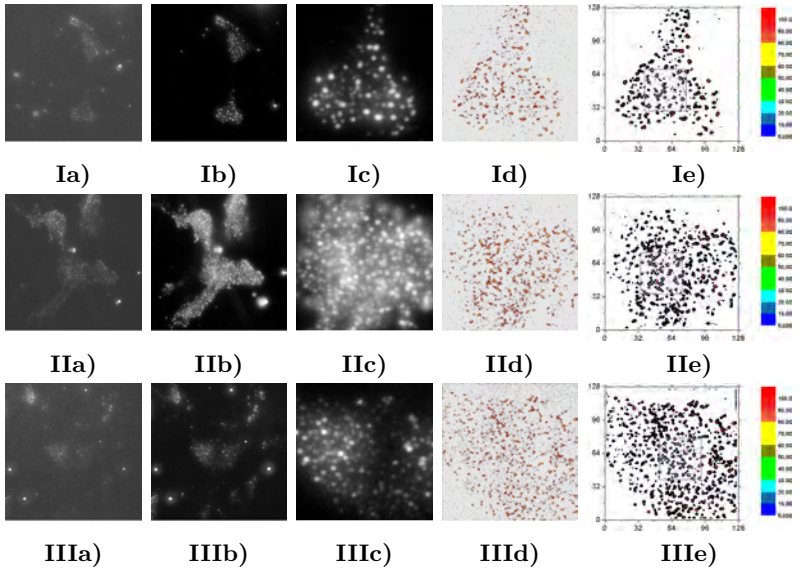

sample: 6 hours of doxicycline induction

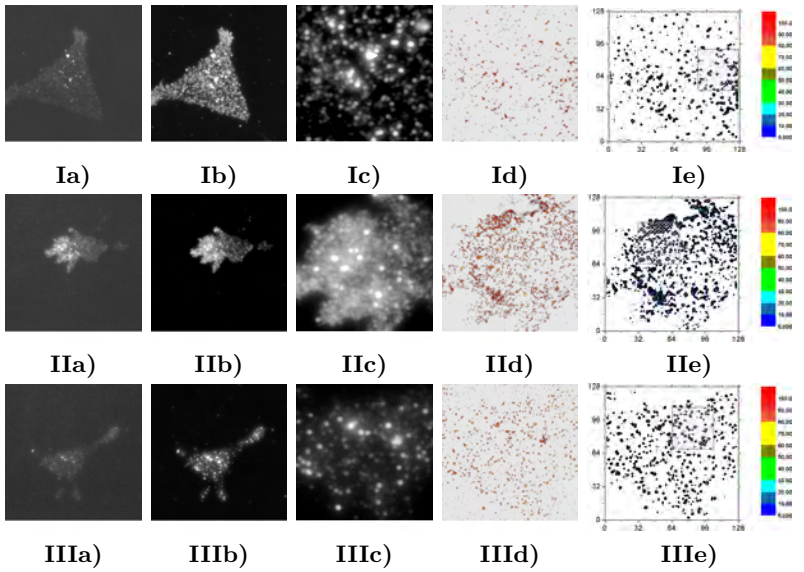

sample: 10 hours of doxicycline induction

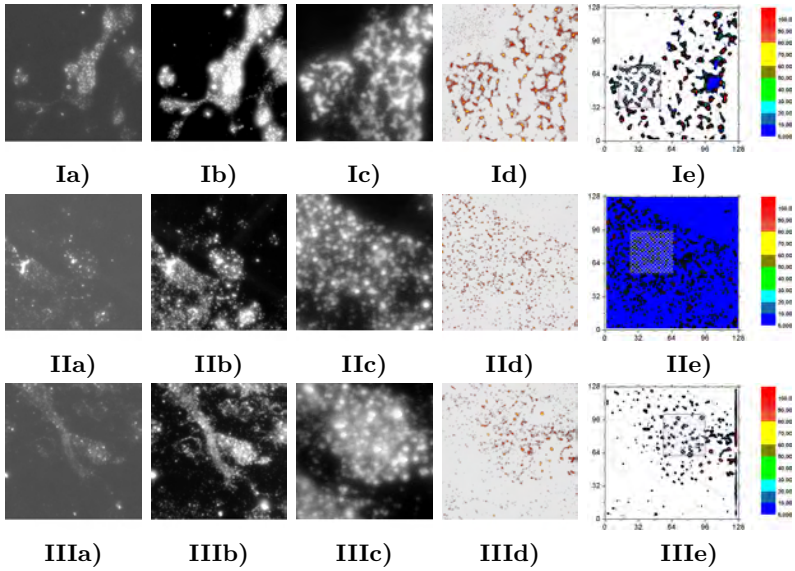

sample: 24 hours of doxicycline induction

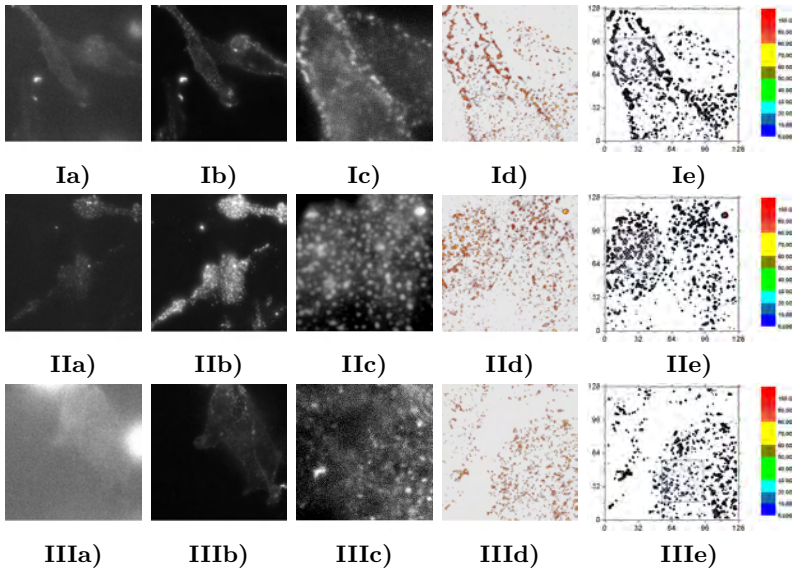

sample: 32 hours of doxicycline induction

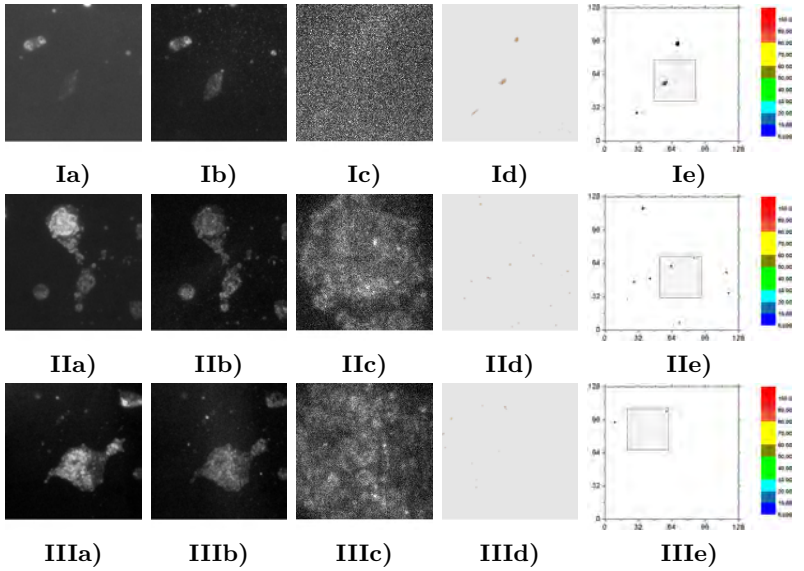

control with only primary antibody: 0 hours of doxicycline induction

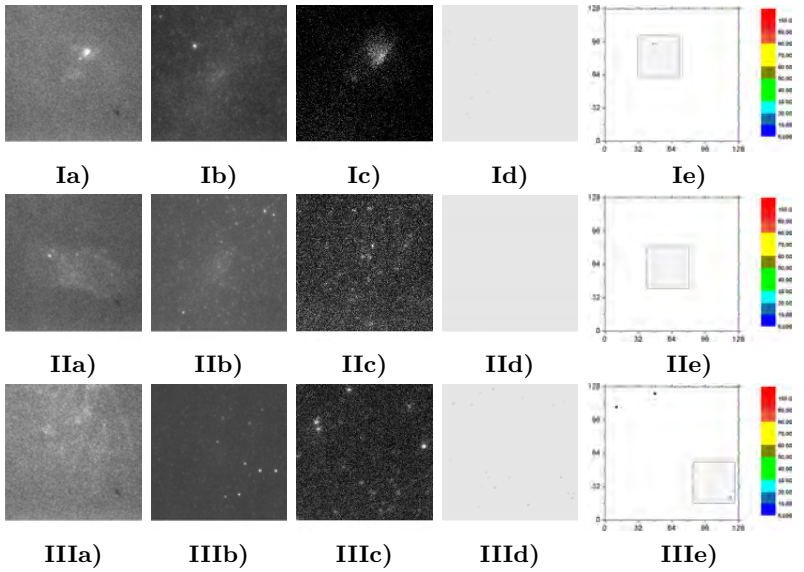

control with only primary antibody: 2 hours of doxicycline induction

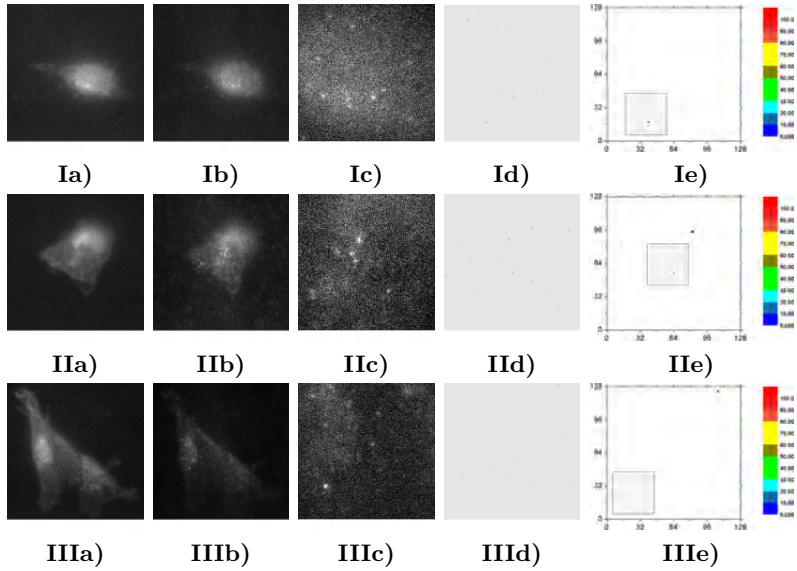

Ia) **Ib)** **Ic)** **Id)** **Ie)**

IIa) **IIb)** **IIc)** **IId)** **IIe)**

IIIa) **IIIb)** **IIIc)** **IIId)** **IIIe)**

control with only primary antibody: 4 hours of doxicycline induction

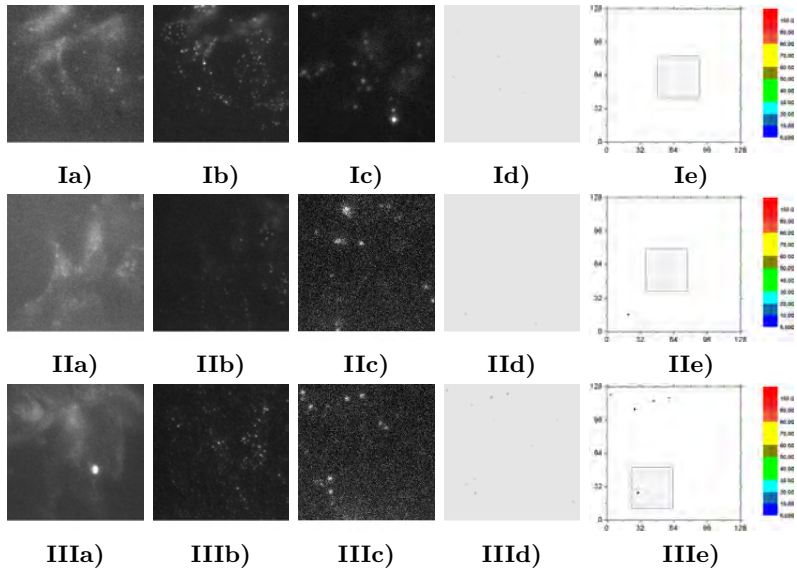

Ia) **Ib)** **Ic)** **Id)** **Ie)**

IIa) **IIb)** **IIc)** **IId)** **IIe)**

IIIa) **IIIb)** **IIIc)** **IIId)** **IIIe)**

control with only primary antibody: 6 hours of doxicycline induction

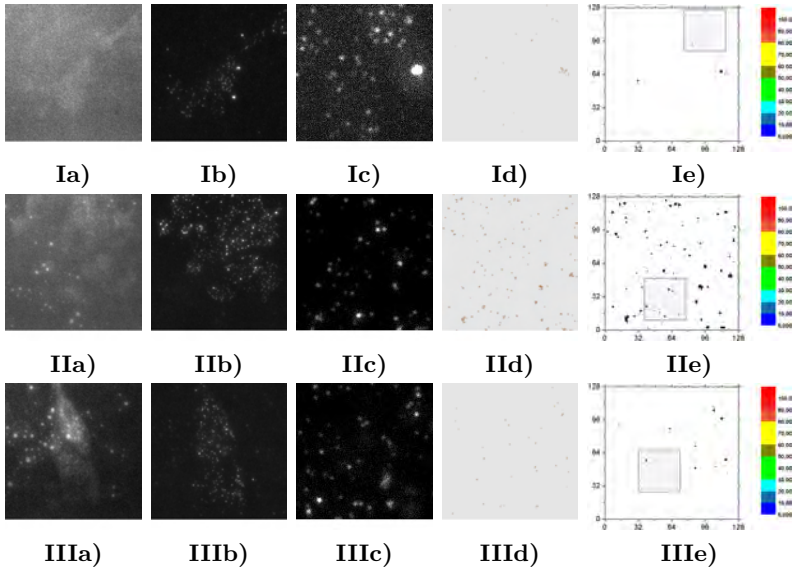

control with only primary antibody: 10 hours of doxicycline induction

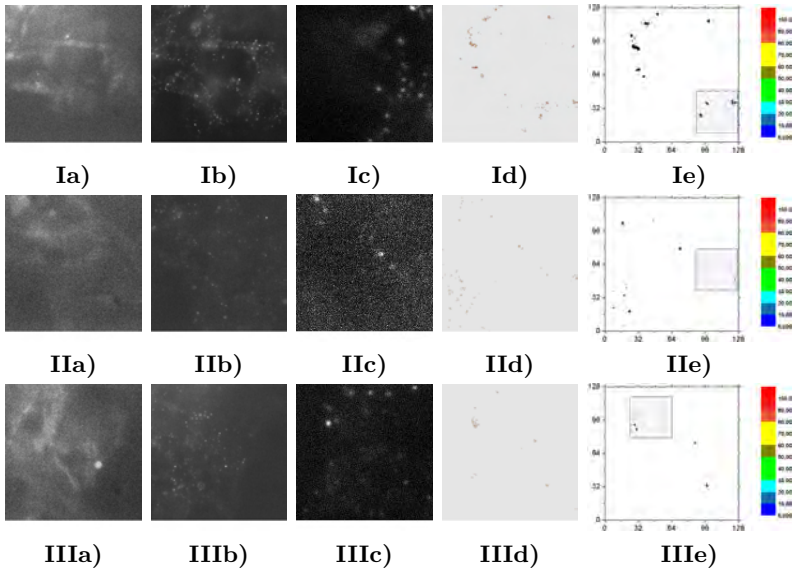

control with only primary antibody: 24 hours of doxicycline induction

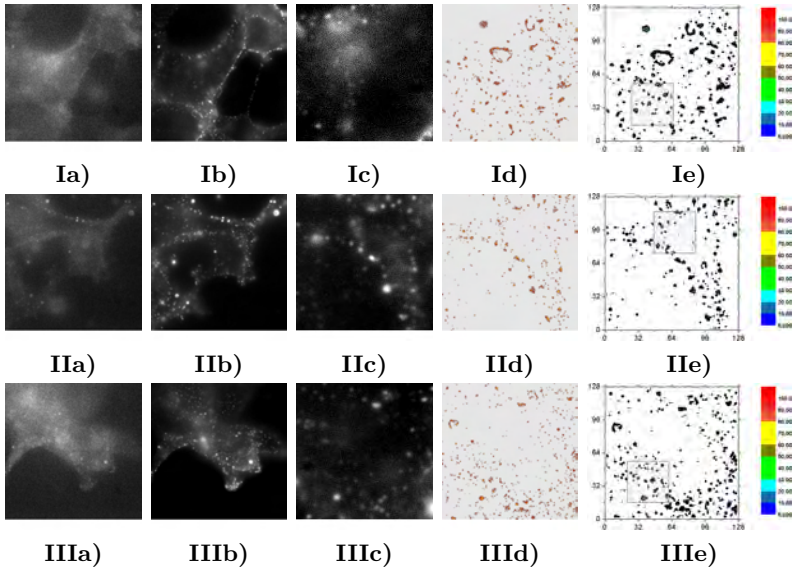

control with only primary antibody: 32 hours of doxicycline induction

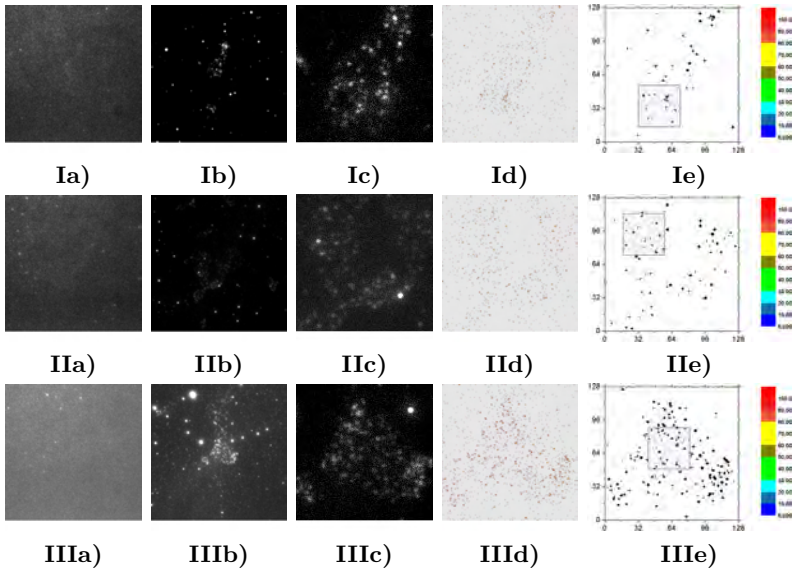

control with only secondary antibody: 0 hours of doxicycline induction

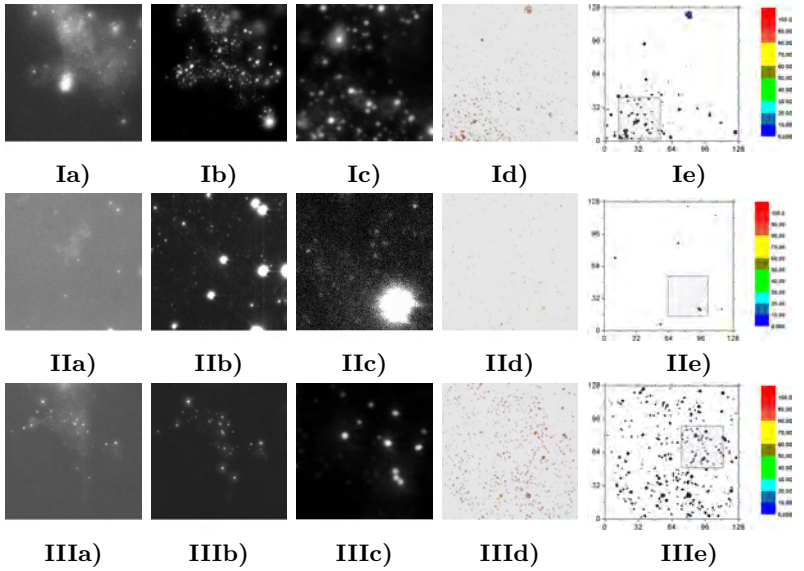

control with only secondary antibody: 2 hours of doxicycline induction

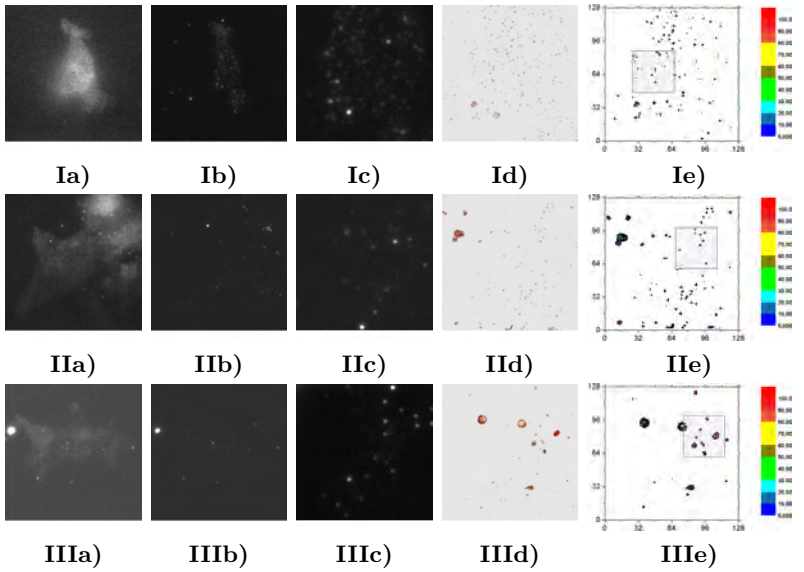

control with only secondary antibody: 4 hours of doxicycline induction

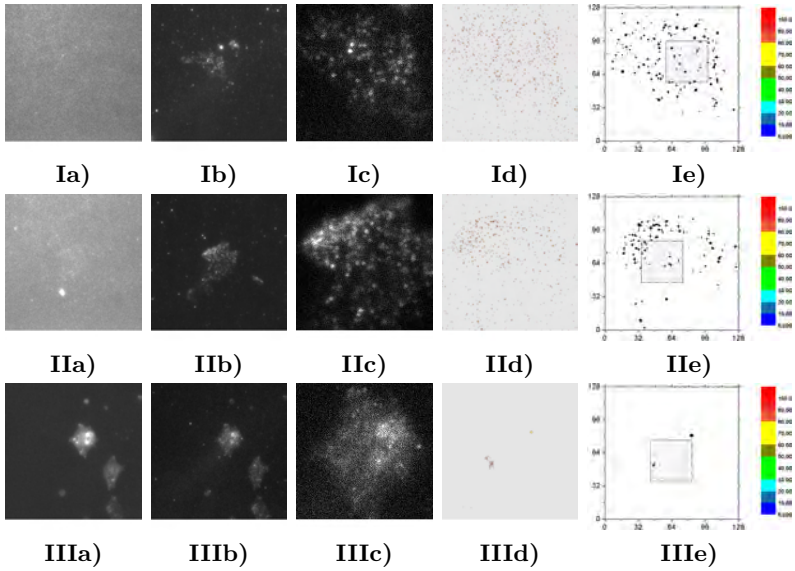

control with only secondary antibody: 6 hours of doxicycline induction

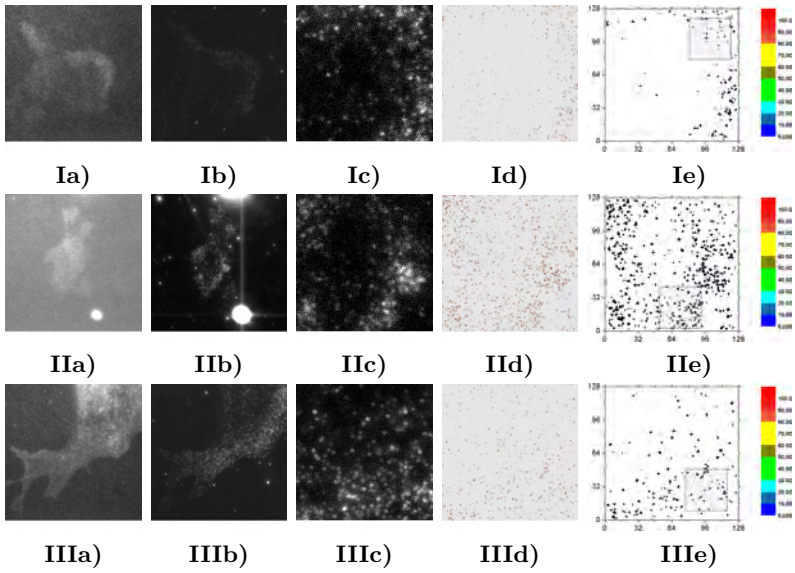

control with only secondary antibody: 10 hours of doxicycline induction

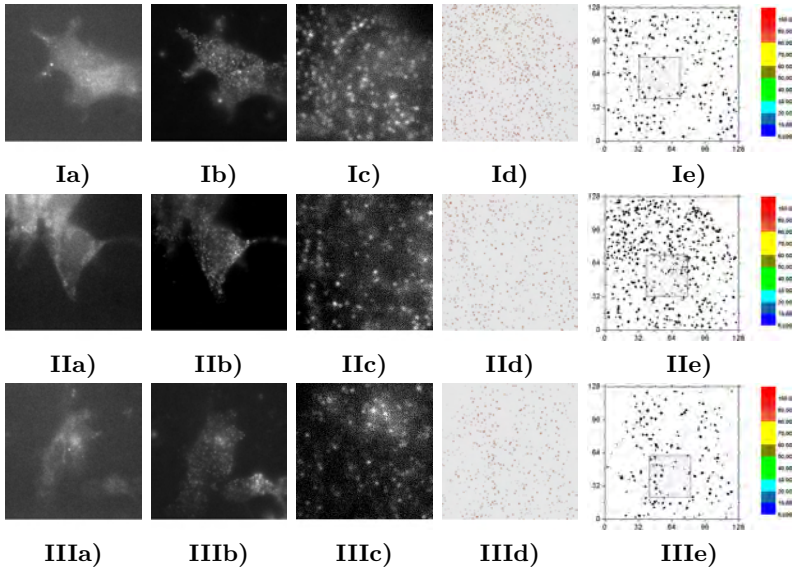

control with only secondary antibody: 24 hours of doxicycline induction

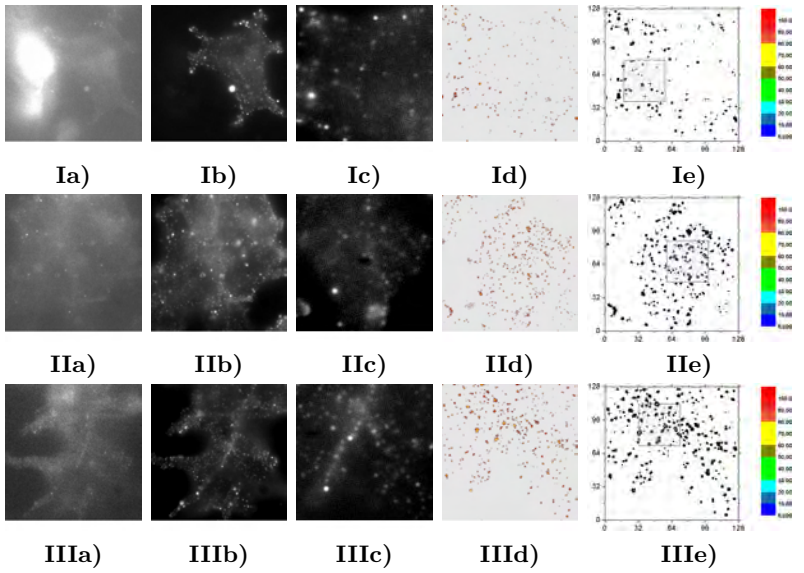

control with only secondary antibody: 32 hours of doxicycline induction

Acknowledgements

I am very grateful to everyone who supported me during the last few years and helped me making this work possible.

First and foremost I want to thank Markus Sauer for giving me the chance to write my PhD thesis in his group of Applied Laser Physics & Laser Spectroscopy at Bielefeld University. He early granted me an unexpected autonomy and a consequential high responsibility. Thus I gathered a lot of unique experiences and valuable knowledge, which I very much appreciate.

Markus Sauer, Sören Doose, Philip Tinnefeld, Hannes Neuweiler, Mike Heilemann and Anindita Mukherjee let me experience a very reliable, motivating and of course helpful assistance throughout my whole PhD time. A special thanks belongs to Gerd Wiebusch, who - next to his great merit of a consequent existence and functioning of a large number of devices and microscopic setups - was always keen to help with and improve my experimental demands as wells as answer any upcoming question.

Also I would like to thank all of my present and former PhD colleagues for fruitful discussions, exchange of knowledge and experiences, good ideas, motivations and cooperations. Here I want to especially mention Jan Vogelsang, Sebastian van de Linde, Robert Kasper, Ralf Brune and Fabian Humpert. For proofreading of this manuscript I want to thank Jan Vogelsang, Martina Lummer and especially Fabian Humpert.

Also I would like to acknowledge Rudolph Böttner and Joachim Ross. If it had not been for them, I wouldn't have ever ended up in the group of Applied Laser Physics & Laser Spectroscopy, writing a PhD thesis. This whole workgroup has always had a great working climate and I thank everyone who has contributed to that.

Furthermore I want to thank Martina Lummer from Molecular Cellphysiology at Bielefeld University for sharing her expertise on cell culture, K.H. Drexhage from Physical Chemistry at University of Siegen for the supply with the oxazine derivative MR121, J. Kopitz from Applied Tumorbiology at University Hospital Heidelberg for the supply with SK-N-MC cell line and Prof. Hans-Georg Kräusslich from the Department of Virology in the University Hospital Heidelberg for the supply with the HeLa cell line.

This work partly evolved out from the 'TumorVision' project, financed by the Biophotonics Program of the German Ministry for Education and Research (BMBF). Therefore I want to thank the BMBF, the Association of German Engineers (VDI) and all groups involved in this project, especially the responsible persons from R-Biopharm AG in Darmstadt, namely Peter Schubert, Rainer Wittig (now at ILM, Ulm University), Markus Böhl, Silvia Vosseler and Maria Reichert for a close cooperation and supply with cells, antibodies, enzyme and a lot of other chemicals and information. Also I would like to thank the project partners from the Laser Research Laboratory (LFL) in Munich - Hilmar Schachenmayr, Tobias Beck, Sabine Sandner and Herbert Stepp for a good cooperation and the authorization to realize experiments on their devices.

Alongside the help and guidance I received in and at work I also received a lot of help and strength from my private life. I can consider myself very glad to have a very reliable, welcoming and patient family, who always takes care, tries to understand my concerns and plans and helps me wherever possible. Also I would like to thank Tobias Siekmann for always being there for eons. Furthermore I am very grateful to Rocco, who tremendously brightened every day life and watched over me and this thesis quite intensively. I hope I was able to reverse all of his attempted typing contributions. For the strongest support to think of in every possible situation I would like to thank Fabian Humpert again. It's very relieving to sense, that there might be a chance to pay him all back one day.

Declaration

I hereby declare that the present thesis has been written by myself without the use of unallowed aids.

Bielefeld, November 18th 2009

Sigrun Henkenjohann

Erklärung

Hiermit erkläre ich an Eides statt, dass ich die vorliegende Arbeit selbstständig und ohne unerlaubte Hilfsmittel durchgeführt habe.

Bielefeld, den 18. November 2009

Sigrun Henkenjohann